Finite Element Modelling of Infant Head Impacts for use in Forensic Reconstructions

Tom Brooks

February 2021

A thesis presented for the degree of
Doctor of Philosophy in Mechanical Engineering.

Department of Mechanical Engineering
University of Canterbury
Christchurch, New Zealand

When you put a date on your dream, it becomes a goal.

When you aim for the goal, it becomes a challenge.

When you beat the challenge, the reward is success.

To have success… you need a dream…

-Raja Akhtar

Abstract

When a child is admitted to an Accident and Emergency department with head injuries considered to be suspicious, the parent or guardian often explains the history of the injury as resulting from a fall or similar accident. However, depending on the nature and seriousness of the injuries, medical professionals may suspect the injuries resulted from non-accidental causes. Without the history being corroborated by a second, reliable, witness, it can be difficult for any prosecution to prove beyond reasonable doubt that a child's injuries were a result of abusive head trauma. One method that has the potential to help improve the chances of a successful prosecution is finite element (FE) modelling. A FE model of an infant head can be used to reconstruct a case to determine whether the observed injuries are likely to have resulted from the history provided. However, infant head FE modelling is a developing field and cannot yet be used accurately, reliably and efficiently in forensic cases.

In this thesis, an extensive review of the existing literature was conducted to determine what is required to further develop infant head FE models. It was found that the greatest limitation was the lack of accurate material property data for the infant head tissues. This was followed by a lack of validation of local parameters (stress and strain), as well as a lack of investigation on the effects of drop height and different impact surfaces.

From these findings, a sensitivity analysis was carried out on the material model parameters of the tissues used in infant head FE models. This was to investigate which material model parameters had the greatest influence on the response of the model, allowing for guidance on future experimental work that will best make use of scarce human infant head tissues. The baseline FE model used in the sensitivity analysis was of a three-month-old infant occipital head impact with an impact speed of 2.4 ms^{-1}. An isotropic elastic material model was used to represent the behaviour of the cranial bones, while Ogden hyperelastic models were used for the scalp, suture and brain. The elastic modulus of the skull was found to have the greatest influence and it is recommended that future experimental work should prioritise increasing the data set for this parameter. The brain hyperelastic constants were found to be important for determining the local response of the brain tissue, while the scalp and suture hyperelastic constants had some influence over the global response. It is recommended that a further sensitivity analysis be conducted to investigate which material parameters are important for accurate prediction of tissue failure. This will be important for relating modelling results to forensic data.

Based on the findings from the sensitivity analysis, three-point bend testing of child cranial bone was conducted to improve the elastic modulus data. Due to the prompt brittle fracture and limitations of the high-speed cameras, elastic moduli data was not obtained; rather, preliminary observations were

made on the behaviour of the failure of child cranial bone at loading rates of 5.65 ms^{-1} (previous experimental work has only investigated up to 2.81 ms^{-1}). It was found that the failure mode in specimens aged two to 18 years was prompt brittle fracture, while bending before fracture occurred in the three-week-old specimens. Impact force ranged from 200 to 6000 N and was higher in the occipital bone than in the parietal or frontal bones. The energy absorbed to failure increased with age and thickness, with the occipital bone having a greater energy absorbing capacity due to its greater thickness.

Drop heights ranging from 0.05 to 1.8 m and impact surfaces consisting of carpet and a combination of carpet and underlay were investigated to determine the effect on the response of the FE model. Peak head acceleration increased, while impact duration decreased as drop height increased. While the softer surfaces of carpet and the carpet and underlay combination increased the impact duration, the peak head acceleration was not significantly affected by the addition of a softer surface. As these investigations did not consider tissue failure, a method of predicting skull fracture was also investigated. It was found that the method of element erosion can predict skull fracture based on where it would be expected to occur due to the maximum principal stress. However, it has limitations, including being dependent on mesh density, as refinement of the FE mesh resulted in a different fracture pattern.

The FE models used for each of these analyses, as well as in the sensitivity analysis, all used simplifying assumptions to make the computational time of the baseline model tractable. These assumptions mostly included neglecting various thin head tissue layers due to an increase in the mesh density required, and the associated increase in computational time. The baseline model consisted of a single layer scalp, cranial bones, suture brain and bonded contact at all tissue interfaces. To assess the validity of these assumptions, the neglected tissues were included in several variants of a higher fidelity FE model. Compared to the baseline model, the addition of each tissue resulted in an increase in the global stiffness due to the limitations associated with a bonded contact condition at the tissue interfaces. A model consisting of all tissues (a dual layered scalp, cranial bones, suture, dura, cerebrospinal fluid (CSF) and brain) and using frictional contact at the dura-CSF and CSF-brain interfaces resulted in a 1.7% and 3% increase in the peak head acceleration and impact duration respectively over the baseline model, but had a 70% greater computational time.

Overall, using FE models of the infant head to accurately reconstruct the injury patterns in forensic cases requires high-fidelity models. However, this comes at a significant computational cost. Standard professional grade computers are inadequate and high-performance computers have significant financial cost. Therefore, trade-offs with the computational cost and model fidelity are required to

make forensic reconstructions tractable. This thesis investigated what is required to further develop infant head FE models. Some of these requirements have been addressed in this thesis, or preliminary research undertaken to provide guidance for future work. As the field of infant head FE modelling develops, and computational power becomes more cost effective, the accuracy of such models and the financial cost will improve. This will allow forensic reconstructions of suspected abusive head trauma to be more easily investigated, bringing justice for those children who have been fatally injured from such trauma or protect survivors from future abuse.

Preface

Some material in this thesis has been published in peer reviewed journals. The author of this thesis has performed the corresponding simulations and experimental work, as well as the writing of the manuscripts.

Finite Element Models and Material Data for Analysis of Infant Head Impacts

Chapter 3 is largely based on this publication, with some content appearing Chapter 2.

Brooks, Tom, Jung Eun Choi, Mark Garnich, Niels Hammer, John Neil Waddell, Warwick Duncan, and Mark Jermy. 2018. "Finite element models and material data for analysis of infant head impacts." *Heliyon* 4 (12):e01010.

Sensitivity of Material Model Parameters on Finite Element Models of Infant Head Impacts

Chapter 4 is largely based on this publication. At the time of writing, the manuscript has been submitted to *Biomechanics and Modelling in Mechanobiology*, peer reviewed, revised and currently undergoing rereview.

Brooks, Tom, Mark Garnich, and Mark Jermy. 2020. "Sensitivity of Material Model Parameters on Finite Element Models of Infant Head Impacts." Under Review.

Preliminary Observations of the Sequence of Damage in Excised Human Juvenile Cranial Bone at Speeds Equivalent to Falls from 1.6 m

Chapter 5 is largely based on this publication.

Brooks, Tom, Johann Zwirner, Niels Hammer, Benjamin Ondruschka, and Mark Jermy. 2020. "Preliminary observations of the sequence of damage in excised human juvenile cranial bone at speeds equivalent to falls from 1.6 m." *International Journal of Legal Medicine*:1-12.

Acknowledgements

Many thanks to my supervisors Professor Mark Jermy and Associate Professor Mark Garnich for their support and guidance throughout my time in the PhD programme. It has been an interesting journey where I have been able to develop my skills as an engineer and I am grateful to you for providing me with this opportunity. I would also like to thank my collaborators from New Zealand and around the world for their help and guidance in this research: Professor Niels Hammer, Dr Benjamin Ondruschka and Dr Johann Zwirner.

Thank you also to David Ranson, Fiona Leahy and Yetunde Daramola of the Victorian Institute of Forensic Medicine for providing the infant head computed tomography scan data that I used in this thesis.

There are many people who have helped me throughout this journey with their expertise, bouncing ideas off, mentoring me or providing me with just a general chat. I have learnt something from you, no matter how small it may be, I thank you all: Paul Southward, Adam Latham, Garry Cotton, David Read, Ken Brown, Scott Amies, Eric Cox, Kevin Stobbs, Julian Phillips, David Rathgen, Dr Natalia Kabaliuk, Associate Professor Paul Docherty, Associate Professor Digby Symons, Tony Doyle, David Fanner, Dr Marzi Anjomrouz, Anton Good and Dr James Hewett.

I would like to make a special mention to Paul Southward and Adam Latham for allowing me the use of several computers in their lab in my final few months. Without these, I would not have been able to run the many thousands of hours of simulations I required in my last few chapters. You provided me with the single biggest resource for my thesis and I extremely grateful for this.

Finally, I would like to thank my family for putting up with me in the months since lockdown while I wrote this thesis.

Thank you to you all.

Tom Brooks

August 2020

Table of Contents

Abstract **3**

Preface **6**

Acknowledgements **7**

List of Abbreviations **13**

Chapter 1 Background, Motivation and Thesis Aims **15**

Introduction **15**

Background **15**

Anatomy of the Human Head 17

Head Injuries 20

Injury Criteria 22

Biomechanics of Head Impacts 23

Importance of Rotational Acceleration 24

Thesis Aims **25**

Chapter 2 Finite Element Theory **27**

Finite Element Method **27**

Geometry 27

Mesh 27

Material Models and Properties 30

Boundary Conditions 32

Contacts 32

Solvers 33

Validation 37

Summary of the FE Modelling Process **37**

Chapter 3 Literature Review and Thesis Aims **39**

Finite Element Models of the Infant Head **39**

Geometry 39

Meshes used in Infant FE Models 42

Properties of Tissues Measured from Human and Animal Samples 43

Material Models used in Infant FE Models to Date 44
Material Model Parameters used in Infant FE Models to Date 46
Boundary Conditions and Results 47
FE Model Validation -Human Infant Cadaver Experimental Head Impact Studies 53
Finite Element Models of the Adult Human Head 54
Human Infant Head Tissue Injury Thresholds 58
Discussion 60
Geometry 61
Meshing 62
Material Models 62
Boundary Conditions 64
Validation of the Complete Head Models 65
Recommendations for Future Work 67
Conclusions 68
Chapter 4 Sensitivity of Material Model Parameters 71
Introduction 71
Origin of Material Model Parameters 71
Methods 75
Geometry Creation 75
Boundary Conditions and Mesh 77
Material Models 79
Validation 80
Sensitivity Analysis 80
Results 82
Validation of Baseline Model 82
Sensitivity Analysis 84
Discussion 85
Validation and Limitations of Baseline Model 85

Sensitivity Analysis 87
Priorities for Future Research 89
Implications for Forensics 91
Conclusions 92
Chapter 5 Preliminary Observations of the Sequence of Damage in Excised Human Child Cranial Bone 95
Introduction 95
Methods 96
Specimen Preparation 96
Spectral Computed Tomography 97
Impact Test Machine 98
High-Speed Imagery 101
Results 102
Observations from High Speed Imaging 102
Average Thickness and HA Density vs Age 106
Maximum Impact Force 107
Energy Absorbed to Failure 108
Minimum Fracture Propagation Speed 108
Discussion 108
Limitations 108
Observations from High Speed Imagery 110
Average Thickness and HA Density 111
Maximum Impact Force 111
Energy Absorbed to Failure 112
Implications for Finite Element Models 113
Digital Image Correlation 113
Conclusions 114
Chapter 6 Applications of the Baseline Model 117

Introduction **117**
Methods **118**
Drop Height 119
Impact Surfaces 119
Impact on Surface Edge 122
Results **123**
Behaviour of Baseline Model 123
Baseline Model Validation 126
Drop Height 128
Impact Surfaces 131
Impact on Surface Edge 136
Discussion **138**
Behaviour of Baseline Model 138
Baseline Model Validation 138
Drop Height 142
Impact Surfaces 144
Impact on Surface Edge 147
Conclusions **148**
Chapter 7 Predicting Skull Fracture **151**
Introduction **151**
Methods **152**
Results **153**
Discussion **161**
Conclusions **167**
Chapter 8 Variations to Baseline Model **169**
Introduction **169**
Methods **170**
Impact Angle 170
Addition of a Dual Layer Scalp 170

Addition of CSF 171
Addition of Dura 172
Addition of Dual Layered Scalp, CSF and Dura 173
Addition of Foramen Magnum 174
Results 175
Impact Angle 175
Dual Layer Scalp 176
Addition of CSF 179
Addition of Dura 179
Addition of Dual Layer Scalp, CSF and Dura 180
Addition of Foramen Magnum 183
Discussion 185
Impact Angle 185
Addition of a Dual Layered Scalp 186
Addition of CSF 188
Addition of Dura 190
Addition of Dual Layer Scalp, CSF and Dura 191
Addition of Foramen Magnum 193
Conclusions 194
Chapter 9 Conclusions and Future Work 197
Conclusions 198
Future Work 202
Final Words 204
Appendix A 206
Appendix B 212
Appendix C 213
References ..... Error! Bookmark not defined.

List of Abbreviations

AHT	Abusive Head Trauma
CAD	Computer Aided Drawing
CSF	Cerebrospinal Fluid
CT	Computed Tomography
DAI	Diffuse Axonal Injury
DIC	Digital Image Correlation
DOF	Degree of Freedom
EDH	Epidural Haemorrhage
FE	Finite Element
FM	Foramen Magnum
FMVSS	Federal Motor Vehicle Safety Standard
FOV	Field of View
FSI	Fluid Structure Interaction
GCS	Glasgow Coma Scale
HA	Hydroxyapatite
HIC	Head Injury Criterion
LHS	Latin Hypercube Sampling
MDF	Medium Density Fibreboard
MP	Maximum Principal
MRI	Magnetic Resonance Imaging
NHTSA	National Highway Traffic Safety Administration
NURBS	Non-Uniform Rational B-Spline
NZ	New Zealand
RHS	Rectangular Hollow Section
ROI	Region of Interest
SD	Standard Deviation
VM	von Mises
WHO	World Health Organisation

Chapter 1 Background, Motivation and Thesis Aims

Introduction

When a child is admitted to an Accident and Emergency department with head injuries deemed to be suspicious, the parent or guardian often explains the history of the injury as resulting from a fall or similar accident. However, depending on the nature and seriousness of the injuries, medical professionals may suspect the injuries resulted from non-accidental causes. Without the history being corroborated by a second, reliable, witness, it is difficult for medical professionals to decide whether there are sufficient grounds to which the case should be referred to the New Zealand (NZ) Police and/or the Ministry for Children. Medical diagnosis can aid in this decision as studies have shown that particular injuries are more likely to have resulted from non-accidental causes rather than accidental causes. However, the decision is often based on the experience of the clinician.

If it is suspected that a child has suffered abusive head trauma (AHT), any prosecution often faces the difficult task with proving beyond reasonable doubt that a child's injuries were as a result of AHT. Medical professionals are called upon to testify on the probability that the injuries were accidental or non-accidental, which, again, is based on their clinical experience. Relevant literature on the types of head injuries observed in proven AHT cases are also often cited.

The problem is that in the absence of a reliable witness, it is difficult to determine whether a child has suffered accidental or non-accidental head injuries. This thesis aims to provide unique contributions to an existing but small field of developing tools in the form of a numerical model. A numerical model can be used in the forensic reconstruction of suspected cases of AHT to predict the nature of the head injuries and compare them to those observed.

Background

Head injury is the most common cause of death for infant and child homicides in the world (Butchart et al. 2006). In the United States, AHT resulted in the deaths of an estimated 2250 infants and children (less than five years old) during a 15 year period between 1999 and 2014 (Spies and Klevens 2016). Data for the number of children subject to AHT in New Zealand is limited, however, one media report details the deaths of 61 children resulting from non-accidental injuries between 2006 and 2015, of which 31 were violently assaulted (Leask 2016). Kelly et al. (2015) analysed data of children under 15 years old who were referred to a hospital child protection team in Auckland, NZ, with suspected AHT

for the 20-year period between 1991 and 2010. Of the 345 children referred, 60% were diagnosed as AHT, with 29% resulting from accidental or natural causes (the remaining 11% were unknown).

Domestic accidental falls are one of the most common causes provided by perpetrators of AHT for head injuries in children (Johnson et al. 2005). Plunkett (2001) reviewed more than 75 000 cases involving head and neck injuries in children that were stated as resulting from the use of playground equipment. Eighteen cases were found to involve short distance falls (mean of 1.3 m, range of 0.6 – 3.0 m) that resulted in fatal injury (age range of one to 13 years) (Plunkett 2001). Plunkett (2001) concluded that short distance falls may cause fatal pediatric head injuries. Some forensic pathologists disagree with this potential lethality and challenge the reliability of the witnesses. This is one of the most intensively discussed topics in clinical forensics, starting from one study by Chadwick et al. (1991). Chadwick et al. (1991) reviewed 317 cases of child injuries where the history was described by the caretaker as being that the child had fallen. In 100 cases where the child had fallen less than 1.2 m, seven were fatal, and in 117 cases of falls between three and 14 m, one was fatal. The seven fatalities in the short falls all had factors in their cases suggesting false histories (histories here is defined as an event or series of events leading to the injuries) (Chadwick et al. 1991). If the histories of these seven cases were to be believed, the results show that the risk of fatal injuries increase with decreasing fall heights.

In light of this controversy, Johnson et al. (2005) reviewed 72 cases of toddlers admitted to one Accident and Emergency department with head injuries resulting from accidental falls and concluded that typical accidental falls of less than one metre that occur in normal domestic situations do not commonly cause skull fractures. They report that “if the height of the fall is below 50 cm it is extremely unlikely to cause skull fracture”; while for falls over one metre, most children had visible cranial soft tissue injuries, with this number increasing over one and a half metres (Johnson et al. 2005). Hobbs (1984) found that skull fractures that were a result of an accident were generally at only one localisation, showing narrow linear fractures without exceeding skull sutures and with only rarely associated intracranial injuries (if at all, epidural bleedings in temporal fractures); however, AHT resulted in multiple, depressed and/or growing fractures along with intracranial injuries such as subdural hematoma (SDH), cortical concussions and diffuse axonal injuries (DAI). Similar results were also found by Chadwick et al. (1991), Williams (1991), and Wilkins (1997). Roach et al. (2014) reviewed data of children aged five years and under from the Children’s Hospital Colorado who sustained head injuries over a 16-year period (1996-2011). Based on the determination of the likelihood of the child’s injuries resulting from AHT or accidental injury by the hospital’s Child Advocacy and Protection Team, and the type of injuries observed in computed tomography (CT) scans, they were able to determine the type of head injuries more commonly seen in cases of AHT and mentioned above. Reece and Sege

(2000) earlier conducted a similar study for children admitted to a children's hospital from 1986 to 1991. In both studies, it was found that SDH and DAI were more common in cases of AHT, whereas skull fracture and epidural hematoma were more common in accidental head injuries. Although such indicators may point to a particular incident being *probably* a result of an accident or abuse, without reliable witnesses to the history of the injury, it is not possible to be sure or to quantify the probability when using only radiological data of the head.

Anatomy of the Human Head

The human head is a complex structure composed of a series of well-organised layers (Figure 1.1), including the skin (dermis) of the scalp, muscles and galea aponeurotica, the osseous skull, the three layers of meninges, and deeper the brain and cerebrospinal fluid (CSF). The skull forms the protective cavity for the brain and is made up of the eight different bones of the neurocranium that are fused together by the syndesmotic sutures. Inside the skull are the meninges, which consists of three layers that support and cover the brain and spinal cord externally (Schmitt 2014). The outermost layer of the meninges is the dura mater, followed by the arachnoidea mater and pia mater (not shown in Figure 1.1). The brain is surrounded by CSF, which cushions it against mechanical shock loading (Schmitt 2014).

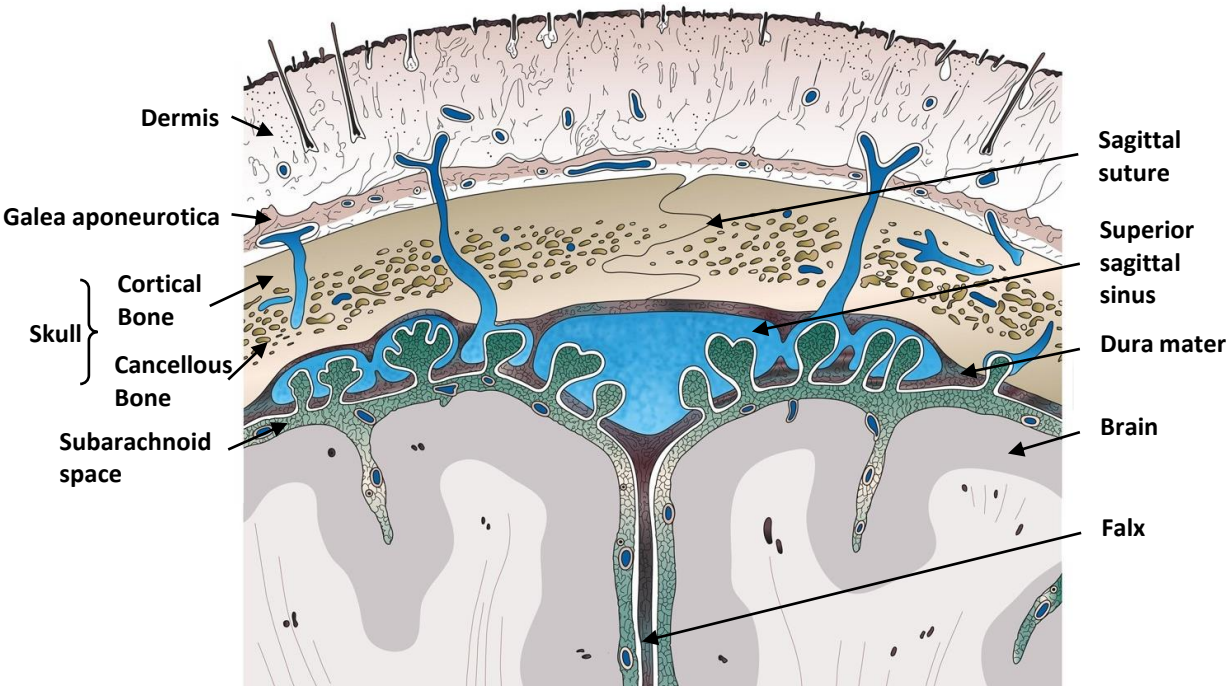

Figure 1.1: Cross-section of the human head ((Brooks et al. 2018), adapted from Waschke and Paulsen (2013)).

Scalp

The outer most layer of the human head is the scalp. It is made up of five layers, with the outer layer being the dermis, followed by the dense connective tissue, aponeurosis, loose connective tissue and periosteum. Scalp thickness varies depending on location (and age), with an average thickness of 3.2 mm for a six-month-old infant (Young 1959, Li, Sandler, and Kleiven 2017). In the context of head

impact biomechanics, the scalp has a significant effect on reducing linear and rotational accelerations and increasing the energy absorbed during the impact (Trotta et al. 2018).

Skull

The skull forms the protective cavity for the brain. It is made up of eight different cranial bones: frontal, occipital, left and right parietal, left and right temporal, ethmoid and sphenoid (Strachan 1970). The infant skull differs from that of an adult in that the cranial bones are thin, pliable plates that are separated by relatively more fibrous sutures.

Cranial Bone

At birth, infant cranial bone resembles a single layer of cortical bone with a fine network of trabeculae radiating outwards from the ossification centres. Between birth and six months old, this structurally differentiates into a composite with inner and outer layers of cortical bone sandwiching a layer of cancellous bone (Margulies and Thibault 2000). Cortical bone is solid with only small openings, primarily to give rise to blood vessels. Cancellous bone has larger openings and hence a higher surface area, leading to higher porosity and different mechanical behaviour. Cancellous bone may be thought of consisting of cylindrical struts (trabeculae) that are orientated approximately in the direction of the prevailing loads and intersecting with each other. In some regions, these struts are plate-like. The variation in shape, size and orientation of the struts gives a high level of anisotropy (Currey 2013).

Both cortical and cancellous bone are composites consisting of Type I collagen (a fibrous protein) surrounded by a crystalline hydroxyapatite (HA) (Currey 2013). Collagen comprises 85 to 90% of the protein in bone, has a relatively high tensile strength, but is weak under compressive loads (Kieser 2012, Currey 2013). Hydroxyapatite has a relatively high compressive strength, but is stiff and brittle (Kieser 2012). Bone is viscoelastic: its mechanical behaviour depends on strain rate, becoming more like a brittle elastic solid at high strain rates (Kieser 2012).

Suture

The suture is a fibrous tissue that fuses the cranial bones together. Areas of the more fibrous tissue sutures, called fontanelles, are present in the infant skull, between the cranial bones; these allow for both compression of the skull during birth and stretching of the skull as the brain grows. When just two cranial bones are joined, the fibrous tissue is called suture, while at the intersection of three or more cranial bones, it is called fontanelle. The two largest regions of fontanelle are the anterior and posterior fontanelles. The anterior fontanelle joins the frontal and the two parietal bones, while the posterior joins the occipital and the two parietal bones. As the cranial bones grow, the sutures start to fuse together and fontanelles gradually close. At approximately the age of two years, the sutures

have largely fused together, with the anterior fontanelle closing at around two and a half years old (Ridgway and Weiner 2004). The suture works in conjunction with the skull to absorb energy during an impact, thus protecting the brain.

Dura

The dura mater is the outer most layer of the three meninges layers and along with the CSF, encapsulates the brain, preventing it from contacting the inner surface of the skull during an impact. The average thickness of the dura ranges from 0.5 to 0.6 mm at a gestational age of 40 weeks (Bylski et al. 1986).

Cerebrospinal Fluid

The CSF is a colourless fluid that surrounds the brain, filling the subarachnoidal space (space between the brain and arachnoidea mater). It supports the brain by distributing the weight over the skull base; that is, the brain essentially floats within the CSF. This also allows it to cushion the brain against mechanical shock loading (Schmitt 2014).

Brain

The brain is one of the most complex organs in the human body, controlling all functions of the body. Therefore, nature has ensured that it is well protected by evolving the head tissues to have energy absorbing capabilities during impacts to the head. The brain consists of three main structures: the cerebrum, cerebellum and brainstem. The cerebrum is the largest of these structures and consists of gray matter around its outer rim and white matter filling the centre. It is divided into the left and right hemispheres, with each controlling different sensory and motor functions. The cerebellum controls muscular movement, while the brain stem connects the sensory input and motor output between the brain and spinal cord.

The brain is the most complex organ in the body. Traumatic brain injury (injury to the blood supply or the neural matter) frequently does not heal, so the consequences, if it is survived, can be lifelong debility (Mouzon et al. 2018, Olver, Ponsford, and Curran 1996, Weil and Karelina 2019).

Differences between the Infant and Adult Head

The infant head cannot be considered as a scaled version of an adult head due to significant morphometric and anatomical differences (Loyd 2011). Morphometrically, the infant head differs from that of an adult in terms of size and mass. At birth, the head makes up approximately 25% of an infant's body height, compared to approximately 14% for an adult (Burdi et al. 1969, Prange et al. 2004). The infant head has a mass of approximately 1 kg compared with approximately 4.5 kg for an adult (Loyd 2011). Anatomically, the infant and adult head differ in the structural arrangement of the

cranial bones. In adults, the cranial bones are rigidly connected by the sutures, making it stiffer and less deformable than an infant head. The infant head is more deformable due to the larger sutures and fontanelles. Infant cranial bones are thinner and largely consist of cortical bone before developing into the sandwich structure but are still much thinner than adult cranial bone. Overall, Loyd (2011) found that the global stiffness of the human head increases with age, with the adult head being three orders of magnitude stiffer than the infant head. The morphometric and anatomical differences mean that the biomechanical properties of the infant head cannot be extrapolated from those of the adult head.

Head Injuries

A head injury is an injury that is sustained to any part of the head, including the scalp, skull or brain. In general, head injuries can be categorised as either open or closed. If the dura mater is injured, then the injury is classified as open, but if it is not, then the injury is classified as closed (Schmitt 2014). Scalp and skull injuries result from contact loading, while brain injuries can result from either contact or inertial loading.

Scalp and Skull

Injuries to the scalp include abrasions or lacerations. They can be useful for determining the type of object that caused the injury, as well as the impact site (Whitfield 2009). Contusion (rupture of blood vessels within the tissue) within the scalp is also a common injury.

Skull fractures require a greater stress than punctures or lacerations to the scalp and, as suggested by Whitfield (2009), indicate that a relatively larger force is involved when the head injury is sustained. There are multiple types of skull fractures, including (Whitfield 2009, Schmitt 2014):

- Linear fracture: the most common fracture; extending out from the impact site along the lines of least resistance in the cranial bones (depending on the individual anatomy of the skull).
- Comminuted fracture: impact force is exerted over a large area of the skull, resulting in multiple fragments.
- Depressed fracture: impact force is exerted over a relatively smaller area of the skull, resulting in cranial bone fragments protruding inwards and potentially indenting the brain.
- Diastatic fracture: the fracture follows the suture lines and is common in children.
- Skull-base fracture: the fracture occurs in the base of the skull and can result in CSF leakage.

Minns and Brown (2005) state that simple linear skull fractures are the most common fracture resulting from an accidental injury. Non-accidental head injuries often result in fracture lines that branch, cross suture lines, are bilateral, are wider than five millimetres, or expands as a growing

fracture (Minns and Brown 2005). Skull fractures become medically important if the cranial bone is depressed into the brain, however, death can still occur without skull fracture. In a legal sense, skull fractures confirm that an impact occurred (Minns and Brown 2005).

Brain

Brain injuries can be classified into two broad categories: focal and diffuse injuries. Focal injuries are those where the damage to tissue is well defined locally and are generally visible with imaging techniques such as CT or magnetic resonance imaging (MRI). Such injuries include (Whitfield 2009, Schmitt 2014):

- Cerebral Contusion: where blood capillaries have ruptured within the brain tissue (bruising), occurring at the impact site (coup) or on the opposite side of the impact site (contra coup), generally as a result of the brain tissue moving against the inner surface of the skull.
- Epidural Haemorrhage (EDH): the blood vessels in the skull or dura rupture, resulting in bleeding in the epidural space (above the dura).
- Subdural Haemorrhage (SDH): bleeding below the dura mater in the subarachnoidal space, resulting from three common phenomena: the tearing of the bridging veins between the brain and dural sinuses, cerebral contusion into the subdural space, and/or direct laceration of arteries or veins from penetration injury (Castellani and Schmidt 2018). Subdural haematoma can be caused by rapid acceleration of the head and so does not necessarily require direct impact to the head.

Diffuse brain injuries are distributed throughout the brain and cannot be observed using CT or MRI imaging. Such injuries include (Schmitt 2014, Whitfield 2009):

- Diffuse Axonal Injury: rapid acceleration, particularly rotational, causing shearing forces to be exerted on axons (nerve fibre) within the central nervous system, resulting in damage to the axolemma (plasma membrane of an axon).
- Diffuse Vascular Injury: rapid acceleration causing shearing forces to be exerted on the blood vessels throughout the brain, resulting widespread haemorrhage.
- Brain Swelling: results in an increase in intracranial brain pressure.
- Concussion: often referred as mild traumatic brain injury and results from an impact to the head causing the brain to ‘shake’ (accelerate back and forth) inside the skull.

Concussion is likely to be the most well-known head injury for those with a non-medical background. In the medical world, there is no clear definition of concussion. The World Health Organisation (WHO) classifies mild traumatic brain injury as “an acute brain injury resulting from mechanical energy to the

head from external physical forces" (Carroll et al. 2004). Clinically, concussion has a variety of symptoms including confusion, disorientation, loss of consciousness for less than 30 minutes, memory loss, nausea, headache and vomiting.

Injury Criteria

Injury criteria can be defined locally or globally. Global injury criteria consider injury to the head as whole, generally in the form of the magnitude and duration of acceleration the head experiences during an impact. At a local level, injury can be defined by individual tissue thresholds, in terms of mechanical strength.

Global Injury Criteria

The human head can tolerate high accelerations for a short period of time or low accelerations for a longer period. However, if the head experiences a high acceleration for a long period of time, then there is the potential for head injury. The potential for injury is therefore a function of both the height and width of the acceleration curve.

The Head Injury Criterion (HIC) has early roots from the work by Gadd (1964) who used the Wayne State Tolerance Curve (WSTC) to develop what became the Gadd Severity Index. Versace (1971) then proposed a version of the HIC that uses a measure of the average acceleration that correlates with the WSTC. The US National Highway Traffic Safety Administration (NHTSA) then proposed the actual version of HIC and included it in the Federal Motor Vehicle Safety Standard (FMVSS) 208 (Schmitt 2014). The HIC can be calculated by:

$$HIC = max\left[\frac{1}{t_2-t_1}\int_{t1}^{t2} a(t)dt\right]^{2.5}(t_2 - t_1) \quad (1.1)$$

Where a is the acceleration (in units of acceleration due to gravity (g)) and t_1 and t_2 are arbitrary time points during the acceleration pulse (t_2 must be greater than t_1). FMVSS 208 requires that the difference between t_1 and t_2 to be no more than 36 ms and that the maximum HIC must not exceed 1000 for the 50th percentile male (Schmitt 2014). An HIC value of 1000 represents a 52% chance of adults sustaining severe injury (FMVSS 201). A proposed equivalent measure for children is an HIC value of 840 (Snyder et al. 1977), while for infants, a value of 390 is suggested (Klinich, Hulbert, and Schneider 2002).

The Glasgow Coma Scale (GCS) was first proposed by Teasdale and Jennett (1974) to complement other assessments of neurological function. At the time, there was no general agreement for a procedure on assessing and monitoring the level of consciousness of a patient (Teasdale and Jennett 1974). In the 40 plus years since its first proposal, the GCS is used by healthcare professionals in more

than 80 countries to assess the level of consciousness in patients (Teasdale et al. 2014). GCS assesses the patient's response to eye opening, verbal response and motor response. Depending on their response, the patient is given a score for each category, as outlined in Table 1.1.

Table 1.1: Glasgow Coma Scale

Feature	Response	Score
Eye Opening	Spontaneous	4
	To Sound	3
	To Pressure	2
	None	1
Verbal Response	Orientated	5
	Confused	4
	Words, but not Coherent	3
	Sounds, but no Words	2
	None	1
Motor Response	Obeys Command	6
	Localising	5
	Normal Flexion	4
	Abnormal Flexion	3
	Extension	2
	None	1

The score for each category can be added to give an overall score that can be used to determine the level of head injury in the patient. A severe head injury is classified as a score of three to eight, a moderate head injury as nine to 12, and a mild head injury as 13 to 15 (Rimel et al. 1982).

Local Injury Criteria

Local injury criteria use measures such as stress, strain, strain rate and pressure to evaluate the level of damage to individual head tissues. These measures are largely used in FE models to assess whether injury occurs and if so, to what severity. A detailed literature review of local injury criteria and tissue thresholds is presented in Chapter 3.

Biomechanics of Head Impacts

Head injuries are the result of either a static or dynamic mechanical load applied to the head. In most cases, the load is dynamic (varies over time). Dynamic loads can be defined as either an impact or inertial load (Gerber and Coffman 2007).

An impact load is where the head makes direct contact with another object; either a moving head contacts a fixed object (such as a fall), or a moving object strikes a stationary head (such as a weapon). Generally, injuries such as contusion in the scalp, skull deformation or fracture, and EDH can immediately be observed at the impact site (Gerber and Coffman 2007). As the impact load is applied to the head, the scalp compresses and the skull bends into the cranium. Stress waves propagate throughout the skull and into the brain (Gilchrist and O'Donoghue 2000). The bending of the skull can

cause fracture within the cranial bones. If the bending is large enough, the irregular surface of the inside of the skull can contact the brain, causing tissue damage to the brain (such as contusion). The load can also be transmitted to other areas of the head, resulting in injuries away from the original impact site. For example, if the head strikes a fixed object, it experiences a rapid deceleration causing it to come to a stop. The inertia of the brain means the brain continues to move in the forward direction, impacting the skull and causing tissue damage in the front portion (Gilchrist and O'Donoghue 2000). This is a coup injury, where injury occurs at the impact site (Schmitt 2014). The brain can then 'bounce' off the inside of the skull, travel rearwards and impact the rear of the skull. This results in damage to the rear portion of the brain and is termed contrecoup as injury occurs on the opposite side of the impact site (Schmitt 2014).

An inertial load is where the head experiences an acceleration (translational and/or rotational) that is a result of a load applied to another part of the body (such as the torso) and transmitted through the neck (Gerber and Coffman 2007, Ommaya, Goldsmith, and Thibault 2002). No contact injury occurs with the skull or scalp; however, the inertia of the brain leads the brain to move within the skull cavity, creating differential motion between the skull and brain (Ommaya, Goldsmith, and Thibault 2002). For example, during a head-on motor vehicle collision, the impact forces cause the vehicle to rapidly decelerate. The momentum of the body causes the body to continue its motion in the forward direction before becoming restrained by the seatbelt and hence starts to decelerate. Due to its inertia, the motion of the head lags that of the body. Relative to the torso, the head moves backwards, and the neck undergoes hyperextension. The inertia of the brain causes it to move in a forward direction relative to the skull, resulting in coup injury. As the torso continues to decelerate to a stop and the neck reaches maximum hyperextension, the inertia of the head then causes it to move in a forward direction, resulting in the neck undergoing hyperflexion. The differential motion of the brain relative to the skull is now rearwards, resulting in contrecoup injury as the brain impacts the rear of the skull (Schmitt 2014). This motion of the head is commonly known as whiplash. Inertial loads often cause injuries such as DAI and SDH due to deformation of the brain tissue from tension, compression and shear. Translational acceleration will cause tension and compression in the brain tissue, while rotational acceleration will cause shear (Gerber and Coffman 2007, Castellani and Schmidt 2018).

Importance of Rotational Acceleration

Holbourn (1943) noted three important physical properties of the brain: it has relatively uniform density, is extremely incompressible (due to high water content) and has a low shear modulus (little resistance to changes in shape compared to changes in size). The latter two properties means that tissue damage is proportional to shearing forces (Castellani and Schmidt 2018). As rotational accelerations cause shear forces within the brain, this means that brain tissue injury can occur through

shearing, even though there is no penetration of the skull. However, in the absence of skull penetration, translational forces, which are largely compressive in nature, have little effect on brain tissue integrity (Castellani and Schmidt 2018). The differential motion between the brain and skull as a result of rotational acceleration cause strains within the bridging veins. Tearing of the bridging veins between the brain and dural sinuses causes SDH. As discussed earlier, SDH has been found to be more prevalent in infant head injuries resulting from AHT rather than accidental falls (Hobbs 1984, Reece and Sege 2000, Roach et al. 2014). Head impacts from AHT could, for example, consist of a weapon impacting the head (impact load), or the infant being shaken (inertial load, often referred as shaken baby syndrome). These types of impacts are more likely to induce rotational accelerations, whereas an accidental fall is most likely to produce translational accelerations (causing injury to the brain by impacting with the inner surface of the skull), although, rotational accelerations can be induced depending on the orientation of the head and body during the fall. This provides a possible explanation for the prevalence of SDH in AHT.

Thesis Aims

The overall goal of this thesis is to make unique contributions to the existing literature on infant head FE models, which is a small but developing field. Improving the accuracy and validity of these models means that they can be used with greater confidence when investigating suspected cases of AHT in infants. However, greater accuracy comes with higher computational cost, which can make such investigations impractical. Therefore, the overarching question of this thesis is:

What is required to further develop infant head finite element models to make them sufficiently accurate for use in forensic reconstructions while having an acceptable computational cost?

A review of the literature was conducted in Chapter 3 and from this, further research aims were developed to guide the direction of this thesis in order to answer this question. These aims are:

1. Determine which material model parameters have the most influence on the response of an infant head FE model.
2. Determine which material model parameters are the most important for future experimental work, based on their influence (Aim #1) and the origin of existing data.
3. Conduct dynamic materials testing on human child cranial bone to advance the current data (based on the findings of Aim #2).
4. Investigate the effects of drop height and different impact surfaces on the response of an infant head FE model.
5. Investigate possible methods for predicting skull fracture in infant head FE models.

6. Investigate how differences in the fidelity of the FE model affect the output metrics and computational cost of an infant head FE model.

These aims are investigated in Chapters 4 to 8. Chapter 2 provides an introduction to FE theory and the modelling process to provide context to the concepts discussed in Chapter 3.

Chapter 2 Finite Element Theory

This chapter introduces finite element theory and the modelling process. Parts of this chapter were presented in Brooks et al. (2018).

Finite Element Method

Finite element (FE) modelling (Reddy 1993, Bathe 2006, Belytschko et al. 2013) is a numerical method of reaching an approximate solution to differential equations over the discretised domain of a problem. Most commonly, structural problems are solved with displacements at nodes as fundamental variables. The discrete displacements are used to interpolate displacements at all points. The primary and secondary calculations are for gradients in displacement that define strains and application of a constitutive law to determine stresses. The FE method involves the creation of a geometry that represents a problem of interest, discretising the geometry into subdomains ('elements'), applying boundary conditions and material constitutive laws, and then solving the resulting equations numerically. The results should be validated against experimental data or 'hand calculations' to ensure the FE model is correctly representing the physical behaviour. Figure 2.1 provides a summary of the FE modelling process.

Geometry

The geometry used in a FE model should be an accurate representation of the physical object being investigated. However, simplifications may be required to ensure the discretisation does not become more complex than necessary. For example, fillets can cause increased discretisation due to their curvature. If the fillet is not specifically in a region of interest (for results) or importance (no boundary conditions are in its vicinity), then it can be removed to simplify the geometric representation of the object.

Mesh

When the geometry of a model is discretised, it is broken up into subdomains called elements. The complete set of elements make up the mesh. Each element is defined by a set of nodes (the number of nodes depends on the element type), with each node being generally a location at which adjacent elements are connected to each other. The nodes are points in the mesh where the degrees of freedom (DOF) are defined. The DOF represent displacement in structural problems with up to six (three translational and three rotational) at each node. The displacement field over the volume of the element is defined by an assumed interpolation function that is generally a polynomial. It is often termed a 'shape function' as it defines the possible deformed shapes of the element. The computed

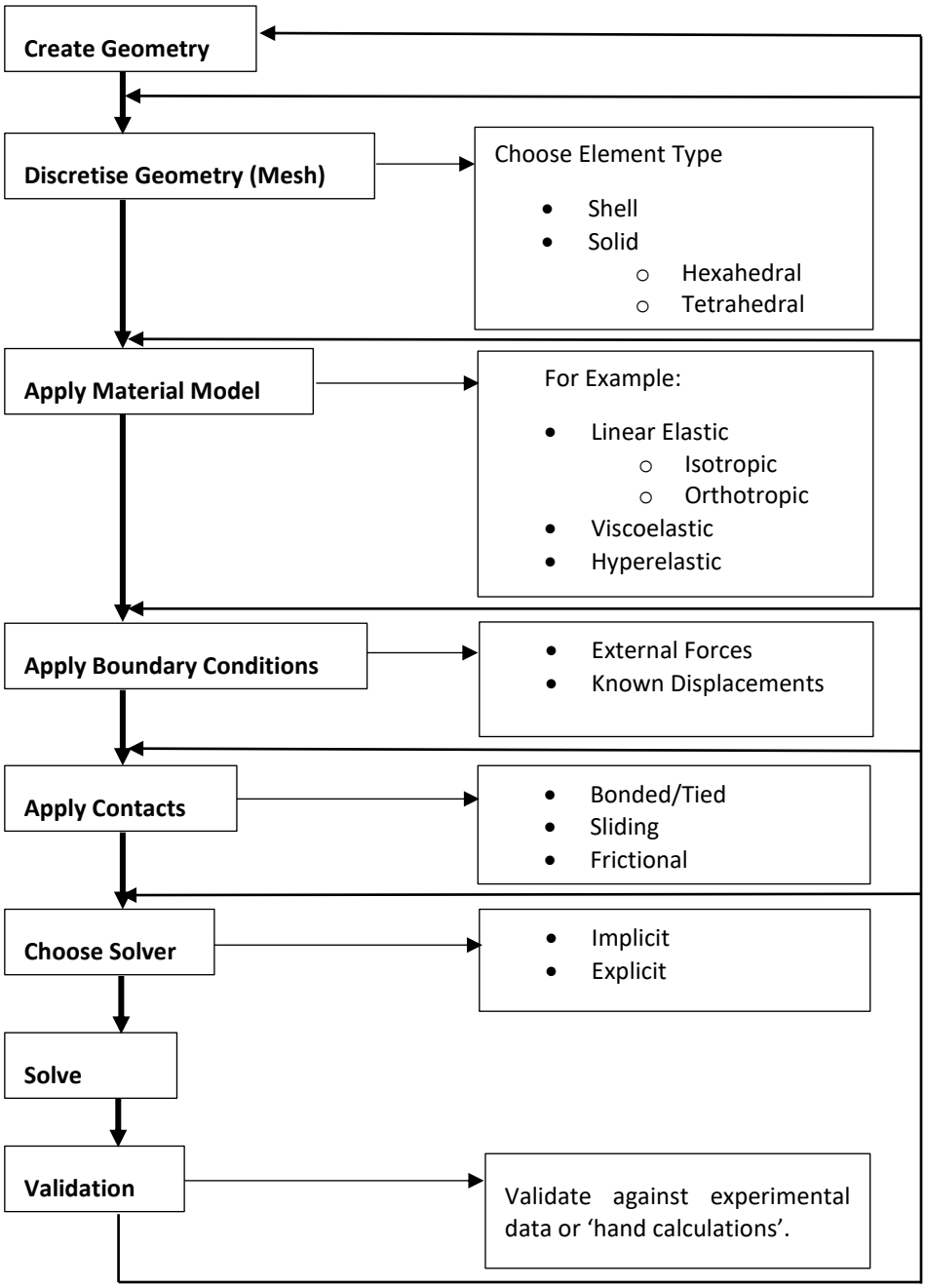

Figure 2.1: Process of finite element modelling.

nodal displacements define the polynomial coefficients. More nodes in an element enables higher order interpolation. However, first and second-order interpolation (linear and quadratic elements respectively) are most common because of their computational efficiency and straightforward application.

The mesh may be refined in areas of importance to ensure an accurate representation of the displacements and stresses are captured.

In a FE mesh, different elements are used depending on the structure being modelled. Common elements for a three-dimensional (3D) model include shell elements and solid elements.

Shell Elements

Shell elements are commonly used to model thin walled structures where simplifying assumptions can be made about the through thickness behaviour. A thickness is associated with them, but they are generally represented by nodes located on the mid-thickness of the structure. Shell elements inherently simplify the kinematics of deformation in the thickness direction; a simplifying assumption that should be validated. In addition, the use of shell elements may limit the choices of material models that can be employed. Typical applications include the modelling of sheet-metal structures, pressure vessels and aircraft wings.

Solid Elements

Sometimes simplifying assumptions about structure behaviour cannot be made and fully 3D representations are required. In these cases, solid (or volume) elements must be used where a 3D volume representation of the structure is created. This generally results in more nodes and therefore higher computational expense. However, very accurate representations of structure behaviour can be achieved.

Solid elements are generally tetrahedral or hexahedral in shape. Hexahedral elements are shaped like a brick and are generally favoured due to their higher computational efficiency, but they lose accuracy when they are significantly distorted from the ideal rectangular shape. Geometric complexity often results in highly distorted hexahedrons, therefore, the less computationally efficient tetrahedral elements are often employed due to the relative ease of creating a mesh, especially on curved surfaces.

Care must be taken when discretising curved surfaces with linear elements as the linear approximation results in mass and volume errors due to the piecewise linear approximation to the curve. Using smaller elements will minimise this loss of information, however there is a trade-off with increasing the computational time.

Reduced integration hexahedral elements are commonly used due to their computational efficiency. Linear, reduced integration elements have a single integration point at the centroid of the element where the stress is calculated. This results in the potential for hourglass deformation, which leads to nonphysical oscillations with no stress in the element. Consider a linear, reduced integration hex element in Figure 2.2. If equal but opposite moments are applied to opposing sides (pure bending), the lengths of the broken lines do not change, along with the angle between them. Therefore, the

stress at the integration point is zero. No strain energy is generated and thus this mode of deformation is a zero-energy mode. In a mesh, this deformation mode is called hourglassing due to the elements creating an hourglass shape. Hourglassing can be controlled by refining the mesh or the addition of artificial viscous damping or stiffness. It is recommended that hourglass energy does not exceed 10% of the total system energy in a FE model.

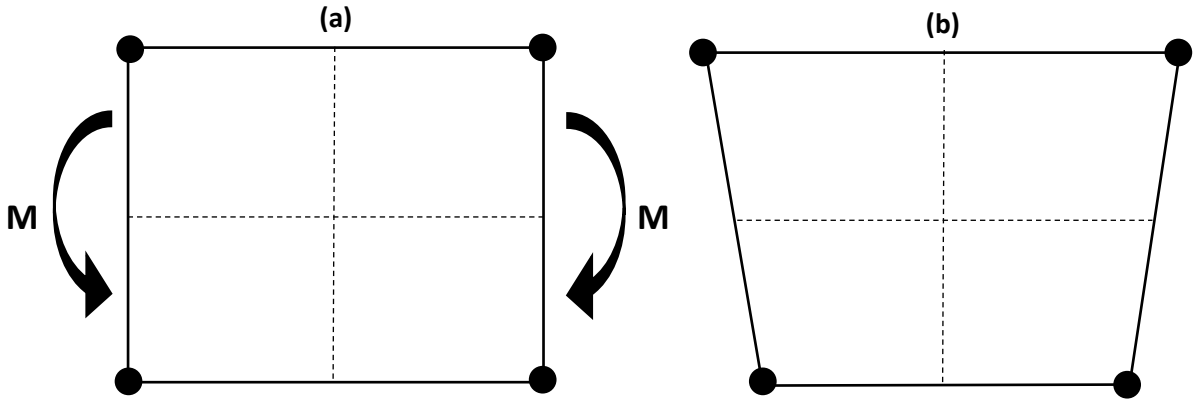

Figure 2.2: Reduced integration hex element experiencing equal but opposite bending moments on opposing sides **(a)** results in no change to the broken lines **(b)** and hence zero stress at the integration point (hourglassing).

Material Models and Properties

In an FE model, material models are selected from a set of alternatives which employ different assumptions about the behaviour of the material. For example, isotropic linear elastic models are commonly used in analyses involving metals and loading conditions that do not exceed the yield strength and may adequately model some biological materials at low strain. Viscoelastic and hyperelastic models reproduce some of the important behaviours of biological materials at high strains, or variable strain rates. High strain rates are common in injury-causing impacts.

Linear Elastic Models

A linear elastic model can be used to represent the behaviour of a material where the stress is proportional to strain, the strain is small, there is no dependence on the rate of loading, and the material will undergo no permanent deformation (that is, it returns to its original shape) (Bower 2009). The model will represent the material up to its elastic limit, which, for traditional engineering materials, is the yield stress.

If the material is isotropic and linear elastic, then only two material constants characterise the material behaviour. For example, Young's modulus and Poisson's ratio. If the material is anisotropic (that is, the properties are different in different directions), then, depending on the assumed type of anisotropy, different numbers of elastic constants are required. For a transversely isotropic material

model, there are five independent constants, while for an orthotropic model, there are nine independent constants (Bower 2009). Other types of anisotropic material models are rarely used.

Viscoelastic Models

A viscoelastic material adds a viscous, dissipative component to the elastic behaviour. Loading or strain rate dependent behaviour can be represented, and the deformation is time dependent. On a stress-strain curve of a viscoelastic model, the loading and unloading curves are different, the hysteresis being due to energy dissipation by the viscous behaviour. The most common type of viscoelastic model calculates the shear modulus, *G*, as a function of time, *t*, by (Ferry 1980):

$$G(t) = G_\infty + (G_0 - G_\infty)e^{-\beta t} \tag{2.1}$$

Where G_∞ is the long-term shear modulus, G_0 is the instantaneous shear modulus and β is the viscoelastic decay constant. This time dependence of material stiffness results in creep strain under constant stress, and stress relaxation under constant strain. Biological tissues typically exhibit noticeable viscoelastic behaviour.

Hyperelastic models

Most materials deviate from a linear stress-strain relationship at large strain. Hyperelastic material models reproduce this nonlinearity by deriving the stress-strain relationship from a strain energy function. They are inherently nonlinear because of the large strain regime they are intended for and different hyperelastic models are accurate over different strain ranges. Different models may also be selected depending on the experimental data that is available. For example, the Ogden model requires at least uniaxial and equibiaxial test data. For an Ogden hyperelastic model the strain energy function is defined as (Ogden 1984):

$$W = \sum_i^N \frac{\mu_i}{\alpha_i}(\lambda_1{}^{\alpha_i} + \lambda_2{}^{\alpha_i} + \lambda_3{}^{\alpha_i} - 3) + \frac{1}{d}(J-1)^2 \tag{2.2}$$

Where λ_i are the principal stretches, μ and α are the Ogden constants, *J* is the determinant of the elastic deformation gradient, *d* is a material incompressibility factor determined from the bulk modulus and *N* is the order of the Ogden model used. For a Mooney-Rivlin hyperelastic model (Mooney 1940, Rivlin 1948), the strain energy function is expressed in terms of the principal invariants, I_i, and can be defined by an infinite series (ANSYS Inc. 2019b):

$$W = \sum_m \sum_n C_{mn}(I_1 - 3)^m (I_2 - 3)^n + \frac{1}{d}(J-1)^2 \tag{2.3}$$

Where C_{mn} are material constants defined by curve fitting stress-strain data from physical testing. The number of parameters in the expansion of the series depends on the accuracy required.

Linear versus Nonlinear Material Models

Linear elastic material models are the most common models used in infant head impact studies to date. The required parameters are easier to measure than those required for more advanced nonlinear models. Linear models are computationally inexpensive. However, they cannot accurately represent the material behaviour at high strains, nor account for nonlinear or time dependence of the relationship between stress and strain.

Nonlinear material models are better able to model material behaviour at high deformations and strains, as well as rate dependent behaviour (although rate dependence can be linear). This allows for accurately modelling of the material under dynamic loads where the rate at which the load is applied can be varied, resulting in different material behaviour. Nonlinear models are however more complex to fit to experimental data. They are also more computationally expensive because an iterative solution is required for each increment in load.

Boundary Conditions

A boundary condition is a known displacement or force that represents the effects of the external environment on the model; that is, the effects of everything else that has not been modelled. These displacements and forces are applied at the nodes. Common boundary condition types include:

- Dirichlet: a value the displacement or force must have at the boundary.
- Neumann: a value the derivative of the solution must have at the boundary.

In structural problems, Dirichlet boundary conditions are common as known forces can be directly applied to the boundary, or constraints used to limit the motion of nodes on the boundary in the form of zero displacements that restrict all or some of the DOF. Neumann boundary conditions are common in, for example, thermal analyses, where a heat flux may be specified at a boundary.

Symmetry can be used to simplify a model where the geometry and boundary conditions are symmetrical. When symmetry is used, the nodes on the symmetry plane are fixed in the direction normal to the symmetry plane, along with rotation about the two axes that define the symmetry plane.

Contacts

Often it is desirable to simulate the contact between two bodies or even self-contact of a single body. Two bodies that are in contact with each other do not interpenetrate. In an FE model, elements do not know when they overlap one another and therefore the model needs to know what boundaries are likely to result in contact so that contact checking calculations can be efficiently performed. Algorithms can then be used to detect when element overlap occurs, with contact detection in the

form of either surface-surface or node-surface contact. Node-surface contact is less complex and so is more commonly used. This type of contact detection looks for nodes of a slave surface penetrating a master surface. When such contact is detected, a constraint is created between the penetrating nodes of the slave surface and the nodes in the adjacent area of the master surface. This results in contact forces at the nodes on the contact surfaces and the resultants are equal and opposite on the slave and master surfaces. There are a variety of algorithms for enforcing the contact constraints, such as the Lagrange multiplier method, penalty method and augmented Lagrangian method (Wu and Gu 2012). The penalty method is common in explicit dynamics analyses. In general, this involves determining the contact force using a contact penalty stiffness to minimise penetration of the master surface.

Generally, the analyst must determine the type of contact that defines the interaction between two bodies. Typical contact types include, bonded (nodes cannot separate or slide relative to one another after contact), sliding (nodes can slide relative to each other but not separate), or frictional (nodes can separate and slide relative to one another, with frictional coefficients used to determine the frictional forces).

Solvers

Depending on the type of FE model being created, an implicit solver or an explicit solver can be used. In implicit methods, the dependent variables are defined by coupled equations which must be solved simultaneously, typically with iterative or matrix methods. They have an advantage of being more numerically stable than explicit methods and so larger step sizes can be used. Implicit solvers are, for example, most often used in analyses involving static loading conditions. Implicit solvers can also be applied to dynamic problems but are computationally expensive due to the repetitive solution of simultaneous equations at each time increment. An explicit solver solves a system of equations each describing a variable in the later state in terms of the known current state. All equations need not be solved simultaneously which is much more efficient and amenable to parallel processing with large numbers of processors. This has an advantage of being relatively quick to solve, however, there is a stability requirement that generally requires much smaller time steps than for implicit solvers. Explicit solvers are used in FE models that simulate dynamic events (such as impacts or blasts) or nonlinear structural mechanics (such as complex material behaviour combined with contact conditions). They can deal with highly nonlinear problems without the convergence issues that are common when using an implicit solver.

Explicit Dynamics Solution Method

In general, the solution method for an explicit dynamics analysis involves two inter-related stages: nodal calculations and element calculations. For the nodal calculations, Newton's second law is used to calculate the nodal accelerations, which are then integrated explicitly (using a central difference method) in time to calculate the nodal displacements. The element calculations use the nodal displacements to compute the strain rates and subsequently the element strain increments. Constitutive equations are then used to compute the stresses, which in turn are used to calculate the internal nodal forces. Boundary conditions (external forces and constraints) and contact conditions are used to calculate the external nodal forces.

When an explicit analysis begins, the initial conditions are used to calculate the initial nodal displacements. The element calculations are then carried out, with the resulting internal and external nodal forces substituted into Newton's second law so that the nodal calculations can be performed. The solution time is advanced by one timestep and the process is repeated until the final time is reached.

Equations of Motion

Consider a body, B_t, in motion (with a velocity $\dot{\boldsymbol{u}}$), subject to body forces, $\boldsymbol{f}_i$, (per unit mass) and surfaces forces, $\boldsymbol{t}_i$, acting on the surface, S, with a normal vector $\boldsymbol{n}_i$ (Figure 2.3). The linear momentum of B_t is:

$$\boldsymbol{L} = \int_{B_t} \dot{\boldsymbol{u}}\, dm = \int_V \rho \dot{\boldsymbol{u}}\, dV \tag{2.4}$$

Where ρ is the mass density.

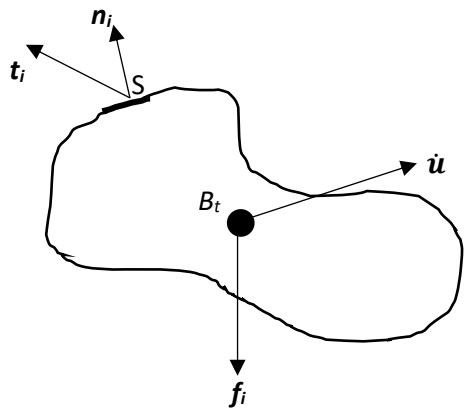

Figure 2.3: Body in motion subject to body and surface forces.

The principle of linear momentum states that the rate of change of linear momentum of a body is equal to the resultant forces (both body and surface forces) acting on it.

$$\frac{D}{Dt}\int_V \rho\dot{\boldsymbol{u}}\, dV = \int_S \boldsymbol{t}_i\, dS + \int_V \rho\boldsymbol{f}_i\, dV \tag{2.5}$$

By applying $\boldsymbol{t} = \sigma\, \boldsymbol{n}$ and the divergence theorem to convert the surface integral to a volume integral, and that the derivative of velocity is acceleration, then:

$$\int_V \rho\ddot{\boldsymbol{u}}\, dV = \int_V \nabla\cdot\sigma_{ij}\, dV + \int_V \rho\boldsymbol{f}_i\, dV \tag{2.6}$$

Where σ_{ij} is the Cauchy Stress. If the integral is valid for the whole volume:

$$\rho\ddot{\boldsymbol{u}} = \rho\boldsymbol{f}_i + \nabla\sigma_{ij} \tag{2.7}$$

This is the governing equation in an explicit dynamics analysis.

By setting the virtual work to zero, discretising the domain into a series of finite elements and using interpolation functions, a form of Newton's second law can be derived (readers are referred to Bathe (2006), Wu and Gu (2012), or Belytschko et al. (2013) for further derivation details):

$$\ddot{\boldsymbol{u}}^N M_{ii} = \boldsymbol{F}_E^N - \boldsymbol{F}_I^N \tag{2.8}$$

Where *N* is the node number, *M* is the mass matrix, $\boldsymbol{F}_E$ and $\boldsymbol{F}_I$ are the external and internal nodal forces respectively at node *N*. Nodal accelerations can be calculated by:

$$\ddot{\boldsymbol{u}}^N = M_{ii}^{-1}(\boldsymbol{F}_E^N - \boldsymbol{F}_I^N) \tag{2.9}$$

The mass matrix here is generally lumped; that is, it is assumed the mass of the element is modelled at the nodes of the element, resulting in a diagonal matrix. Using a diagonal matrix makes the inversion computationally trivial. Equation 2.9 is an ordinary differential equation of second order in time. It has been discretised in space but not time.

The internal and external nodal forces are functions of both time and nodal displacements. The nodal displacements and their derivatives determine the strains and strain rates. Using the constitutive equations, stresses can be calculated from the strains. The stresses are then used to calculate the internal nodal forces. The external nodal loads are generally prescribed as functions of time (resulting from the system boundary conditions) and can be functions of the nodal displacements if they depend on the configuration of the body (such as when pressure forces are applied to surfaces that undergo large deformations). The internal and external nodal forces are calculated from (see Bathe (2006), Wu and Gu (2012), or Belytschko et al. (2013) for derivations):

$$F_I = \sum_{k=1}^{N_k} \left[\int_{V_e} \sigma_{ij} \frac{\partial Q}{\partial x_j} dV_e \right] \tag{2.10}$$

$$F_E = \sum_{k=1}^{N_k} \left[\int_{V_e} \rho f_i Q \, dV_e + \int_{S_e} t_i Q \, dS_e \right] \tag{2.11}$$

Where N_k is the total number of elements, Q is the interpolation function for the elements and subscript e denotes the element volume or surface.

Using these equations for the nodal forces, the nodal accelerations can be calculated using equation 2.9. The central difference method is used for explicit integration of the nodal accelerations to calculate the nodal velocities and displacements.

Let the time of the simulation be $0<t\leq t_f$ where t_f is the final time of the simulation. Divide the simulation time period into time steps of Δt^n where n = 1 to n_T (n_T is the total number of time steps). A variable time step is required as the stable time step can change as the mesh deforms and the wave speed changes. The time increments are defined by:

$$\Delta t^{n+\frac{1}{2}} = t^{n+1} - t^n, \; t^{n+\frac{1}{2}} = \frac{1}{2}(t^{n+1} + t^n), \; \Delta t^n = t^{n+\frac{1}{2}} - t^{n-\frac{1}{2}} \tag{2.12}$$

The central difference method for acceleration is:

$$\ddot{\boldsymbol{u}}^n = \frac{\dot{\boldsymbol{u}}^{n+\frac{1}{2}} - \dot{\boldsymbol{u}}^{n-\frac{1}{2}}}{t^{n+\frac{1}{2}} - t^{n-\frac{1}{2}}}$$

$$= \frac{\dot{\boldsymbol{u}}^{n+\frac{1}{2}} - \dot{\boldsymbol{u}}^{n-\frac{1}{2}}}{\Delta t^n} \tag{2.13}$$

The velocity can be calculated by rearrangement:

$$\dot{\boldsymbol{u}}^{n+\frac{1}{2}} = \dot{\boldsymbol{u}}^{n-\frac{1}{2}} + \Delta t^n \ddot{\boldsymbol{u}}^n \tag{2.14}$$

Substitution from equation 2.9 gives:

$$\dot{\boldsymbol{u}}^{n+\frac{1}{2}} = \dot{\boldsymbol{u}}^{n-\frac{1}{2}} + \Delta t^n M^{-1}(\boldsymbol{F}_E^n - \boldsymbol{F}_I^n) \tag{2.15}$$

The velocities here are defined from the midpoints of the time intervals. Nodal displacements can be calculated using the central difference method for velocity:

$$\dot{\boldsymbol{u}}^{n+\frac{1}{2}} = \frac{\boldsymbol{u}^{n+1} - \boldsymbol{u}^n}{t^{n+1} - t^n}$$

$$= \frac{1}{\Delta t^{n+\frac{1}{2}}}(\boldsymbol{u}^{n+1} - \boldsymbol{u}^n)$$

$$\therefore \boldsymbol{u}^{n+1} = \boldsymbol{u}^n + \Delta t^{n+\frac{1}{2}} \dot{\boldsymbol{u}}^{n+\frac{1}{2}} \tag{2.16}$$

Now that the increment in nodal displacements have been calculated, the algorithm advances to the next time step (n+1) and the subsequent nodal strains, stresses, forces, accelerations and velocities are calculated, continuing until t_f is reached.

Providing the mass matrix is diagonal, the update of nodal velocities and displacements can be carried out without solving any equations. This is a characteristic of explicit methods, where the time integration of the discrete momentum equations do not require the solution of simultaneous equations (Belytschko et al. 2013). Explicit time integration is a simple, robust method and easily implemented. However, a trade-off for the simplicity is the conditional stability. The solution will grow unbounded if the time step exceeds a critical value, Δt_{cr}. The critical time step is the smallest time step such that a stress wave cannot travel further than the smallest element characteristic length, h, in a mesh, in a single time step. It is defined by (Courant, Friedrichs, and Lewy 1928):

$$\Delta t_{cr} = \min_e \left(\alpha \left[\frac{h}{c} \right] \right) \tag{2.17}$$

Where α is the stability time step factor and c is the speed of sound in the element material. The element characteristic length is calculated depending on the element type. In ANSYS Explicit Dynamics (ANSYS, Inc., Canonsburg, Pennsylvania, USA), for a tetrahedral element, it is calculated as the minimum distance of any element node to its opposing element face, while for a hexahedral element (ANSYS Inc. 2019b):

$$h = \frac{V_e}{l^2} \sqrt{\frac{2}{3}} \tag{2.18}$$

Where l is the length of the longest diagonal in the element.

Validation

Validation of a FE model is one of the most important steps in the modelling process as it allows the analyst to determine how well the simplified model represents the physical system. Generally, the FE model is used to predict the response of a real-world case in which experimental data exists. Comparisons can be made between the predicted model and experimental data. As with all engineering analyses, it is up to the engineer to determine the level of agreement required for the FE model to be deemed valid. Consideration of any simplifying assumptions needs to be made when making this determination.

Summary of the FE Modelling Process

The FE modelling process involves many steps that all require careful consideration in order to develop a valid and accurate representation of the physical system of interest. Consideration needs to be given

to the complexity of the geometry, element type used, material models, appropriate boundary conditions, solver type and suitable validation methods. Modelling of biological systems have additional complexity in these areas over traditional engineering analyses due to their often-complex geometries, age and rate-dependent material properties, and complex boundary conditions. Therefore, it is important that appropriate decisions are made for all steps in the FE modelling process so that it models the biological system as accurately as possible. The degree to which a model represents a real biological system is termed biofidelity.

Chapter 3 Literature Review and Thesis Aims

This chapter provides a literature review of finite element models of the infant head, as published in Brooks et al. (2018). Additions have been made to cover subsequent publications. A brief review of adult finite element models and tissue injury thresholds is also provided. Background information on the anatomy of the human head, and different head injuries is presented in Chapter 1.

Finite Element Models of the Infant Head

Biological systems are inherently difficult to model due to complex geometry, heterogeneity, nonlinear behaviours of the materials involved and often poorly defined boundary conditions. Generalised finite element (FE) models of the infant head are far more challenging than those for the adult head due to the rapid development a child undergoes in the first few years of life, and the material properties of the infant's head tissues change as the infant grows. Exacerbated by the scarce availability of infant cadaver samples, determining the material properties of the tissues that constitute the infant head is the primary limiting factor in infant head FE models. To date, only a handful of published studies have been carried out that involve infant head FE models (Margulies and Thibault 2000, Coats, Margulies, and Ji 2007, Roth et al. 2007, Roth, Raul, and Willinger 2008, Roth, Raul, and Willinger 2010, Ponce and Ponce 2011, Li et al. 2013, Li, Luo, and Zhang 2013, Li, Liu, et al. 2015, Li, Sandler, and Kleiven 2017, Hajiaghamemar et al. 2018, Khalid et al. 2019, Li, Sandler, and Kleiven 2019, Burgos-Flórez and Garzón-Alvarado 2020). Table 3.1 provides a brief summary of these. A valid FE model for the infant head needs the correct geometry, material properties and boundary conditions. The following sections will outline how these requirements have been tackled by previous infant FE models.

Geometry

Human head geometries are more complex than most geometries used in traditional engineering structures due to the large number of curved surfaces. As a result, it is difficult to create an accurate head geometry with Computer Aided Drawing (CAD) software. Instead, most studies begin from Computed Tomography (CT) or Magnetic Resonance Imaging (MRI) data. CT uses X-ray absorption measurements on many different lines of sight to create cross sectional images. Multiple cross-sectional images are stacked to construct a three-dimensional (3D) image (Cierniak 2011). MRI scanners use oscillating magnetic fields to stimulate radio frequency emissions from hydrogen nuclei. Gradients in a steady magnetic field allow the location of the emitting nuclei to be determined (Brown et al. 2014). While CT usually has a greater resolution, it involves a dose of ionising radiation,

therefore, MRI is preferred if it yields satisfactory images. With the data from either CT or MRI, the shape of individual organs or structures of interest can be extracted (segmentation) and converted into 3D geometry formats that can be imported into FE software packages so that a mesh can be generated.

Most FE models involving infant head impacts use geometric data from a single individual of a given age (Coats, Margulies, and Ji 2007, Roth et al. 2007, Roth, Raul, and Willinger 2008, Roth, Raul, and Willinger 2010, Li et al. 2013, Li, Luo, and Zhang 2013, Li, Sandler, and Kleiven 2017, Hajiaghamemar et al. 2018, Khalid et al. 2019, Li, Sandler, and Kleiven 2019, Burgos-Flórez and Garzón-Alvarado 2020). This ensures realistic representation of that specific individual but may not reliably account for variations in geometric features between individuals and the anatomical differences of the infant skull as it develops. In contrast, several research groups have CT scan data to develop generic geometric representations that can be morphed to represent different age classes of infants. For example, Li, Park, et al. (2015) created a statistical model for the zero to three month old infant skull, using CT scan data from 56 children. Geometric features of the infant skull, such as the skull size, shape and thickness, as well as suture width, were quantified using CT images and statistical analysis. A model was then created so that the geometry of an actual infant skull could be generated based on the age and head circumference of the infant. Li et al. (2013) created a statistical model of an infant's cranium geometry using multiple CT scans and a combination of multivariate regression and principal component analyses. The geometry was then used to create a baseline FE model that could be morphed into FE models with geometries representing a new-born, one-and-a-half-month-old and three-month-old infants. This removes the need to expose further infants to radiation from a CT scan; and, due to the ease of generation, multiple geometries can be modelled at any one time. Li et al. (2016) shortened the time taken to generate FE models by creating a method to extract anatomical landmarks from CT scans, with these points representing the morphology of the infant head. A mesh-morphing method was then created to automatically morph a baseline FE model into an FE model with the geometry extracted from the CT scans.

The anatomic features that were commonly modelled were the skull, sutures and brain; however, as the models became more advanced, the scalp, dura mater and cerebrospinal fluid (CSF) were added. These six features are the most important to model as together they provide the greatest contribution to the global stiffness of the infant head, due to making up the bulk of the head. Features such as the eyes, neck, jaw, teeth, tongue and vertebrae are not modelled as they are generally not part of the load path in a head impact. Table 3.1 includes a summary of the anatomic features modelled in previous studies.

Table 3.1: Summary of FE models of the Infant Head

Study	Age of Infant being Modelled	Anatomic Features Modelled	Purpose and Application	FE Code
Margulies and Thibault (2000)	1 Month	Skull, suture, brain	Impact loading to investigate the effect of cranial bone properties.	LS-Dyna
Coats, Margulies, and Ji (2007)	5 Weeks	Scalp, skull, suture, brain	Study skull fracture from occipital impacts	ABAQUS /Explicit
Roth et al. (2007)	6 Months	Skull, fontanels, CSF, scalp, brain, bridging veins	Compare vigorous shaking and inflicted impact.	Not Stated
Roth, Raul, and Willinger (2008)	6 Months	Scalp, skull, face, sutures, CSF, brain	Comparison of child head model from CT scans and scaled adult head. Impact against rigid wall.	Radioss
Roth, Raul, and Willinger (2010)	17 Days	Scalp, skull, sutures, meninges, CSF, brain	FE model of newborn head, with validation against experimental data.	Radioss
Li et al. (2013)	1.5 and 3 Months	Scalp, skull, sutures, dura mater, CSF, brain	Create statistical head geometry. Parametric study to determine material parameter sensitivity.	LS-Dyna
Li, Luo, and Zhang (2013)	6 Months	Scalp, skull, suture, dura mater, pia mater, CSF, brain	Investigate effects of different drop heights and impact surfaces.	LS-Dyna
Li, Liu, et al. (2015)	From Li et al. (2013)	From Li et al. (2013)	Reconstruct 50 cadaver drop tests using parametric infant FE head model.	LS-Dyna
Li, Sandler, and Kleiven (2017)	New-born, 5 and 9 Months	Scalp, skull, suture, dura mater, CSF, brain	Addition of nonlinear material models. Head impact and compression simulation.	LS-Dyna
Hajiaghamemar et al. (2018)	5 Weeks	Scalp, skull, suture, brain	Determine threshold values associated with skull fracture and develop skull fracture risk curves.	ABAQUS /Explicit
Khalid et al. (2019)	10 Days	Scalp, skull, suture, brain	Investigate regional and localised injury vulnerability.	ABAQUS /Explicit
Li, Sandler, and Kleiven (2019)	3 and 4 Months	Scalp, skull, suture, dura mater, CSF, brain	Reconstruct two cases of suspected abuse.	LS-Dyna
Burgos-Flórez and Garzón-Alvarado (2020)	4 Weeks	Skull, suture, CSF, brain	Investigate skull trauma resulting from low height falls, with differing degrees of suture ossification.	ABAQUS /Explicit

Meshes used in Infant FE Models

Table 3.2 summarises the meshes used in previous studies, with descriptions of the meshing method outlined in most of them. Using the correct element type for the specific application is an important step in any FE model as different elements model deformation differently.

Table 3.2: Element Types used in Previous Infant FE Model Studies

Study	Element Type				Number of Elements
	Scalp	Skull	Suture	Brain	
Margulies and Thibault (2000)		4 node linear shell	4 node linear shell	8 node linear brick	12 772
Coats, Margulies, and Ji (2007)	Hexagonal 8 node solid	Hexagonal 8 node shell	2D 4 node membrane	Tetrahedral 10 node	32881
Roth et al. (2007)	Brick	Shell	Shell	Brick	69 324 brick, 9187 shell
Roth, Raul, and Willinger (2008)	As Above				
Roth, Raul, and Willinger (2010)	Brick	Shell	Shell	Brick	30 000 solid, 3700 shell
Li et al. (2013)	Mesh Morphing Model				38 916 solid, 7 680 shell
Li, Luo, and Zhang (2013)	Shell	Shell	Shell	Hexahedral	50 404
Li, Liu, et al. (2015)	Baseline model same as Li, Luo, and Zhang (2013) above				
Li, Sandler, and Kleiven (2017)	Hexahedral				5.3 million for nine month old infant
Hajiaghamemar et al. (2018)	Hexahedral 8 node	8 node shell	2D 4 node membrane	Tetrahedral 4 node	33 855
Khalid et al. (2019)	10 node tetrahedral				2 626 855
Li, Sandler, and Kleiven (2019)	Hexahedral				5.68 million (three month), 4.13 million (four month)
Burgos-Flórez and Garzón-Alvarado (2020)	Tetrahedral				540 248

Properties of Tissues Measured from Human and Animal Samples

As an infant grows, the material properties of the tissues making up their head also change (Margulies and Thibault 2000, Coats and Margulies 2006). This, along with the lack of availability of infant cadaver samples, are the limiting factors in all previous infant head FE models as there is a severe scarcity of test data for infant tissue mechanical properties.

Margulies and Thibault (2000) investigated the age dependent changes in the material properties of the infant skull and sutures by carrying out three-point bend tests on human and porcine infant cranial bones. The samples were frozen at -4 °C during storage and then defrosted to room temperature in a bath of saline before the tests were conducted. Once it was confirmed that the material properties of the porcine and infant cranial bones agreed, further three-point bend and tensile tests on porcine samples were carried out to represent the infant skull. From these tests, and comparisons with previously published data on the adult human head, it was found that the elastic modulus, ultimate tensile stress and energy absorbed to failure increase with the age of the cranial bone; while the ultimate strain decreases. For the sutures, it was also found that the elastic modulus, ultimate stress and energy absorbed to failure increase with age; however, there are significant differences in the magnitudes of these mechanical properties between the cranial bone and sutures. For infant cranial bone and suture, the elastic modulus and stress at fracture (termed by Margulies and Thibault (2000) as rupture modulus) increases with loading rate; however, the energy absorbed to failure does not. Jaslow (1990) demonstrated experimentally that in mature skulls, the suture absorbs a much larger amount of energy to failure than cranial bone during an impact, thus showing that the suture plays a shock absorbing role in the skull. Margulies and Thibault (2000) found that this does not occur for the infant skull as infant suture absorbs less energy before failure than adult suture.

Coats and Margulies (2006) conducted dynamic three-point bend and tension tests on infant cranial bone and suture, respectively, at impact velocities between 1.2 and 2.8 ms^{-1}. This allowed for the determination of the rate dependent material properties of infant cranial bone and suture for rates associated with low height falls. During storage, the samples were frozen and then thawed in mock CSF solution before testing. It was found that as the age of the infant increased, the elastic modulus and ultimate stress of cranial bone also increased. Similar to Margulies and Thibault (2000), it was also found that infant suture deforms by a significantly greater amount (30 times) than infant cranial bone before failure. This means that due to the flexibility of the skull, brain injury can still occur from the forces of the impact even though there is no skull fracture. Based on the difference in material property data for the cranial bones making up the skull, the impact location can influence whether skull fracture occurs or not. It was also found that strain rate does not affect the modulus of elasticity or ultimate stress of infant cranial bone; although the effect of fibre orientation on the material

properties at different strain rates needs further investigation. For the infant suture, the material properties were not affected by strain rate or age which contradicts Margulies and Thibault (2000), but it was suggested that this may be due to Coats and Margulies (2006) testing a bone-suture-bone segment rather than just a suture segment like Margulies and Thibault (2000). The reported failure locations of the bone-suture-bone samples were at the bone-suture boundary, with no visible damage to the suture, therefore the ultimate stress and strain reported for the suture is that of the suture-bone interface.

Davis et al. (2012) carried out four-point bend tests on 47 specimens of cranial bone from one six-year-old human head to investigate the effects of loading rates and the structure of cranial bone on the elastic modulus and bending stiffness. They found that the elastic modulus varies between the suture, cortical bone and the sandwich bone of cortical-cancellous-cortical (1.10 GPa, 9.87 GPa and 3.69 GPa respectively), with the loading rate having no effect. The bending stiffness of the sandwich bone was found to be much greater than that of the cortical bone and suture (12.32 Nm^2m^{-1}, 5.58 Nm^2m^{-1} and 3.7 Nm^2m^{-1} respectively), where the bending stiffness was defined as *EI* (*E* is the elastic modulus and *I* is the second moment of area). Due to a difference in the widths (measured perpendicular to the suture) of each specimen (resulting from the harvesting procedure), the bending stiffness was normalised by the width (giving the reported units of Nm^2m^{-1}). The variation in the elastic modulus and bending stiffness for the two types of cranial bone needs to be accounted for in future FE models.

Wang et al. (2014a) conducted three-point bend tests to determine the mechanical properties of cranial bone and sutures from one to two-year-old infants. Samples were obtained from seven human infant cadavers, with eight samples from each cadaver from the frontal and parietal bones, and the sagittal and coronal sutures. The mechanical properties of interest were the elastic modulus, ultimate stress and ultimate strain. It was found that for the frontal bone, the elastic modulus and ultimate stress was higher than those of the parietal bone. With the sutures, there was no difference in the properties of interest between the two locations. The ultimate stress and elastic modulus in the cranial bones were higher than in the sutures, while the opposite was found for the ultimate strain.

Material Models used in Infant FE Models to Date

Due to the lack of material property data for the infant head, it has been common for isotropic, linear elastic material models to be used for the scalp, skull, sutures, dura and CSF, and a viscoelastic model for the brain. Table 3.3 summarises the material models used in previous infant FE models.

Li, Sandler, and Kleiven (2017) are currently the only researchers who have used nonlinear material models in their infant FE modelling. They included the scalp, skull, sutures, dura mater, CSF and brain

in their models. The scalp, sutures and dura mater contain much collagen and therefore exhibit nonlinear elastic behaviour, hence more advanced material models are needed. For the sutures, a first order Ogden hyperelastic model was created by fitting it to the stress-strain data of infant suture published by Coats and Margulies (2006). The scalp was modelled as two layers, an adipose tissue layer and the connective tissue layer. These layers were both modelled using a first order Ogden hyperelastic model with parameters adjusted from those of adult scalp presented in Fahlstedt et al. (2015). The adipose tissue layer Ogden parameters were assumed to be the same for infants as adults due to the lack of paediatric data, while the Ogden parameters for the connective tissue layer were assumed to be one tenth of those for adults due to the softer scalp in infants. For the dura mater, a Mooney-Rivlin hyperelastic model was used, with the parameters determined from data presented in Bylski et al. (1986). The skull was modelled using an orthotropic material model. The three-point bend data of Coats and Margulies (2006) was used to determine the elastic modulus in the direction

Table 3.3: Material Models used for the Infant Head FE Models

Study	Tissue					
	Scalp	**Skull**	**Suture**	**Dura**	**CSF**	**Brain**
Margulies and Thibault (2000)		Linear Elastic	Linear Elastic			Linear Viscoelastic
Coats, Margulies, and Ji (2007), Hajiaghamemar et al. (2018)	Linear Elastic	Orthotropic Elastic	Linear Elastic			Ogden Hyperelastic
Roth et al. (2007), Roth, Raul, and Willinger (2008), Roth, Raul, and Willinger (2010)	Linear Elastic	Linear Elastic	Linear Elastic		Linear Elastic	Linear Viscoelastic
Li et al. (2013), Li, Luo, and Zhang (2013), Li, Liu, et al. (2015), Li et al. (2016)	Linear Elastic	Linear Elastic	Linear Elastic	Linear Elastic	Linear Elastic	Linear Viscoelastic
Li, Sandler, and Kleiven (2017, 2019)	Ogden Hyperelastic	Orthotropic Elastic -Age Dependent	Ogden Hyperelastic	Mooney-Rivlin Hyperelastic		Ogden Hyperelastic
Khalid et al. (2019)	Linear Elastic	Orthotropic Elastic	Linear Elastic			Linear Elastic
Burgos-Flórez and Garzón-Alvarado (2020)		Linear Elastic	Linear Elastic		Linear Elastic	Linear Viscoelastic

perpendicular to the direction of the fibres in the skull, where the fibre direction was determined by observation. Using an anisotropy ratio obtained from the data of Kriewall (1982) and the data from Coats and Margulies (2006), the elastic modulus in the direction parallel to the fibre direction was calculated. The elastic modulus in the through-thickness direction was assumed to be the same as that in the direction perpendicular to the fibres.

Material Model Parameters used in Infant FE Models to Date

The model parameters currently existing in the literature are summarised in Table 3.4. Many of the studies used values for the material properties of the skull from Coats and Margulies (2006), sutures from Margulies and Thibault (2000), CSF from Willinger, Taleb, and Kopp (1995) and brain from Thibault and Margulies (1998). Roth et al. (2007), Roth, Raul, and Willinger (2008), Roth, Raul, and Willinger (2010), Li et al. (2013), Li, Luo, and Zhang (2013), and Li, Liu, et al. (2015) used adult values for the material properties of the CSF and the latter three studies also used adult values for scalp.

Table 3.4: Material Model Parameters used in Previous Infant FE Models

Tissue	Linear Models			Study
	Elastic Modulus (MPa)	Poisson's Ratio	Density (kg/m^3)	
Scalp	16.7	0.42	1200	Zhou et al. (1997) (Adult)
Skull	500	0.22	2150	Coats and Margulies (2006)
Suture	8	0.22	2150	Coats and Margulies (2006)
Membranes	31.5	0.45	1140	Zhou et al. (1997) (Adult)
CSF	0.012	0.49	1040	Willinger, Taleb, and Kopp (1995) (Adult)
	Nonlinear Models			
	Viscoelastic	**Ogden Hyperelastic**		
Brain	G_0=5.99e-3 MPa, G_∞=2.32e-3 MPa, β=0.09248 s^{-1}	μ_1 = 53.8 Pa, α_1 = 10.1, μ_2 = −120.4 Pa, α_2 = −12.9		Thibault and Margulies (1998), Li, Sandler, and Kleiven (2017)
Suture		$\mu_1 = 1.48 \times 10^4$ Pa, α_1 = 6.9		Li, Sandler, and Kleiven (2017)
Scalp		Outer: $\mu_1 = 1.30 \times 10^4$ Pa, α_1 = 24.2 Inner: $\mu_1 = 3.99 \times 10^3$ Pa, α_1 = 8.8		Li, Sandler, and Kleiven (2017)
Skull	(Orthotropic Elastic, Age Dependent) Five-month-old infant: E_1=650.9 MPa, E_2=E_3=392.9 MPa, G_{23}=111.8 MPa, G_{12}=G_{31}=194.8 MPa			Li, Sandler, and Kleiven (2017)
		Mooney-Rivlin Parameters		
Dura		C_1=1.18 MPa, C_2=0.295 MPa		Li, Sandler, and Kleiven (2017)

Boundary Conditions and Results

Margulies and Thibault (2000) constructed FE models of a one-month-old infant head using the paediatric skull material properties for one simulation and the adult skull properties for another. Each model was subjected to impact loading based on accelerations measured in a study of shaken baby syndrome published by Duhaime et al. (1987). This consisted of half sinusoidal load-time input with peak magnitudes of 1000 N and 5000 N (to represent minor and major impacts respectively) and a pulse duration of 10 ms. The location of the impacts were in the parietal region, 45° from the vertical axis. From these models, it was found that the maximum intrusion of the impactor was 100% greater in the infant cranial bone compared to the adult cranial bone. The resulting strains on the brain, using the infant cranial material properties, caused diffuse, bilateral hemispheric distribution of maximum principal strains. Therefore, using this simplified model, it has been shown that impact loading may produce diffuse injury in infants.

Coats, Margulies, and Ji (2007) developed a geometrically accurate FE model to predict skull fractures in infants resulting from impacts. An initial velocity that represented a fall from 0.3 m was applied to the head, and the impacting surface modelled as a fixed, rigid plate. They found that small variations in the thickness or width of the suture did not affect the principal stress in the infant cranial bone. However, large sutures (>10 mm) decreased the estimated occurrence of fracture resulting from an impact, thus showing that there is a relatively significant injury risk due to unusual anatomic variations. Through a parametric study of the parameters for the visco-hyper-elastic material model used for the brain (based on the work of Prange and Margulies (2002)), they found that decreasing the shear modulus of the infant brain by half does not affect the principal stress; but decreasing the stiffness by greater than one order of magnitude will significantly increase the principal stress in the cranial bone. They also found that changing the Poisson's ratio (from 0.499 to 0.49 and 0.4999) changes the bulk modulus and significantly varied the principal stress by 30 to 77%, thus showing the importance of determining the compressibility of the brain in a numerical model. Overall, their model was able to predict skull fracture resulting from an impact with a hard surface to good agreement with previous studies using infant cadavers.

Roth et al. (2007) created an FE model of a six-month-old infant head to compare vigorous shaking and an inflicted impact. The shaking was modelled by taking one angular velocity cycle from the data recorded by Prange et al. (2003) and applying it to the centre of rotation of the system. For the inflicted impact, the head was modelled as hitting a rigid wall at 3.0 ms^{-1}. The von Mises stresses and pressure were significantly higher in the inflicted impact model (14 kPa occurring in the occipital region, and 80 kPa respectively) than the shaking model (3.2 kPa occurring in the vertex region, and 22 kPa respectively). Both the shaking and inflicted injury models experienced similar relative displacements

of the brain in the sagittal plane, leading to the rupture of bridging veins. The strain in the bridging veins was determined to be 100% and 90% strain for the impact and shaking simulations respectively. The strain calculation was based on the original lengths of the bridging veins and the relative displacement in the sagittal plane (for the elongation of the bridging veins). The similarity in the bridging vein strains shows that shaking can cause subdural haemorrhaging, even though there may not be the physical trauma (such as skull fractures) present from a possible inflicted impact.

Roth, Raul, and Willinger (2008) carried out numerical simulations of a six-month-old infant head model using geometry derived from CT scans (real geometry) and comparing the results with models that used geometry based on scaling an adult head. Their model used an impact velocity of 1 ms^{-1}, against a rigid wall. Between the two geometries, the stress distributions in the skull and brain were very different, both for the magnitude and location of the maximum stress. For an impact to the frontal bones, the peak pressure in the occipital region was 19 kPa and 38 kPa for the real geometry and scaled adult geometry respectively. The von Mises stress in the brain, in the occipital region, was 0.8 kPa and 2 kPa respectively, while the maximum von Mises stress in the skull was 4.4 MPa and 3.7 MPa respectively. These differences show that a scaled adult head geometry is not suitable for infant head FE modelling. The major difference between the two models was the thickness of the skull. For the scaled adult model, the skull thickness did not correspond to that of the CT scan from the six-month-old child (the scaled adult skull thickness was thicker than the six-month-old child). This means that in the scaled adult model, there was a smaller skull deflection and hence smaller stress in the brain. Overall, they found that scaling down the adult head does not appear relevant for use in child numerical simulations.

Roth, Raul, and Willinger (2010) developed an FE model of a new-born head and validated it against experimental data of Prange et al. (2004). The head was compressed by simulating a plate moving at 50 mms^{-1} contacting the head at the desired location, with the reverse side of the head placed against a rigid wall. Overall, good correlations were found for the force-displacement curves of the simulated impact and the experimental results. They also conducted a parametric study on the parameters of the brain viscoelastic model to determine the influence of the brain tissue on the skull deformation. It was found that large variations in the viscoelastic parameters of the brain material model led to very small changes in the skull stresses, skull deformation and peak acceleration of the head. Only when the bulk modulus was significantly increased from 2.11 GPa to 21.10 GPa, was there more than a 15% difference in results. Therefore, they concluded that brain material properties have minimal influence on the stresses and skull deformation, which conflicts with the conclusions of Coats, Margulies, and Ji (2007). To demonstrate the capability of their model, they also simulated a real-world accidental fall where a one-month-old infant fell from one metre onto a concrete surface. Comparisons of the

resulting skull fracture lines showed good accordance with those observed in the medical images in the patient's medical file. However, they noted that validation of skull fractures cannot be performed as the experimental cadaver tests used to validate the FE models do not investigate fracture.

Ponce and Ponce (2011) used FE models to simulate the effects of impacts to an infant's head to predict, locate and quantify diffuse brain injuries. The original FE model was to simulate the vibrations of an infant's head when they are shaken so that its effect on the first through to fourth cervical vertebrae could be investigated. A 400 N load was applied to the occipital region of the head, while the head was free to rotate about the spinal cord in the axis of impact. The resulting stress in the brain was greater than the acceptable limit for areas far from each other, thus indicating potential damage to the neurological tissue.

Li et al. (2013) created a statistical model of an infant's cranium geometry using multiple CT scans and a combination of multivariate regression and principal component analyses. This model was then used to create geometries of a new-born, one and a half month old and three-month-old infants to be used in FE models. The FE models were used to carry out a parametric study where the sensitivity of various material parameters were quantified, under near-vertex impact loading conditions. Boundary conditions included an initial velocity calculated based on a drop height of 0.3 m and a frictional contact (with a coefficient of 0.2) for contact between the head and rigid surface. The elastic modulus of the skull, suture, dura mater and scalp, along with the long- and short-term shear moduli and decay constant for the brain were the parameters of interest in the parametric study. The maximum principal stress and strain in the skull and suture, as well as the peak head acceleration, were used to evaluate the changes in the above parameters. From the parametric study, it was found that changes in the skull elastic modulus resulted in significant differences in each of the resulting parameters. An increase in the elastic modulus resulted in all output parameters increasing except for the maximum principal strain of the skull, which decreased. Model validation and material model parameter optimization was carried out by simulating the drop test experiments carried out by Prange et al. (2004). A parametric study found that the viscoelastic material properties of the brain had little effect on the result parameters, so were excluded from the optimisation study. Values for the elastic moduli of the skull, suture, scalp and dura mater were optimised to fit the data from the experimental tests by Prange et al. (2004). These optimised material model parameters were then used to create simulations replicating the tests from Prange et al. (2004) to validate the models.

Li, Luo, and Zhang (2013) created an FE model of a six month old infant to simulate compression and drop tests that have been experimentally carried out by Loyd (2011). For the compression simulations, the head was compressed between two plates from the anterior-posterior direction and left-right

direction, with velocities of 15 mms^{-1} and 45 mms^{-1}. A frictional contact boundary (with a friction coefficient of 0.2) was prescribed for contact between the head and plate. Comparison of the force-time plots for the simulations with those from the experimental data showed that the compression forces were slightly higher in the simulation. Therefore, the global head stiffness was a little stiffer than in reality. For the drop test simulations, an initial velocity was applied to the head based on drop heights of 0.15 and 0.30 m. The impact occurred between the head and an aluminium plate and had the same contact conditions as the compression tests. Five different impact orientations were simulated (forehead, occipital, vertex and parietal). There was an acceptable correlation between the simulation and experimental acceleration-time curves, with peak resultant accelerations around 80 g for all head orientations from the 0.3 m drop height. These were around 10 to 20% higher than those recorded by Loyd (2011). This again shows that the FE model is globally slightly stiffer than the cadaver head. A parametric study of the elastic modulus for each tissue was also conducted. For each tissue the elastic modulus was decreased by half of the original value, as well as increased by a factor of two. It was found that the elastic modulus of the skull and scalp had the most significant effect on the peak acceleration, and the von Mises stress and maximum principal strain in the skull. For example, the increase in the modulus of the skull resulted in an increase of the peak acceleration from approximately 75 g to around 85 to 90 g, and the von Mises stress increased from around 30 MPa to 50 MPa. Simulations were also carried out to determine the effects of drop height and the stiffness of the impact surface on the head responses. Impact surface types included concrete, wood fibre board and hard, soft and rigid foam. Drop heights of 0.15, 0.30, 0.60, 0.90 and 1.20 m were used, with the impact location being in the occipital region. Overall, the head peak acceleration, maximum von Mises stress and first principal strain of the skull all increased with increasing drop height and surface stiffness.

Li, Liu, et al. (2015) used a parametric infant FE model based on Li et al. (2013) to predict paediatric skull fractures. By using the model to reconstruct previous infant cadaver tests, skull fracture risk curves were able to be generated for children less than nine months old. Using mesh morphing techniques, head geometries were created from data of age, head size/shape and skull thickness that was reported in the cadaver tests. Overall, it was found that the stress responses in the skull were better at predicting skull fracture rather than kinematic based measures, such as peak head acceleration.

Jiang et al. (2017) created a simplified computational model of the infant head to simulate the skull response to blunt impacts. Only the skull and sutures were included in the geometry and a linear elastic material model was used. Initial simulations were carried out for an impact test replicating experimental tests on piglet skulls. It is claimed that this simulation showed a good match for the skull

fracture patterns between the simplified model and piglet heads. However, there is very little in regard to describing the boundary conditions used in this model. As commented by Johnson and Auer (2018), this FE model is overly simplified and cannot be considered a qualitatively or quantitatively validated model.

As discussed in the material models and properties section earlier, Li, Sandler, and Kleiven (2017) used nonlinear material models for the scalp, sutures, dura mater and skull. They modelled drop and compression tests for infant heads as carried out experimentally by Loyd (2011) so that the material models could be validated against cadaver tests. FE models of a new-born, five and nine-month-old infant were created, with the same material properties used for each age. For the drop tests, an initial velocity was applied to the model head that simulated a drop height of 0.3 m, and five different head impact orientations were used (forehead, occipital, vertex, left and right parietal). The acceleration-time curves from the drop tests correlated well with the experimental data across all impact locations and ages. For the compression tests, the head was simulated to be compressed between a fixed plate and a plate moving at a velocity calculated to obtain a strain rate of 0.3 mm ($mm^{-1}s^{-1}$). The force-deflection curves all showed an increase in the stiffness at large displacements, also seen in the experimental tests. To further validate the nonlinear material models, the same FE simulations were carried out for the frontal and parietal impacts, with linear elastic material models for the scalp, sutures and dura mater. For the frontal impacts, the linear elastic suture model resulted in an increase of 22.4% in the peak acceleration, while the linear elastic scalp model resulted in an increase of 49.2% when compared to the use of their respective nonlinear models. A 22.4% decrease in the von Mises stress in the skull occurred when using the linear elastic scalp model due to the stiffening effect of the linear elastic model (there was less bending in the skull). The linear elastic model for the dura resulted in an increase of 20% for the peak acceleration and little change in the von Mises stress. Absolute values for the von Mises stress in the skull were not presented. Overall, these linear elastic models resulted in a stiffer model. This is due to the linear elastic models not allowing for the uncrimping in soft tissues, which causes a period of lower stiffness.

Hajiaghamemar et al. (2018) used the model of Coats, Margulies, and Ji (2007) to determine skull fracture threshold values and develop skull fracture risk curves for low height falls. Eleven real-world cases were evaluated and reconstructed using a full body anthropomorphic infant and FE models. Force traces from accident reconstructions were used to propose biomechanical parameters for predicting skull fracture in a FE model. These parameters were the first principal stress and strain, shear stress and von Mises stress. A detailed discussion of the skull fracture thresholds is discussed later in this chapter.

Khalid et al. (2019) developed an FE model of a 10-day-old infant that was used in conjunction with physical surrogate testing to investigate regional and localised injury vulnerability. The geometry was created from a CT scan, with segmenting of the cranial bones, suture and brain. The CSF was not modelled due to having fluid-like properties and, they claim, fluid structure interaction is in its relative infancy (although no citation is provided to back up such a claim). A sliding interface between the skull and brain was used instead. Global validation was carried out with the cadaver experiments of Prange et al. (2004), while regional validation was carried out with a physical surrogate developed by the same research group (Jones et al. 2017). Drop heights of 0.15, 0.3, 0.6 and 0.82 m were used, along with orientations of vertex, frontal, occipital and parietal. The findings from their study showed that the current approach of using global acceleration as a response indicator is insensitive to regional variations. For example, a 60 g global acceleration produces a different response for a parietal impact compared to an occipital impact and therefore could be more or less injurious. Compared to the global acceleration, the local acceleration impact response (at the impact site) was found to be two to three times greater. Measuring the deformation and acceleration in different regions and comparing to the physical surrogate allowed for greater FE model validation than compared to just using global acceleration parameters. However, the regional deformation of the physical surrogate has not been independently validated with experimental human infant cadaver impacts. This likely due to a lack of such experiments that can provide regional acceleration and deformation data.

Li, Sandler, and Kleiven (2019) used the FE model described in Li, Sandler, and Kleiven (2017) to reconstruct two cases of suspected abuse. Subject specific geometry (aged three and four months) was generated for each case. The fall as described by the caregiver was replicated in each case to determine whether it was likely that it would produce the skull fracture patterns observed from medical imaging. In the case of the three-month-old infant, the caregiver claimed the infant fell from their arms at a height estimated to be around 0.84 m. It was possible the infant impacted a dog bed that when examined was found to have a thin structure and therefore offered little protection to the infant. In the case of the four-month-old, the caregiver claimed the infant fell approximately 1.1 m from a baby changing table onto linoleum flooring over concrete. Both cases were initially suspected as being abuse, hence the question the study aimed to answer was whether the histories provided by the caregivers could explain the observed fractures. From the FE model reconstructions, it was found that it was possible that the skull fractures could be explained from the provided histories. Both FE models predicted fractures in the skull that were similar in location, orientation and length to those observed from medical imaging. Special care was taken to ensure the impact location and head orientation were as accurate as possible (determined using observed injuries and medical imaging observations) as both have been found to be influential on FE model results. Although there are still

uncertainties with how cranial bone material properties influence fracture patterns, their study demonstrates the potential for FE models to provide biomechanical evidence to aid forensic investigations.

Burgos-Flórez and Garzón-Alvarado (2020) developed an FE model to investigate infant skull trauma resulting from low height falls, with differing degrees of ossification of the sutures. The geometry was created from CT scans of the cranial bones (aged four-weeks-old), with 3D modelling techniques used to generate the sutures, CSF, brain and fontanelles. The scalp was not modelled to avoid excessive complexity in computational implementation. Drop heights of 0.3 and 0.5 m were simulated, with impacts onto the lambdoid suture (occipital) and right parietal bone. Six cases with differing degrees of suture ossification were simulated: unossified suture and fontanelles, full ossification (mechanical properties assumed to be the same as the cranial bones), and the four remaining cases being different types of craniosynostosis (sagittal, metopic, right lambdoid and right coronal). Frictional contact between the skull and impact surface was used (friction coefficient of 0.2). The impact surface was modelled as a rigid surface with material properties similar to a ceramic (elastic modulus and Poisson's ratio of 150 GPa and 0.17 respectively). It was found that the impact force was greater for the parietal impact than the occipital, however, more significant stress was transferred to the brain in the occipital impacts. The fully ossified skull (full ossification of suture) had lower maximum principal strain in the cranial bones and much greater maximum von Mises stress (27.6 versus 15.2 MPa for the fully ossified skull and normal skull respectively). It also showed less deformation overall and lower van Mises stress in the brain. This is to be expected given that the fully ossified skull assumed the material properties of the suture were those of the cranial bones.

FE Model Validation -Human Infant Cadaver Experimental Head Impact Studies

Only four studies involving human infant cadaver experimental head impacts have been published (Weber 1984, 1985, Prange et al. 2004, Loyd 2011). Only Prange et al. (2004), Loyd (2011) provide quantitative data that can be used to validate FE models. Loyd (2011) builds on the work first started by Prange et al. (2004).

Prange et al. (2004) conducted compression experiments on the heads of one, three and 11-day-old infant cadavers that were unembalmed and fresh-frozen. Impact testing was also carried out by dropping the specimens from heights of 0.15 and 0.30 m. The cadaver heads did not include the neck. This allowed for an isolated head in free-fall that experienced no translational or rotational motion prior to impact. Five head orientations were used: vertex, occiput, forehead, left and right parietal bone. The cadaver heads were dropped onto a flat smooth anvil with a load cell that measured the impact force. Impact duration, peak acceleration and the head injury criterion were obtained from the

acceleration-time plots, with acceleration calculated from the force data and measured head mass. It was found that the infant head is a lot more compliant than an adult head as, compared to previous adult test data, there were longer pulse durations and lower peak accelerations for the infant. For the infant drop tests, it was found that the impact response did not depend on the location of impact. The average peak head acceleration across each orientation and age was 55 g for the 0.3 m drops. The average impact duration was 18 ms.

Loyd (2011) studied 14 human paediatric heads to obtain structural stiffness and impact properties of the human paediatric head. Adult and anthropomorphic test devices (ATD) were also studied. Similar to Prange et al. (2004), the specimens were dropped onto a rigid plate from heights of 0.15 and 0.3 m. Twelve human paediatric heads were tested (the one and 11-day-old subjects from Prange et al. (2004) were also included in this analysis to give the total of 14), ranging from 34 weeks gestation to 16 years, with nine specimens under 12 months. Overall, across all paediatric and adult tests, impact location, drop height and age were significant predictors of peak acceleration. For the paediatric tests less than 12 months, impact duration and drop height were the most significant predictors. Peak acceleration nearly doubles from the 0.15 to 0.3 m drop heights. Impact duration was found to be independent of location and drop height, while age was a significant predictor. The parietal impacts had statistically longer durations than other locations. Duration decreased as age increased.

The impact tests of Loyd (2011) found that the mechanics of the head impact are controlled by the local contact stiffness, not the global quasi-static stiffness. The dynamic stiffness was more than five times greater than the quasi-static stiffness. If the impacts were governed by the quasi-static stiffness, the two would be the same and the head would exhibit elastic behaviour, be rate independent and have small deformation during impact. Hysteresis in the compression and impact tests, and different responses at different drop heights, showed the heads were not elastic. As maximum compression and maximum force did not occur at the same time, the heads were rate dependent. The paediatric heads all involved large deformations relative to head width and length. When these factors are taken into consideration, it was concluded that the local stiffness governed the mechanics of the head impact.

Specific data from the datasets described above are referred to in subsequent chapters as a means of validating the FE models presented in this thesis.

Finite Element Models of the Adult Human Head

As summarised by Raul et al. (2008) and Tse, Lim, et al. (2014), the first two-dimensional (2D) FE model was developed by Hardy and Marcal (1973) in the early 1970's and only consisted of a skull. This was

improved on by Shugar (1975), however, the 2D models provided unrealistic results due to the lack of availability in computational resources, limiting the size of the models. The first 3D models were simplified geometrically by using spherical or ellipsoidal head geometries, and mainly consisted of the brain and skull. As the availability of computational resources increased in the 1990's, the development of more realistic 3D models increased. Ruan, Khalil, and King (1993) developed the Wayne State University Brain Injury Model (WSUBIM), which was subsequently improved on by Zhou, Khalil, and King (1995), Zhang et al. (2001) and King et al. (2003) to become one of the most widely used adult FE models. Other adult FE models include the University of Louis Pasteur (ULP) Finite Element Head Model developed by Kang et al. (1997); the Kungliga Tekniska Högskolan (KTH) developed by Kleiven and Hardy (2002); the Simulated Injury Monitor (SIMon) FE model proposed by Takhounts et al. (2003); and the University College Dublin Brain Trauma Model (UCDBTM) developed by Horgan and Gilchrist (2003). The material models used in each of these models are summarised in the following sections.

Wayne State University Brain Injury Model

As summarised by Tse, Lim, et al. (2014), the Wayne State University Brain Injury Model (WSUBIM) was built by Ruan, Khalil, and King (1993) to simulate the anatomy of the skull and brain, and included the CSF, scalp, dura and falx cerebri. Zhou, Khalil, and King (1995) then improved the WSUBIM to include separate areas of white and gray matter in the brain, as well as ventricles. Later, Zhang et al. (2001) added a sliding interface between the brain and skull. The revised model consists of the anatomical features of a 50^{th} percentile male head, and includes facial bones, brainstem, ventricles, gray and white matter hemispheres of the brain, CSF, pia, tentorium, falx cerebri, dura, three layered skull and the scalp. The various versions of the WSUBIM have been used in many research publications, such as Zhang, Makwana, and Sharma (2013).

Zhang et al. (2001) further developed the WSUBIM so that it was capable of simulating impacts with combined rotational and translational accelerations up to 12 000 $rads^{-2}$ and 200 g. In this FE model, brain tissue was modelled as elastic for its hydrostatic behaviour and viscoelastic in shear. To account for the different material compositions of the gray and whiter matter, the shear modulus of the white matter was set 25% higher than that of gray matter. From experimental results of shear tests on pigs' brain by Arbogast and Margulies (1997), the complex shear modulus of the brainstem is 80% higher than cerebrum tissue, so in the model, the short-term shear modulus was set to be 80% higher for the brainstem than that of white matter.

Simulated Injury Monitor FE Head Model

The Simulated Injury Monitor (SIMon) FE head model was developed by Takhounts et al. (2003) and is a part of the SIMon software package. SIMon allows measured crash dummy data to be directly imposed onto a FE model of the human body, in the region of interest. This enables the analysis of the structural response of the FE model and evaluating injury potential (Bandak et al. 2001). The FE model consists of the rigid skull, dura, CSF, brain, falx cerebri and bridging veins (Takhounts et al. 2003). A viscoelastic material model was used to model the brain, while the skull, CSF, falx cerebri and bridging veins were modelled as linear elastic.

Takhounts et al. (2008) improved the SIMon FE head model by including cerebrum, cerebellum, tentorium, a combined CSF and pia arachnoid complex (CSF PAC), ventricles, brainstem and parasagittal blood vessels. In this improved model, the CSF PAC, cerebrum, cerebellum and brain stem were modelled as Kelvin-Maxwell viscoelastic, while the remaining tissues were modelled as linear elastic.

Kungliga Tekniska Högskolan

Kleiven and Hardy (2002) created the parameterised KTH model that was validated against cadaver impact experiments. The model included the scalp, skull, meninges, CSF, brain and pairs of bridging veins. A Mooney-Rivlin hyperelastic material model was used for the brain to account for large elastic deformations. Although not explicitly stated, the material properties listed for the skull and scalp suggest that linear elastic models were used.

University College Dublin Brain Trauma Model

Horgan and Gilchrist (2003) created the University College Dublin Brain Trauma Model (UCDBTM) of the human head to model head impacts of simple pedestrian accidents. The FE model consists of the brain, CSF, facial bone, falx, pia, dura, trabecular bone, cortical bone and scalp. A linear viscoelastic material model, combined with large deformation theory, was used to model the brain. CSF was modelled as solid elements with relatively low shear moduli, while the scalp, cortical bone, trabecular bone, dura, pia, falx and facial bone were modelled as linear elastic. Horgan and Gilchrist (2004) later further refined the UCDBTM baseline model by validating it against a series of cadaver tests. Six different configurations were also created to investigate their influence on the results. One of these configurations distinguished between white matter, gray matter and ventricles, and modelled as viscoelastic, using properties from the WSUBIM (Zhang et al. 2001).

Applications of Adult Head FE Models

Finite element modelling of the adult head is used in applications such as blasts, ballistics, falls and other head impacts. Many studies relating to these applications use one of the specific FE models discussed in the previous sub-sections, while others create their own models.

Studies involving ballistics (Mota et al. 2003, Daniel and Rémy 2005, Aare and Kleiven 2007, Raul et al. 2007, Lee and Gong 2010, Tan et al. 2012, Pintar et al. 2013, Salimi Jazi et al. 2014) largely investigate different military combat helmet designs and the prediction of injuries to the head. Those involving blasts (Zhang et al. 2009, Panzer et al. 2012, Dagro et al. 2013, Ganpule et al. 2013, Kulkarni et al. 2013, Zhang, Makwana, and Sharma 2013, Jenson and Unnikrishnan 2015) also largely focussed on military combat helmet designs as well as investigating blast effects on the head and brain. Studies involving falls and other head impacts (Horgan and Gilchrist 2003, Belingardi, Chiandussi, and Gaviglio 2005, Doorly and Gilchrist 2006, Kleiven 2006, Raul et al. 2006, Tse, Tan, et al. 2014) simulated head injuries from real life cases and investigated the type of resulting injuries.

Material Models

Table 3.5 provides a summary of the material models used and the respective studies they were used in. Many of the studies use a viscoelastic model for the brain and a linear elastic model for the skull and scalp. Of the studies that specifically described the material model for CSF, linear elastic solid and elastic fluid models were used, while studies involving blasts used Equations of State (EOS) as pressure wave affects were being modelled (Panzer et al. 2012, Jenson and Unnikrishnan 2015).

Table 3.5: Material models used for the different tissues in adult head FE models

Tissue	Material Model	Study
Brain	Linear Viscoelastic	Zhang et al. (2001), Horgan and Gilchrist (2003), Takhounts et al. (2003), Belingardi, Chiandussi, and Gaviglio (2005), Ganpule et al. (2013), Salimi Jazi et al. (2014), Tse, Tan, et al. (2014)
	Kelvin-Maxwell Viscoelastic	Takhounts et al. (2008), Zhang et al. (2009)
	Mooney-Rivlin Hyperelastic	Kleiven and Hardy (2002), Kleiven (2006), Dagro et al. (2013)
Skull	Linear Elastic	Takhounts et al. (2003), Horgan and Gilchrist (2004), Belingardi, Chiandussi, and Gaviglio (2005), Kleiven (2006), Takhounts et al. (2008), Dagro et al. (2013), Ganpule et al. (2013), Salimi Jazi et al. (2014), Tse, Tan, et al. (2014), Jenson and Unnikrishnan (2015)
Scalp	Linear Elastic	Takhounts et al. (2003), Horgan and Gilchrist (2004), Belingardi, Chiandussi, and Gaviglio (2005), Kleiven (2006), Takhounts et al. (2008), Dagro et al. (2013), Ganpule et al. (2013), Salimi Jazi et al. (2014)
CSF	Linear Elastic	Takhounts et al. (2003)
	Elastic Fluid	Salimi Jazi et al. (2014)
	Linear Shock EOS	Jenson and Unnikrishnan (2015)
	Mie-Gruneisen EOS	Panzer et al. (2012)

Human Infant Head Tissue Injury Thresholds

Given that human infant head tissue property data is limited, data for tissue injury thresholds is also very limited. Margulies and Thibault (2000), and Coats and Margulies (2006) are the only studies to have conducted physical testing of human infant cranial bone where the ultimate stress and strain were measured. While there is some research on adult human brain injury thresholds (Bain and Meaney 2000, Morrison et al. 2003), no such data exists for human infants.

Cranial Bone

The experimental tests of Margulies and Thibault (2000), and Coats and Margulies (2006) have been discussed previously. Table 3.6 details the cranial bone ultimate stress and strain data.

Table 3.6: Ultimate stress and strain values for infant cranial bone, as determined from experimental data.

	Coats and Margulies (2006) Averaged for 19 days to 4.5 months	**Margulies and Thibault (2000)** 25 weeks gestation to one week	**Margulies and Thibault (2000)** 6 months
Ultimate Stress (MPa)	30.95	9.3	52.8
Ultimate Strain	0.072		

In forensics, skull fractures are the most easily observable head injury from medical imaging. Therefore, the use of FE models in this area is largely focussed around whether skull fracture is likely to occur and/or the fracture patterns particular impacts may generate. To date, only Li, Liu, et al. (2015), and Hajiaghamemar et al. (2018) have developed skull fracture risk curves for infant cranial bone, while Li, Sandler, and Kleiven (2019) reconstructed suspected abuse cases to investigate the skull fracture patterns.

Hajiaghamemar et al. (2018) reconstructed 11 well-witnessed cases of infant head impacts using a whole-body anthropomorphic infant surrogate. Five reconstructions of each case were carried out to determine a range of possible impact forces generated from the fall. A load cell on the impact surface was used to measure the force-time history of each impact. Finite element models of each case were created, with the first, second and third quartile force-time histories used as the loading condition. Initial velocity was adjusted until the FE models could reproduce the force-time histories to within 5% of the reconstructed data using the surrogate. It should be noted here that it seems to be that the peak impact force was used to compare the data to within 5% as some force-time traces of the FE models presented are clearly not within 5% of the experimental trace (Figure 2 in Hajiaghamemar et al. (2018)). However, the FE model traces do, in general, correlate well with the experimental data. Of the 11 real cases, seven experienced skull fracture. The FE model stress and strain distributions were compared to the medical images to ensure the areas of high stress and strain were occurring in similar locations. Adjustments to the impact location and head orientation were made until the models were predicting the distributions correctly. Maximum principal stress, maximum principal strain, maximum shear stress and von Mises stress were used to develop skull fracture risk curves in the parietal bone. Table 3.7 details the threshold values for a 50% and 95% probability of skull fracture occurring. These threshold values correlated well with the ultimate stress and strain values presented in Coats and Margulies (2006) (Table 3.6). Fracture thresholds were unable to be determined for the occipital bone as the medical images showed no cases had fracture in the occipital bone.

Li, Liu, et al. (2015) built FE models to reconstructed the cadaver tests of Weber (1984, 1985). The maximum principal stress threshold values for a 50% probability of fracture for zero, three, six and nine-month-olds were found to be 8.1, 10.7, 13.4 and 16.1 MPa respectively. These threshold values are lower than those found by Hajiaghamemar et al. (2018). This is likely due to the use of a skull elastic modulus of 164.3 MPa, which is significantly smaller than that used by Hajiaghamemar et al. (2018) and every other FE model published up to 2015. This low elastic modulus was determined using optimisation methods to match the FE model response to the cadaver experimental impacts of Prange et al. (2004).

Table 3.7: Skull fracture threshold values from Hajiaghamemar et al. (2018).

Threshold Predictor	Probability of Fracture	
	50%	95%
Maximum Principal Stress (MPa)	25.3 (24.3-26.1)	36.0 (34.9-36.9)
Maximum Principal Strain	0.0464 (0.0447-0.0475)	0.0669 (0.0650-0.0672)
Maximum Shear Stress (MPa)	17.9 (16.9-18.5)	28.1 (26.7-29.6)
von Mises Stress (MPa)	33.9 (32.0-34.7)	54.0 (51.1-55.5)

Note: values in parenthesis are the range of thresholds based on the first and third quartile of the measured force-time plots.

Brain

To date, there is no tissue injury threshold data for the human infant brain. However, literature exists for thresholds of human adult brain tissue. Bain and Meaney (2000), and Morrison et al. (2003) have shown that strain correlates well with diffuse axial injury. Bain and Meaney (2000) produced axonal injury by dynamically stretching optic nerve of guinea pig (evidence suggests that the mechanical behaviour of the central nervous system tissues is similar between guinea pigs and humans). The optimal threshold for predicting morphological injury corresponded to a strain of 0.21, for a 25% probability of injury. Morrison et al. (2003) stretched brain tissue at various strain rates. They found that Lagrangian strains of less than 0.1 at 5, 10, 20 or 50 s^{-1} strain rates caused very little tissue damage. Tissue damage started to occur at strains greater than 0.2.

Discussion

Finite element modelling of the human head has been in progress since at least 1993, with more sophisticated models developed as FE methods and computational resources have progressed. These models have mostly involved adult heads and have been used for investigations into the head response in automotive collisions and military applications (ballistics and blasts). Models specifically dealing with the infant head first appeared in 2000, but due to their additional complexity, have not

advanced as far as adult head models. As this thesis is focussed on infant head FE models, the discussion herein is for such models only.

To date, only seven complete, distinct FE models have been previously created for the infant head. These include Margulies and Thibault (2000), Khalid et al. (2019), Burgos-Flórez and Garzón-Alvarado (2020), as well as the models that have been used in multiple studies by Coats, Margulies, and Ji (2007), Hajiaghamemar et al. (2018); Roth et al. (2007), Roth, Raul, and Willinger (2008), Roth, Raul, and Willinger (2010); Li et al. (2013), Li, Luo, and Zhang (2013), Li, Liu, et al. (2015), Li et al. (2016); and Li, Sandler, and Kleiven (2017, 2019). These models include the relevant anatomy and boundary conditions subject to simplifying assumptions which appear to be consistent with the goal of modelling impact injury at a computational demand which can be achieved on at least high-end desktop computers.

Two further models should be noted. The model of Jiang et al. (2017) considered only the skull and sutures, which is overly simplified given that the whole infant head, with all of its tissues, is of interest. The model by Ponce and Ponce (2011) focused on modelling the vibration from shaking in an infant's cervical vertebrae, but also modelled the effects of an impact to the infant head, with the head rotating about the spinal cord. The kinematic effects of the head and neck are important if the primary force (impact or shaking) is applied to the torso, rather than the head. These features come at the cost of added complexity and computational expense. As a result of their limitations, these two studies are not considered as being as relevant to the present thesis as those focusing on the modelling of the infant head.

The above seven complete models consist of suitable geometry, mesh, material models, boundary conditions, solution method and validation to simulate head impacts in infants. A reasonable amount of research has already been completed to achieve the state of current infant head FE models to date. However, for use as a tool to investigate head injuries that may have been caused by accident or abuse, there is room to further improve several aspects of the models, as described below.

Any FE analysis requires inputs of geometry, discretisation method (meshing), material models, boundary conditions and solver, along with suitable validation (Mac Donald 2011). Some points regarding these inputs from the current FE models are discussed here to identify areas for further improvement.

Geometry

In regards to geometry, Li, Park, et al. (2015) and Li et al. (2016) have developed methods to create geometries of infant heads quickly, efficiently and accurately based on statistical models and CT scans.

If required, specific geometry of an individual infant's head can be obtained from CT scans, and software used to convert the data into 3D geometry formats. Obtaining geometries of an infant head is relatively straight forward if scan data is available and therefore is not an important limiting factor to creating an accurate and valid infant head FE model. Li, Sandler, and Kleiven (2019) have shown that subject specific geometry can be used to reconstruct possible injury histories to a reasonable level of accuracy. Suitable methods for generating patient specific geometry exist, hence time should be spent on developing other areas of the FE models.

Meshing

The choice of element type is largely a decision of the analyst and is generally based on aspects specific to the model (for example, whether the geometry consists of thin bodies that can be meshed with shell elements). Early infant head FE models used shell elements for thin tissues such as the skull, suture and/or dura (Coats, Margulies, and Ji 2007, Roth et al. 2007, Li, Luo, and Zhang 2013), while more recent models use solid elements for all tissues, regardless of thickness (Li, Sandler, and Kleiven 2017, Khalid et al. 2019, Burgos-Flórez and Garzón-Alvarado 2020). This move to solid elements is likely due to an increase in computational power, making models with a greater number of nodes more feasible. Li, Sandler, and Kleiven (2017) used hexahedral elements, while Khalid et al. (2019) and Burgos-Flórez and Garzón-Alvarado (2020) used tetrahedral elements. Both element types have advantages and disadvantages (as discussed in Chapter 2), therefore, future work could investigate any differences in using each type (for the same model). This could provide guidance on whether one type will provide more accurate results over the other, allowing for a greater understanding of the trade-offs with each when deciding on which type to use.

Li, Sandler, and Kleiven (2017) had the greatest number of elements (5.3 million) of all studies presented here. As discussed later in this chapter, they also had the best validated models, suggesting that there is some correlation (among other factors such as more accurate material models) with the number of elements and FE model validity. Given no other study is as well-validated or had such a relatively large number of elements (refer Table 3.2), it cannot be said whether such a large number of elements is required to achieve this level of validation. A larger number of elements increases the computational time; therefore, mesh convergence should be an important aspect in future work to ensure that accuracy is balanced with computational cost to make infant head FE models more practical for use in forensics.

Material Models

The material models currently available for the various tissues of the infant head are the most important factors limiting the accuracy of FE models to date. Given the scarcity of experimental data

on the mechanical properties of infant tissues, material models are generally determined from animal tissues (such as pigs). While infant porcine tissues, such as cranial bone, have been shown to be similar to human infants (Margulies and Thibault 2000), there can be no substitute for directly determining material properties from human infant tissues. To date, the model created by Li, Sandler, and Kleiven (2017) using nonlinear material models is the most valid given that its results show a better correlation against cadaver test results, compared to those for a similar model using linear elastic materials by Li, Luo, and Zhang (2013) that was validated against the same cadaver tests. All other studies used linear elastic material models, which resulted in FE models that were not as well validated against experimental data compared to the model by Li, Sandler, and Kleiven (2017). As Li, Sandler, and Kleiven (2017)'s peak accelerations were within 10% of those measured in the cadaver drop tests (Li, Luo, and Zhang (2013) had a difference of 10-20%), there is clearly an increase in the accuracy when using nonlinear models.

In the studies using linear elastic material models, only the skull and suture models contain parameters measured from infant tissue samples (along with those for the viscoelastic model for the brain). As noted in Table 3.4, the parameters used for the scalp, membranes and CSF are those for the adult tissues. This is due to the lack of specific data for the infant tissues and the scarcity of human infant tissue samples to conduct the required experiments on. Adult skull has an elastic modulus of around 8 GPa (Hubbard 1971), while 500 MPa has been previously used for the infant skull. Adult suture has been shown to have similar properties to the adult skull and therefore also has an elastic modulus of around 8 GPa, while 8 MPa has been used for the infant suture (Hubbard, Melvin, and Barodawala 1971). These significant differences in the elastic moduli for the infant and adult tissues show the need for specific data relating to the infant tissues. Hence the use of adult data for the scalp, membranes and CSF are a limitation to the respective FE models.

Tissue failure is not considered in any of the seven complete models, although two have been used in subsequent studies to reconstruct real-world falls and predict skull fracture (Hajiaghamemar et al. 2018, Li, Sandler, and Kleiven 2019). Although, these studies do not specifically discuss the methods of predicting skull fracture they use. Some work has been conducted in predicting skull fracture, with Li, Liu, et al. (2015), and Hajiaghamemar et al. (2018) developing skull fracture risk curves, while Coats and Margulies (2006) is the only study to have measured the ultimate stress of infant cranial tissue. Methods for predicting skull fracture in FE models requires further investigation in order to be able to use them in reconstructing suspected cases of abusive head trauma.

The scarcity of human infant tissues has also limited the ability to gather data for more advanced material models that may better represent the behaviour of the infant head tissues. The scalp can

have a fluid-like response during an impact and may be better modelled as viscoelastic or hyper-viscoelastic (Brewick, Saunders, and Bagchi 2017). These models better represent this behaviour than isotropic linear elastic or hyperelastic models that have been used previously. For the skull, due to its hierarchical composite make-up resulting in structures that have different length scales, it could also be modelled as viscoelastic (Yue et al. 2008, Brewick, Saunders, and Bagchi 2017). An elastic-plastic model may also represent the behaviour of the skull better, especially when considering skull fracture, as it starts to incorporate plastic deformation. This would be especially applicable to the infant skull which is not as brittle as that of an adult. Future work is required to further investigate more advanced material models that can better represent the behaviour of the infant head tissues. This will require infant head tissues, however, other methods of verifying material properties may need to be developed if there is not an increase in the availability of human infant tissues for research.

Boundary Conditions

Many of the FE models to date use boundary conditions replicating low height falls and/or compression of the head (Roth, Raul, and Willinger 2010, Li et al. 2013, Li, Luo, and Zhang 2013, Li, Sandler, and Kleiven 2017, Khalid et al. 2019, Burgos-Flórez and Garzón-Alvarado 2020). Low height falls are often given as the history of the cause of an infant's head injuries (Chadwick et al. 1991), therefore modelling these types of head impacts is of value. However, only Roth et al. (2007) modelled an impact velocity higher than that experienced in a fall from one metre. To estimate the maximum impact speeds of blunt weapons in deliberate assaults, Williams (2008) found that the maximum speed of a fit adult male swinging a baseball bat (the longest weapon commonly employed in assault) was 36.2 ms^{-1}. Impacts with similar characteristics to that of a baseball bat swung at 36 ms^{-1} (tip speed) should be investigated to understand the injury patterns which may result from deliberate physical abuse. The parameters which determine the acceleration experienced, peak force and energy transferred in an impact are the velocities, masses and stiffness of the two (or more) colliding objects.

In the six studies noted above, the boundary conditions were typically applied to the models by specifying an initial velocity calculated from the simulated drop height and the mass of the head. Simulated drop heights were mostly 0.15, 0.30 or 0.82 m depending on the experimental data the models were being validated against. The impacting surface was generally a fixed, rigid plate and either had a frictionless or frictional boundary condition. Only Li, Luo, and Zhang (2013) investigated the effect of drop height and impact surface stiffness on the response of the model. Further investigation of both is warranted as infants can fall from a range of heights and onto different surfaces (such as various household furniture and domestic flooring types). Investigation of impacts to different surface types other than a flat surface should also be carried out. This could include an impact to the edge of furniture (for example, an infant falls from the arms of a caregiver onto the edge of a table).

Contact conditions between each head tissue is rarely discussed in any of the existing FE models. It can be reasonably assumed that most tissues are bonded together (see Chapter 2 for contact type definitions). Only Coats, Margulies, and Ji (2007), and Khalid et al. (2019) discuss contact conditions between the CSF and brain. Khalid et al. (2019) use sliding contact at the brain-skull interface, but do not specify a friction coefficient, while Coats, Margulies, and Ji (2007) use frictional contact with a coefficient of 0.2.

Validation of the Complete Head Models

Validation of an FE model is important to determine the overall accuracy of the model in simulating real world problems. Roth, Raul, and Willinger (2010), Li et al. (2013), Li, Luo, and Zhang (2013), Li, Sandler, and Kleiven (2017, 2019), Khalid et al. (2019), and Burgos-Flórez and Garzón-Alvarado (2020) all validated their FE models against experimental cadaver tests. Roth, Raul, and Willinger (2010), Li et al. (2013), Khalid et al. (2019), and Burgos-Flórez and Garzón-Alvarado (2020) validated their models against the experimental results from Prange et al. (2004). For the compression tests, both Roth, Raul, and Willinger (2010), and Li et al. (2013) described their models as having a good correlation with the experimental results for the force-displacement curves. However, Prange et al. (2004) describes the curve as being an exponential function, but the curves from the FE models do not accurately reflect this. For the drop tests, Li et al. (2013) had a range of both small and large variations in the results for peak head acceleration when compared to the cadaver drop tests. The smallest difference was around 2 g and the largest being approximately 20 g. Roth, Raul, and Willinger (2010) conducted a statistical analysis based on the standard deviations provided by Prange et al. (2004) and found that the error between their results and the cadaver tests was 51% and 45% for the occipital and parietal impacts respectively. The peak acceleration for Khalid et al. (2019)'s FE model with a drop height of 0.3 m had differences ranging from 18% to 48%. However, Khalid et al. (2019) compare their data with three-day-old experimental data from Prange et al. (2004) rather than the 11-day-old data, which is of a similar age (10-days). If comparisons are made with the 11-day-old data, the peak acceleration differences range from 21% to 180% across the different impact locations. For Burgos-Flórez and Garzón-Alvarado (2020)'s model at the same height, the differences range from approximately 40% to 50%. However, they use a skull elastic modulus of 200 GPa, which is less than half of that used in many other models and the experimental data measured by Coats and Margulies (2006). All studies state the global stiffness of their FE models correlate well with experimental data; however, this is highly subjective. Therefore, there is room to improve the FE models to better predict the peak acceleration responses.

Li, Luo, and Zhang (2013) and Li, Sandler, and Kleiven (2017) validated their FE models against the cadaver tests from Loyd (2011). For the compression tests, Li, Luo, and Zhang (2013) found that their

model predicted slightly higher forces on the force-displacement plot, while the model created by Li, Sandler, and Kleiven (2017) produced a curve that followed the general exponential shape of the experimental curve. For the drop tests, Li, Luo, and Zhang (2013) found that the peak acceleration was 10 to 20% higher than the cadaver tests, while Li, Sandler, and Kleiven (2017) found a difference of, at most, 10%. As Li, Sandler, and Kleiven (2017) used nonlinear material models in their FE model, their results indicate the importance of accurately modelling the materials to improve the accuracy and validity of the infant head FE models. It should also be noted that Li, Luo, and Zhang (2013) used a model for a six month old infant compared to the five month old cadavers used by Loyd (2011), which could explain the higher stiffness of their model, given that the stiffness of the infant skull increases with age (Margulies and Thibault 2000, Coats and Margulies 2006). However, also of note, an accurate FE model and a cadaver test might be completed with different individuals of the same age but produce different results due to inter-individual differences.

The model by Li, Sandler, and Kleiven (2017) is the only model that is validated to within 10% of experimental tests. Validation was completed for the combined FE model consisting of all tissues, however, the individual models for each of the tissues were not validated in isolation. There is scope to validate the individual tissue material models to assess whether the model parameters are suitable. This could involve a range of physical testing of an individual tissue and using the resulting data (such as displacements or strains) to validate an FE model replicating the physical testing. Other FE models are largely limited by the material models used as they are often limited to linear elastic models, which do not include rate dependent behaviour of the biological tissues involved. The use of linear elastic models can also result in FE models that have a relatively larger stiffness as they do not allow for uncrimping in soft tissues. As soft tissues are placed under load, the individual collagen fibres start to elongate and align with the load direction. This creates a toe-region on the stress-strain curve where the stiffness is lower than when the fibres are uncrimped (Meyers et al. 2008).

For the studies that were validated against cadaver tests, global parameters, such as acceleration for the drop tests and force-deflection curves for the compression tests, were compared. There are an infinite number of combinations of local parameters that could satisfy these global parameters. That is, highly inaccurate local parameters could lead to accurate global results. This means that local stresses and strains are not necessarily modelled with the same level of accuracy. Therefore, the validation of individual material models will reduce the likelihood of a combination of inaccurate local parameters resulting in accurate global parameters.

Recommendations for Future Work

Overall, the greatest limitation in the current infant head FE models is the modelling of the tissues' material behaviour. There are many factors influencing the behaviour of the tissues under a given load, including the loading rate and age dependence. Accounting for each of these factors is the challenge for future models.

Tissue Tests

In determining the influence of loading rate and age dependence on the behaviour of the tissues, experimental testing of infant tissues is required. This will allow the determination of the parameters for the material models of infant tissues. However, the greatest limitation to this is the availability of suitable specimens for physical testing. Obtaining specimens of infant head tissues is often difficult due to their limited availability and for ethical reasons. This results in limited experiments that can be conducted to determine different material model parameters, and any available specimens are likely to be used for other studies deemed to be more significant. Often, animal tissue substitutes (such as infant porcine tissues) are used for such physical testing as they have similar properties to that of infant tissues. The use of simulant materials could also be used, but these require their validity to be proven, so do not eliminate the need for animal or human tissue tests.

When tissue specimens are available, it is critical to ensure that they are preserved in a state that allows them to exhibit the same mechanical properties as living tissues. Due to technical and logistical reasons, human tissues cannot usually be tested mechanically at the time of harvest or in sufficient sample sizes. In order to preserve the tissues and prevent autolysis or bacterial contamination, they are usually treated chemically, using ethanol or formaldehyde, or frozen. Tissues used in previous research have been frozen and then defrosted to room temperature in saline baths or mock CSF solution (Margulies and Thibault 2000, Coats and Margulies 2006).

Chemical fixation is known to impair tissue mechanics of both soft and hard tissues, in particular of the organic matrix. In a series of studies, Hammer et al. (2014) showed that both ethanol and formaldehyde cause changes in the properties of human bone and that the mechanisms of denaturation vary for the chemicals. The effects of freezing of biological tissues on their mechanical properties have given controversial results, of which the freezing protocol appears to play a major role (Hammer et al. 2014). A key aspect in the limited validity of results obtained from tissues that have been frozen appears to be the formation of ice needles in the tissues. If a relatively slower cooling rate is used, the ice needles tend to increase in size, resulting in the tissues being intrinsically destroyed by their formation, with subsequent loss of water. Vice versa, it appears that a rigorous pre-cooling of the tissues close to the freezing point prior to snap freezing, and a rapid warming of the frozen tissues

prior to testing, may minimise such alterations of tissue integrity. In determining the behaviour of the infant head tissues, these preservation effects need to be considered in order to be able to accurately model the material behaviour in an FE model.

Age Dependence

In terms of the effect of age dependence, only Li, Sandler, and Kleiven (2017) use a parameter set for the skull that is a function of age, with most other FE models using parameters that have been obtained from specimens of a similar age to that of which they are trying to model. Given that the material properties of the infant head tissues change with age (Margulies and Thibault 2000, Coats and Margulies 2006) (and are significantly different to those for adults), material models need to be a function of the age of the infant. An ideal infant head FE model would be one that can be parameterised in terms of age so that model components such as the geometry and material models can be adapted for the desired age. Therefore, there is a future need for the material models to be age dependent. However, this is likely to require a large amount of work and resource as each tissue, at a range of ages, would have to undergo physical testing and a model created based on the results.

Impact with different Objects

Another area of interest is the simulation of blunt force impacts from weapons. As discussed earlier, previous FE models simulated falls onto flat surfaces. Roth et al. (2007), and Roth, Raul, and Willinger (2008) simulated an inflicted impact, but the object contacted was a rigid wall, which is mechanically identical to a fall with the same impact velocity. There have been no previous studies simulating blunt force impacts from non-flat weapons. These types of impacts are important to model in future research so that there is a greater understanding of the differences in the injury patterns resulting from impacts such as falls from less than a metre, falls greater than a metre and from potential weapons. Impacts from objects with curved or angular surfaces are likely to exhibit injury patterns that differ from those with large flat surfaces (such as a floor). Therefore, understanding the differences will allow medical professionals to make more informed observations on whether an infant is likely to have suffered accidental or non-accidental head injuries.

Conclusions

A valid infant head FE model requires accurate geometric representation of the head, a suitable discretisation method, material models that model the effect of loading rate, age dependence and directional dependence, boundary conditions that accurately model the different loading conditions, and validation against experimental tests. There are only seven complete FE models in the current literature that are close to meeting these requirements.

- For the geometry, a lot of work has already been carried out for obtaining both specific and generalised geometry of the infant head. Therefore, future work should be concentrated in other areas of the modelling process.
- A variety of finite element types have been used to create the meshes in these models. Future work could investigate any difference in the results of a FE model when only element type is changed, especially for solid elements (hexahedral and tetrahedral), where there are trade-offs for each element type. The number of elements required to balance model accuracy with computational cost should also be considered in future work so that infant head FE models can have practical use in forensics.
- Li, Sandler, and Kleiven (2017)'s model using nonlinear material models for most head tissues is the best validated model to date. Before this model, isotropic elastic models were mostly used. Due to ethical considerations, human infant tissues are scarce, hence only data for the skull and suture are from such tissue. All others are either obtained directly or scaled from adult data. The lack of available human infant tissue to obtain tissue material properties is by far the greatest limitation of infant head FE modelling.
- Most FE models to date are used principally to model low height falls onto a flat, rigid surface. There is value in investigating the effects of drop height and impact surface stiffness on the response of the FE model, as well as different surface types (such as an edge of a surface) and blunt force impacts from weapons. This would allow for greater understanding of the predicted injury patterns expected from such impacts. Contact conditions at tissue interfaces in the current FE models also lack details and would benefit from further investigation, as would methods for predicting skull fracture.
- Validation of the FE models to date largely consists of comparing acceleration and force-deflection plots to cadaver drop and compression tests, with only a few studies comparing stress and strain patterns with observed fracture patterns (Hajiaghamemar et al. 2018, Li, Sandler, and Kleiven 2019). Comparison of the acceleration and force-deflection plots allows for validation of the models at a global level but does not necessarily mean that the local parameters are accurate. Validation of individual material models for each of the tissues can be further improved to increase the global accuracy of the FE model, as well as ensuring they can model the effects of loading rate, age and direction dependence.

Overall, the most significant deficiency in infant head FE models is the lack of validated combinations of material models for the different head tissues, as these are age dependent up to maturity. As the gap is filled by further research, FE modelling of the head offers the possibility of accurate, reliable

prediction of the injury site and severity from defined impacts. FE modelling of infant head impacts is likely to find a role in the investigation of suspicious injuries, and in the design of safety equipment.

In this thesis, Chapter 4 investigates Aim #1 and #2 so that future experimental work can be focussed towards areas that will provide the most benefit to improving infant head FE models as human infant tissues are scarce. Chapter 5 conducts dynamic impact testing on human child skull specimens (Aim #3) to increase the knowledge in this area. Together, Chapters 4 and 5 hope to go some way towards improving the gaps in the literature regarding material model parameter data and which are the most important to have as accurate as possible. Aim #4 is covered in Chapter 6 where different impact surfaces and drop heights are investigated to improve understanding around how they affect the dynamic response of the infant head. This will allow future work to gain a greater understanding of the predicted injury patterns expected from such impacts. In Chapter 7, Aim #5 is investigated to determine what is required from a FE modelling perspective to be able to model skull fracture patterns, which can be used in future work to validate FE models against observed fracture patterns in real-world cases. Aim #6 is presented in Chapter 8 where various models with different levels of fidelity are investigated to determine how simplifying assumptions used to decrease the computational cost will affect the results.

Chapter 4 Sensitivity of Material Model Parameters

This chapter is based on the study presented in Brooks, Garnich, and Jermy (2020). Additions have been made where content was summarised for the purposes of journal publication.

Introduction

A review by Brooks et al. (2018) (Chapter 3 of this thesis) found that most published finite element (FE) models of the infant head (up to 2018) use isotropic elastic material models for important tissues and reliable data for material model parameters is lacking. Only one FE model used nonlinear material models for each of the head tissues (Li, Sandler, and Kleiven 2017). There have been experiments conducted to investigate the material properties of infant head tissues (Margulies and Thibault 2000, Prange and Margulies 2002, Coats and Margulies 2006). Nevertheless, ethical considerations mean infant tissue is rarely used and infant data remains scarce (Brooks et al. 2018), complicated by the dependence of some parameters on the age of the subject and the strain rate. To fill this gap, many of the tissues are modelled using data measured from adult specimens.

A sensitivity analysis of the material model parameters on FE models can identify which parameters have the greatest influence on the response of the model. This can guide future experimental campaigns to ensure that precious human tissue is used in the most efficient way to improve FE material models. It can also provide an understanding on the level of influence less accurate data has on model outputs.

Coats, Margulies, and Ji (2007), Li et al. (2013), Li, Sandler, and Kleiven (2017) have investigated the sensitivity of material model parameters, but in a limited capacity. No detailed sensitivity analysis of material model parameters on FE model outputs for infant head impacts has been carried out to date. The present study is a detailed sensitivity analysis on an infant head impact FE model as it concerns how changes to the material model parameters influence relevant metrics such as peak acceleration and local maximum stresses and strains in the head tissues. A brief literature review on the origin of the material model parameters commonly used in existing FE models, and the confidence in their accuracy, is also presented.

Origin of Material Model Parameters

Of the infant head FE models published to date, Li, Sandler, and Kleiven (2017) use the most sophisticated material models, combined with parameters sourced from studies of infant head tissue material or scaled from adult studies. That model is the basis for the discussion that follows. Table 4.1 summarises the material model parameters used for the nonlinear material models. Detail on each

material model is provided in Brooks et al. (2018) and Chapter 2 of this thesis. The origin of the parameters is reviewed below.

Brain

A second order Ogden hyperelastic model (equation 2.2) was used for the brain. Kleiven (2007) used data from Franceschini et al. (2006) to fit an Ogden model. Franceschini et al. (2006) carried out uniaxial, cyclic loading tests on brain tissue. While the age is not explicitly stated, it is assumed that the data from Franceschini et al. (2006) was obtained from adult specimens due to the greater availability of such specimens, compared to infant specimens, and that Kleiven (2007)'s FE model is for an adult.

Dura

A two parameter Mooney-Rivlin hyperelastic model (equation 2.3) was used for the dura. Bylski et al. (1986) carried out biaxial tension tests on foetal dura (30 to 42 weeks gestation) and fitted the data to the Mooney-Rivlin model.

Skull

An orthotropic elastic model was used for the skull to account for the directional variations in the elastic modulus (E) of the infant skull. During early infancy, grain fibre patterns in the skull are easily visible, but become invisible around the age of six months (McPherson and Kriewall 1980, Margulies and Thibault 2000, Coats and Margulies 2006). Coats and Margulies (2006) conducted three-point bend drop tests on infant skull samples with ages ranging from 21 weeks gestation to 13 months. The E in the direction of the fibres is here defined as E_1, while the direction perpendicular to the fibres is E_2 (measured by Coats and Margulies (2006)), and the through thickness direction is E_3. The FE model by Coats, Margulies, and Ji (2007) used an E_1 calculated from the data for E_2 and an anisotropy ratio calculated using direction specific data from McPherson and Kriewall (1980). This anisotropy ratio, A_R, accounts for the visible grain fibre patterns and is defined by:

$$A_R = \frac{E_1}{E_2} \tag{4.1}$$

In adults, this ratio approaches one as the adult skull becomes isotropic (McElhaney et al. 1970). Kriewall (1982) measured E_1 and E_2 from 554 specimens of foetal skull (16 calvarias with an age range of 20 to 42 weeks gestation, and a six-year-old) under static loading. Li, Sandler, and Kleiven (2017) fitted a two-term exponential function to the measured data to determine a function for the anisotropy ratio, as a function of age (in months) (Equation 4.2). This function was defined as:

$$A_R(age) = 0.9071e^{-0.3017\times Age} + 1.398e^{-0.00155\times Age} \tag{4.2}$$

Data for E_2 from Coats and Margulies (2006) was used to calculate E_1. This data was used to fit piecewise spline functions to obtain functions for E_1 and E_2 in terms of age (E_3 was assumed to be the same as E_2). The resulting fits had coefficient of determinations, R^2, that were relatively low (0.35 for the E_2 of the occipital bone). This is due to the inherent variability of the skull specimens from the different infant subjects (Li, Sandler, and Kleiven 2017).

Poisson's ratio for the infant skull was assumed to be the same as for adults, with the adult data taken from McElhaney et al. (1970).

Suture

A first order Ogden hyperelastic model was used for the suture. The model was fitted to the uniaxial tensile test data on infant suture specimens from Coats and Margulies (2006). Coats and Margulies (2006) only presented a full data set for specimens from a two-month-old. However, they found that the E did not vary significantly with age. Therefore, the Ogden parameter μ was scaled to represent the average E for all the specimens tested by Coats and Margulies (2006).

Scalp

Two layers were used to model the scalp, based on the work of Fahlstedt et al. (2015), who modified the adult head FE model of Kleiven (2007). The outer layer was Ogden hyperelastic, with the constants obtained from Crichton et al. (2011). Crichton et al. (2011) quantified the viscoelastic and hyperelastic behaviour of skin by performing atomic force microscopy indentation on mouse skin. For the inner layer, also Ogden hyperelastic, the constants were obtained from data presented by Krouskop et al. (1998). No explanation was provided on how the data was used to obtain the constants. Li, Sandler, and Kleiven (2017) scaled the parameters for the infant scalp outer layer to be one tenth of those for the adult model. Those for the inner layer were assumed to be the same as for the adult.

Table 4.1: Origin of Material Model Parameters							
Tissue	**Material Model**	**Parameter**	**Parameter Value**	**Standard Deviation (where available)**	**Age (Months)**	**FE Model**	**Parameter Value Origin**
Outer Scalp	Ogden Hyperelastic	μ_1	13000 Pa		Scaled from Adult	Li, Sandler, and Kleiven (2017)	Crichton et al. (2011)
		α_1	24.23	0.63	Adult		
Inner Scalp	Ogden Hyperelastic	μ_1	3990 Pa		Adult	Li, Sandler, and Kleiven (2017)	Krouskop et al. (1998)
		α_1	8.8		Adult		
Suture	Ogden Hyperelastic	μ_1	14800 Pa		2	Li, Sandler, and Kleiven (2017)	Coats and Margulies (2006), Li, Sandler, and Kleiven (2017)
		α_1	6.9		2		
Skull -Occipital	Orthotropic Elastic	E_1	650.9 MPa		5	Li, Sandler, and Kleiven (2017)	Li, Sandler, and Kleiven (2017)
		E_2, E_3	392.9 MPa	66.0 MPa	5		Li, Sandler, and Kleiven (2017), Coats and Margulies (2006)
		v_{12}	0.22	0.11	Adult		McElhaney et al. (1970)
		v_{23}, v_{13}	0.19	0.08	Adult		
		G_{12}, G_{31}	215.9 MPa				Li, Sandler, and Kleiven (2017)
		G_{23}	165.1 MPa				
Dura	Mooney Rivlin Hyperelastic	C_1	1.18 MPa			Li, Sandler, and Kleiven (2017)	Bylski et al. (1986)
		C_2	0.295 MPa				
Brain	Ogden Hyperelastic	μ_1	53.8 Pa		Adult	Li, Sandler, and Kleiven (2017)	Franceschini et al. (2006), Kleiven (2007)
		μ_2	-120.4 Pa		Adult		
		α_1	10.1		Adult		
		α_2	-12.9		Adult		

Methods

Geometry Creation

A sensitivity analysis requires many simulations. To make computational time tractable, and to achieve some level of generality to a diverse human population, head geometry must be simplified whilst preserving an acceptable degree of biofidelity.

A simplified three-dimensional (3D) head geometry was generated using computed tomography (CT) scan data of a three-month-old infant obtained from the Victorian Institute of Forensic Medicine, Melbourne, Australia (ethical approval ref. EC 12-2018). The length and breadth of the head are approximately 140 mm and 110 mm respectively, giving an approximate head circumference of 424 mm, which represents a 97th percentile male (or an approximately 60th percentile four-month-old male as the age of the patient may have been closer to four months than three). The cranial bones were segmented from the soft tissues using ITK-SNAP (Yushkevich et al. 2006). Automatic thresholding was used to distinguish between the bone and soft tissues, with some manual identification to ensure that areas not identified from the automatic process were included. Individual soft tissues could not be distinguished from one another in the CT scan data. The outer surface of the scalp was also segmented following a similar process.

Meshmixer (Autodesk, Inc., San Rafael, California, USA) was used to smoothen the tessellated triangle surface mesh (resulting from the segmentation process and initially had approximately 1.5 million triangles), remove facial and nasal bones, and fill in the eye sockets, nasal cavity and foramen magnum to make a watertight geometry. Some areas of the cranial bones had holes where the segmentation process did not pick up the difference in grayscale values. These holes were also filled over. The segmentation process also did not fully segment the area of suture between each cranial bone. This resulted in some areas of the 'gap' for the suture being filled with bone geometry. These areas were removed and then all areas of suture were filled in to create a complete skull geometry with no suture. Figure 4.1 shows the skull geometry before and after the smoothening and patching process.

A STL (stereolithography) file of the skull geometry was imported into Geomagic DesignX (3D Systems, Inc., Rock Hill, South Carolina, USA) so that the tessellated mesh could be transformed into NURBS (non-uniform rational B-spline) surface geometry, allowing for easier manipulation in SOLIDWORKS (Dassault Systèmes SOLIDWORKS Corp, Waltham, Massachusetts, USA) to generate the remaining head tissues. This conversion process was largely trial and error in order to get a correct surface patching that conformed to the curvature of the original geometry. The NURBS geometry was then exported to SOLIDWORKS.

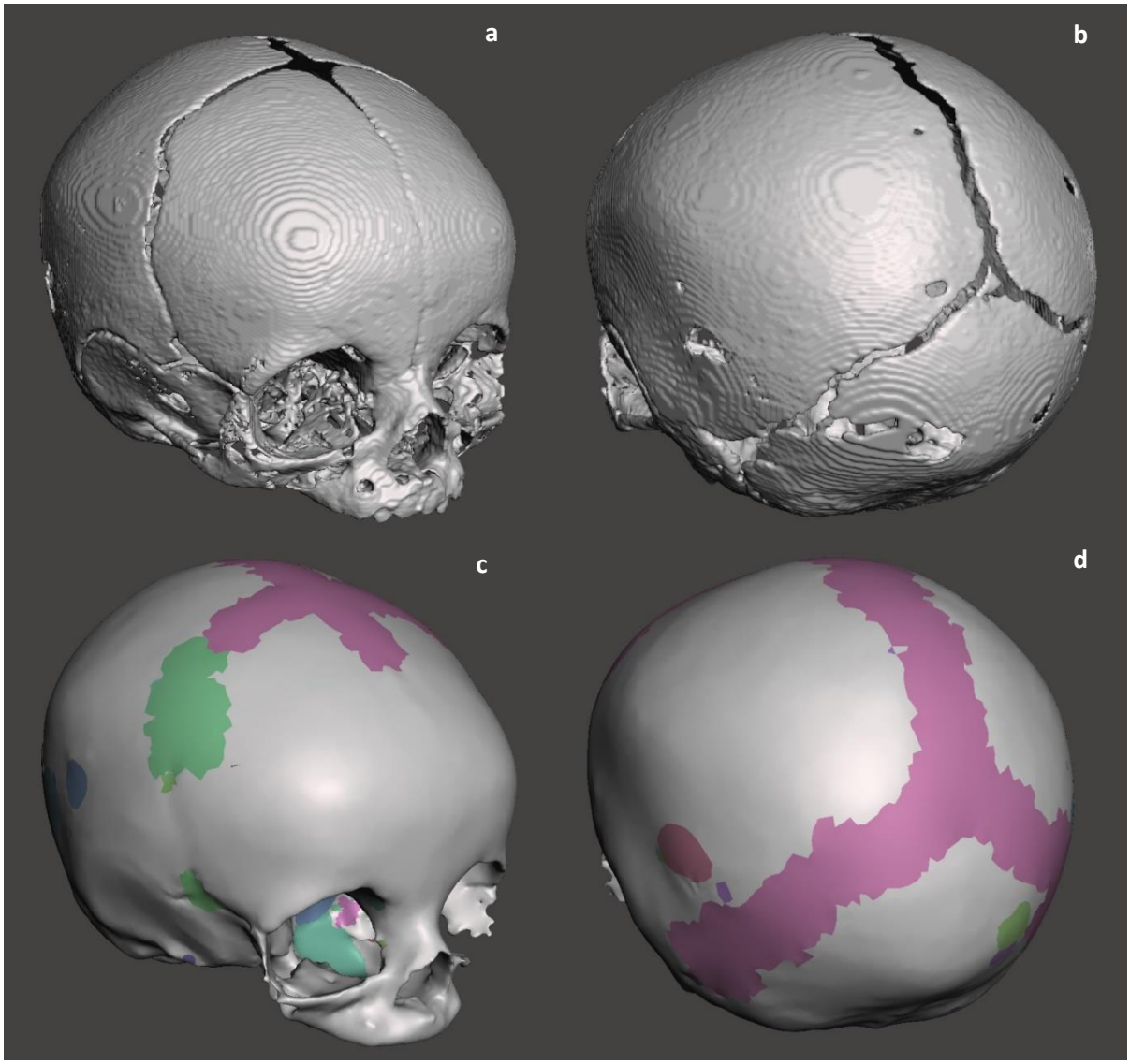

Figure 4.1: Skull geometry as segmented from CT scan (**(a)** and **(b)**), and after smoothening and patching of suture and holes (**(c)** and **(d)**). Note: patch colouring here does not mean anything.

The suture was generated in SOLIDWORKS by overlaying the skull geometry with no suture with a copy of the geometry that included the suture 'gap'. The general outline of the suture could then be projected onto the no suture geometry, using surface splines. As described earlier, the segmentation process had trouble distinguishing the boundaries of the soft tissue with the cranial bones due to similar grayscale values. Therefore, the suture was much wider than would realistically be expected, hence the manual generation of the suture. The suture outline was modified slightly along the sagittal plane so that the geometry could be split along the sagittal plane in the future; the front fontanelle was also adjusted for similar reasons. The outline of the suture was projected onto the skull so that it split the faces making up the skull. These new faces were copied to create a surface body of the suture. This surface body was thickened 5 mm inwards and the SOLIDWORKS 'combine' function used to create a geometry that was 'common' to both the suture and the original skull. An analogy to this is a Venn diagram, with the new suture geometry being the overlap between the two circles. This created

a suture geometry that had the same through-skull thickness as the cranial bones. The suture geometry was subtracted from the original skull to create a cranial bone geometry with the 'gap' for the suture. The skull consisted of the parietal, occipital and frontal bones, with the latter two being connected by a fully enclosed base of the skull. The finished cranial bone and suture are shown in Figure 4.2 (a) and (b).

The scalp was created by first using a similar process as the skull to convert the STL tessellated mesh geometry into NURBS surfaces, using DesignX. The solid geometry was then overlaid with the skull geometry and a Boolean operation used to subtract the skull from the scalp. This left two solid bodies, with the outer as the scalp geometry (including the facial region) and the inner solid body used to create the brain. The dura and cerebrospinal fluid (CSF) were neglected, hence the brain (without sulci or fissures) filled the entire cranial cavity. All geometric bodies were split in the sagittal plane and one half deleted so that symmetry boundary conditions could be used. Figure 4.2(c) shows all tissue layers.

The removal of the facial and nasal bones from the skull means there are no supporting structures within the facial region, hence 'sagging' behaviour would occur in the softer facial tissue. Therefore, all facial soft tissue was removed and replaced with a layer of 'scalp' tissue. Anatomically correct scalp thickness was maintained in the frontal, vertex, parietal and occipital regions.

Boundary Conditions and Mesh

An occipital head impact onto a 100 x 100 mm rigid floor was modelled. The floor was located so that it was just touching at the beginning of the simulation. An impact velocity of 2.4 ms^{-1} was applied to the head geometry. This is equivalent to a 0.3 m drop height, similar to that used in the experimental studies of Prange et al. (2004), and Loyd (2011). Contact between each layer was set to bonded (layers could not separate or slip relative to one another), while frictionless body interaction was set between the scalp and impact surface. A fixed constraint was applied to the impact surface and symmetry applied to the faces on the sagittal plane. ANSYS Explicit Dynamics (ANSYS, Inc., Canonsburg, Pennsylvania, USA) with the ANSYS AUTODYN (ANSYS, Inc., Canonsburg, Pennsylvania, USA) solver was used to simulate the first 11 ms after initial impact. The sensitivity analysis outputs were evaluated at a time point of 2.5 ms, which balanced computational time against ensuring a reasonable level of deformation to assess the outputs. Forces through the neck, resulting from the effect of the rest of the body, were neglected.

Four-node tetrahedral elements were used to mesh the head geometry in ANSYS Meshing (ANSYS, Inc., Canonsburg, Pennsylvania, USA). A series of local mesh refinements were used within the contact region. Impact force and the maximum principal stress in the occipital bone (located at a vertex where a node is created in every mesh) were used to check mesh convergence. As shown in Figure 4.3, the

percentage difference between each mesh and the densest mesh (consisting of approximately 249 000 nodes) converges to within 5% at around 58 000 nodes. Global element size was 6 mm, with local refinement sizes ranging from 0.5 to 1 mm within a 25 mm radius of the impact location and 2 mm within a 50 mm radius (Figure 4.2(d)). This resulted in a mesh consisting of 64 640 nodes and 325 251 elements, with at least two to three elements through the thickness of the skull in the refined region.

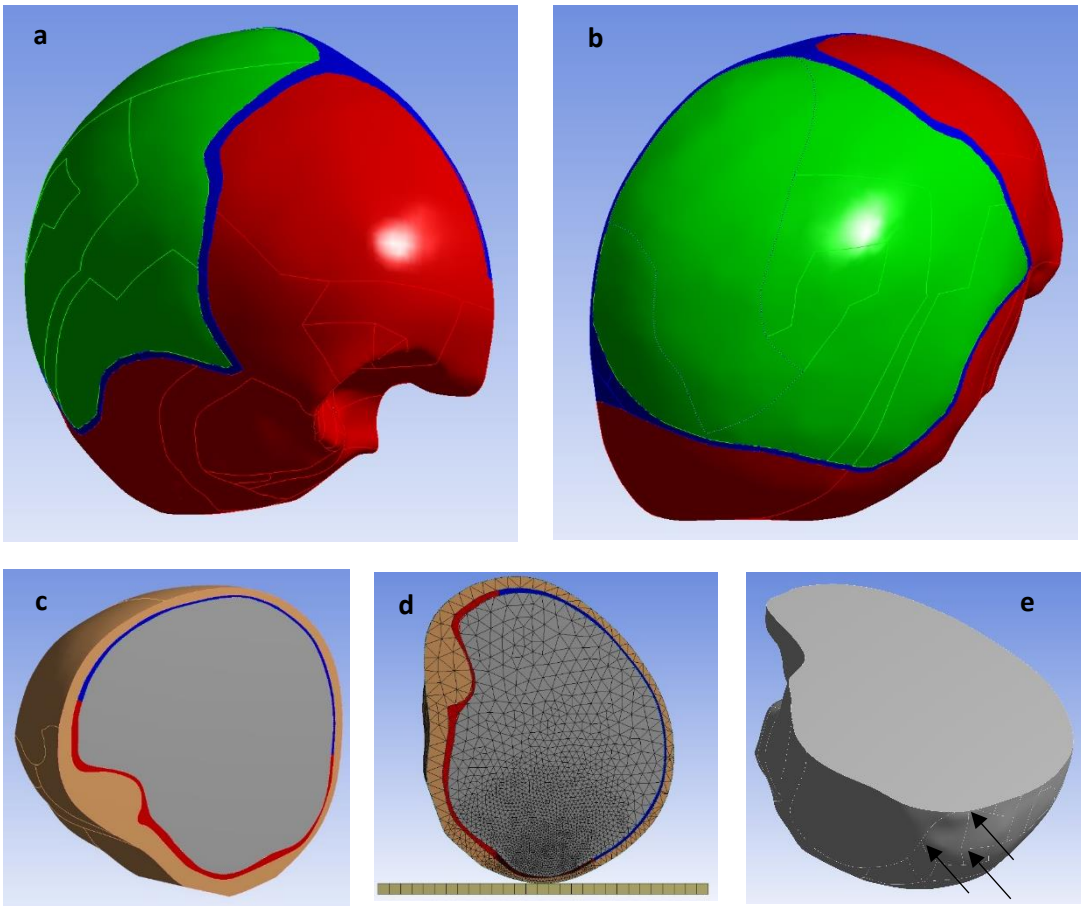

Figure 4.2 Simplified 3D head geometry with symmetry in the sagittal plane. **(a)** and **(b)** show cranial bones and suture. **(c)** shows all tissues and symmetry plane. **(d)** shows tetrahedral mesh with refinement in contact region. **(e)** Arrows indicate location of vertices used to assess local outputs in the brain (similar locations are used for the local outputs in the skull).

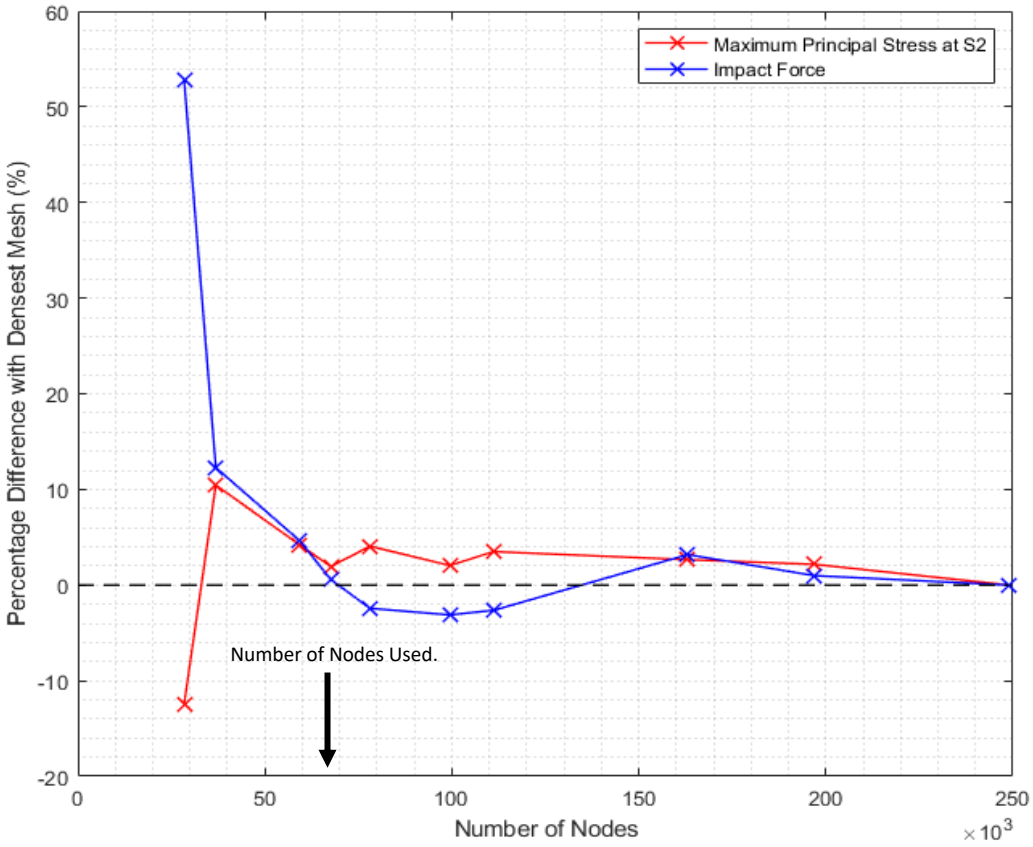

Figure 4.3: Mesh convergence of baseline model (refer to 'outputs' section for description of S2).

Material Models

The brain, suture and scalp were modelled as hyperelastic materials. For the baseline model, parameters were taken from Li, Sandler, and Kleiven (2017). As the scalp in the present study was one layer, the parameters for the outer scalp were used. The material incompressibility factor, *d*, for the Ogden hyperelastic models were not presented by Li, Sandler, and Kleiven (2017), although Poisson's ratio was. Parameter *d* can be calculated from the bulk modulus, *K*, using equation 4.3:

$$d = \frac{2}{K} \tag{4.3}$$

In the absence of further data, *d* was determined from a bulk modulus that was derived from the isotropic elastic relations, using data where available. For the scalp, *K* was determined using the Poisson's ratio from Li, Sandler, and Kleiven (2017) (0.49) and elastic modulus from Zhou et al. (1997) (16.7 MPa) as summarised by Brooks et al. (2018) (Chapter 3 of this thesis). For the suture, the Poisson's ratio from Li, Sandler, and Kleiven (2017) (0.499) and the average elastic modulus (8.1 MPa) they used to fit the hyperelastic model to was used; while for the brain, a bulk modulus of 2.1 GPa was used from McElhaney, Roberts, and Hilyard (1976).

An isotropic elastic model was used for the skull rather than an orthotropic elastic model similar to Li, Sandler, and Kleiven (2017). The elastic modulus was calculated by averaging the modulus of the three

principal directions of an orthotropic model. These moduli were obtained by averaging data from Coats and Margulies (2006) and using a calculated anisotropy ratio from Li, Sandler, and Kleiven (2017). The E_2 modulus data from Coats and Margulies (2006) for a three-month-old occipital bone is 463.5 and 1317.6 MPa (from the same donor), which is not very consistent. Therefore, the data for occipital bone was averaged for ages from 1.5 to 4.5 months. An anisotropy ratio of 1.75 (calculated from equation 4.2) was used to calculate E_1. Using $E_2=E_3$ and averaging the principal directions, the elastic modulus used in the isotropic elastic material model was 430 MPa. Although this value is approximate, it is a legitimate basis for sensitivity calculations since only the sensitivities are of interest and not the quantitative predictions themselves. A Poisson's ratio of 0.19 was used (McElhaney et al. 1970), while the same elastic modulus was used for each cranial bone. The data for the material properties used are outlined in Table 4.2.

Validation

The baseline model was validated against the infant cadaver experimental studies of Prange et al. (2004), and Loyd (2011) for an occipital impact from a drop height of 0.3 m (head only, no neck). Comparisons to the FE model of a five-month-old infant by Li, Sandler, and Kleiven (2017) are also made, as well as a recent FE model by Burgos-Flórez and Garzón-Alvarado (2020) of a four-week-old infant. Data of interest was the acceleration-time traces, peak head acceleration and impact duration.

Sensitivity Analysis

The Parameters Correlation module of ANSYS DesignXplorer (ANSYS, Inc., Canonsburg, Pennsylvania, USA) was used to automate the analysis. Multiple simulations were run, with the input values varied within a specified range (design space). Random values were selected from the design space with Latin Hypercube sampling (LHS) (McKay, Beckman, and Conover 1979). LHS (a form of Monte Carlo sampling) ensures no two values for an input parameter can be the same, limiting clustering. The minimum number of simulations required for a credible result is n^2, where n is the number of inputs. In the present study, 14 input parameters were used, and 300 simulations conducted. Spearman's rank correlation was used to calculate the correlation between the input and output parameters (ANSYS Inc. 2019a, Spearman 1904). The sensitivity of an output parameter is generally driven by the variation range of an input parameter and the amount by which it varies across this variation range (ANSYS Inc. 2019a). Spearman's correlation coefficient takes both of these factors into consideration. Only the material model parameters were changed in the analysis; the mesh and boundary conditions were the same for each simulation.

Input Parameters

In Table 4.1, the standard deviation (SD) for each parameter was presented if it was provided in the original study. The upper and lower bounds of the design space for these parameters were defined using one SD, assuming a Gaussian distribution. Many of the parameters have no published uncertainty or SD, therefore engineering judgement was used to determine suitable bounds for the design space. For a sensitivity analysis, it is common to use a parameter uncertainty of ± 10%. However, due to the inherent variability in biological tissues, the uncertainty is generally much greater than that for the material properties of traditional engineering materials. The standard error of the cranial bone elastic modulus presented in Coats and Margulies (2006) ranged from 13-33%. In the absence of further data, the upper and lower bounds were defined using an uncertainty of ± 25% for parameters where SD or uncertainty data was unavailable. Table 4.2 lists the input parameters and their respective nomenclature, which is used hereafter, along with the uncertainty used to define the design space.

Table 4.2: Sensitivity Analysis Inputs

Tissue	Parameter	Nomenclature	Value	Uncertainty
Scalp	Hyperelastic constant μ_1	$\mu_{1\ scalp}$	13 000 Pa	± 3 250 Pa
	Hyperelastic constant α_1	$\alpha_{1\ scalp}$	24.23	± 0.63
	Hyperelastic constant d_1	$d_{1\ scalp}$	7.18e-10 Pa^{-1}	± 1.8e-10 Pa^{-1}
Skull	Elastic Modulus	E_{skull}	430 MPa	± 72.3 MPa
	Poisson's Ratio	v_{skull}	0.19	± 0.11
Suture	Hyperelastic constant μ_1	$\mu_{1\ suture}$	14 800 Pa	± 3 700 MPa
	Hyperelastic constant α_1	$\alpha_{1\ suture}$	6.9	± 1.72
	Hyperelastic constant d_1	$d_{1\ suture}$	1.5e-9 Pa^{-1}	± 3.75e-10 Pa^{-1}
Brain	Hyperelastic constant μ_1	$\mu_{1\ brain}$	53.8	± 13.5 Pa
	Hyperelastic constant α_1	$\alpha_{1\ brain}$	10.1	± 2.5
	Hyperelastic constant μ_2	$\mu_{2\ brain}$	-120.4	± 30.1 Pa
	Hyperelastic constant α_2	$\alpha_{2\ brain}$	-12.9	± 3.2
	Hyperelastic constant d_1	$d_{1\ brain}$	9.52e-10 Pa^{-1}	± 2.4e-10 Pa^{-1}
	Hyperelastic constant d_2	$d_{2\ brain}$	9.52e-10 Pa^{-1}	± 2.4e-10 Pa^{-1}

Output Parameters

The output parameters were split into two categories, local and global. Local outputs are located at specific nodes in the tissue of interest and allow for direct comparison of results for every change in the FE model. Global outputs are the maximum values in the tissue of interest and are commonly used in published studies of infant head impacts. While the magnitude of a global output may be similar, the location may change significantly from model to model. Table 4.3 lists the output parameters. The

locations of B1, B2, B3 for the brain and S1 and S2 for the skull occipital bone were vertexes on the geometry, at or near the contact area, in their respective tissues. The use of geometric vertexes ensured a node was created at the same location regardless of the mesh size used. The location of these vertices are shown in Figure 4.2 (e).

Table 4.3: Sensitivity Analysis Outputs

Output	Tissue	Parameter	Baseline Values
Global	**Brain**	MP Strain	0.297
		Max VM Stress	0.044 MPa
	Skull-Occipital	MP Stress	20.3 MPa
		MP Strain	0.048
		Max VM Stress	33.6 MPa
	Suture	MP Stress	9.92 MPa
		MP Strain	0.326
		Max VM Stress	0.134 MPa
	Whole Head	Impact Force	330 N
Local	**Brain**	MP Strain at B1	0.164
		MP Strain at B2	0.178
		MP Strain at B3	0.191
	Skull-Occipital	MP Stress at S1	18.4 MPa
		MP Stress at S2	3.26 MPa
		MP Strain at S1	0.042
		MP Strain at S2	0.009

MP=Maximum Principal; VM=von Mises

Results

Validation of Baseline Model

The FE model in this present study has a peak head acceleration of 79 g and impact duration of 10.2 ms. Peak head acceleration and impact duration data for the validation studies is presented in Table 4.4, while acceleration-time plots are presented in Figure 4.4 comparing the present results to available data. The peak head acceleration is comparable to that of the five-month-old cadaver experiment from Loyd (2011) (79 g versus 81 g respectively), while the impact duration is approximately 2 ms shorter (10.2 versus 12.3 ms respectively). Similar results are observed for comparison against the five-month-old FE model of Li, Sandler, and Kleiven (2017) (79 versus 78 g and 10.2 versus 12 ms respectively).

Table 4.4: Comparison of peak head acceleration and impact duration for 0.3 m drop height

Study	Age	Cadaver Experiment/FE Model	Peak Head Acceleration (g)	Impact Duration (ms)
Prange et al. (2004)	1 Day	Cadaver Experiment	55.9	18.8
Prange et al. (2004)	11 Days	Cadaver Experiment	52.9	20.6
Loyd (2011)	5 Months	Cadaver Experiment	81.0	12.3
Loyd (2011)	9 Months	Cadaver Experiment	71.6	14.2
Li, Sandler, and Kleiven (2017)	5 Months	FE Model	78*	12*
Burgos-Flórez and Garzón-Alvarado (2020)	4 Weeks	FE Model	79*	8+*
Present Study	3 Months	FE Model	79.1	10.2

*No specific data provided; inferred from Fig. 7 and Fig. 5 of Li, Sandler, and Kleiven (2017) and Burgos-Flórez and Garzón-Alvarado (2020) respectively.

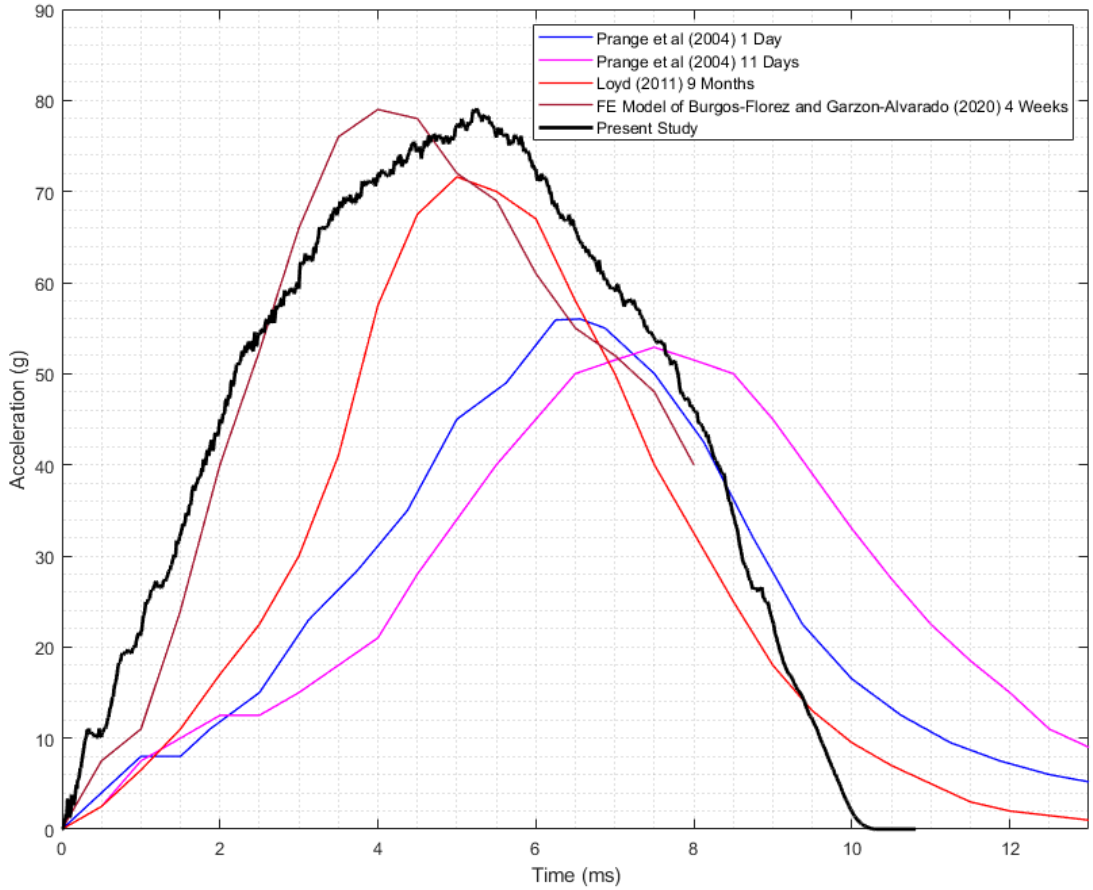

Figure 4.4: Acceleration-time plot for experimental and FE model impacts for a drop height of 0.3 m.

Sensitivity Analysis

Figure 4.5 shows the global and local sensitivities (Spearman's correlation coefficient) of the outputs with respect to the inputs. The closer the sensitivity is to one or negative one, the more sensitive the output is to that input. A value of positive one or negative one indicates the output has a perfect monotonic dependence on the input. The E_{skull} features prominently, especially for the occipital bone

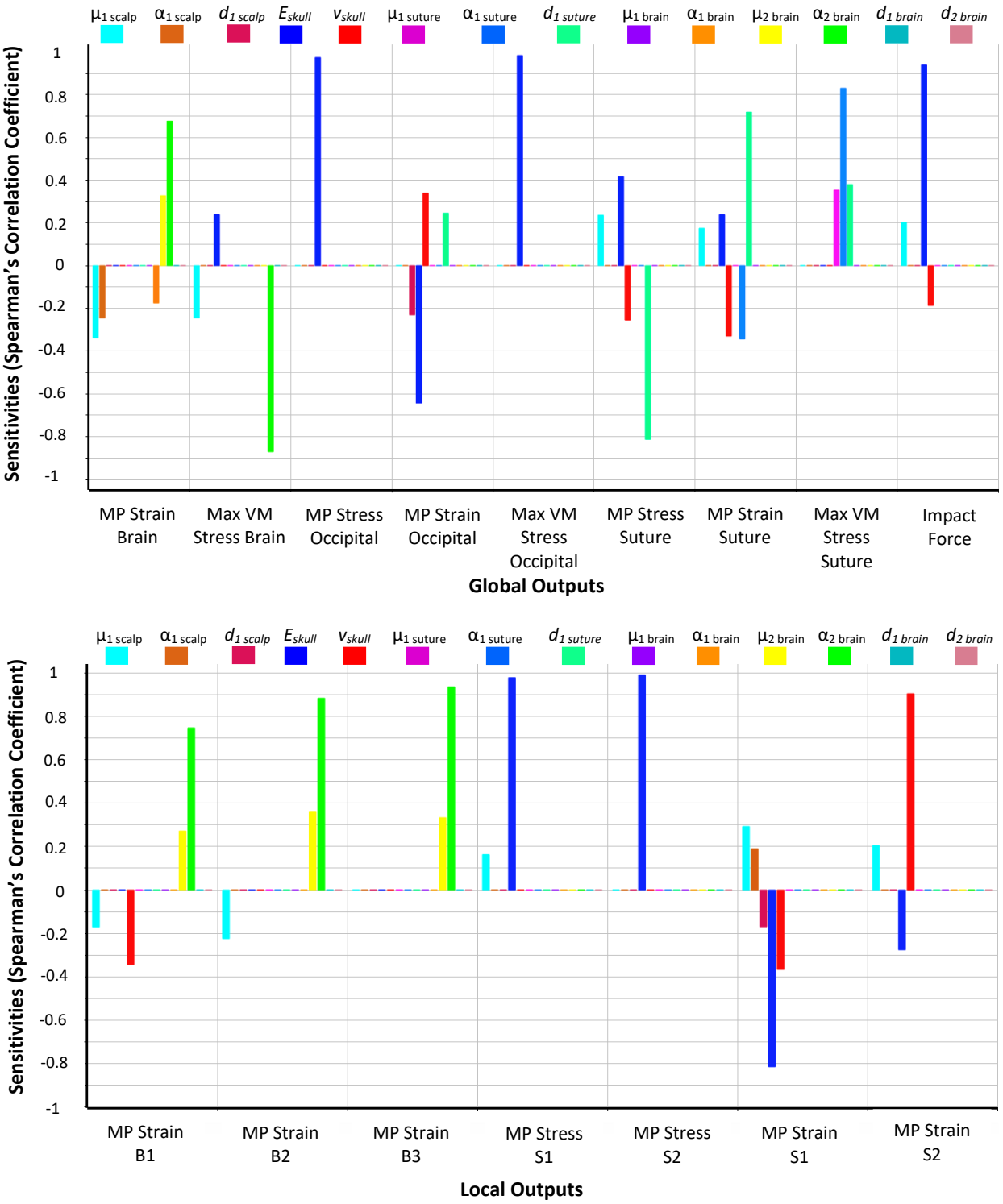

Figure 4.5: Sensitivity plots for global and local outputs. MP=maximum principal; VM=von Mises.

outputs and impact force. This is followed by the v_{skull}, which mainly influences the occipital strain outputs. All brain outputs are most sensitive to changes in $\alpha_{2\ brain}$, followed by $\mu_{2\ brain}$. The cranial bone inputs have no influence over the brain outputs, except for v_{skull} having some influence on MP Strain B1. Scalp parameter $d_{1\ scalp}$ is the most influential parameter on the global suture outputs. Parameter $\mu_{1\ scalp}$ has a small influence over the majority of both the global and local outputs. Figure 4.6 shows a scatter plot for the impact force against E_{skull}. There is relatively little scatter, with a R^2 of 0.88 for a linear fit. The impact force is most sensitive to changes in E_{skull}.

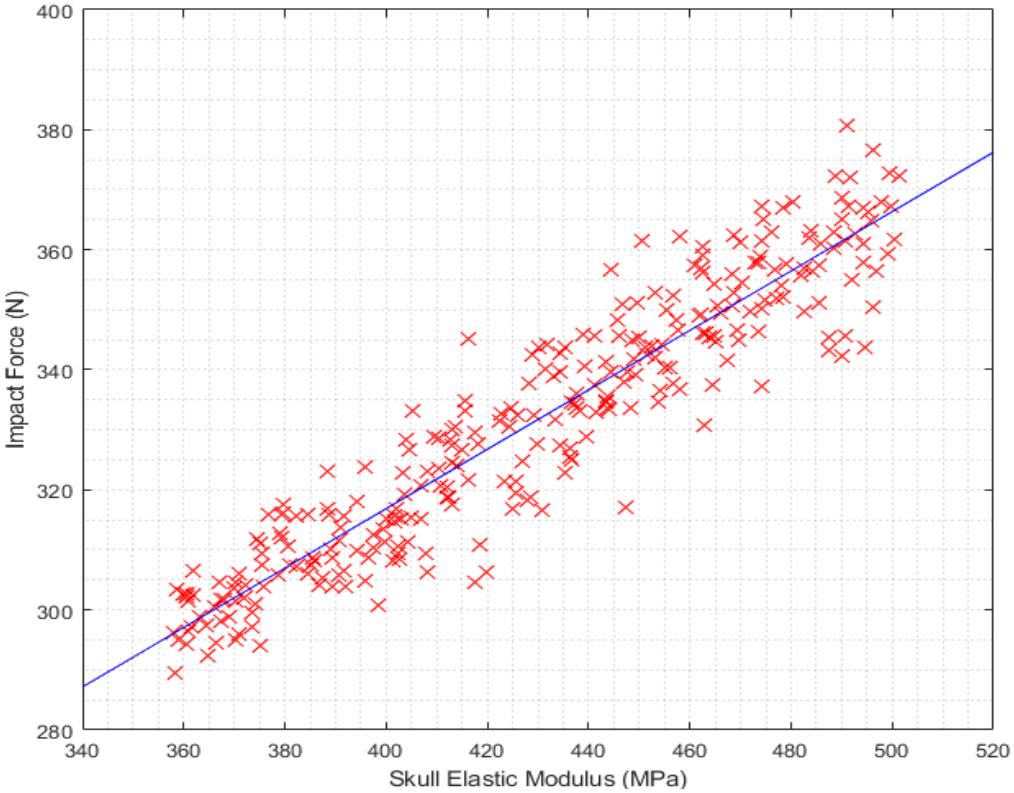

Figure 4.6: Scatter plot with linear correlation for impact force versus skull elastic modulus. R^2=0.88.

Discussion

Validation and Limitations of Baseline Model

No experimental data exists for a three-month-old infant head impact, so the baseline model was validated against experimental data for a range of ages. Data from drop tests of one and 11-day-old infants from Prange et al. (2004), and five and nine-month-olds from Loyd (2011) were used. As the infant head becomes stiffer with age (Prange et al. 2004, Coats and Margulies 2006), it would be expected an ideal FE model would fit somewhere in between the data of Prange et al. (2004) and Loyd (2011). The peak acceleration and impact duration of the baseline FE model is greater and shorter respectively than the one, 11-day and nine-month-old experimental data. Compared to the five-month-old data, the peak acceleration is similar while the duration is shorter (this is similar when compared to the five-month-old FE model data presented by Li, Sandler, and Kleiven (2017)). It should

be noted that the five-month-old peak head acceleration is around 14% greater than the nine-month-old data and does not fit the general observations of stiffness increasing with age. Loyd (2011) does not present acceleration-time curves for the five-month-old cadaver experiment, so no direct comparison can be made. While the FE model does not fit within the 'ideal' range, the relatively favourable comparisons against experimental data of a similar age provide confidence that the model is behaving in a realistic manner. This is despite modelling decisions such as the element type used and a simplified geometry that were made to simplify the model for the purpose of conducting a sensitivity analysis, as well as limitations within ANSYS Explicit Dynamics that restricted the material model for the cranial bones to isotropic elastic. Only validation against experimental acceleration-time data could be carried out as no experimental stress or strain data is presented in the studies of Prange et al. (2004) and Loyd (2011).

The decision to use tetrahedral elements was made in order to increase the minimum characteristic element length. The minimum characteristic length in the mesh contributes to the size of the timestep used in an explicit solver (refer to Chapter 2 of this thesis). The smaller the minimum characteristic length, the smaller the timestep and hence an increase in computations. Although hexahedral elements are generally preferred, the use of tetrahedral over hexahedral elements resulted in an increase in the timestep by two orders of magnitude. Generally, fewer hexahedral elements are needed for an accurate solution, but the cost savings associated with the time step size favour the tetrahedral elements in this case.

The FE model by Burgos-Flórez and Garzón-Alvarado (2020) also used tetrahedral elements for all tissues, although they had a full 3D head geometry (but did not include the scalp). Their model was stiffer than the 11-day-old data from Prange et al. (2004), with possible reasons provided as due to the use of tetrahedral elements, slight discrepancy in head mass, the method of calculating the acceleration and not including the scalp. The model had a similar peak acceleration to the baseline model in the present study. However, Burgos-Flórez and Garzón-Alvarado (2020) used an elastic modulus of 200 MPa for the cranial bones, which is less than 50% of that used in the present study and most other published FE models (Brooks et al. 2018), suggesting the model could actually be much stiffer. Although there could be other contributions to this discrepancy, the difference in elastic modulus is likely to be the most dominant, due to the cranial bones being the stiffest head tissue. Therefore, the baseline model in the present study is not as stiff as another model using a similar element type.

A simplified head geometry also helped to increase the size of the timestep in the present model by increasing the size of the smallest element. The geometry neglected the nasal and facial bones and

smoothed out many of the natural irregularities in the skull to make a smooth surface. Other geometric simplifications included neglecting the dura and CSF, and not using a two-layer scalp. The dura and outer scalp layer are relatively thin tissues and therefore require smaller elements, which decreases the characteristic length. Using a two-layered scalp would have reduced the global stiffness of the model as the inner scalp is much softer than the outer scalp and therefore would provide additional energy absorbing capability.

The CSF was neglected for similar reasons as the dura and outer scalp as initial geometric modelling showed it was relatively thin in some regions and the size of the elements required were contributing to impractical solve times. A number of existing FE models of the infant head also neglect the CSF, such as Coats, Margulies, and Ji (2007), who provide no explanation for their decision, and Khalid et al. (2019) who describe the modelling of CSF as requiring fluid-structure interaction, which is "in its relative infancy", although no citation is provided to justify this claim. Neglecting the CSF would have had some influence on the global stiffness and sensitivity results due to the partial decoupling, mainly in shear, between the motion of the brain and skull. This would act to protect the brain, thus affecting the response of the brain outputs.

The inability of ANSYS Explicit Dynamics to use an anisotropic material model defined in local coordinates resulted in the use of an isotropic elastic model for the skull instead of the orthotropic model used by Li, Sandler, and Kleiven (2017). An orthotropic model has been found by Li, Sandler, and Kleiven (2017) to be more accurate than an isotropic model in modelling the differences in cranial bone stiffness due to the fibre directions before ossification is fully completed.

Similar to the FE models already presented in the literature, the material models in the baseline model are not rate dependent. Although infant cranial bone material properties have been found to be independent of strain rate (Coats and Margulies 2006), the viscoelastic and fluidic behaviour of other tissues such as the brain and scalp mean they could be strain rate dependent. The hyperelastic material model used in the present study does not account for rate affects in the scalp. Future work in this area is required.

Sensitivity Analysis

In the pre-existing literature for infant head FE models, Coats, Margulies, and Ji (2007), Li et al. (2013), and Li, Sandler, and Kleiven (2017) all performed parametric studies of some sort on the material model parameters for various tissues. All three studies used a one-at-a-time method, where one change was made and the results considered in terms of the difference from their respective baseline models. Coats, Margulies, and Ji (2007) investigated the relative influence of brain stiffness and compressibility on the principal stress in the skull. Li et al. (2013) conducted a parametric study of

material model parameters as a part of their study. They found that the elastic modulus of the skull (modelled as isotropic) had the most important effect on most of the head response measurements, while brain material properties (modelled as linear viscoelastic) had little effect. Li, Sandler, and Kleiven (2017) changed the material models for the scalp, suture and dura to isotropic elastic and evaluated the differences against their baseline model that consisted of nonlinear models. The use of an isotropic elastic model increased the stiffness of the model in all cases (greater peak accelerations). They also conducted a parametric study on the scalp material constants (for the nonlinear model). The stiffness of the scalp was both halved and 10 times greater, resulting in a decrease in peak acceleration of 1% and an increase of 1.8% respectively.

Of all the input parameters, E_{skull} and v_{skull} were found in the present study to be the most important inputs with regard to the sensitivity of the outputs. The skull is by far the stiffest head tissue in the model, therefore, any changes to E_{skull} and v_{skull} will have a significant effect on the global stiffness of the model. Hence the significant influence they have on many outputs. This finding supports the parametric study in Li et al. (2013). The strong correlation of E_{skull} with impact force indicates that E_{skull} is also the most influential material parameter on the global stiffness of the FE model. Maximum impact force is used to calculate peak head acceleration, which, along with impact duration, is a common parameter for validating an infant head FE model against experimental data.

The brain hyperelastic constants are the most important for the brain outputs as they have the most influence. Parameter $\alpha_{2\ brain}$ had the most significant influence, followed by $\alpha_{1\ brain}$ and $\mu_{2\ brain}$ having some limited influence. The presence of both Ogden constants α in the sensitivity plots indicates that this constant has a greater influence than Ogden constant μ. Scalp parameters $\mu_{1\ \mathrm{scalp}}$ and $\alpha_{1\ scalp}$, and skull parameter v_{skull} have some minor influence on the brain outputs. Many published FE models also use a viscoelastic material model for the brain (Brooks et al. 2018). The present study only considered a hyperelastic model, although future investigation should be considered given biological materials typically exhibit viscoelastic behaviour.

The suture hyperelastic constants had influence over the global suture outputs. Parameter $d_{1\ suture}$ is the most important as it has the greatest influence of all other parameters. The suture parameters had no influence over other outputs and therefore are only important when considering the individual response of the suture. The suture has been found to be an important energy absorbing tissue (Margulies and Thibault 2000, Coats and Margulies 2006), so it could influence the global head stiffness as a whole. However, no influence was found for the suture material parameters on impact force.

The hyperelastic constant $\mu_{1\ scalp}$ was found to have some influence on almost all outputs. Some influence of the scalp parameters is expected given that the scalp is a relatively soft tissue and therefore will provide some energy absorption capacity. The $\mu_{1\ scalp}$ is not the most dominant parameter on any of the outputs, hence does not significantly affect the global stiffness, similar to the findings from the parametric study of Li, Sandler, and Kleiven (2017).

Priorities for Future Research

From the findings of this sensitivity analysis, priorities for future research can be established. It is recommended that the order of priority be E_{skull}, v_{skull}, $\alpha_{2\ brain}$, $\mu_{1\ scalp}$ and then $d_{1\ suture}$.

The elastic stiffness of the skull has significant influence on most outputs (aside from the brain outputs), so future work should be directed to ensuring there is a full understanding of how infant skull material behaves at a range of loading rates. The E_{skull} has a SD (72.2 MPa) that is 16.8% of the mean, which is relatively low compared to other inputs (and for biological material testing in general). Current E_{skull} data from Coats and Margulies (2006) was obtained from human pediatric samples ranging from 21 weeks gestation to 13-months-old, for three-point impact tests at impact speeds of 1.58 and 2.81 ms^{-1} (equivalent to falls of 0.13 and 0.40 m respectively). Using statistical analysis, they found that age was the most significant factor on E, while loading rate did not have an effect. Brooks et al. (2020) (Chapter 5 of this thesis) conducted preliminary investigations into human child cranial bone at impact speeds around 5.65 ms^{-1} (equivalent to a fall height of 1.60 m). They found that prompt brittle fracture occurs in specimens from at least two-years-old, while for an age of three weeks, some bending occurred before fracture. However, they did not obtain E_{skull} data. As E_{skull} data has only be obtained at a loading rate of up to 2.81 ms^{-1} (equivalent to 0.4 m), loading rates equivalent to falls greater than one metre should be investigated to determine the effect on E_{skull} as a fall at this height is more likely to lead to severe or fatal head injuries in infants (Johnson et al. 2005). This should include age effects, given Coats and Margulies (2006) findings on the significance of age on E_{skull}. Having a bigger data set for E_{skull} as a function of age would also help improve the mathematical functions presented by Li, Sandler, and Kleiven (2017). Currently, their models have relatively low R^2 (0.56 and 0.35 for A_R and E_1 (occipital bone) respectively). These models could also be extended to include loading rate if such a relationship is found.

Material models for the infant skull can also be improved with further research into determining the Poisson's ratio. The standard deviation of v_{skull} (0.11) was approximately 50% of the mean value. Given the relationship between v and shear modulus, increasing or decreasing v_{skull} by up to 50% will have significant effect on the shear stiffness, hence the need for improvement. Current data for v_{skull} is obtained from McElhaney et al. (1970), which is for adults. Given the proven differences in cranial

bone elastic modulus as a function of age, it is highly likely that v_{skull} will also be highly dependent on age.

The significance of $\alpha_{2\ brain}$ on the brain outputs shows the importance of having a material model that can predict the brain behaviour to a reasonable level of accuracy if the local brain tissue response is of interest. The hyperelastic constants for the brain were obtained using adult experimental data. Although the adult data was used by Li, Sandler, and Kleiven (2017), who have the best validated infant FE model to date, they did not include any specific validation for the local brain response. Therefore, it is unknown how well the data for the hyperelastic material model represents the behaviour of the infant brain. The lack of influence over FE model outputs by the brain model parameters was also found by Li et al. (2013), although they used a viscoelastic material model. No research has been conducted on the material properties of human infant brain tissue under impact loading. Previous work by Thibault and Margulies (1998) and Prange and Margulies (2002) used infant pigs, of which it has been shown that brain growth in months of life for a human is comparable to weeks in pigs (Dickerson and Dobbing 1967, Dobbing 1981). Margulies and Thibault (2000) found that porcine and infant cranial bone properties were comparable, hence porcine tissue data is often substituted for humans. This substitution is due to the scarcity of human infant samples and the inherent difficulty in preserving brain tissue. Any experiments involving brain tissue would have to be carried out within hours of being harvested to minimise tissue degradation. This limits the viability of using human infant brain tissue to improve the material model for the brain. Until improvements can be made, local brain tissue responses should be used with caution when determining whether injury has occurred (using brain tissue threshold measures).

The scalp hyperelastic parameter data was not obtained from human infants. The influence of $\mu_{1\ scalp}$ on some outputs shows that it is important to develop a hyperelastic model using human infant experiments. Although Li, Sandler, and Kleiven (2017) decreased the hyperelastic constants for the adult scalp to account for the softer infant scalp, they do not state the justification or experimental basis for the level of decrease. Their FE model does correlate well with experimental cadaver impact data and the parametric study identified insignificant changes in peak acceleration due to relatively large changes in the hyperelastic constants, suggesting their choice of parameter values is suitable. Parameter $\mu_{1\ scalp}$ was found in the present study to have some influence on the impact force (used to calculate peak acceleration). Therefore, experimental data from infant tissue would improve the scalp material model. Predicting scalp tissue damage in FE models, however, is not as important as other head tissues as scalp damage is easily observable in real-world cases. Although, it is just as important to accurately model as any tearing or other tissue damage to the scalp will result in some energy absorption, thus affecting the energy the skull must absorb in order to best protect the brain. If scalp

injury can be predicted, and if their observable characteristics should be sensitive to the impact parameters, they might have great forensic value.

Suture material model parameters have been obtained from human infant experiments, giving a relatively high degree of confidence in the suitability to be used in infant FE models (Coats and Margulies 2006). However, the parameter $d_{1\ suture}$ was determined from a bulk modulus that was calculated from an isotropic elastic model, which has been shown by Li, Sandler, and Kleiven (2017) to increase the peak acceleration by around 20%. Ideally, experiments to specifically measure the bulk modulus of human infant suture would be carried out. This will be especially important for accurately determining the stresses and strains in the suture given the relatively significant influence of $d_{1\ suture}$ on the suture outputs.

As the dura was not included in the FE model, its influence on the model response was not determined. Although it is modelled in some FE models presented in the literature (Brooks et al. 2018), it is also often neglected due to its relatively small thickness (as was the case for the present study) (Coats, Margulies, and Ji 2007, Burgos-Flórez and Garzón-Alvarado 2020). Experimental data for the hyperelastic constants originates from human foetal experiments, but future work could extend this to ages of one to 12 months to improve the material model. Future sensitivity analyses should determine the influence of the dura on the FE model outputs in order to prioritise such experimental work.

Implications for Forensics

As E_{skull} and v_{skull} are the most significant parameters, having accurate data for them is of importance when using FE models to investigate legal cases. A common question in cases being investigated is whether an observed pattern of skull fracture could have been caused by a specific hypothetical sequence of actions (such as in Li, Sandler, and Kleiven (2019)). Therefore, it is more important to have accurate and reliable data for skull material models rather than for other tissues such as the brain. Due to the scarcity of samples and ethical issues of conducting physical experiments on human infant cranial bone tissue, only a limited number of different individuals have been tested (23 individual cadavers of different ages in Coats and Margulies (2006)). Hence, there is currently not enough data to determine how much variation there is from one individual to another, or to form explicit mathematical functions to calculate them as a function of age. Ideally, for use in legal cases, there would be enough data to accurately create such mathematical functions, or a standardised method to quickly and accurately harvest and then test cranial bone tissue of an individual to measure the parameter values. Either of these would ensure subject specific FE models can be used to accurately predict possible head injuries.

Visible tissue damage patterns are also important forensic evidence. Predicting such tissue damage in the scalp will require accurate material models for the scalp. This will allow FE models to be used to establish whether a specific impact may cause tissue damage to the scalp that has been observed.

The use of FE models in forensics to determine whether skull fracture or scalp tissue damage is likely to occur requires the use of material models that incorporate damage variables. Including tissue failure requires accurate stresses and strains, which is where the present study hopes to provide direction for improvement. The present study does not include material failure. Future studies could investigate material failure in a similar way to determine which parameters are important for obtaining accurate results for forensic purposes.

While accurate material model data is important for use in forensics, validation of the material models, and the FE model as a whole is just as important. As discussed earlier, it is common for infant head FE models to be validated against acceleration-time data of experimental drop tests involving infant cadaver heads. Due to the scarcity of such cadavers, and that biological tissues have complex material models, there is only a limited data set to which models can be validated against. Some studies, such as (Hajiaghamemar et al. 2018) and (Li, Sandler, and Kleiven 2019) are validating their predicted injuries or fracture patterns against those observed in real-world cases. This allows for greater verification of their model results, however, it relies on having an accurate understanding of factors such as head orientation, fall height and impact surface properties, which is often at the centre of cases that end up in legal courts. The use of simulant materials that closely represent biological tissues has benefits in that once validated against human tissue, multiple scenarios can be investigated and used to compare against FE models. Until such materials exist, more human infant tissues are donated for research, or well-documented cases are presented, validation of infant head FE models will remain a challenge for researchers. With these limited methods of validation, results must be used with caution. This, in turn, adds challenges to determining how accurate a FE model needs to be, to be accepted as evidence in a court of law. Infant head FE modelling, if properly conducted, offers additional indirect evidence which can be weighed with other types of evidence during the legal process.

Conclusions

A sensitivity analysis was conducted for the material model parameters on a FE model of an infant occipital head impact. The scalp, skull, suture and brain tissues were included in a simplified geometry of a three-month-old infant with symmetry in the sagittal plane. As 300 simulations were required for the sensitivity analysis, compromises with the mesh and the biofidelity of the model had to be made in order to reduce the computational time. Overall, the global stiffness of the baseline FE model was

slightly greater than existing experimental data for human infant head impacts. The peak head acceleration is comparable with experimental data, although the impact duration is around 17% shorter.

From the sensitivity analysis, it was found that the material model parameters for the skull had significant influence on most of the model outputs. The elastic modulus was found to be the most influential, especially for the maximum impact force. Although existing data for the elastic modulus is reliable, further improvements to understanding the effect of loading rate would be beneficial. This is currently lacking in the literature, with the highest loading rate used to determine elastic modulus data being 2.81 ms^{-1} (equivalent to a 0.4 m fall). Due to existing data for the skull Poisson's ratio originating from human adults, and its significant influence of many output parameters, further measurements are also of high importance.

The brain hyperelastic constant α_2 was found to have correlations with the brain output parameters. Similar to the skull Poisson's ratio, the hyperelastic data is from human adults and has not been validated at a local tissue level to determine whether the model accurately predicts injury to brain tissue. Brain injury related outputs should therefore be used with caution until improvements to the material models can be made. It is acknowledged though that experimental work with brain tissue is more challenging than using other tissues such as cranial bone.

The suture hyperelastic constants were found to correlate to outputs related to the suture only. Parameter $d_{1\,suture}$ is the most important and needs to be improved further with specific measurements of the suture bulk modulus. Data for suture parameters is obtained from human infants and therefore is relatively more reliable. The scalp hyperelastic constant μ_1 was found to have strong correlations with most outputs. As with the brain, the scalp hyperelastic data is modified from adult data and therefore could be improved by conducting appropriate experiments on human infant scalp tissue.

It is recommended that future research should prioritise increasing the data for the skull elastic modulus, especially for higher loading rates, followed by obtaining data for the skull Poisson's ratio, developing a material model for both the brain and scalp using tissues from human infants, and improving data for the bulk modulus of infant suture. Although current infant head FE models are becoming more accurate, more work is still required to further improve the nonlinear material models they use. This sensitivity analysis has provided guidance on which tissues are the most important for future work. The next step in human infant head modelling would be to delve into tissue failure and damage modelling to determine the most important parameters that accurate data would be required for such modelling. This will, of course, be important for relating modelling results to forensic data.

Chapter 5 Preliminary Observations of the Sequence of Damage in Excised Human Child Cranial Bone

This chapter is largely made up of the findings presented in Brooks et al. (2020). Additions include a more detailed description of the impact machine and discussion around the original intended use of digital image correlation and why it was not used. Specimens of human child cranial bone were available for materials testing and the results of the sensitivity study in Chapter 4 guided the choice of which material properties these specimens should be used to obtain such data.

Introduction

The first studies on infant cranial bone acquired their data under static loading conditions (McPherson and Kriewall 1980, Margulies and Thibault 2000). McPherson and Kriewall (1980) tested 83 samples of human infant cranial bone (gestational age range of 25 to 40 weeks) in three-point bending at a rate of 0.5 mm/min. Margulies and Thibault (2000) also conducted three-point bend tests on 12 samples of human infant cranial bone (age range of 25 weeks gestation to six months) at loading rates of 2.54 and 2540 mm/min. Both studies investigated the elastic modulus as a function of age, with agreement between the two. Margulies and Thibault (2000) also investigated the stress at fracture and energy absorbed to failure. Cranial bone data obtained under static loading conditions is limited for children up to 18 years. Wang et al. (2014b) conducted three-point bend testing on 56 samples of cranial bone and suture from one to two-year old children at a loading rate of 1.5 ms^{-1}. Davis et al. (2012) conducted four-point bend tests on 47 samples of cranial bone from a six-year-old child (average strain rates of 0.045, 0.44 and 2.2 s^{-1}). The only study to date that has investigated the rate dependence of the material properties for infant cranial bone is that of Coats and Margulies (2006). Coats and Margulies (2006) conducted three-point bend impact testing on 46 infant skull bone samples at fall heights of 0.3 and 0.9 m, resulting in impact speeds of 1.58 and 2.81 ms^{-1} respectively. The published data on infant head tissue properties, up to 2018, is reviewed in (Brooks et al. 2018). Ommaya, Goldsmith, and Thibault (2002) reviewed studies of the causative mechanisms of traumatic brain injury, and the effect of differences between adult and juvenile physiology. They noted that skull fracture severity correlates with age-dependent cranial bone thickness and the state of the cranial sutures.

This chapter reports high speed imaging observations on the behaviour of human infant bone in three-point bend impacts at a speed equivalent to a fall of up to 1.6 m. To the best of the author's knowledge, there are no published studies that have conducted impact testing on infant or child cranial bone at

speeds greater than that equivalent to ‘higher than a one metre fall’ or captured high-speed imagery of the impact. Observations of energy absorbed to failure, minimum fracture speed and maximum impact force are interpreted in terms of trends with average bone thickness, age and hydroxyapatite (HA) density and the cranial plate from which the sample was taken (frontal, occipital, parietal or temporal).

It was originally intended that digital image correlation (DIC) would be used to measure the displacement and strain of the cranial bone specimens as they deformed. However, the deformation happened much faster than anticipated and hardware limitations resulted in not enough data to reliably use DIC. This is discussed later in this chapter. An introduction to DIC theory is presented in Appendix A of this thesis.

Methods

Specimen Preparation

Eleven specimens from seven cadavers were obtained from the Institute of Legal Medicine, University of Leipzig, Germany (ethics approval 486/16-ek). Donor ages ranged from three weeks to 18 years to fully display the age spectrum of paediatric samples from infants to teenagers.

Following the total removal of the soft tissues of the cranium, including the skin, periosteum externally and the dura mater internally, the specimens were sectioned into samples measuring approximately 10 by 20 mm. Following this, the samples were precooled at 4°C prior to shock freezing them for storage and transportation purposes. Prior to the experiments, the samples were thawed and sectioned into their final shape using a piezo surgery device (PIEZOSURGERY white, Mectron s.p.a, Genova, Italy). Table 5.1 lists the age, sex, dimensions and cranial bone localisation for each of the specimens used in the given study. All specimens of the same age are from the same donor.

The surfaces of the specimens were spray painted white and a speckle pattern was created by grinding pencil lead graphite into a sieve and sprinkling it over the face for DIC usage.

To determine the average thickness of the specimens, the thickness at each end and in the middle was measured using digital calipers.

Table 5.1: Human specimen information

Specimen #	Age (Years)	Sex	Cranial Bone	Span (mm)	Width (mm)	Thickness (mm)
1	3 weeks	Male	Occipital	20.5	11.4	1.1
2	3 weeks	Male	Parietal	20.7	9.5	1.0
3	2	Male	Frontal	14.7	9.5	2.1
4	4	Male	Frontal	16.5	10.0	3.2
5	4	Male	Parietal	22.4	10.8	3.7
6	12	Female	Frontal	18.7	9.9	5.0
7	13	Female	Occipital	16.4	10.8	6.1
8	13	Female	Parietal	15.3	9.6	4.8
9	17	Male	Frontal	15.6	10.4	5.6
10	17	Male	Temporal	18.2	10.1	6.2
11	18	Female	Occipital	15.2	7.7	6.7

All measurements have error of ± 0.1 mm

Spectral Computed Tomography

Spectral CT (Anjomrouz 2017) was used to image each specimen before the impacts were conducted so that each samples' mineral density could be measured using a MARS 10 (Medipix All Resolution System) scanner (MARS Bioimaging Ltd., Christchurch, New Zealand). Scan settings included an exposure time of 200 µs and a slice thickness of 80 µm, with a 1.96 mm thick aluminium filter. The specimens were mounted in a 3D printed capsule using Blu Tack (Bostik, Milwaukee, USA), as shown in Figure 5.1.

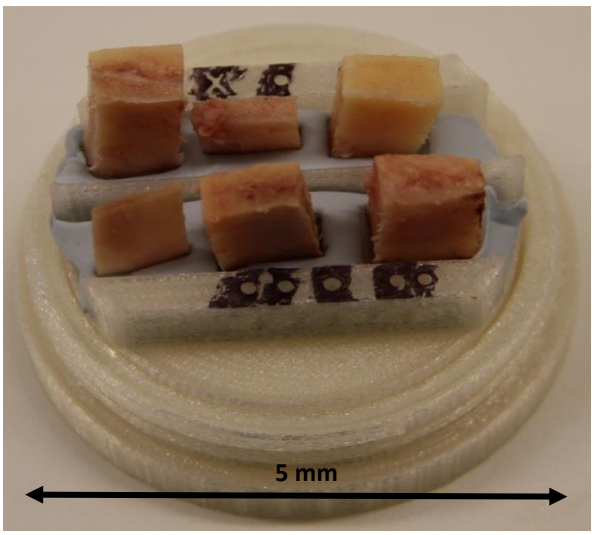

Figure 5.1: Specimens mounted in 3D printed capsule (cover removed) for CT scanning.

The geometry of the specimens was reconstructed using the MARS Vision software. A material decomposition (MD) analysis was carried out on the reconstructed images using the MARS-MD algorithm (Bateman 2015). This created a set of images for each of HA, water (hydrophilic content) and lipid (lipophilic content), illustrating their concentrations.

The HA concentration was measured using a bone analysis code by Matanaghi et al. (2019). This code is a plugin for the ImageJ (Schneider, Rasband, and Eliceiri 2012) distribution FIJI (Schindelin et al. 2012) and allows the cortical and cancellous layers of the bone to be segmented separately so as to be able to determine the density of each.

Impact Test Machine

Machine Overview

An existing impact machine developed in the Department of Mechanical Engineering, University of Canterbury for a previous project was used for the impact experiments. The machine consists of two A-frames (75 x 75 mm rectangular hollow section) joined by a support member at the top, as shown in Figure 5.2. Medium Density Fibreboard (MDF) is used as the base, which is mounted to a steel frame that has adjustable wheels that can be raised or lowered in order to move the machine around. Initial impact testing using the MDF as a base found there was approximately 0.4 mm deflection in the MDF during the impact. To minimise this deflection, the area of MDF below the pneumatic cylinder was cut out and replaced with a 25 mm thick steel plate to act as a relatively stiffer anvil. This plate rests on 150 x 150 rectangular hollow section that is a part of the base frame, providing a direct load path to ground consisting of steel that has a significantly greater stiffness than MDF.

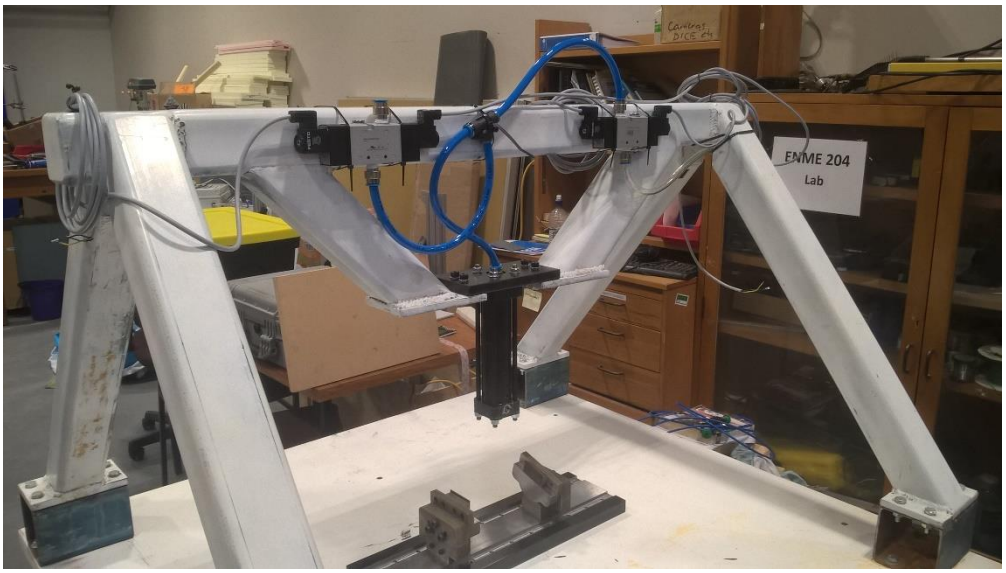

Figure 5.2: Impact machine used for experimental tests.

The impact machine uses a pneumatic system to create the impact force required for the physical testing. A pneumatic cylinder with a stroke of approximately 150 mm and a cylinder diameter of 44 mm is supplied with air to accelerate a mass from rest to a desired impact velocity. Using a pneumatic cylinder allows for greater impact velocities than can be achieved by more traditional methods of impact testing, such as using gravity for a drop test. The cylinder is mounted in a bracket that is bolted to the A-frame structure of the impact machine. The height of the cylinder above the anvil can be

adjusted by adding or removing spacers that fit between the cylinder mounting plate and the A-frame structure.

So that any experiments conducted on the impact machine can be replicated in a FE model, it is important that conservation of energy is maintained during the impact as far as possible. For such experiments, this requires that the impactor is travelling at a constant velocity just before impact. Therefore, the pressure in the cylinder needs to be equalised with the atmosphere so that no further acceleration occurs. To do this, the cylinder is controlled by a 5/3 solenoid valve with a switching time of 11 ms. A NodeMCU 12E with a microcontroller (ESP8266) was used to control the activation of the impact machine. A proprietary circuit board (developed by Gerry Kirk, retired Department of Mechanical Engineering technician) consisting of relays and the NodeMCU was used. The solenoids required a 12 V power supply to switch the valves, however, the output voltage of the NodeMCU was 5 V, hence the use of the relays. To activate the impact machine, a button had to be pushed. When the microcontroller received this input, an output was set to HIGH, which switched the relay controlling the solenoid to open the valve. After 10 ms, the relay controlling the closing of the valve was triggered. This cut off the supply pressure and vented the system to atmosphere. As a safety measure, the activation button had to be set to *active* in the code so that it could not be pushed accidently. A second safety measure was the use of an open/close valve on the air supply side of the system. The valve had to be held down to allow the air to flow to the solenoid valve. If the valve was released, air could not be supplied to the main control valve. The use of this valve and the activation button required the user to use both hands to operate the impact machine, thus ensuring that their hands were away from the impactor. Additional safety measures included mounting sheet steel on the sides to act as a shield against potential flying objects and keep bystanders from placing their hands inside the impact zone. The light and highspeed cameras on the remaining two sides of the machines meant that it was difficult for a bystander to physically place their hand in the impact zone. Perspex shields were mounted above the lights and cameras to stop objects flying out. Safety glasses were to be worn by the user and all bystanders. User training included the reiteration of checking that no one was within the vicinity of the impact zone before they activate the machine.

A supporting structure was required to place the specimens on during the impact testing. This structure had to accommodate a variety of specimen size and shapes and be used for three-point bending. Testing of the impact machine was carried out on aluminium 6061 specimens 100 x 50 x 6 mm in size. However, the human infant skull specimens had approximate dimensions of 20 x 10 x 10 mm and had an irregular shape that would not allow them to have both ends fully sitting on the support beams. With this in mind, the design requirements for the structure were:

- Minimise any deflection from the impact forces.
- Have adjustment for the span of the specimens.
- Have adjustment for rotation about the longitudinal axis to ensure the specimen can sit flat.
- Accommodate a variety of radii used for the supports.

The final design of the structure is shown in Figure 5.3. It consists of a mild steel base that has a set of grooves machined out of it to create a sliding mechanism for two uprights that contain the support beams. The span can be adjusted by moving the uprights in the longitudinal axis; a slot allows for the bolting of the uprights to the base to secure them in position. The uprights include a swivel structure that can be swivelled so that the support beams can be rotated about the longitudinal axis. This allows for possible irregularities in the specimens so that each end may sit on the support beams evenly. The swivel structure has a machined recess that allows the support beams to be mounted. Support beams with different radii can be machined and bolted to the uprights. Different radii support beams are required depending on the size of the specimens being tested. When the impact machine was being setup, 10 mm radii support beams were used for the aluminium test specimens at a span of 80 mm.

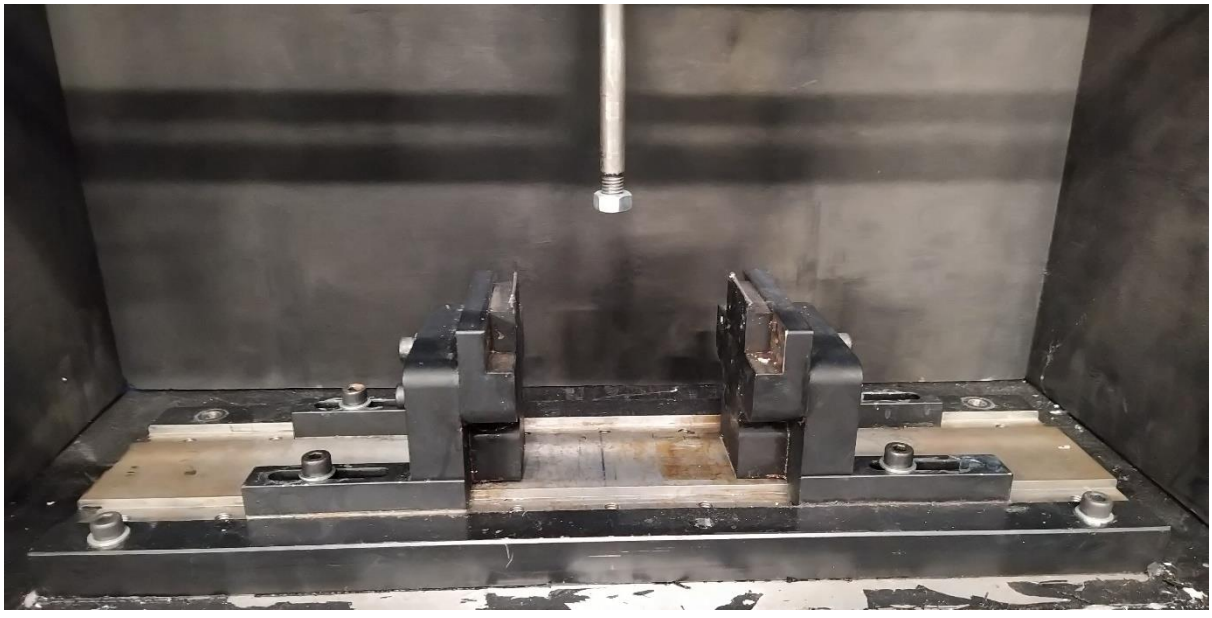

Figure 5.3: Support structure used in impact experiments.

The impactor head was bolted to the pneumatic cylinder using a mild steel adapter. Similar to the support beams, this allowed different size impactor heads to be used, while protecting the thread on the cylinder piston by way of parts not being unscrewed multiple times. The end of the thread on the piston was machined to a slightly smaller diameter than the thread. This allowed it to be screwed into the adapter and sit against the bottom of the adapter hole, thus allowing the impact load to be transferred through contact with the piston bottom rather than through the threads. This also protected the threads on the piston from damage.

Experimental Use

The support beams and impactor heads used in the present study were manufactured from S1 steel (an impact grade steel). A radius of 2 mm was used for the impactor, while 1 mm was used for the support beams. The impactor head was painted black with white tracking dots so that its speed could be measured from the image sequence. Due to the three-dimensional curvature of the specimens, there was no position in which there was continuous contact with the supports at each end of the specimen, hence the supports were not rotated for these tests. The lack of continuous end contact resulted in compression of the specimen onto the supports during the impact tests. This would have occurred regardless of the orientation of the supports used. Figure 5.4 shows the experimental setup.

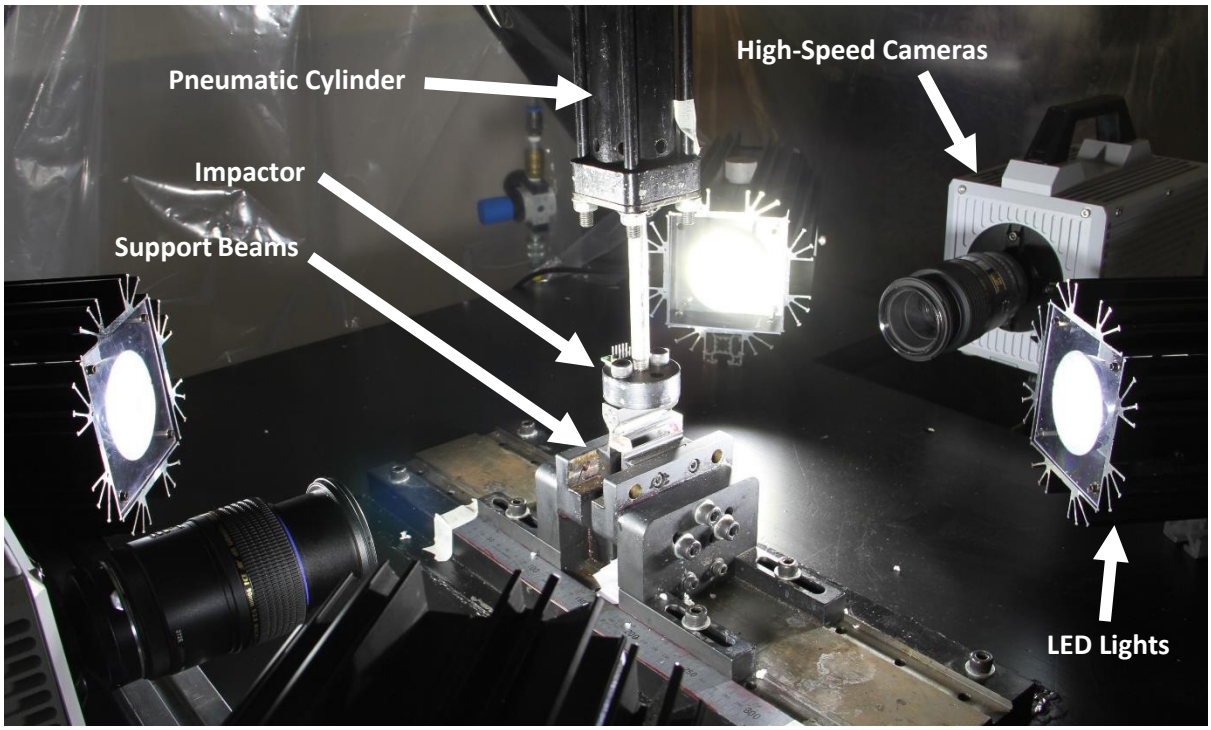

Figure 5.4: Impact test machine, including high-speed camera and pneumatic cylinder.

High-Speed Imagery

Two SA5 cameras (Photron, Tokyo, Japan) were used to image the impact from the front and rear of the specimen (that is, perpendicular to the face of the impactor head). The cameras were synchronised so that their images were acquired simultaneously. The imaging settings are outlined in Table 5.2.

Table 5.2: Camera settings.

Setting	
Frame Rate (s^{-1})	20 000
Shutter Speed (s)	1.09E-05
Resolution (pixels)	704x520

Impact velocity was measured in GOM Correlate Professional (GOM GmbH, Braunschweig, Germany) by tracking the white dots on the impactor head during the image sequence. Distances in the image were calibrated using the known dimensions of the impactor head. The displacement and acceleration of the impactor were also measured using GOM Correlate Professional.

The high-speed image sequences were used to calculate:

Impact force using the acceleration and mass of the impactor (0.572 ± 0.001 kg).

Energy Absorbed to Failure using the change in kinetic energy of the impactor and normalised with respect to the volume of the specimen. It was assumed that all the energy lost by the impactor was absorbed by the specimen. The change in the kinetic energy was based on the change in velocity of the impactor from when it first contacted the specimen to when the first osseous discontinuity appeared.

Minimum Fracture Propagation Speed by measuring the distance the crack tip travelled between image frames. Distance was measured using the 'measure' function in the Photron FASTCAM Viewer (PFV) software (Photron, Tokyo, Japan). The crack propagated through the thickness of the specimen in less than the time between image frames, so it was only possible to infer a lower bound on speed, here termed as the 'minimum'.

Using the images of the deformation, it was intended that DIC be used to calculate the displacements and strains of the specimens during the impact. A FE model of the experiment, using the CT scan data obtained earlier for the geometry of the specimen, could be built. Parametric studies for the material parameters could then be undertaken to find the values that predict similar displacements and strains.

Results

Observations from High Speed Imaging

The sequence of events leading to the fracture of the specimens is similar across all samples. Figure 5.5 shows a typical series of images (here illustrated for the impact of the 12 year old frontal bone (specimen #6)). Due to the curvature in the specimens, the ends of the specimen are not fully sitting on the support beams. This results in torsion within the sample as the impactor settles the edges onto the support beams. Within one frame (50 μs) of settling, prompt brittle fracture occurs. Very little bending (if at all) is observed at this frame rate.

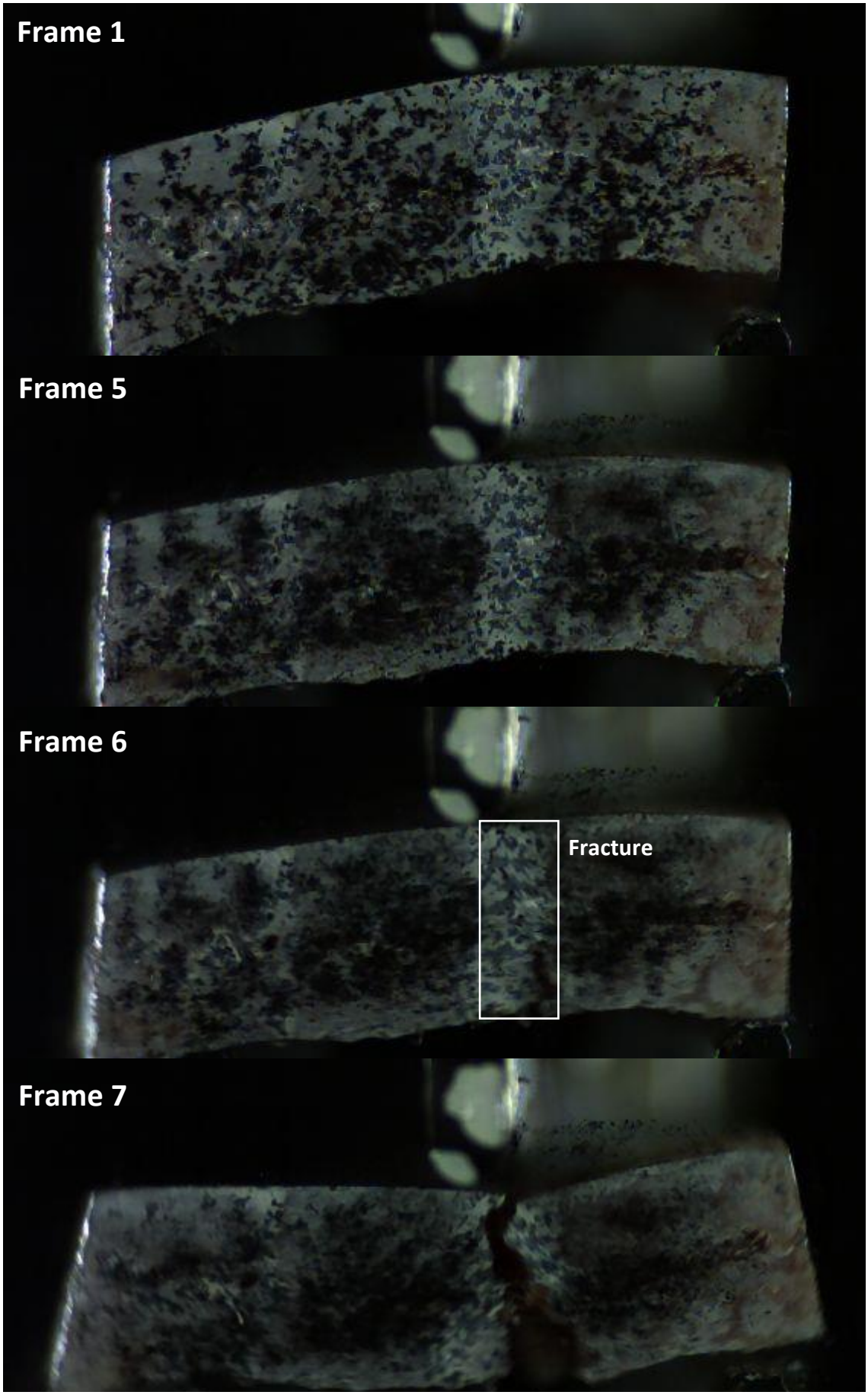

Figure 5.5: High-speed imagery sequence for specimen #6. Frame 1 (F1) is just before impact; impactor has speed of 5.75 ± 0.33 ms^{-1}. During F2-F4 (not shown), the specimen 'settles' onto the support beams. In F5, internal compression in cancellous layer occurs. Fracture appears in F6 (boxed outline); initiates at the bottom. In F7, the specimen is broken into two pieces.

A force-displacement plot for the impact of specimen #6 is shown in Figure 5.6. In the frame sequence, the plot data corresponds to frames two through to six (initial contact to fracture). As initial contact occurred between frames one and two, the initial displacement is not zero as expected, but rather, is the distance the impactor travelled between frames one and two. From frame two through to five, the force increases up to a maximum of approximately 3000 N. This corresponds to the point where the specimen is settling onto the supports and internal compression within the specimen is occurring and bending starts. The impact force halves within one frame, corresponding to the fracture that is observed as the bone fails.

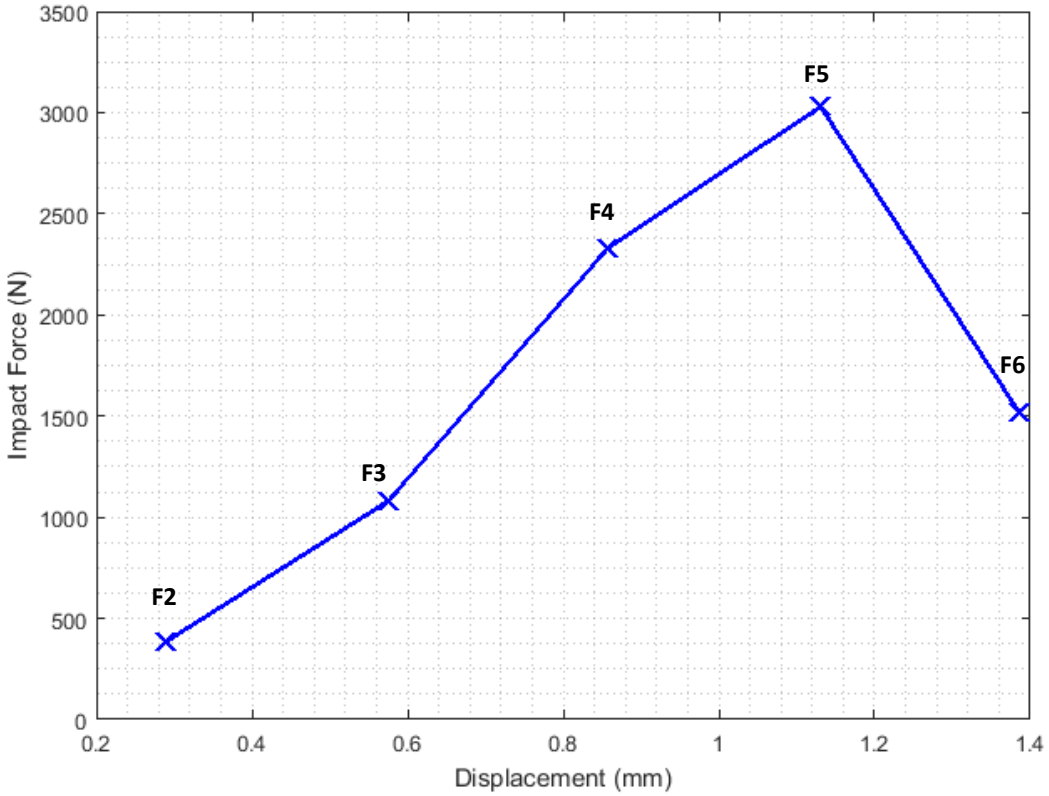

Figure 5.6: Force-displacement plot for specimen six. Data points correspond to frames two (F2) through to six (F6).

The force-displacement plot of Figure 5.6 is typical of the impacts for the specimens where one or both ends were not able to fully sit on the supports. Where there was very little settling of the specimen onto the supports, fracture occurred within one or two frames of initial contact, after which force decreased as the fracture propagated.

The sequence of events leading to the failure in specimens #1 and #2 (three-weeks-old) were slightly different than the older specimens. Although all specimens were orientated so that they were loaded 'naturally' from outside to inside (the impactor head loads from the convex side), these very elastic three-weeks-old specimens bend and become concave on the loading side before fracture occurs. Figure 5.7 shows the sequence of events exemplified for specimen #2.

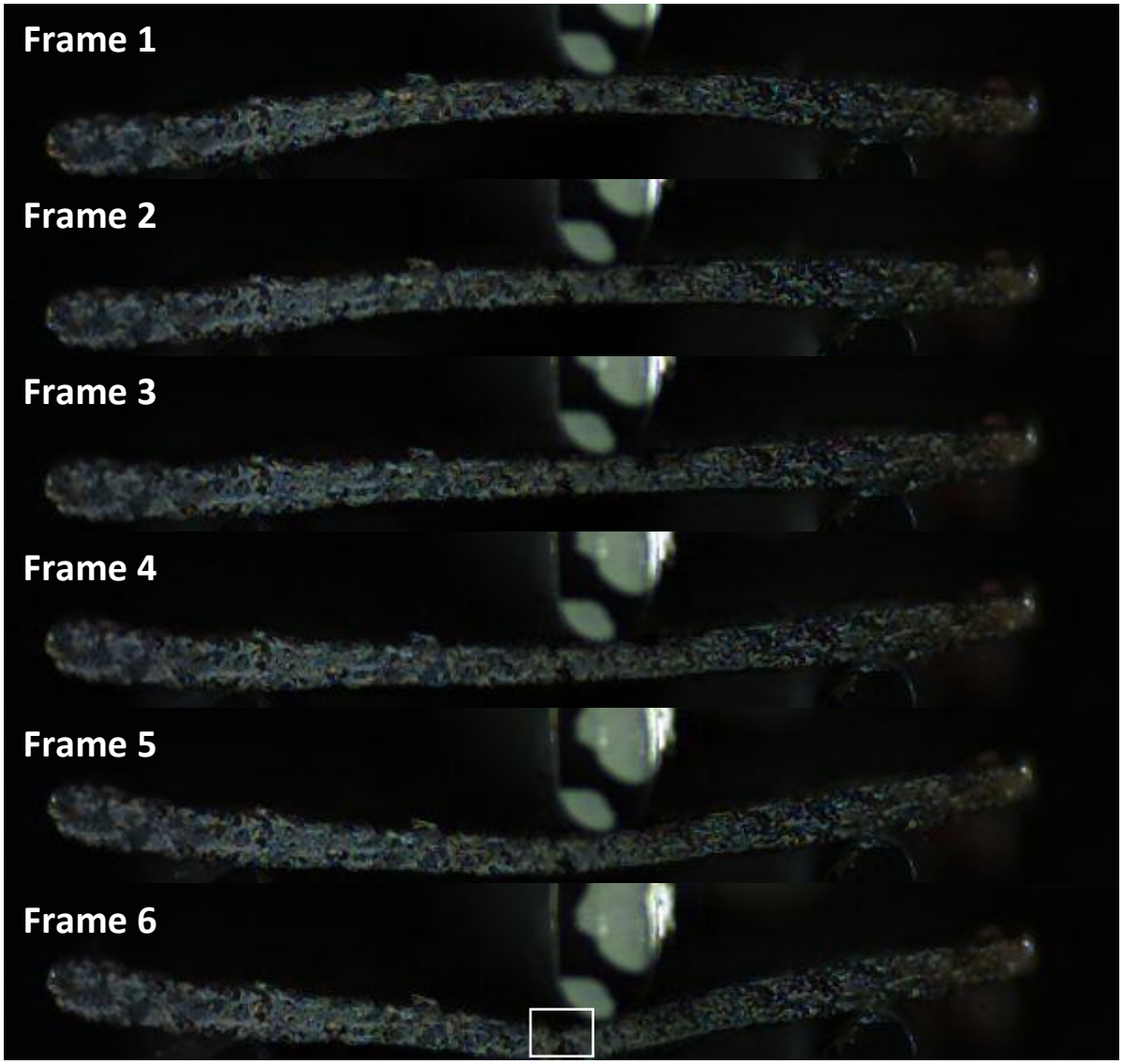

Figure 5.7: Sequence of events for specimen #2. Frame 1 (F1) is just before the impact; the impactor has a speed of 5.80 ± 0.34 ms^{-1} and the specimen is concave down. From F2 to F5, bending occurs. In F6, fracture occurs (boxed outline).

A force-displacement plot for the impact of specimen #2 is shown in Figure 5.8. As with Figure 5.6, the plot data corresponds to frames two through to six. The impact force increases from approximately 10 N up to a maximum of 140 N before fracture occurs. These forces are significantly less than those for specimen #6.

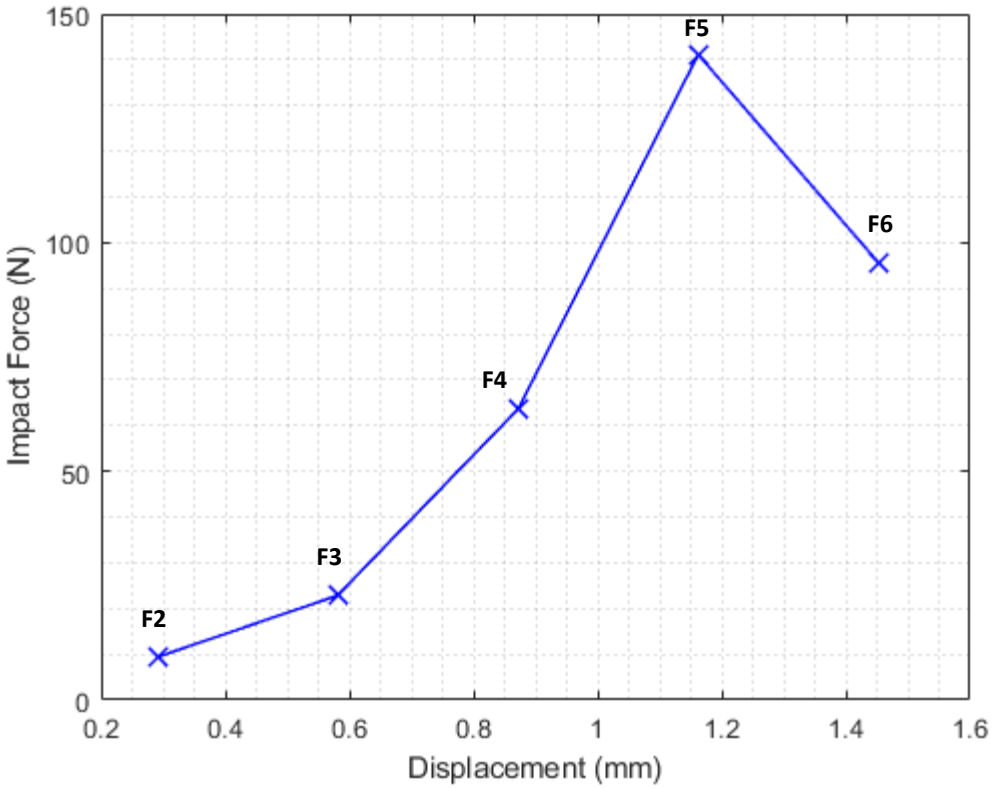

Figure 5.8: Force-displacement plot for specimen two. Data points correspond to frames two (F2) through to six (F6).

Average Thickness and HA Density vs Age

The average thickness increases linearly with age for each cranial bone (R^2=0.94, R^2=0.99 and R^2=0.79 for the frontal, occipital and parietal bone respectively), as shown in Figure 5.9(a). Only one data point exists for the temporal bone, hence no regression line could be fitted. The logarithmic fit for all data points had R^2=0.81.

For each cranial bone, HA density varies linearly with age, as shown in Figure 5.9(b). Both the occipital and parietal bone show clear increases in HA density with age (R^2=0.98 and R^2=0.77 respectively for linear fits). However, the regression line for the frontal bone shows an approximate constant HA density with age. The logarithmic fit for all data points had R^2=0.84 and exceeded the linear fit of R^2=0.44.

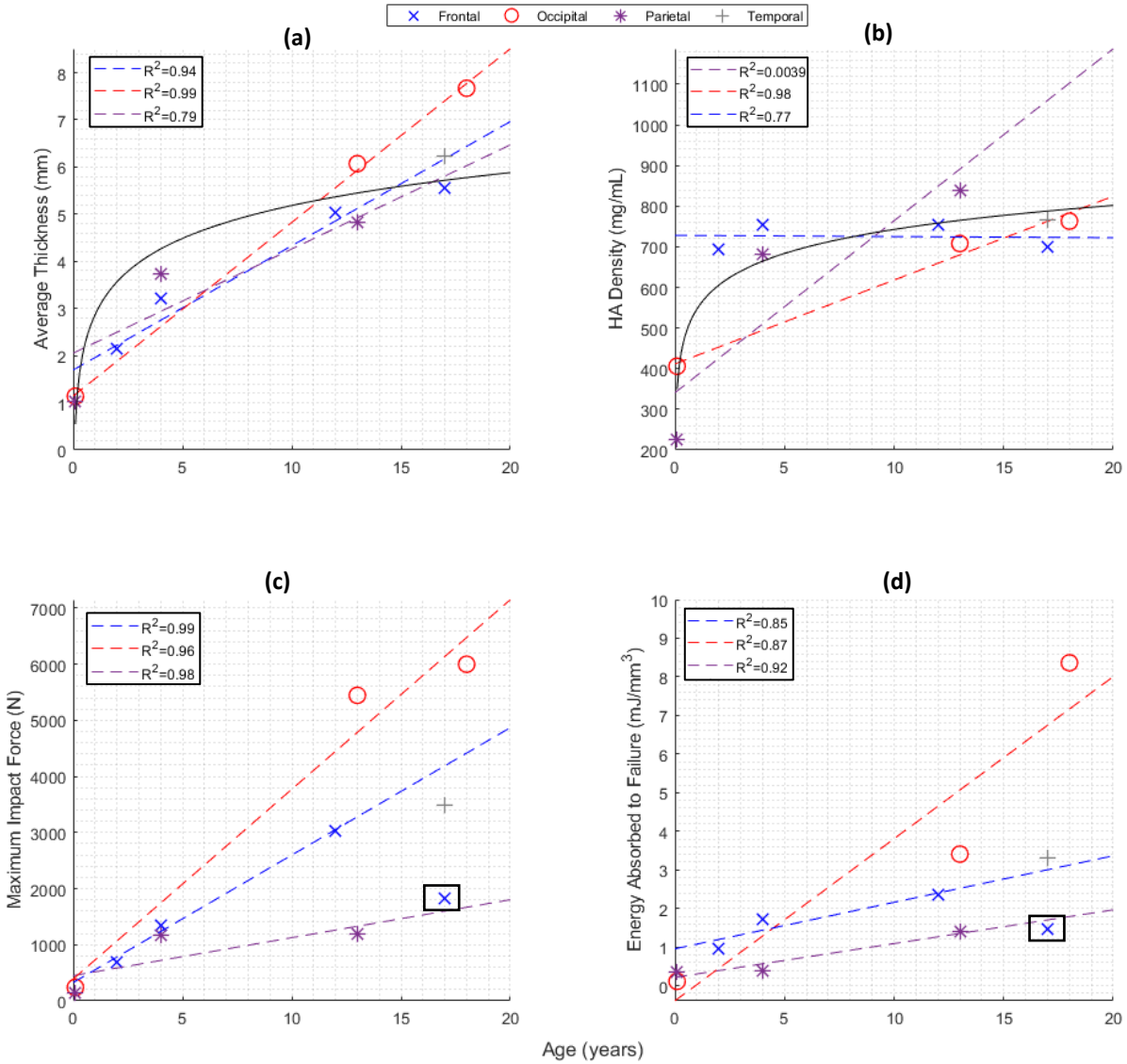

Figure 5.9: Plots of average thickness **(a)**, HA density **(b)**, maximum impact force **(c)** and energy absorbed to failure **(d)** versus age. Dashed regression lines correspond to respective cranial bone data by colour. Solid black curves correspond to logarithmic fit (used in pre-existing literature) for all data points. Boxed data points in **(c)** and **(d)** signify outliers and were not used in the regression analysis. Uncertainties are ± 0.02 mm, ± 5.8% and ± 12% for average thickness, maximum impactor force and energy absorbed to failure respectively; **(c)** and **(d)** are presented with these uncertainties in Appendix B of this thesis for clarity.

Maximum Impact Force

Across all specimens, the maximum force on the impactor ranges from around 200 N through to approximately 6000 N (Figure 5.9 (c)). The force measured in the occipital bone specimens (different individuals) is much greater than the other bone regions. For each cranial bone, the regression lines support a linear relationship with age (R^2=0.99, R^2=0.96, R^2=0.98 for frontal, occipital and parietal bone respectively).

Specimen #9 (boxed data point in Figure 5.9 (c)) does not fit the general trend of increasing with age. Review of the high-speed imagery showed that the impactor was misaligned and impacted the specimen near the edge, close to the righthand support. This resulted in a small section of the

specimen breaking off, and the fracture did not extend through the full thickness of the specimen. This would have resulted in the lower maximum impact force measured and therefore it was treated as an outlier and not used for generating the regression line.

Energy Absorbed to Failure

For each cranial bone, the energy absorbed to failure (normalised with respect to volume) increased with age (Figure 5.9 (D)). Regression lines show a linear increase (R^2=0.85, R^2=0.87, R^2=0.92 for frontal, occipital and parietal bone respectively). The occipital bone (the thickest calvarial segment investigated) absorbs the most energy before failure. As with maximum impact force, specimen #9 was treated as an outlier (boxed data point in Figure 5.9 (D)).

Minimum Fracture Propagation Speed

There were no observable trends for the minimum fracture speed in relation to age or average thickness (not shown graphically). Speeds ranging from 28 to 100 ms^{-1} were measured, however, these are the minimum speeds consistent with the data, and not necessarily the actual fracture speed due to limitations with the camera frame rate.

Discussion

This study is a preliminary investigation into the behaviour of infant and child cranial bone at impact velocities equivalent to falls greater than one metre (1.6 m) (under three-point bend loading conditions). Due to the scarcity of human child specimens, future experimental work needs to be designed rigorously to maximise the data that can be obtained. Although the experimental procedures can theoretically be tested on animal bone or surrogates, there is, to date, no satisfying substitute for human specimens in general and paediatric samples in detail, especially when information on the specimens (such as physical dimensions and estimated biomechanical properties) may not be available during the design process.

Limitations

As with many experimental studies involving human tissues, there are limitations to the data presented in this study. Such limitations include the number and physical size of samples, and the lack of surrounding tissues that make up the human head.

The greatest limitation in this study is the size of the data set. Only eleven samples from seven donors were used. Although this sample size may not be representative to fully investigate the trends observed, it provides some important data as there is little published data on child cranial material properties to date. The physical size of the specimens ranged from 15 to 22 mm in span and seven to

12 mm in width, which are not representative of an intact skull, but are similar in size to the specimens used by Coats and Margulies (2006). The 11 samples were from three females and four males, which is also not enough to determine whether sex has any influence on the results obtained. However, it is well established in the medical world that sex does not have any influence on the mechanical strength of human bone (Katzenberger et al. 2020, Zwirner 2021).

Impact experiments were conducted on bare cranial bone, with all surrounding tissues removed. This limits the data to that of the cranial bone alone and cannot be used to infer how the cranial bone would behave in its correct anatomical context. The surrounding tissues will have some influence on how the cranial behaves during an impact. Scalp and suture tissues are much softer than the cranial bone and would likely absorb some energy, hence reducing the likelihood of skull fracture occurring. The presence of brain and CSF would also offer some resistance to the deformation of the cranial bone.

Due to the relatively small physical size of the specimens, the impactor head had to be small (radius of two millimetres). This does not represent the physical size of an impact surface likely to be experienced during a fall or weapon. Such a size is more representative of an edge, such as falling onto the edge of household furniture.

The frame rate was a limiting factor in capturing the deformation of the specimen during the impact before fracture occurred. Although high intensity lighting was used, more light was required so that a faster camera frame rate could be used. This would have allowed for the use of DIC to measure displacement and strain, which in turn could be used to calculate elastic modulus and ultimate strength, as well as in parametric finite element models to improve material models.

The calculation of the energy absorbed to failure assumed that the kinetic energy lost by the impactor was transferred to the specimen. However, there is likely to be some energy dissipation due to the frictional contact between the impactor and specimen. Any frictional losses are likely to be similar in magnitude for each impact and therefore only affect the reported values. Any relationships observed will be the same and hence any losses were assumed to be negligible. There were also frictional losses where the shaft of the impactor was in contact with the pneumatic cylinder bushing. This affects the speed of the impactor, however, the relatively short distance over which the impactor-specimen contact took place means that any energy loss would be minimal. Although the air supply was shut off after 10 ms and the pneumatic cylinder simultaneously vented to atmosphere, the residual pressure in the cylinder accelerates the impactor until the pressure is equalised.

In specimen #4, zigzagged discontinuities were observed in the CT scans. The zigzag nature indicates it is likely to be the metopic suture, which is still not fully ossified in the given age. From closer inspection of the images, it does not appear that the impact fractures initiated at the site of the suture. However, it cannot be certain if the suture had any relevant effect on the test failure of the specimens.

Observations from High Speed Imagery

The mean (± standard deviation) impact velocity was 5.65 ± 0.14 ms^{-1}. This is equivalent to a fall of approximately 1.6 m and all specimens exhibited fracture at this speed. No observations during the impact process on infant cranial bone at this high loading rate have ever been published to our knowledge, with the highest speed in prior studies being 2.81 ms^{-1} (Coats and Margulies 2006).

Except for the two three-week-old specimens, all specimens had virtually no bending before brittle fracture occurred. Specimens #1 and #2 were more flexible than the other specimens as visible bending occurred before they fractured. This is consistent with previous literature where the infant skull has been found to be more compliant than a child or adult skull (Margulies and Thibault 2000, Baumer et al. 2010, Loyd et al. 2015).

The stiffness of any beam theory for a simply supported beam is the product of the elastic modulus and the beam's second moment of area (a function of beam thickness). McPherson and Kriewall (1980), Margulies and Thibault (2000), and Coats and Margulies (2006) showed that the elastic modulus of paediatric cranial bone increases with age. The present specimens show a consistent trend of thickness increasing with age. Therefore, in these specimens, both elastic modulus and second moment of area increases with age, hence it is expected that the older the specimen, the less flexible it is.

The prompt brittle fracture of specimens #3 to #11 is likely to be due to the relatively greater HA density. It is well established that HA density increases with age and that an increase in HA density increases the brittleness of bone (Kieser 2012). In these samples, the fractures started at the bottom, with the crack tip propagating upwards towards the top. This is expected due to the highest tensile stresses occurring at the bottom surface. The fracture often zigzagged, especially where there were clear transitions from the cortical to cancellous layers (and vice versa). This is likely due to the difference in the osseous microstructure and hence material behaviour of the two types of bone.

Force-displacement data would ideally be used to calculate the elastic modulus of the various cranial bones tested. However, no deflections were captured in the images due to the fractures appearing within one frame of the specimens settling onto the supports. The displacement data was that of the

impactor and largely a result of the specimens undergoing bending and torsion until both ends were on the support beams.

Average Thickness and HA Density

Delye et al. (2015) measured cranial bone thickness using 181 CT scans of 187 patients, ranging from zero to 20 years of age. They found that there was a rapid increase in the skull bone thickness in the first year of life, with the rate of increase slowing during year two. The thickness continued to increase further up to the age of 20, but the rate of increase slows substantially. A logarithmic relationship was determined for the skull thickness as a function of age. The data presented here fits the general trends found by Delye et al. (2015), with magnitudes within one standard deviation of their mean values. Linear increases with age were identified for each cranial bone in this given study. A logarithmic curve fit was carried out for all data points to compare with Delye et al. (2015). The present data does not have enough points to determine whether a logarithmic or linear relationship fits the data better. Delye et al. (2015) found no differences in thickness between male and female and our own autopsy experience show only negligible overall differences in cohorts of hundreds of cadavers, therefore differences in sex were not considered in this study.

Delye et al. (2015) found a similar trend for the general increase in HA density with age as that for the skull thickness (logarithmic relationship). However, there was a steep increase in the density at the age of six years, reaching a peak at seven before dropping quickly at eight and returning to the general increase at age nine. When considering all data points in the present study, a logarithmic fit better represents the data than a linear fit, similar to that found by Delye et al. (2015). Due to no specimens being in the age range of five to 10 years, the sudden increase in density from ages six to eight cannot be tested with our data. The higher R^2 values for the linear relationships found for individual cranial bones is most likely due to the very small number of data points for each region. This is most apparent for the frontal bone where the constant HA density with increasing age is unexpected based on the findings of Delye et al. (2015).

Maximum Impact Force

Although maximum force data is not presented in the three or four-point bend test studies of Margulies and Thibault (2000), Coats and Margulies (2006), and Davis et al. (2012), it can be inferred from the specifications of the load cells used that the maximum force did not exceed 250 N. A force-displacement plot presented by Coats and Margulies (2006) shows that a maximum force of around 7 N was measured for static three-point bending of a parietal bone from a two-month-old donor. The maximum forces experienced by the three-week-old specimens in the present study were approximately 140 N (parietal) and 240 N (occipital). Without specific data to compare too, these

magnitudes are higher than that of the similar age group in Margulies and Thibault (2000), and Coats and Margulies (2006). This is expected due to the higher impact velocity.

In the data presented here, the maximum impact force ranges from approximately 200 N up to 6000 N. As there is limited data for human cranial bone up to 18 years in the literature, and that no previous studies exist for similar impact speeds, it cannot be determined if these magnitudes are to be expected. Given that the scalp, periosteum and dura mater were removed prior to testing, there is no energy absorption by these softer tissues and therefore the maximum force would be expected to be higher than that experienced in a real head impact. On the other hand, the cerebrospinal fluid and brain are also absent in this experimental protocol and thus not providing support to the cranial bones, presumably resulting in smaller maximum force magnitudes. In real-world impacts, the deformation pattern and force versus time curve may differ due to the stiffness and shape of the impacting surface, the soft tissue layers covering the skull and the orientation of the head. Head orientation could have reasonable influence on the deformation pattern as the shape of the human head means that each orientation will have a different contact area and thus affect the resulting stresses.

Energy Absorbed to Failure

Margulies and Thibault (2000) presented energy absorbed to failure data for their three-point bend tests under static loading conditions. For their six-month-old samples, the energy absorbed to failure was approximately 0.10 – 0.20 mJ/mm^3 and 0.40 – 0.45 mJ/mm^3 for loading rates of 2.54 and 2540 mm/min respectively. For a similar age group in the present study, specimens #1 and #2 had energy absorbed to failure of approximately 0.11 and 0.35 mJ/mm^3 indicating that energy absorbed to failure is similar for static and dynamic loading conditions at least in this age group.

Energy absorbed to failure increased with increasing age and hence average thickness. The data from all bone locations show this same general trend, with occipital bone having a much greater energy absorbing capacity than the others. This is to be expected given that the orientation of the head during an impact can influence the stress the cranial bones experience. For example, due to the (generalised) ellipsoidal shape of the human head, an impact to the parietal region is spread out over a larger area, reducing the peak force and increasing the impact duration. This was, in general, observed in the infant head cadaver drop tests by Loyd (2011), where the peak head acceleration was around 10 to 20 *g* lower than that for an occipital impact. The stress experienced in the parietal region is likely to be lower due to the impact force acting over a relatively larger area. Therefore, the parietal bone does not need to be as thick as the occipital bone and hence does not need the same energy absorbing capacity. The frontal and occipital regions of the human head have a lower impact area relative to the parietal region and therefore require a greater energy absorbing capacity than the parietal bone.

Implications for Finite Element Models

It is already known that bone behaviour is rate (velocity) sensitive and becomes more brittle elastic increasing strain rates (Kieser 2012). The results of McPherson and Kriewall (1980), Margulies and Thibault (2000), Coats and Margulies (2006), and Davis et al. (2012) show that infant and child cranial bone can exhibit noticeable elastic or plastic deformation without failure at low impact speeds (equivalent to falls less than one metre), while this study has shown that cranial bone exhibits prompt brittle fracture at relatively higher impact speeds (equivalent to falls of 1.6 m). Therefore, finite element models used for modelling head impacts in children need a suitable rate-dependent model for the cranial bone. The data presented here will help to verify predictions based on such models. There is also a future research question in that what strain rate or impact speed does the 'transition' from more compliant to relatively less compliant behaviour occur? Having a quantifiable value on this would help an analyst ensure that they are using a suitable material model that will account for the different behaviour of the cranial bone, especially for models of young children and teenagers.

Digital Image Correlation

Due to the prompt brittle fracture of most specimens, only one or two images were obtained before the fracture occurred. As previously noted in the limitations discussion, this was a result of not enough lighting to use a higher frame rate. With a higher frame rate, more data is produced per unit time, while there is a limited storage capacity. That is, the higher the frame rate, the total imaging time decreases, along with the maximum resolution of the images. Balancing the reduction in resolution with the frame rate was the main driver for the frame rate selected. This was so that an appropriate resolution that captured the whole specimen (and left room for deformation) could be used. As a result, fracture occurred within one or two frames of the specimens settling on the support beams. This was not enough for DIC to be used to obtain any meaningful results.

Ideally, this analysis would have involved obtaining a minimum of ten frames to use in a DIC analysis. Displacements and strains would then be calculated. Using the CT scan data of each specimen, a FE model of the impact would be created. A parametric study for the material model parameters would be conducted, where the parameters would be varied until the model predicts a similar strain field as that measured using DIC. From there, data for the elastic modulus and, importantly, the rate dependence of elastic modulus could have been obtained and contributed to increasing the current data set on infant and child cranial bone material properties.

Another factor limiting such an analysis to be conducted was that Blu tack was used to secure the specimens in the capsule for CT scanning. Blu tack ended up having a similar spectral intensity as the specimens and therefore the specimens could not be segmented from the Blu tack. Manual

segmentation would have been required, which would have resulted in less accurate geometry of the specimens.

The use of DIC has significant future potential now that the experimental limitations are known, and suitable methods can be developed to overcome these. Due to the scarcity of human infant tissues, it is challenging to design experiments that will allow one to obtain all desired data without prior testing. Unfortunately, researchers cannot simply purchase large quantities of material to test their experimental setups as can be carried out for materials testing of traditional engineering materials. Therefore, this preliminary work provides details for any future experimental work of a similar nature so that the precious tissues can be better utilised.

Conclusions

The questions of current debate in the identification of AHT in children may be divided into the forensic (what injuries or injury patterns discriminate between AHT and accidental injury) and the mechanical (what are the elastic moduli, ultimate tensile strength and energy absorbed to failure of each of the head tissues, and how do they vary with strain rate and age). The results of the present study address a few of the latter:

- The failure mode in impacts of a 2 mm radius impactor at 5.65 ± 0.14 ms^{-1} was brittle fracture (with little or no bending observed) for samples aged two to 18 years. For the two specimens aged three-weeks, bending (resulting in inverted curvature of the specimens) occurred, followed by brittle fracture.
- Impact force peaks at 200 to 6000 N, increasing with age (or thickness). Impact force is higher for occipital than parietal or frontal bone.
- The energy absorbed to failure follows the same trend of increase with age or thickness. It was highest for occipital bone. The values of energy absorbed to failure were 0.11 and 0.35 mJ/mm^3 for age three-weeks, agreeing with previously published static tests, and increase with age up to around 9 mJ/mm^3 for 18-year-old occipital bone.
- The increase in stiffness with age and the differences in mechanical properties of the different cranial bones as seen by others is supported by the present data.
- The use of this data in FE modelling will contribute to answering the mechanical as well as the forensic questions in the identification of AHT.

The sample size is small, but the observations of the impact failure process, and the measurements of impact force and energy absorbed to failure are unique. To the best of the authors' knowledge, no

data has yet been published for child specimens at this high loading rate; the highest speed in prior studies being 2.81 ms^{-1}.

Chapter 6 Applications of the Baseline Model

Introduction

One of the primary purposes of developing infant head finite element (FE) models is to reconstruct the events of real-world cases of suspected abusive head trauma to determine whether observed head injuries are consistent with the history provided by caregivers. To do this, many factors, including the geometry, material models, mesh and boundary conditions need to be considered. In cases where the history is explained as a fall, the height from which the infant falls and the stiffness of the impacting surface are important boundary conditions to consider. Both the drop height and impact surface will vary from case-to-case. Therefore, it is important to understand how each can influence the response of the infant head during an impact so that appropriate modelling decisions can be made, and incorrect assumptions are not used.

As summarised in Chapter 1, there already exists much literature on the type of head injuries likely to be observed for falls from different heights (Chadwick et al. 1991, Plunkett 2001, Johnson et al. 2005). However, the review of the current literature for infant head FE models in Chapter 3 of this thesis found that only the work of Li, Luo, and Zhang (2013) has investigated various drop heights and impact surfaces other than those used for the purposes of validating FE models against experimental data. Most of the existing FE models are used to principally model low height falls onto a flat, rigid surface.

Domestic household flooring surfaces generally consist of a base flooring surface, such as concrete or a wooden structure consisting of floorboards supported by joists. Carpet or a combination of carpet with underlay is generally overlaid on the base flooring surfaces. Flooring surfaces vary from household to household, and often vary in different parts of the house (for example, the kitchen may have tiles or linoleum, while bedrooms are likely to have carpet). There exist many types of carpet and underlay, making for a multitude of combinations. Carpet construction can generally be divided into two types: loop piled (fibres are bent into loops, provides limited cushioning) or cut pile (yarn tips are cut so there are no loops, piles are denser and softer). The fibres can be manufactured from materials such as nylon, polyester or wool, which all have different wear resistance and cushioning (for comfort) properties. Underlay is generally used underneath carpet to provide additional cushioning, smooth out minor imperfections in the base flooring surface, and provide acoustic and thermal insulation. Thicknesses typically range from five to 15 mm for carpet, and five to 12 mm for underlay (Look Floors 2018, McKenzie and Willis 2020).

This chapter uses the baseline FE model presented in Chapter 4 to investigate the response of the infant head from different drop heights and onto common domestic household surfaces. This will build on the current literature, especially for the different impact surfaces where there is limited data and a large number of household flooring combinations. Additionally, an impact to the edge of a surface is investigated to determine how the response differs to that for a flat surface.

Methods

The baseline model used in this chapter is the same as that presented in Chapter 4 and so uses the same geometry, mesh, material models and boundary conditions. The only difference is the parietal cranial bone uses an elastic modulus of 592 MPa, which is due to infant parietal bone typically having a greater modulus than occipital bone (Coats and Margulies 2006). A similar method as described in Chapter 4 is used to calculate the parietal elastic modulus. Due to the small difference in the baseline model, results and discussion for validating it against the same experimental cadaver impact data and existing FE models is presented.

Contact between each tissue layer is modelled as bonded. This means that the nodes at the interfaces of each tissue cannot slip or separate relative to one another. A bonded contact method does not accurately reflect the interface between the skull and brain as the cerebrospinal fluid (CSF) causes a partial decoupling, mainly in shear, between the motion of the brain and skull. A sliding contact, where the nodes can slip but not separate relative to one another, is a better representation of the brain-skull interface. ANSYS Explicit Dynamics (ANSYS, Inc., Canonsburg, Pennsylvania, USA) does not support a sliding contact (termed 'no separation' in ANSYS Explicit). Instead, frictional contact, where the nodes can slide and separate relative to one another, was also used in the following drop height and impact surface models. However, separation of the brain from the skull would create a void in the baseline model, which, in reality, would be filled by the CSF. Therefore, bonded and frictional contact represent the two extremes, with the real physical case of sliding contact lying between the two. Static and dynamic friction coefficients of 0.2 were used for the frictional contact between the brain and skull (Miller et al. 1998).

The analysis in this chapter is largely focussed around three result outputs: peak head acceleration, impact duration and the Head Injury Criterion (HIC). Peak acceleration is calculated from the maximum impact force output and the mass of the head (0.616 kg for the half geometry), while impact duration is determined from the time the impact force reaches zero. As described in Chapter 1, the HIC is calculated using a time duration that maximises the HIC value (equation 1.1); this gives HIC_{max}. As a way to compare HIC for different impacts, the duration from which HIC is calculated can be either 15

or 36 ms (HIC_{15} and HIC_{36}). In this chapter, HIC_{max} is used as the total impact duration was often considerably less than 15 ms.

Drop Height

For the drop height parametric studies, the impact velocity was calculated using conservation of energy:

$$\dot{u}_{impact} = \sqrt{2gh} \tag{6.1}$$

Where *g* is the acceleration due to gravity and *h* is the drop height. Drop heights ranged from 0.05 m to 1.8 m, with the latter being an upper limit for possible heights that an infant is likely to experience in the home. Table 6.1 details each drop height investigated and the associated impact velocity.

Table 6.1: Investigated drop heights and their corresponding velocities.

Drop Height (m)	Impact Velocity (ms^{-1})
0.05	0.99
0.10	1.40
0.15	1.72
0.30	2.43
0.40	2.80
0.50	3.13
0.60	3.43
0.70	3.71
0.80	3.96
0.90	4.20
1.00	4.43
1.20	4.85
1.50	5.42
1.60	5.60
1.80	5.94

Note: Bolded heights are standard drop heights that were also used in the impact surface investigation.

Impact Surfaces

To investigate the effect the impact surface type has on the response of the infant head FE model, a parametric study of six different surfaces was conducted for each of the standard drop heights (Table 6.1). Base flooring surfaces of concrete and wood were used, with each having the bare surface, the addition of carpet and the addition of a combination of carpet and underlay. A thickness of 7 and 8 mm was used for the carpet and underlay respectively as these represent average thicknesses found in domestic houses (averaged from Look Floors (2018), McKenzie and Willis (2020) as well as measurements from the author's own house). With the six flooring combinations, the parametric

study included 36 simulations. A further 36 simulations were carried out for the frictional contact between the brain and skull, resulting in 72 simulations for the impact surfaces analysis.

The bottom surface of the concrete (thickness of 100 mm) was fixed, representing the foundation sitting on the ground. For the wooden base surface, a fixed-fixed beam of 300 mm in span and 18 mm thick was used. This represented a typical flooring surface attached to joists (of which the joists are assumed to be fixed). The impact location was in the centre of the beam where maximum deflection of the floor would occur. At the ends, the fixed boundary conditions are more representative of a rigid surface. Table 6.2 summarises the different flooring types used in this analysis.

The concrete base flooring surface was modelled using eight-node hexahedral elements, with element sizing biased towards the top surface. This was similar for the wooden base flooring surface. The carpet and underlay were modelled using four-node tetrahedral elements. Mesh refinement in the form of a sphere of influence (radius of 50 mm and element size of 2 mm) was used at the centre of the impact site. Figures 6.1 and 6.2 show the combination of carpet and underlay with the concrete and wooden base floorings respectively.

Table 6.2: Impact surface details

Impact Surface		**Thickness (mm)**
Base Surface	**Top Surface Layer**	
Concrete	Nil	100
	Carpet	7
	Carpet + Underlay	7+8=15
Wood	Nil	18
	Carpet	7
	Carpet + Underlay	7+8=15

Material models for the concrete and wood were obtained from the ANSYS Explicit material library (‘CONC140MPA’) and the ANSYS Granta Design Sample Materials (‘Pine Wood’) respectively. For the carpet and underlay, hyperelastic material models were used, with parameters obtained and modified from Hajiaghamemar et al. (2018). The hyperelastic constants are presented in Table 6.3. The carpet and carpet-underlay combination had shared topology with the base floor surface, that is, the nodes at each interface were shared between the different bodies.

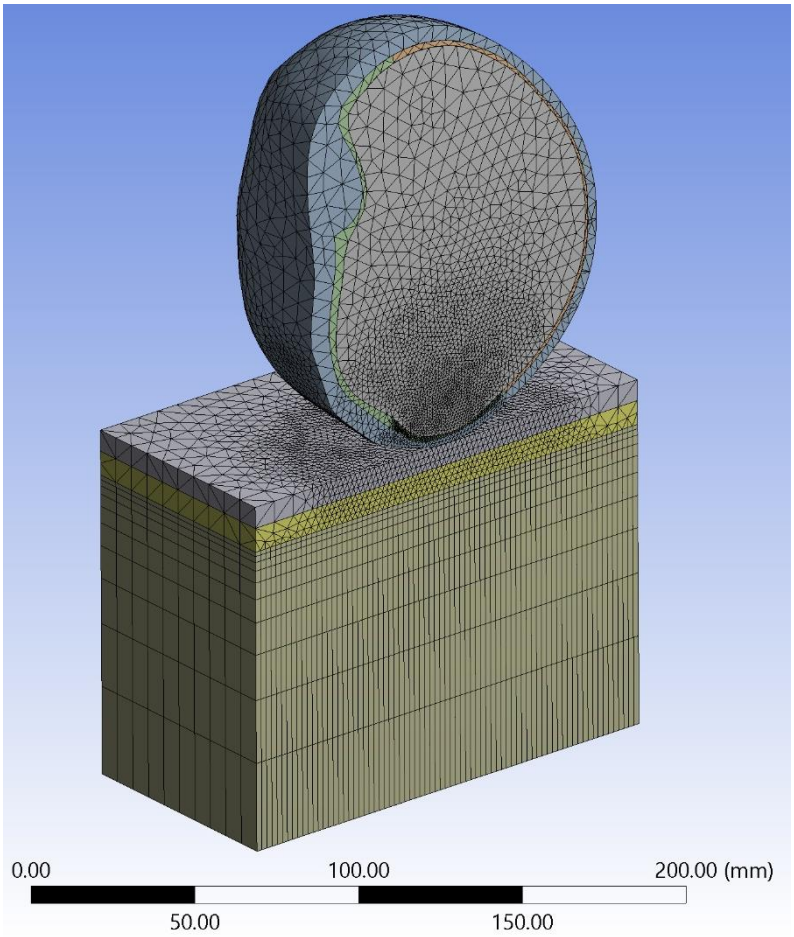

Figure 6.1: Geometry and mesh for combination of carpet and underlay with a concrete base flooring.

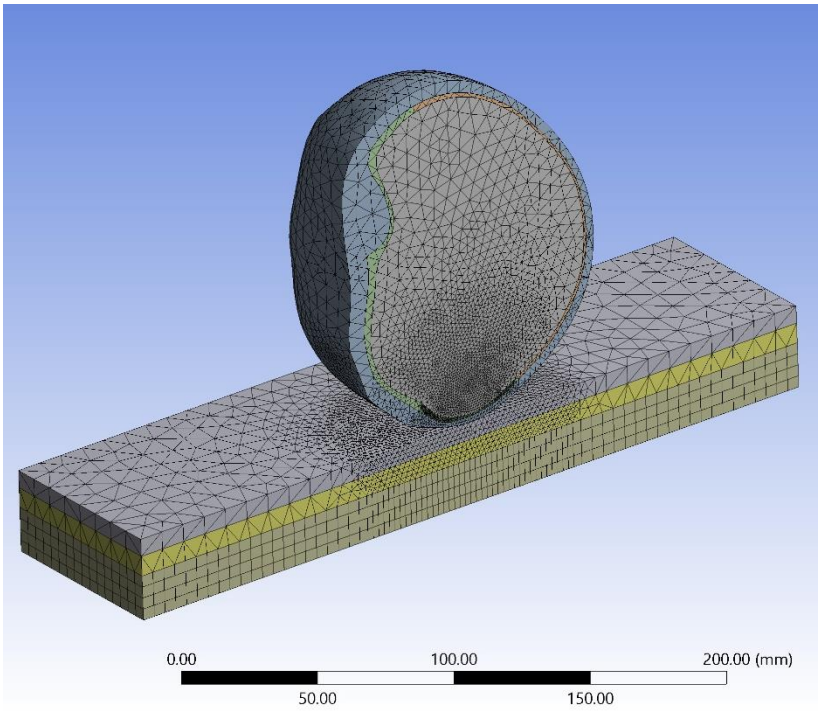

Figure 6.2: Geometry and mesh for combination of carpet and underlay with wooden base flooring.

Table 6.3: Material models used for the impact surfaces.

Impact Surface	Material Model	Model Parameter	Parameter Value	Source
Concrete	Polynomial Equation of State	Density	2520 kgm^{-3}	ANSYS Explicit material library ('CONC140MPA')
		Shear Modulus	22 060 MPa	
		Parameter A1	35 270 MPa	
		Parameter A2	39 580 MPa	
		Parameter A3	9 040 MPa	
		Parameter B0	1.22	
		Parameter B1	1.22	
		Parameter T1	35 270 MPa	
		Parameter T2	0 MPa	
Wood	Isotropic Elastic	Density	487 kgm^{-3}	ANSYS Granta Design Sample Materials ('Wood')
		Elastic Modulus	9 300 MPa	
		Poisson's Ratio	0.374	
Carpet	Ogden hyperelastic	Density	200 kgm^{-3}	Hajiaghamemar et al. (2018)
		μ_1	20 Pa	
		α_1	25	
		μ_2	4 640 Pa	
		α_2	7.38	
Underlay	Ogden hyperelastic	Density	90 kgm^{-3}	Hajiaghamemar et al. (2018)
		μ_1	6 420 Pa	
		α_1	8.99	

Impact on Surface Edge

Household furniture offer edges on which an infant may experience a head impact which, for example, could result from being dropped from the caregiver's arms. To investigate how a head impact with the edge of household furniture differs to that of a flat surface, the impact surface of the baseline model was modified so that the contact point was on the edge of a rigid surface, as shown in Figure 6.3. The orientation of the head geometry was unchanged from that of the baseline model, as were the boundary conditions, contact methods and mesh. The surface edge was a sharp corner, that is, it had a zero radius of curvature.

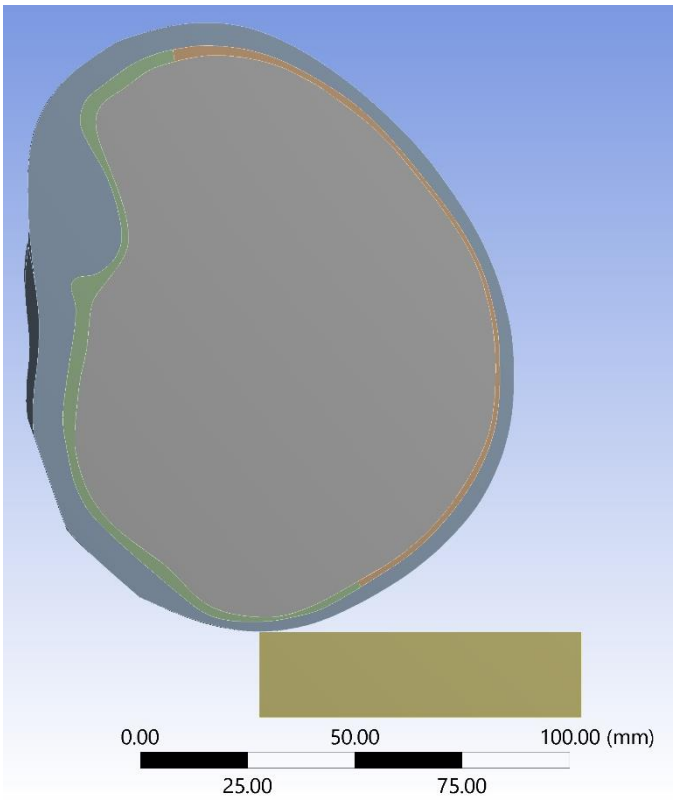

Figure 6.3: Baseline head geometry impacting edge of a rigid surface.

Results

Behaviour of Baseline Model

Figure 6.4 shows the sequence of deformation for the baseline model during an occipital impact (impact velocity of 2.43 ms^{-1}). During the first millisecond of the impact, the head tissues flatten out, conforming to the impact surface. As the impact proceeds, a depression starts to form at the impact site; the head shape goes from convex to concave at this localised area. At approximately 5 ms, peak impact force is reached; this corresponds to the maximum deformation of the head tissues. The concave depression of the scalp and occipital bone protrude into the brain. The relatively softer brain material results in larger deformation, as shown by the displacement contours in Figure 6.4 radiating out from the centre of the depression. At this point, the skull is bending in a convex manner at the outer edges of the depression, while it is bending in a concave manner at the centre. From around 5 to 6 ms, the head starts to rebound, and the depression becomes smaller, eventually forming back to its original shape. No permanent deformation is observed. Figure 6.5 (a) and (b) show larger views of the depression at peak impact force.

At peak acceleration, the contact surface area was approximately 1809 mm^2. Figure 6.6 shows the scale bars used to estimate the average radius of the contact area.

The baseline model took an average of 13 hours to run on an Intel i7 9700 central processing unit, running four cores at a frequency of 4.2 GHz (32 GB of random access memory and using a M2 Solid State drive). Although a large variety of computers were used to run these models, the above specification represents a typical consumer grade computer and provides some idea of the time required to compute the FE models.

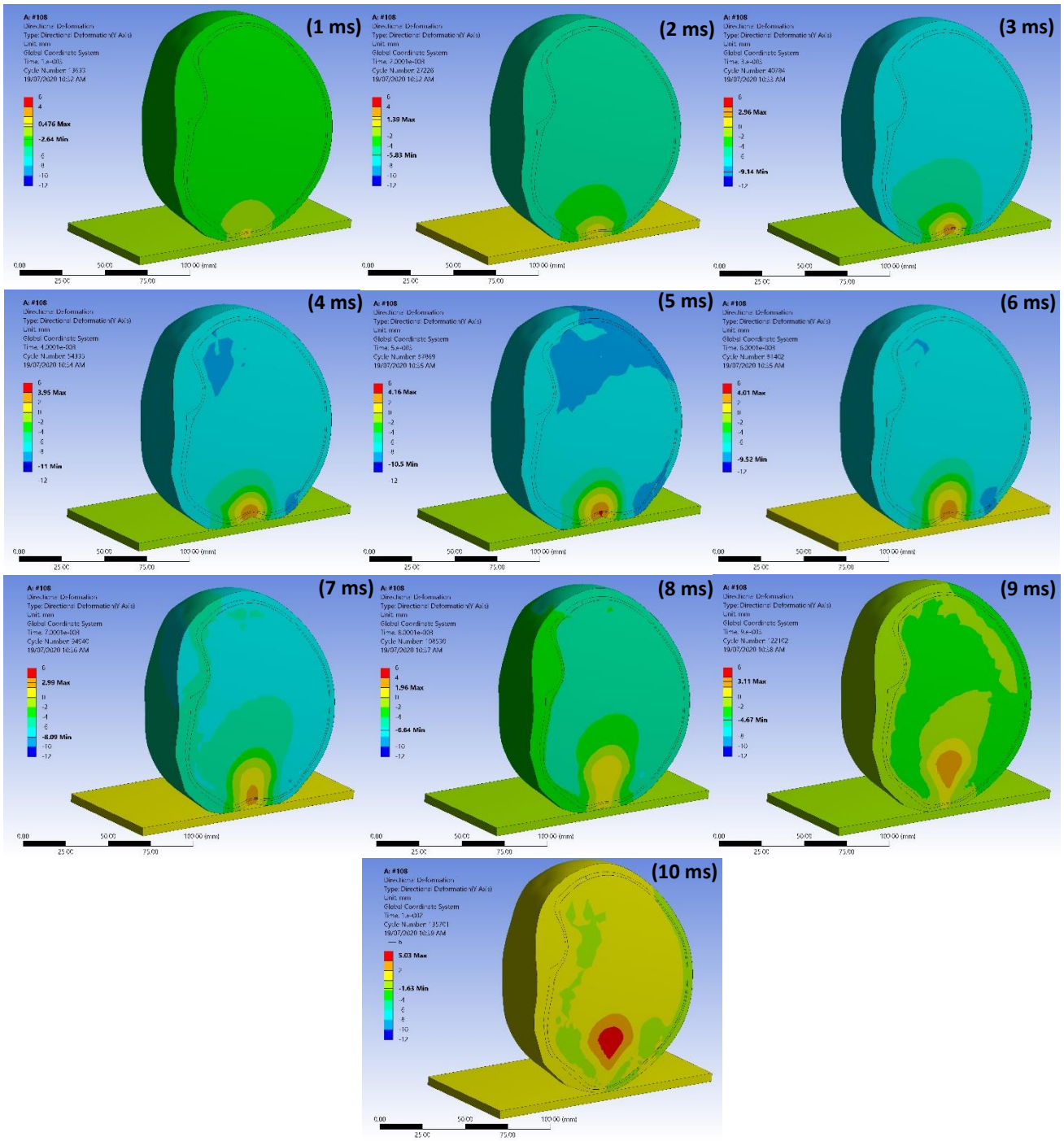

Figure 6.4: Sequence of deformation for baseline model in 1 ms intervals.

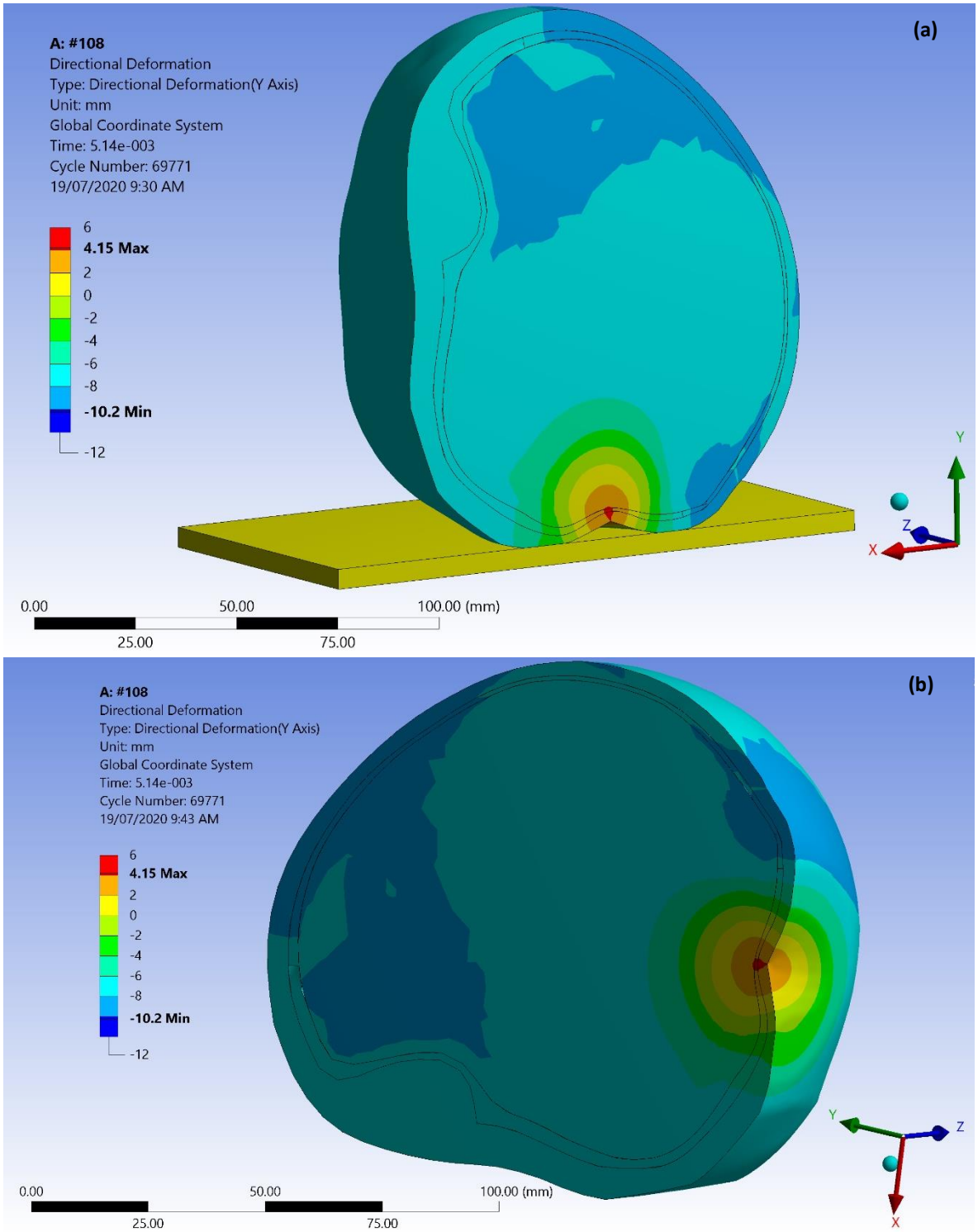

Figure 6.5: Vertical displacement at peak acceleration for baseline model. **(a)** is view in real-world orientation, **(b)** shows resulting depression at impact site.

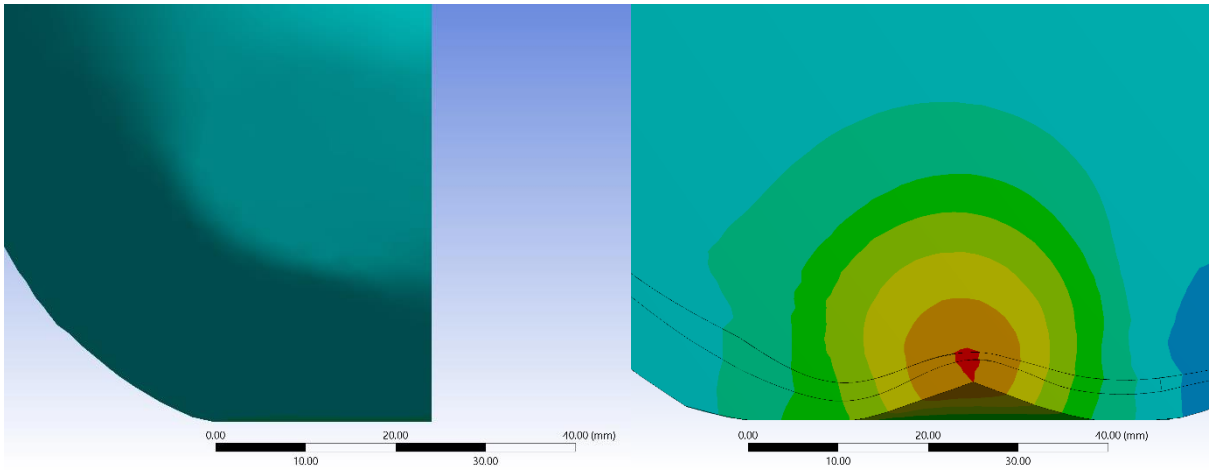

Figure 6.6: Average radius of contact area for the baseline model at peak acceleration was estimated using the scale bars.

Baseline Model Validation

The baseline model for a drop height of 0.3 m had a peak head acceleration of 83.8 g, impact duration of 9.9 ms and HIC_{max} of 221. For a drop height of 0.15 m, these values were 56.0 g, 10.2 ms and 93 respectively. Figure 6.7 presents the acceleration-time traces for each of the experimental and existing FE models. Table 6.4 presents peak acceleration, duration and HIC_{max} data for the baseline model, experimental cadaver results and existing FE models where such data for an occipital impact was presented. The cadaver impact experiments were onto a rigid surface and only consisted of a head (no body from the neck down).

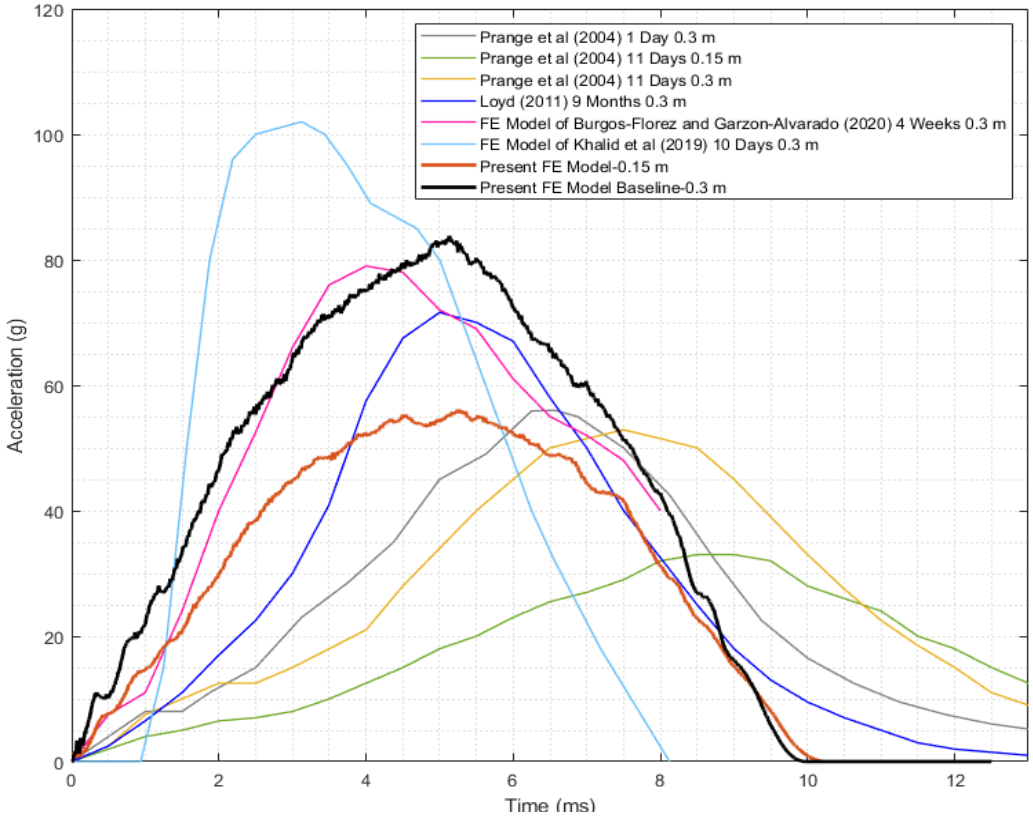

Figure 6.7: Comparison of acceleration-time plots for baseline, experimental cadaver results and existing FE models of occipital impacts.

Table 6.4: Comparison of Peak Head Acceleration and Impact Duration for Occipital Impact

Study	Age	Experiment/FE Model	Drop Height (m)	Peak Head Acceleration (g)	Impact Duration (ms)	HIC
Prange et al. (2004)	1 Day	Cadaver Experiment	0.30	55.9	18.8	71
Prange et al. (2004)	11 Days	Cadaver Experiment	0.15	32.7	23.5	25
Prange et al. (2004)	11 Days	Cadaver Experiment	0.30	52.9	20.6	75
Loyd (2011)	5 Months	Cadaver Experiment	0.15	43.7	14.4	42
Loyd (2011)	5 Months	Cadaver Experiment	0.30	81.0	12.3	132
Loyd (2011)	9 Months	Cadaver Experiment	0.15	37.6	17.2	31
Loyd (2011)	9 Months	Cadaver Experiment	0.30	71.6	14.2	115
Li, Sandler, and Kleiven (2017)	5 Months	FE Model	0.30	78*	12*	
Burgos-Flórez and Garzón-Alvarado (2020)	4 Weeks	FE Model	0.30	79*	8+*	
Khalid et al. (2019)	10 Days	FE Model	0.30	101	8*	
Present Study	3 Months	FE Model	0.15	56.1	10.2	93
Present Study	3 Months	FE Model	0.30	83.8	9.9	221

*Data inferred from plots presented in respective studies; no specific data provided

Figure 6.8 presents a comparison of the acceleration-time curves for the baseline model that uses bonded contact at the brain-skull interface, and for the case where frictional contact is used. For the frictional contact, the peak head acceleration decreases to 76.0 g and the impact duration increases to 10.9 ms.

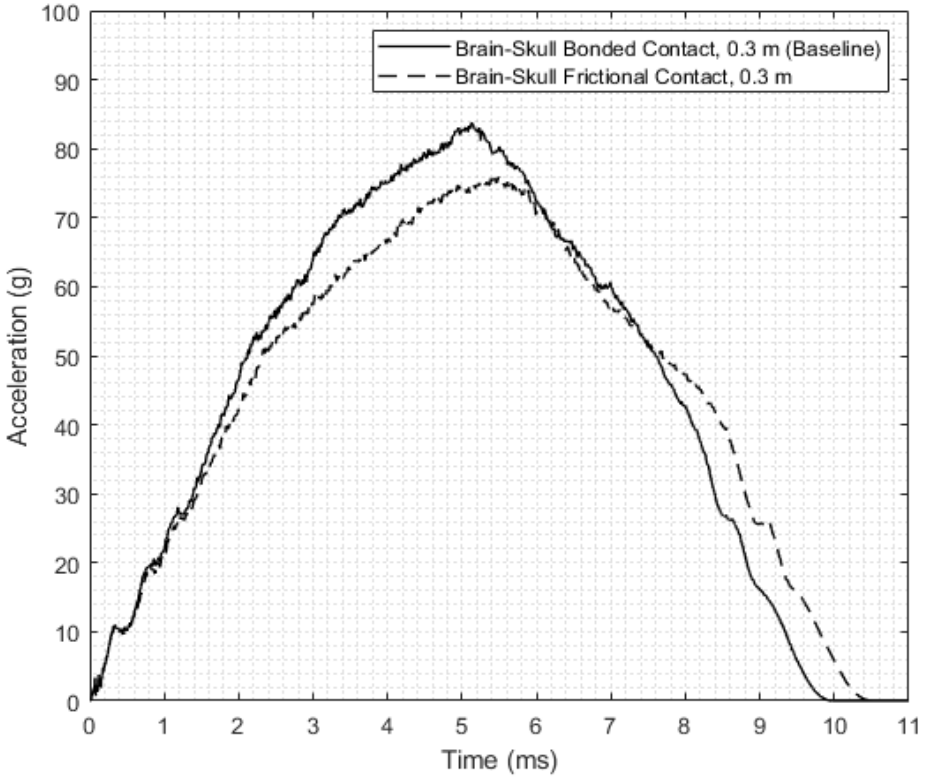

Figure 6.8: Comparison of bonded contact and frictional contact at brain-skull interface.

Drop Height

The peak acceleration ranges from 36.1 g at a drop height of 0.05 m up to 314.9 g at 1.8 m, while the impact duration and HIC_{max} range from 10.5 to 7.4 ms and 23 to 3400 respectively. Table 6.5 presents the peak acceleration, duration and HIC_{max} data for all drop heights. All three parameters can be fitted with a power law for the relationship with drop height, as shown in Figure 6.9. In Figure 6.9 (b) for the impact duration, the data for drop heights of 0.05 to 0.15 m do not quite fit the power law trend. A separate power law was fitted over the 0.3 to 1.8 m drop height data range. This provided a better coefficient of determination value (R^2 of 0.8928 versus 0.9981 for the inclusion and exclusion of the outlier data respectively).

Figure 6.10 presents the acceleration-time curves for each drop height. There is a clear shift of the peak up and to the left as the drop height increases, corresponding with the increase and decrease of the peak acceleration and duration respectively. A secondary peak is prominent in the drop heights of 1.5, 1.6 and 1.8 m. This secondary peak occurs at the time that the depression formed in the head rebounds to its original convex shape.

Figure 6.11 presents the acceleration-time plots for selected drop heights that were modelled using a frictional contact at the brain-skull interface. A similar trend as for the bonded contact in Figure 6.10 is observed, with the magnitudes of the peak acceleration and duration being smaller and longer respectively.

Table 6.5: Data for Drop Heights

Drop Height (m)	Peak Head Acceleration (g)	Impact Duration (ms)	HIC_{max}
0.05	36.1	10.5	23
0.10	46.6	10.3	57
0.15	56.1	10.2	93
0.30	83.8	9.9	221
0.40	107.6	9.5	347
0.50	128.1	9.1	487
0.60	145.4	8.8	647
0.70	161.5	8.5	814
0.80	177.6	8.3	1007
0.90	191.3	8.2	1208
1.00	205.7	8.0	1421
1.20	235.1	7.8	1868
1.50	273.5	7.5	2603
1.60	287.6	7.4	2869
1.80	314.9	7.3	3400

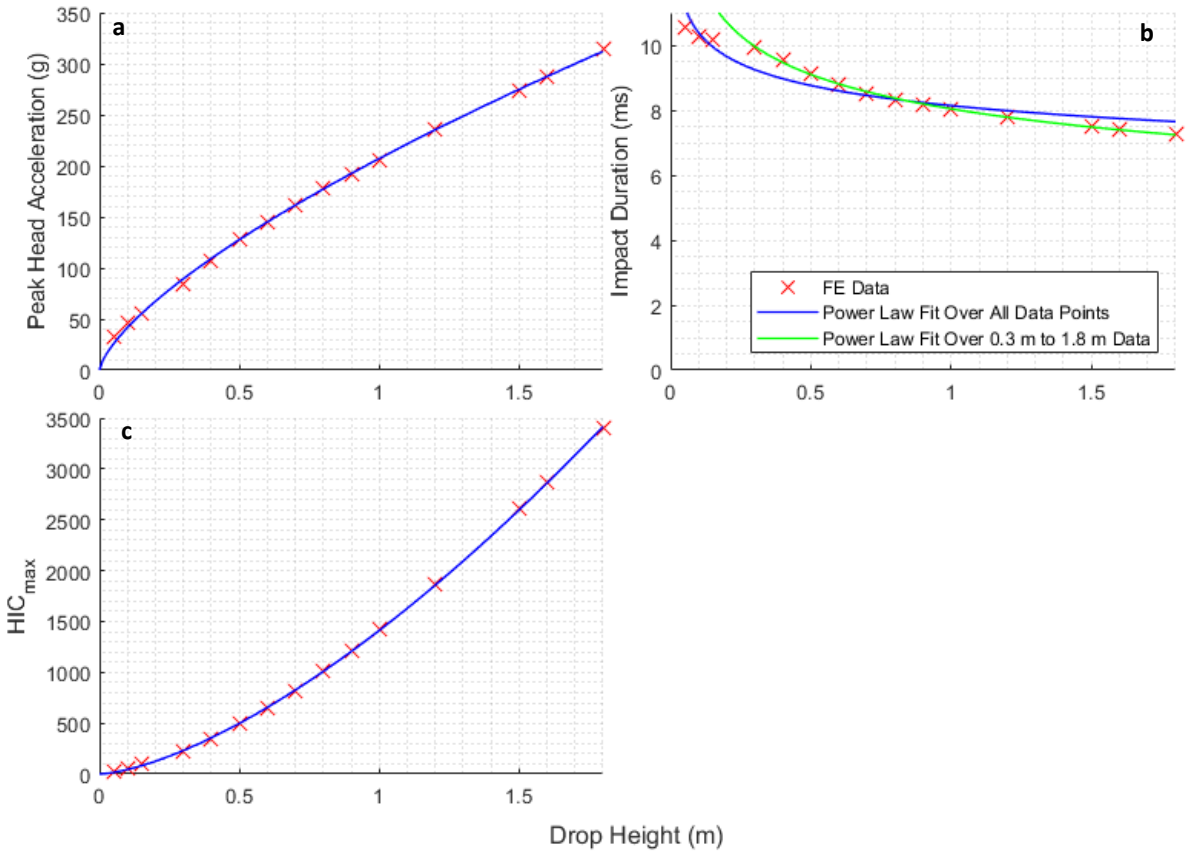

Figure 6.9: Peak head acceleration (**a**), impact duration (**b**) and HIC_{max} (**c**) plotted against drop height. Solid blue line represents power law fit (R^2 is 0.9989, 0.8928 and 0.9999 respectively). Solid green line in **(b)** represents power law fit over 0.3 to 1.8 m due to apparent outliers from 0.05 to 0.15 m (R^2 of 0.9981).

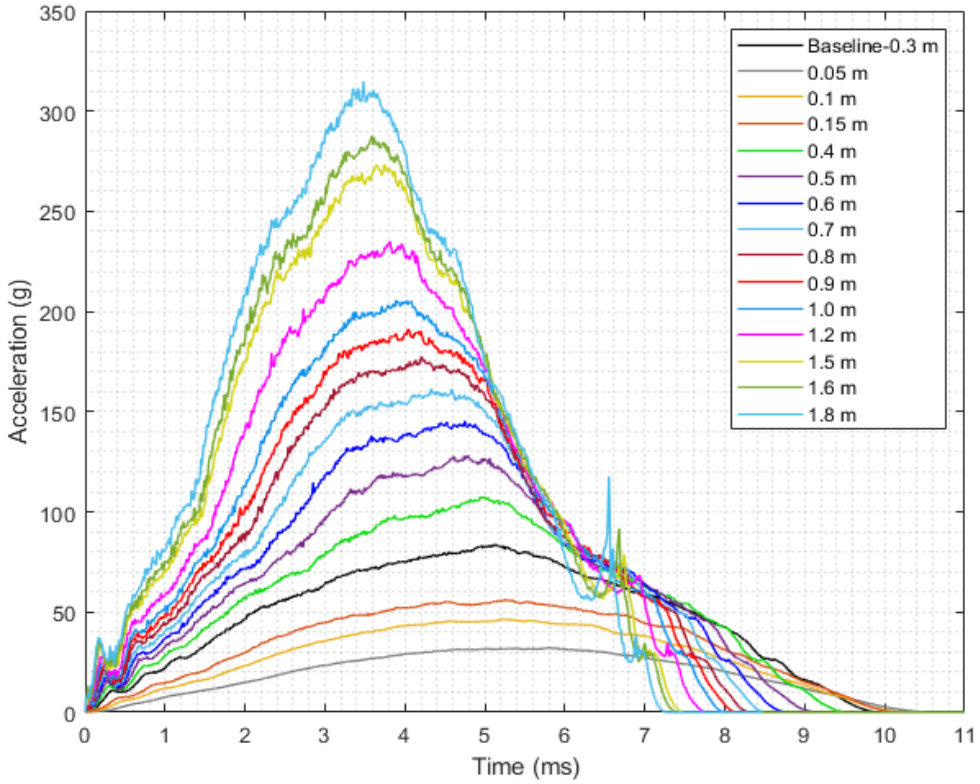

Figure 6.10: Acceleration-time plots for each drop height modelled.

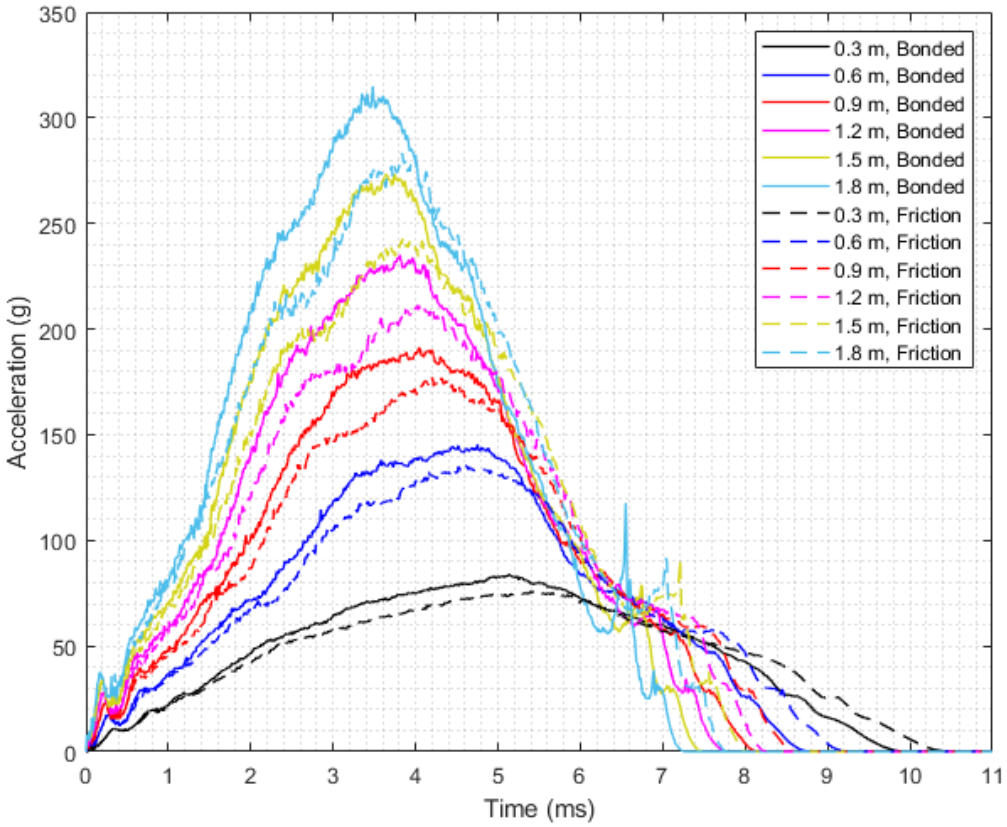

Figure 6.11: Acceleration-time plots for bonded and frictional contact at the brain-skull interface.

Impact Surfaces

Figure 6.12 shows the acceleration-time plots for the occipital impact on each surface, for a drop height of 0.30 m. There is a clear difference between the surfaces that have no top surface layer and those that do. The concrete surface is essentially the same as that of the baseline model (rigid surface), while the wooden surface has only a slightly smaller peak acceleration and slightly longer impact duration.

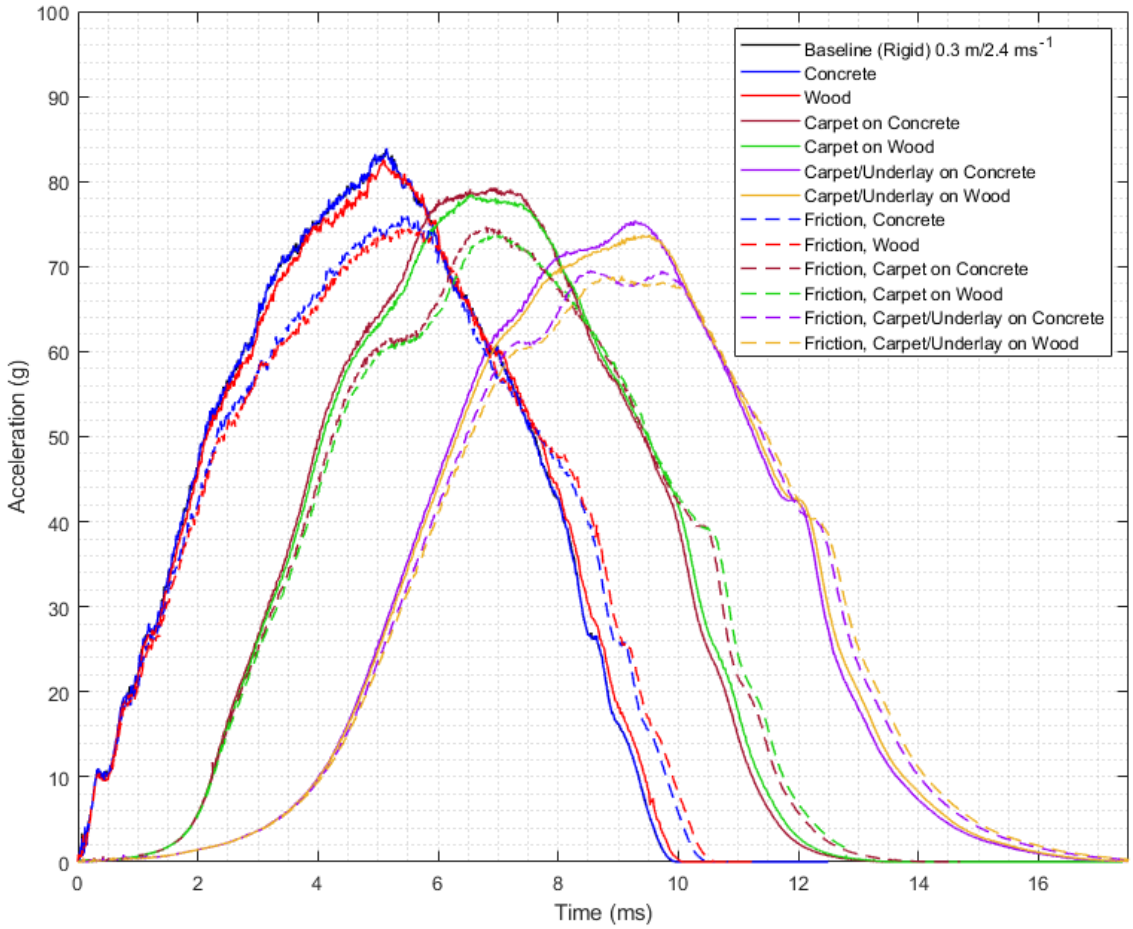

Figure 6.12: Acceleration-time plot for each impact surface for a drop height of 0.3 m. Solid lines represent bonded contact at the brain-skull interface, while broken lines represent frictional contact. Note: the 'concrete' trace overlays that of the baseline, making the baseline somewhat indistinguishable.

For both the concrete and wooden surfaces overlaid with the carpet, with respect to the baseline, the peak acceleration decreases by 5.4% and 6.5% respectively (83.9 g and 82.6 g to 79.3 g and 78.4 g respectively), while for both surfaces overlaid with the combination of carpet and underlay, it decreases by 10% and 12% respectively (to 75.4 g and 73.7 g respectively). The impact duration increases by 33% and 34% for the concrete and wooden surfaces overlaid with the carpet respectively, while the carpet with underlay increases the duration by 74% and 75% respectively. Similar trends are observed for all drop heights investigated, with the percentage differences decreasing as drop height increases. Tables 6.6, 6.7 and 6.8 present all data for the peak acceleration, impact duration and HIC_{max}

for each drop height, while the acceleration-time plots for the remaining drop heights are presented in Appendix C of this thesis. Figures 6.13, 6.14 and 6.15 present the magnitudes for peak acceleration, duration and HIC_{max} respectively.

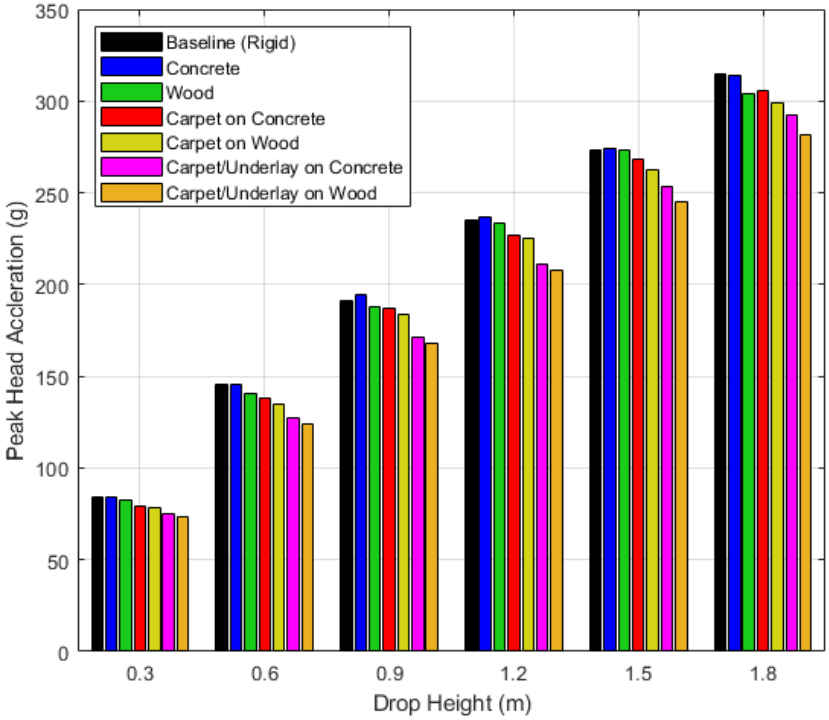

Figure 6.13: Peak head acceleration for each impact surface and drop height.

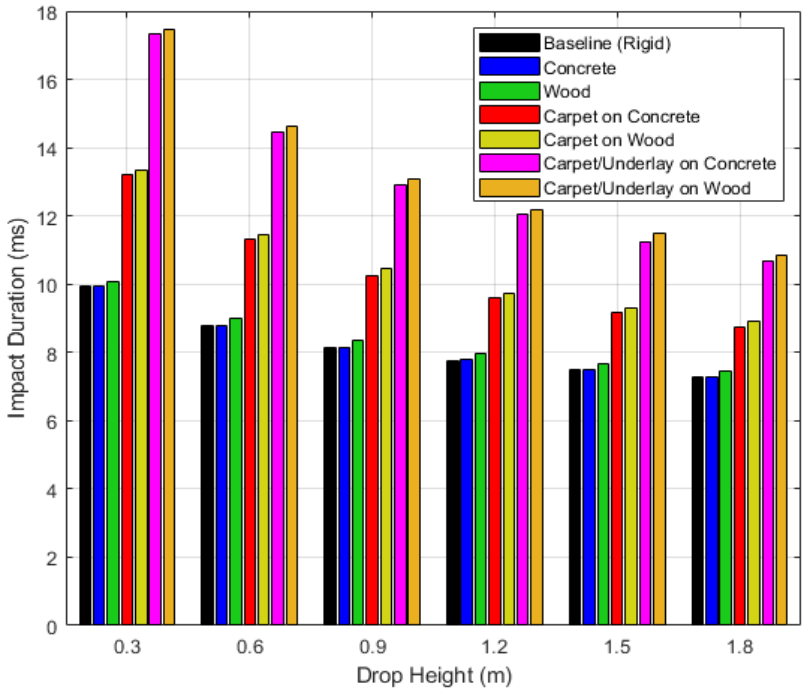

Figure 6.14: Impact duration for each impact surface and drop height.

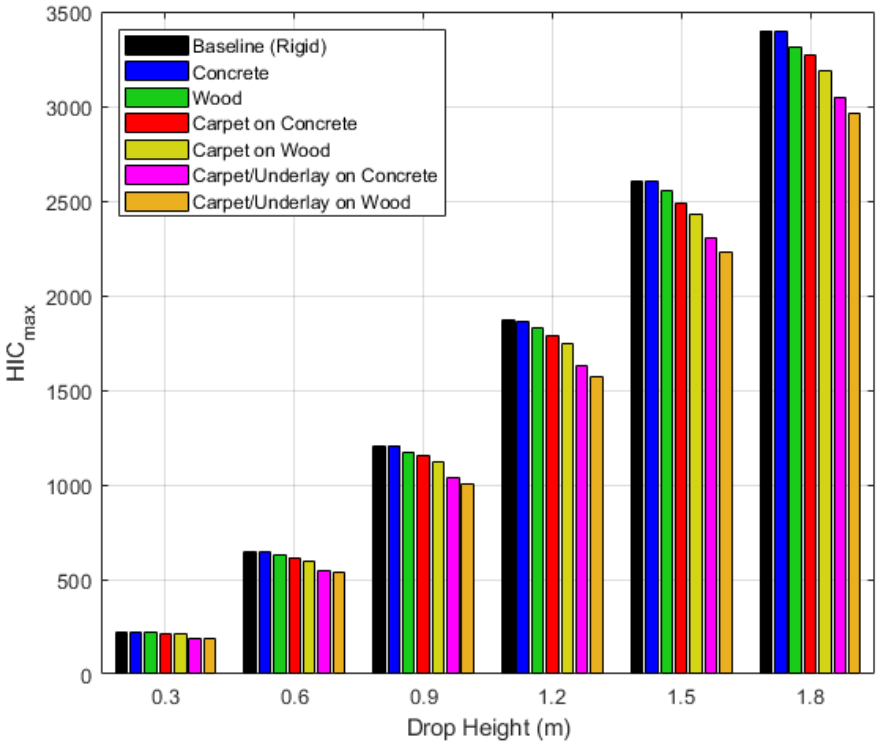

Figure 6.15: HIC_{max} for each impact surface and drop height.

Table 6.6: Peak Acceleration for different Impact Surfaces

Drop Height (m)	Surface												
	Rigid/ Baseline	Concrete		Wood		Carpet on Concrete		Carpet on Wood		Carpet/Underlay on Concrete		Carpet/Underlay on Wood	
	Peak Acc (g)	Peak Acc (g)	Percentage Difference wrt Rigid	Peak Acc (g)	Percentage Difference wrt Rigid	Peak Acc (g)	Percentage Difference wrt Rigid	Peak Acc (g)	Percentage Difference wrt Rigid	Peak Acc (g)	Percentage Difference wrt Rigid	Peak Acc (g)	Percentage Difference wrt Rigid
0.3	83.8	83.9	0.1	82.6	-1.5	79.3	-5.4	78.4	-6.5	75.4	-10.1	73.7	-12.1
0.6	145.4	145.4	0.0	140.6	-3.3	138.3	-4.9	135.0	-7.2	127.1	-12.6	124.1	-14.7
0.9	191.3	194.1	1.5	187.7	-1.9	187.0	-2.2	183.5	-4.1	171.1	-10.6	167.9	-12.2
1.2	235.1	236.4	0.5	233.1	-0.9	227.1	-3.4	225.1	-4.3	211.2	-10.2	207.4	-11.8
1.5	273.5	274.4	0.3	273.2	-0.1	268.5	-1.8	262.6	-4.0	253.6	-7.3	245.0	-10.4
1.8	314.9	313.8	-0.4	304.0	-3.5	305.4	-3.0	298.7	-5.1	292.2	-7.2	281.5	-10.6

Note: wrt=with respect to.

Table 6.7: Impact Duration for different Impact Surfaces

Drop Height (m)	Surface												
	Rigid/ Baseline	Concrete		Wood		Carpet on Concrete		Carpet on Wood		Carpet/Underlay on Concrete		Carpet/Underlay on Wood	
	Duration (ms)	Duration (ms)	Percentage Difference wrt Rigid	Duration (ms)	Percentage Difference wrt Rigid	Duration (ms)	Percentage Difference wrt Rigid	Duration (ms)	Percentage Difference wrt Rigid	Duration (ms)	Percentage Difference wrt Rigid	Duration (ms)	Percentage Difference wrt Rigid
0.3	9.9	9.9	-0.1	10.1	1.2	13.2	33.0	13.4	34.4	17.3	74.3	17.5	75.7
0.6	8.8	8.8	-0.1	9.0	2.2	11.3	28.7	11.5	30.4	14.5	64.6	14.6	66.3
0.9	8.2	8.2	0.0	8.3	2.2	10.3	25.7	10.4	27.9	12.9	58.5	13.1	60.4
1.2	7.8	7.8	0.1	8.0	2.3	9.6	23.6	9.7	25.1	12.0	54.8	12.2	56.8
1.5	7.5	7.5	-0.1	7.7	2.0	9.2	22.5	9.3	24.1	11.3	50.0	11.5	53.2
1.8	7.3	7.3	0.3	7.5	2.8	8.8	20.4	8.9	22.7	10.7	47.0	10.9	49.2

Note: wrt=with respect to.

Table 6.8: HIC Max and Duration

Drop Height (m)	Surface													
	Rigid/ Baseline		Concrete		Wood		Carpet on Concrete		Carpet on Wood		Carpet/Underlay on Concrete		Carpet/Underlay on Wood	
	HIC_{max}	Duration (ms)	HIC_{max}	Duration (ms)	HIC_{max}	Duration (ms)	HIC_{max}	Duration (ms)	HIC_{max}	Duration (ms)	HIC_{max}	Duration (ms)	HIC_{max}	Duration (ms)
0.3	221.2	6.5	221.1	6.4	217.5	6.5	213.2	6.5	209.2	6.5	189.0	6.7	185.6	6.8
0.6	647.1	5.2	647.3	5.1	629.2	5.5	615.5	5.3	596.8	5.5	549.3	5.7	535.7	5.8
0.9	1207.8	4.1	1207.2	4.1	1173.1	4.1	1153.0	4.3	1122.1	4.3	1034.5	4.9	1005.6	5.1
1.2	1867.7	3.9	1866.2	3.9	1829.1	3.9	1786.2	4.1	1744.3	4.0	1627.1	4.3	1573.3	4.5
1.5	2603.4	3.8	2604.6	3.8	2550.5	3.8	2487.6	3.9	2429.1	3.9	2306.4	4.0	2225.4	4.1
1.8	3400.0	3.8	3396.8	3.8	3313.5	3.8	3267.6	3.7	3188.7	3.9	3049.0	3.8	2964.5	3.9

Note: Duration is the Δt that maximises HIC.

Impact on Surface Edge

The impact to the edge of a surface resulted in slightly different behaviour than compared to the baseline model. As shown in Figure 6.16, a depression at the impact site is formed, similar to that of the baseline model. However, the centre of the depression is in the region that is in contact with the impact surface, whereas in the baseline model, it was at the centre of the impact site. The region of the infant head not in contact with surface deforms down past the top of the surface. This causes a slight change in the orientation of the head during the rebound phase, as shown in Figure 6.17 where the wireframe shows the original orientation.

Figure 6.18 shows the acceleration-time plots for the impact to the surface edge compared to the baseline model. An impact to the surface edge results in a lower peak acceleration and longer impact duration compared to the baseline model (80.5 g versus 83.8 g and 12.5 ms versus 9.9 ms respectively). The HIC_{max} is 163 versus 221 for the baseline model.

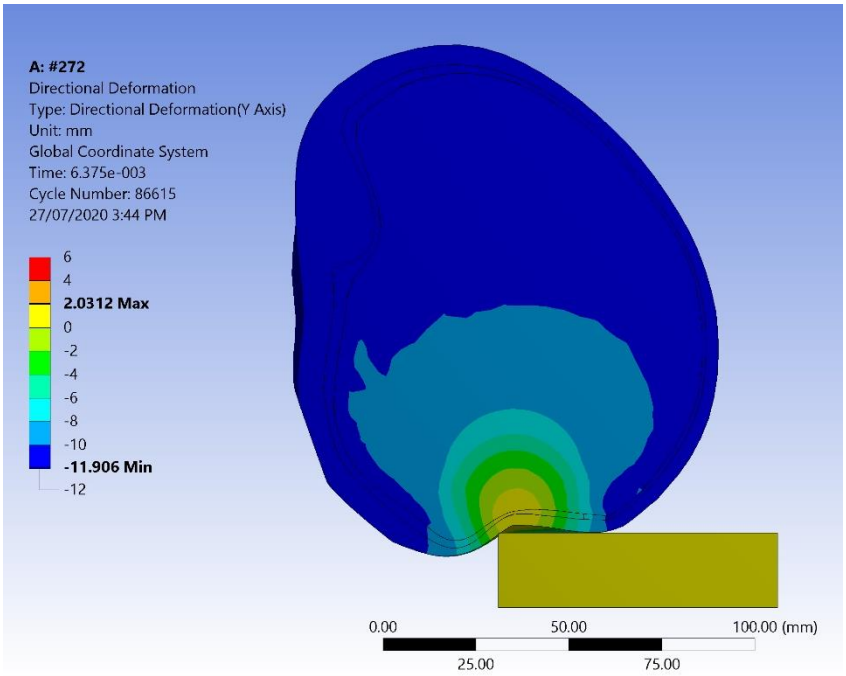

Figure 6.16: Deformation (vertical) of infant head during impact to surface edge.

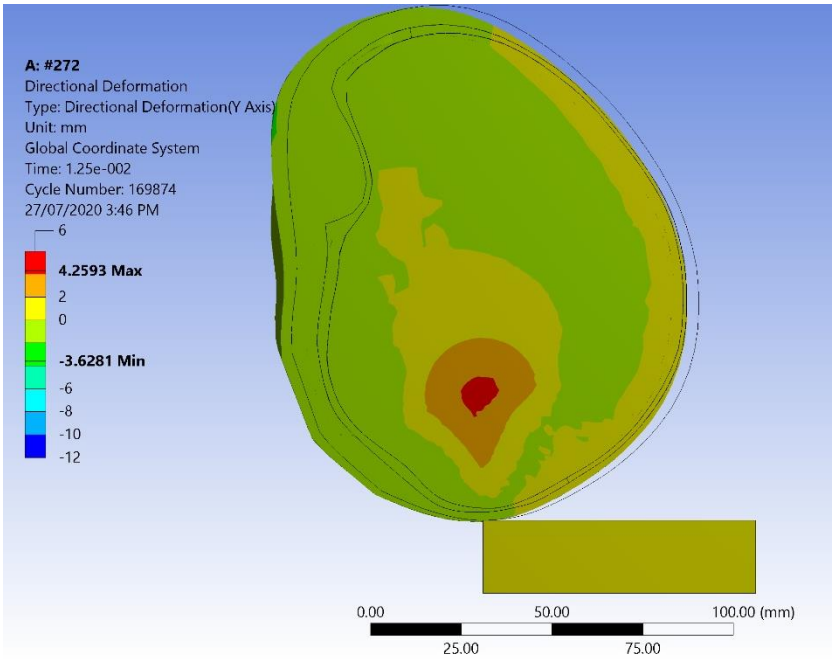

Figure 6.17: Slight change in head orientation as a result of impact to surface edge. Wireframe shows original orientation just before impact occurs.

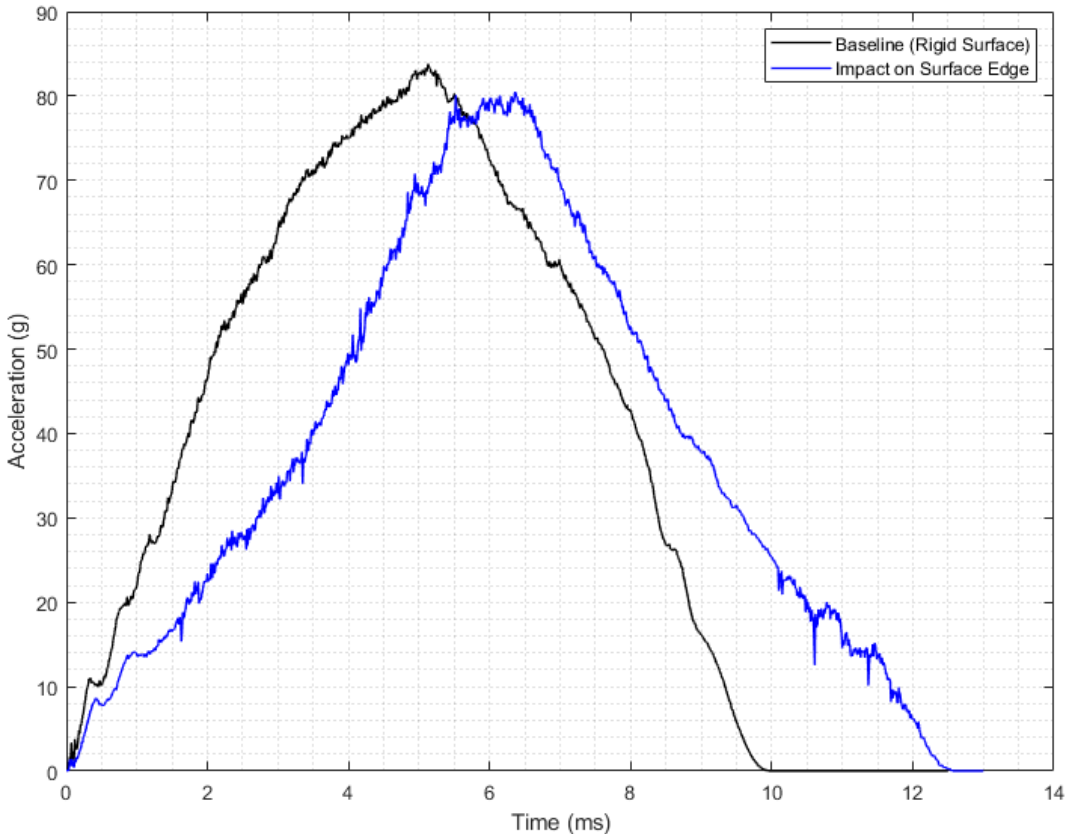

Figure 6.18: Acceleration-time plot for impact with surface edge compared to baseline model.

Discussion

Behaviour of Baseline Model

For an impact against a flat surface, the deformation of the infant head in the present FE model was found to include a depression at the centre of the impact site. Similar behaviour was described by Roth, Raul, and Willinger (2010) when they used their model to reconstruct a well-witnessed real-world case. Such behaviour is often described as the 'ping-pong' affect due to its similarity with a depression created by forcibly impacting a ping-pong ball with a flat surface. It is common in infants who have experienced an impact to the head, as well as being well documented in cases of childbirth (Gurdjian, Webster, and Lissner 1950, Braakman 1972, Oh 1983, Ersahin et al. 1996, Dupuis et al. 2005).

Physical reasoning for the creation of this depression can be thought of in terms of a two-dimensional deformable circle (the infant head) impacting a fixed line (the flat surface). Initially, the natural curvature of the circle at the impact site is convex. As deformation begins, the reaction force created by the impact surface causes the circle to flatten out and conform to the shape of the line. Internal forces are induced within the circle in the circumferential direction due to the deformation. These internal forces are compressive, resulting in slight bulging at the outer extremes of the contact patch. As deformation progresses, if the material of the circle is flexible enough, the compressive internal circumferential forces and momentum of the radial motion causes the flattened shape to turn concave inwards, creating a depression. That is, the curvature of the circle in the contact region becomes concave. Therefore, the depression observed in the behaviour of the baseline model is not unexpected. In adults, the skull is much thicker and stiffer, so fracture is likely to occur before such a depression would form.

Baseline Model Validation

Very little data is available for whole infant head experimental cadaver drop tests. Only Prange et al. (2004) and Loyd (2011) have conducted such experiments and presented acceleration-time data that can be used to validate infant head FE models. Acceleration-time data is often used to validate the global stiffness of such models (Li, Zhang, and Hu 2013, Li, Sandler, and Kleiven 2017, Khalid et al. 2019, Burgos-Flórez and Garzón-Alvarado 2020). No experimental data exists for a three-month-old infant, so no direct comparison of the baseline model can be made. An ideal FE model would have an acceleration-time plot that lies between the one and 11-day old data of Prange et al. (2004) and the five and nine-month-old data of Loyd (2011), given that the infant head becomes stiffer with age (Prange et al. 2004, Coats and Margulies 2006, Loyd 2011). Although it is well concluded in the literature that the stiffness of the infant head increases with age in general, some discrepancy does

exist in the data. This is apparent in that the peak acceleration and impact duration for the 11-day-old infant head is lower and longer respectively than the one-day-old infant head in Prange et al. (2004) (52.9 g and 20.6 ms versus 55.9 g and 18.8 ms respectively for the 0.30 m drop height). A similar observation for the five and nine-month-old data of Loyd (2011) can also be made (81.0 g and 12.3 ms versus 71.6 g and 14.2 ms respectively for the 0.30 m drop height). Given the inherent variability in biological systems, it is not unreasonable for such discrepancies to exist.

The baseline model has a peak acceleration that is comparable to the five-month-old experimental data of Loyd (2011) for the 0.30 m drop height (83.8 g versus 81.0 g respectively), while the impact duration is around 20% shorter (9.9 ms versus 12.3 ms respectively). For the 0.15 m drop height, the peak acceleration and impact duration of the baseline model is 28% greater and 29% shorter respectively than the five-month-old experimental data. In general, the baseline model is stiffer than experimental cadaver data of a similar age and does not fit within the 'ideal' range. However, the relatively favourable comparisons against the experimental data provides confidence that the model overall stiffness is realistic. In regard to HIC, the present model predicts higher HIC_{max} values than the experimental values provided by Loyd (2011) (93 versus 31 and 221 versus 115 for drop heights of 0.15 and 0.30 m respectively. While not specifically stated in Loyd (2011), it is assumed that the HIC data provided is that of HIC_{max} as the time duration over which HIC is calculated was indicated on the acceleration-time plots.

Compared to existing FE models, the baseline model has a comparable peak head acceleration to the five-month-old model of Li, Sandler, and Kleiven (2017) (83.8 g versus 78 g for a 0.30 m drop height), while the impact duration is around 17% shorter (9.9 ms versus 12 ms respectively). These differences between the five-month-old model and the baseline model indicate the baseline model is slightly stiffer. The peak acceleration for the four-week-old FE model of Burgos-Flórez and Garzón-Alvarado (2020) was 79 g, also comparable to the baseline model. For the 10-day-old FE model of Khalid et al. (2019), the peak acceleration was 101 g, which is 17% greater than the baseline model. As with the experimental data, the baseline model is comparable to existing FE models, given the differences between each model.

Li, Sandler, and Kleiven (2017) report an impact surface area of 1900 mm^2 for their five-month-old FE model experiencing an occipital impact. The baseline model of this study had an impact surface area of 1809 mm^2. Impact surface area is related to the degree of deformation (more deformation will generally result in a greater impact surface area), which is related to factors such as the global head stiffness and skull geometry. However, the 4.7% difference in the surface area to an FE model of a similar age provides additional confidence that the baseline model is behaving in a realistic manner.

Loyd (2011) does not provide surface area data for the five-month-old occipital impact, so no comparison to experimental data can be made. However, the surface area data for Li, Sandler, and Kleiven (2017)'s FE model are similar to Loyd (2011)'s reported surface area data for other ages and impact locations (Table 3 of Li, Sandler, and Kleiven (2017)). Therefore, their surface area data is likely to be in the general vicinity of the real impact surface area for a five-month-old infant occipital impact.

Modelling decisions and simplifying assumptions used in the baseline model are the likely contributors to the greater global stiffness. The use of an isotropic elastic material model for the cranial bones and the contact condition between the skull and brain were modelling decisions that had to be made due to limitations with the ANSYS Explicit software. Element type and the geometry used are simplifying assumptions that were made to reduce the total computational time in order to conduct the numerous simulations required for the drop height and impact surface parametric studies.

As with the FE model used in the sensitivity analysis in Chapter 4 (repeated here for importance), the decision to use tetrahedral elements was made in order to increase the minimum characteristic element length and hence increase the size of the timestep used in the explicit solver. The minimum characteristic length in the mesh contributes to the size of the timestep used in an explicit solver. The smaller the minimum characteristic length, the smaller the timestep and hence an increase in computations. Although hexahedral elements are generally preferred, the use of tetrahedral over hexahedral elements resulted in an increase in the timestep by two orders of magnitude. Generally, fewer hexahedral elements are needed for an accurate solution, but the cost savings associated with the time step size favour the tetrahedral elements in this case.

The discussion in Chapter 4 regarding the comparison of the FE model by Burgos-Flórez and Garzón-Alvarado (2020) and the baseline model also applies here, given the baseline model in the present chapter is similar to that in Chapter 4. This also applies to the discussion around the simplifying geometry and inability of ANSYS Explicit to use an anisotropic material model defined in local coordinates.

Contact boundary conditions between each head tissue are very rarely discussed in the existing literature of infant head FE models. It can be reasonably assumed that contact between tissues such as the scalp and skull are tied or bonded, where the nodes of each tissue cannot separate or slip relative to one another, as that represents a realistic condition between such tissues unless material failure occurs. Where the CSF has not been modelled, it is common to use sliding or frictional contact between the brain and inner surface of the skull (Coats, Margulies, and Ji 2007, Khalid et al. 2019). A sliding contact allows the two surfaces to slide relative to one another, but not separate, whereas separation of the surfaces can occur for frictional contact. Both require a friction coefficient to

determine when sliding is initiated. Khalid et al. (2019) use sliding contact at the brain-skull interface, but do not specify a friction coefficient, while Coats, Margulies, and Ji (2007) use frictional contact with a coefficient of 0.2. The baseline model uses bonded contact between the brain and inner skull surface. This has the effect of over-stiffening the model in that the brain surface cannot move relative to the skull. A sliding contact is not supported in ANSYS Explicit and therefore was not used in the baseline model. Sliding contact is deemed to be more representative of the interface between the brain and skull if the CSF is not modelled. This is because if the brain moves within the skull cavity, CSF is redistributed around the brain due to pressure gradients. In the absence of CSF (as with the baseline model), a void would be created. Hence bonded contact is deemed to be at one extreme, while frictional contact, where separation of the brain-skull interface can occur, is at the other. Therefore, as a comparison, the contact between the skull and brain was changed to frictional (coefficient of 0.2 as used by Coats, Margulies, and Ji (2007)). This resulted in the peak acceleration and impact duration increasing and decreasing respectively by approximately 9%. Therefore, the frictional contact results in a decrease in the effective global stiffness by 9%. If a sliding contact was used, the stiffness of the model can be expected to lie between these two extremities for a given coefficient of friction.

Another reason for the discrepancy between the baseline model and the cadaver experiments is the impact angle. Li, Sandler, and Kleiven (2017) found that impact angle has a profound influence on the acceleration-time curve characteristics and peak head acceleration for a parietal impact, however, the influence was not as profound for an occipital impact. In the baseline model, the head was rotated so that the impact location was on the line of action of the centre of mass. This was to minimise the amount of rotation during the impact. Li, Sandler, and Kleiven (2017) suggest that for an occipital impact, the impact angle has minimal influence but recommend that further investigation should be undertaken. The effect of impact angle on the baseline model is presented later in Chapter 8.

The simplifying assumptions used for the baseline model were to reduce the computational cost of each simulation. While fewer simulations were required than the sensitivity analysis in Chapter 4, the duration simulated was much greater (12.5 ms or greater compared to 2.5 ms). Li, Sandler, and Kleiven (2017)'s infant head FE model is the best validated model to date and consisted of over three million elements (for their five-month-old head). If a solution within a day is required, the model would have to be solved using a high-performance computer that has a significant number of central processing unit cores (for a total simulated time of up to 14 ms). Using such a computer would have a high financial cost. A FE model of this size would take many days or weeks to solve on the fastest consumer or professional grade computers available at the time of writing. To make forensic case work feasible, models would have to be solved on such computers, hence the use of simplifying assumptions that do not lead to errors that would result in unusable results.

Drop Height

Experimental cadaver tests have largely consisted of dropping infant cadaver heads from low heights of 0.15 and 0.30 m (Prange et al. 2004, Loyd 2011). For Prange et al. (2004), this was due to the cadaver heads being used in another study and therefore damage had to be avoided. Loyd (2011) carried out drops from 2 m to investigate fracture characteristics, while Weber (1984) conducted drops from around 0.8 m to investigate skull fracture. No experimental cadaver studies have looked at a larger range of drop heights. This is most likely due to the scarcity of human infant cadaver heads. In place of using cadaver heads, anthropomorphic infant surrogates can be used to investigate falls from a range of heights as the cadaver scarcity problem is eliminated. This requires well validated surrogates. Coats and Margulies (2008) developed an anthropomorphic infant surrogate and used it to measure the angular accelerations and forces associated with falls from 0.30, 0.60 and 0.90 m.

Of the existing infant head FE models, only Li, Luo, and Zhang (2013) have used their FE model to model the response of the infant head at a range of drop heights. They used drop heights up to 1.2 m onto five different impact surfaces for an occipital impact. While not explicitly stated, the findings of Li, Luo, and Zhang (2013) for peak acceleration and HIC_{15} versus drop height can be represented by a power law if their data is extrapolated to intercept at the origin.

Compared to the findings of Li, Luo, and Zhang (2013), the present study had peak accelerations that were comparable at a height of 0.30 m (83.8 g versus approximately 80 g for the present study and Li, Luo, and Zhang (2013) respectively), and differed by up to 24% at a height of 1.20 m (235 g versus approximately 190 g respectively). In the present study, peak acceleration was found to have a strong power law correlation with drop height (power of 0.69 and R^2 of 0.9989). A power law fit is suitable for the data presented here as at a drop height of zero metres, the peak acceleration would be zero as no impact occurs (this is same for the impact duration and HIC_{max} data). Applying this logic to the data of Li, Luo, and Zhang (2013), then their peak acceleration data follows a similar power law trend, supporting the findings of the present study.

The HIC data presented by Li, Luo, and Zhang (2013) is for an impact duration of 15 ms. In the present data, the impact duration that gave the maximum HIC value was used as the total impact durations were considerably less than 15 ms (longest duration was 10.5 ms for the 0.05 m drop height). Therefore, the HIC_{max} data presented here has greater magnitudes than Li, Luo, and Zhang (2013) and so no direct comparisons can be made. The data presented here was found to have a very strong power law correlation with drop height (power of 1.50 and R^2 of 0.9999), while the HIC_{15} data of Li, Luo, and Zhang (2013) follows a similar trend. Therefore, both studies support a finding of HIC having a power law relationship with drop height.

It is common for HIC data to be used in assessing motor vehicle impact safety. A HIC_{36} (HIC value over a time duration of 36 ms) of 1000 is used by the Federal Motor Vehicle Safety Standard (FMVSS) to represent an upper limit at which adult occupants can experience during a motor vehicle collision. This represents a 52% chance of adults sustaining severe injury (FMVSS 201). For children, a value of 840 is recommended as an equivalent measure (Snyder et al. 1977), while for infants, this is a value of 390 (Klinich, Hulbert, and Schneider 2002). As these values are for HIC_{36}, no direct comparison with the HIC_{max} data from the present study can be made with regard to the HIC values exceeding those used as a measure of severe head injury. Overall, there is no suitable data in which to check the HIC_{max} data is valid across a range of drop heights. Validation of such data would require dropping infant cadaver heads or anthropomorphic infant surrogate heads from various heights and recording the acceleration to measure the HIC. Using the above HIC threshold values, a critical height can be obtained (for a particular impact surface) at which above it would be expected that severe head injuries would occur. This method was used by Shields and Smith (2009) to determine critical heights for common surfaces used by cheerleaders, providing a height at which stunts should not be performed above to avoid head injuries if a fall was to occur. If the HIC data from a FE model can be validated, then the FE model could be used to determine such a height in the context of an infant fall.

Li, Luo, and Zhang (2013) do not present data for impact duration, so no comparison can be made. In the present study, impact duration was found to correlate with drop height using a power law, although the fit is not as strong as that for peak acceleration and HIC_{max} (power of -0.17 and R^2 of 0.8928 for duration).

As the drop height increased, there was a flattening or slight increase in the acceleration-time curve near the end of the impact. At heights of 1.5, 1.6 and 1.8 m, there is a distinct increase in acceleration, with a second peak occurring. The acceleration is calculated using the external reaction force between the impact surface and the head as a whole (essentially the acceleration at the centre of mass of the head). Therefore, for a second peak to occur, and in the absence of any other external forces, the only cause of the secondary peak can be from additional impact of the head with the impact surface. This additional impact is a result of the depression that forms earlier in the impact rebounding to its original convex shape. When the velocity of the head is zero, the depression is at its greatest. As the head starts to rebound, the depression also rebounds, and the tissue contacts the impact surface once again. As the drop height decreased, the secondary peaks or flattening of the acceleration-time curve occurred later in the impact time sequence, corresponding with the increase in impact.

As with the validation of the baseline model, a series of drop heights were modelled with frictional contact at the skull-brain interface. Trends similar to that of using bonded contact were observed,

with the magnitudes of the peak acceleration and impact duration being smaller and longer respectively.

The biggest limitation with the drop height analysis presented here is that it does not consider skull fracture or other tissue damage. Therefore, the results here should only be used to support trends for where skull fracture does not occur, mainly in falls below a height of 1.0 m where it is less likely that skull fracture will occur (Johnson et al. 2005). Skull fracture prediction is investigated in Chapter 7 of this thesis.

Impact Surfaces

Physical testing and statistical analysis of the various surfaces children and infants are exposed to has largely been focused around playground surfaces (Lewis et al. 1993, Chalmers et al. 1996, Laforest et al. 2001). Weber (1984) conducted experimental cadaver drop tests of infant heads onto a variety of surfaces, including stone tiles, carpeted floor, foam backed linoleum, foam mat 20 mm thick, and a folded camel hair blanket 80 mm thick. However, only fracture patterns were reported, no quantitative data was provided. Li, Zhang, and Hu (2013) conducted drop tests onto similar surfaces as Weber (1984), using a three-year-old child dummy test head. Aside from Weber (1984), no other experimental testing of infant cadaver heads onto surfaces with varying degrees of stiffness have been conducted. Coats and Margulies (2008) used their anthropomorphic infant surrogate to conduct drop testing onto concrete, carpet of 6 mm in thickness, and a 150 mm thick mattress. The same surrogate was used by Hajiaghamemar et al. (2018) to reconstruct well-witnessed infant head impacts to help establish skull fracture thresholds. Cory and Jones (2006) developed a simulation system to conduct impact testing of flooring surfaces in situ to be able to establish the surface stiffness at a scene where a child has allegedly suffered head injuries from a fall.

Like the physical testing, little research has been conducted using FE models to model the response of the infant head on different surfaces. In conjunction with their investigation of drop heights, Li, Luo, and Zhang (2013) modelled the head response onto surfaces of concrete, wood fibre board, soft foam, hard foam and rigid foam. They chose surface thicknesses so that the head would not bottom out during the impact (no specific thicknesses were provided). This means that there is no effect of the underlying surface on the response parameters. Li, Luo, and Zhang (2013) found that there was little difference in the peak acceleration and HIC_{15} for the concrete and wood fibre board surfaces, for all drop heights. The soft foam surface resulted in the lowest peak accelerations and HIC_{15} as would be expected, with the hard and rigid foams in between the soft foam and concrete surfaces.

The thicknesses used by Li, Luo, and Zhang (2013) for their surfaces do not represent an actual floor surface that an infant is likely to fall on in domestic houses. It is common for domestic floors to have

either a concrete foundation or wooden flooring that is supported by joists. A top surface layer consisting of carpet or a combination of carpet with underlay is commonly laid over top of the main flooring structure. The thickness of the carpet and underlay can vary significantly depending on the characteristics a homeowner wants. Typical carpet thicknesses range from five to 15 mm. In the present study, thicknesses of 7 mm and 8 mm were used for the carpet and underlay respectively (giving a combined thickness of 15 mm for the combination of carpet and underlay). These different flooring combinations are more representative of an actual floor than the surfaces used by Li, Luo, and Zhang (2013).

The concrete and wooden surfaces were found in the present study to produce a similar response to an infinitely rigid surface for an occipital impact. This is supported by the findings of Li, Luo, and Zhang (2013) where there was little difference in the response parameters for concrete and wood fibre boards. Li, Luo, and Zhang (2013) used an elastic modulus of 30 GPa and 3 GPa for the concrete and wooden surface material models respectively. In the present study, a polynomial equation of state material model was used for the concrete surface, so no direct comparison can be made in terms of the relative stiffness between the two studies. For the wooden surface, an elastic modulus of 9.3 GPa was used in the present study, which is at least three times greater than that used by Li, Luo, and Zhang (2013). The little difference in results found in the present study and by Li, Luo, and Zhang (2013) for the concrete and wooden surfaces indicates that any discrepancy in the elastic modulus is not of high importance as they are an order of magnitude bigger than that of the elastic modulus of the skull. Therefore, the stiffness of the flooring surface relative to that of the infant head is the dominant factor.

When carpet was added to both the concrete and wooden surfaces, the peak acceleration decreased by 3-6% across both flooring types and height ranges, with respect to the rigid surface, while the impact duration increased by 20-34%. For the carpet-underlay combination, the peak acceleration decreased by 7-14%, and the impact duration increased by 47-75%. Although direct comparisons cannot be made with the peak acceleration data of Li, Luo, and Zhang (2013) due to the different surface combinations and thicknesses, visual inspection of Figure 10 (a) of Li, Luo, and Zhang (2013) clearly shows that the peak acceleration varies by more than 14% between the soft foam and concrete. This suggests that the thickness of the softer surfaces and the underlying floor structure influence the peak acceleration as would be expected.

The percentage differences in the peak accelerations between the various surface combinations are far less than those for the impact durations. This indicates that the carpet and carpet-underlay combinations have little effect on the peak acceleration the infant head experiences but do

significantly affect the duration. This is shown in the acceleration-time curves, where there is a distinct difference in the shape of the 'tails' of the curves compared to the bare concrete/wooden surfaces. For example, for the 0.30 m drop height, an acceleration of 10 g is reached in less than 0.5 ms, while for a top surface of carpet, it takes around 2.25 ms, and 4 ms for the carpet-underlay combination. This shows that the carpet and carpet-underlay affect the early response of the head. At about 10 g, the acceleration of all three combinations increase at a constant rate until around 60 *g*, where it starts to taper off until reaching peak acceleration.

The finding that there is very little difference in peak acceleration for the different surface types is supported by the findings of Coats and Margulies (2008), who noted that there was very little difference in the peak angular acceleration for drop heights of 0.6 and 0.9 m onto concrete and carpet overlaid on concrete. They hypothesised that full compression of the carpet occurred and therefore the response was dominated by the greater stiffness of the concrete.

The relatively low stiffness of the infant head means that it is highly deformable. Therefore, as it deforms during an impact, the contact area becomes relatively large. A larger contact area increases the effective impact stiffness of the underlying surface. For a given mass and impact velocity, the area under the force-time curve for an impact is the same regardless of the underlying surface stiffness. The effect of the carpet on the tails of the curve adds little area to the curve. Once the contact area spreads to where a high effective stiffness is achieved, the response becomes similar to that without carpet to achieve the same area under the curve. This means that the peak force, and hence peak acceleration, for an impact onto carpet is nearly as high as that without carpet. The relatively less stiff carpet will also deform, increasing the contact area and hence the force is distributed over a greater area, bringing the effective stiffness up to near what it is without a layer of carpet. This means that the magnitude of the force acting at a finite point on the head is less, resulting in lower stresses and strains that would cause tissue failure (injury). This explains the little difference in the peak acceleration between the different impact surfaces. To significantly alter the physics of the impact, a much thicker layer of carpet will be required. The infant head is quite soft, so it requires a thick soft layer to significantly alter the global physics of the impact. Coats and Margulies (2008) found that a 150 mm thick innerspring crib mattress did not affect the peak acceleration across a range of drop heights (impact velocities); that is, greater impact velocities onto the mattress did not affect the peak acceleration. This was said to be due to the compliant nature of the mattress overwhelming any influence of drop height.

Only six combinations of flooring surface were investigated in this study. Given the multitude of carpet, underlay and base flooring surfaces commonly found in domestic households, more work is

required to build a data set that would cover a greater number of combinations. Future work could also look at what the thickness of carpet would be required to alter the physics of the impact to reduce the peak acceleration.

In forensics, it is important for a pathologist or other investigator to be able to say whether a given surface mitigated a fall, when comparing to other falls in their experience. While carpet and underlay may increase the duration by reducing the acceleration of the head during the compression and rebound phases of the carpet, the peak acceleration will largely be dependent on the stiffness of the infant head, unless the surface was of sufficient thickness to significantly alter the physics of the impact. Knowing the effect of thickness would allow investigators to make more informed decision on the likelihood of a particular surface mitigating the effects of a fall.

Impact on Surface Edge

To the best of the author's knowledge, no previous study has investigated the effects of an infant head impact to a surface or object other than that of a flat surface. The reconstructed real-world cases performed by Hajiaghamemar et al. (2018), and Li, Sandler, and Kleiven (2019) were all cases involving an impact to a flooring surface or the ground. In a domestic household setting, it is possible that an infant could experience a head impact with the edge of a piece of furniture by, for example, falling from the arms of a caregiver.

The occipital impact to a surface edge presented in this study makes a first step at determining any differences compared to an impact to a flat surface, using a FE model. It was found that the deformation of the head started to 'wrap' around the surface edge, with a similar depression as that occurring in the baseline model forming at the impact site. Peak acceleration was comparable with the baseline model, but the impact duration was 26% longer. The edge of the surface was located at the point the head geometry is tangential to the surface. Therefore, rather than deforming onto a flat surface, the region not impacting the surface was able to move below the top of the impact surface. This caused the slight change in head orientation that is observed during the rebound.

Neither the present model or the baseline model presented in this thesis include the inertial effects of the torso, legs and arms. There are an infinite number of possibilities in terms of relative body orientation and motion that will have an effect on the impact velocity of the head when it strikes any surface type. Including the inertial effects of the body into the FE model is an important factor required for future work. No detailed whole-body FE models of the infant exist, although highly simplified FE models, often scaled from adults or child FE models, are used in automotive crash and infant restraint models, such as Bondy et al. (2014), Tushak, Maheshwari, and Belwadi (2019). Therefore, significant work is required to develop a detailed whole-body infant FE model. Simplifications could be included

for the rest of the body if local injuries to these areas are not of interest, as only the inertial effects would be required to induce realistic motion of the head. However, a detailed model of the neck would be required in order to accurately model the inertial effects on the head motion. Experimental work with an infant surrogate, such as that developed by Coats and Margulies (2008) could be of use to validate the global response of the head motion for an impact.

Conclusions

This study investigated the effect of drop height and different impact surface materials on the peak head acceleration, impact duration and HIC_{max} for an infant occipital impact. An impact on a rigid surface edge was also investigated. Due to the large number of simulations required, the same baseline FE model as that in Chapter 4 was used.

As would be expected, the peak head acceleration increased with increasing drop height, while the impact duration decreased and HIC_{max} increased. It was found that all three parameters of interest formed a power law relationship with drop height. Peak acceleration had a power of 0.69 and R^2 of 0.9989; HIC_{max} had a power of 1.50 and R^2 of 0.9999; and impact duration had a power of -0.17 and R^2 of 0.8928. Tissue failure was not modelled, therefore the results, especially those of drop heights greater than one metre, should only be used for cases where tissue failure (such as skull fracture) does not occur.

Impact surfaces consisting of carpet and a combination of carpet with underlay were modelled, with both overlaying concrete and wooden flooring bases. It was found that the addition of the carpet or combination of carpet with underlay did not significantly affect the peak head acceleration. This was due to the compliant nature of the infant head resulting in high deformation, leading to an increase in the contact area. A larger contact area increases the effective impact stiffness of the underlying surface, bringing it near to what it is without the additional top surface layer. The deformation of the carpet itself affected the early contact stiffness, resulting in the increased impact duration. Further work is required to validate the carpet and underlay material models, as well as obtain data for the many different types of both materials. This will allow further FE models to be constructed and used to determine if there is a practical thickness of carpet and underlay that would significantly alter the physics of the impact. This would help investigators determine whether a particular surface mitigated the effects of a fall.

Existing infant head FE models have only investigated impacts on flat surfaces. An impact to a surface edge was modelled in this study as a preliminary investigation into different impact types. Compared to an impact with a flat surface, a similar depression as that observed in the baseline model occurred,

however, the area of the head not in contact with the surface passed down below the surface, causing it to ‘wrap’ around the edge of the of the surface. Peak head acceleration was comparable to the baseline model, while the impact duration increased by 26%.

Chapter 7 Predicting Skull Fracture

Introduction

In cases of suspected infant abusive head trauma (AHT), the type and extent of skull fracture is a common method for determining the level of impact the infant's head likely experienced. Each case has a unique sequence of events resulting in varying degrees of injury. Analysis of proven accidental and AHT cases has found that some types of skull fracture feature more prominently than others in accidental versus AHT cases. Hobbs (1984) found that skull fractures resulting from events classified as accidental were linear fractures that do not exceed the sutures and are generally only at one localisation. However, documented cases of AHT resulted in multiple, depressed and/or growing fractures. Through clinical experience, medical professionals develop an understanding of the types of skull fractures that are likely the result of either accidental or AHT injuries. It is this experience that is often used in the prosecution of cases of suspected AHT.

Finite element (FE) models have the potential to be used to predict whether skull fracture is likely to occur for a certain loading sequence, and if so, the fracture pattern that is likely to result from such a sequence. Accurately predicting skull fracture requires the ability to accurately model local variables, such as stress, in the head tissues. As identified in Chapter 3, while existing FE models have been validated to a reasonable degree of success, very little validation of local variables has been carried out.

There are multiple methods of predicting material fracture in FE models, including the extended finite element method (XFEM), interelement crack method and element erosion (deletion). The XFEM is a method for the modelling of cracks of arbitrary geometry without remeshing by reformulating the elements along the crack path (Song, Areias, and Belytschko 2006, Song, Wang, and Belytschko 2008). Another common method for modelling crack growth is adding the crack to the geometry and remeshing the model. However, this is computationally expensive when the crack advances over a large part of the mesh (Song, Wang, and Belytschko 2008). Therefore, the ability to model crack geometry without remeshing in XFEM makes it a favourable method. Another method, known as the interelement crack method, models the crack by separation between the edges of the elements (Xu and Needleman 1994, Song, Wang, and Belytschko 2008). Element erosion (also known as element deletion) is where elements are effectively deleted from the mesh by reducing the element stress to zero when a failure criteria is reached (Song, Wang, and Belytschko 2008).

Of the existing infant head FE models, only Roth, Raul, and Willinger (2010), Li, Liu, et al. (2015), Hajiaghamemar et al. (2018), Li, Sandler, and Kleiven (2019) have considered tissue failure in the form of skull fracture. Both Li, Liu, et al. (2015), and Hajiaghamemar et al. (2018) compare their predicted stress distributions to medical images to determine if the resulting areas of high stress occur in similar regions as to where skull fracture is observed. Li, Sandler, and Kleiven (2019) use their model to reconstruct real-world cases in order to predict whether the observed fracture pattern could have resulted from the history provided by witnesses. However, they do not specify the method used to determine whether fracture occurred or not. He et al. (2020) recently developed a computational framework that uses linear elastic fracture mechanics and adaptive remeshing to predict fracture propagation in infant head FE models. This method has the potential to accurately predict skull fracture.

The likelihood of skull fracture, in general, increases with impact velocity (Johnson et al. 2005). Therefore, in any analysis of drop height, tissue failure should be considered. The analysis presented in Chapter 6 of this thesis did not consider such tissue failure. This chapter presents an initial investigation into skull fracture prediction. Element erosion is used as the method of representing material failure and is considered for its suitability to predict skull fracture.

Methods

In this study, the same geometry, material models, mesh and boundary conditions are used as that for the baseline model in Chapter 6. However, a drop height of 0.6 m was used, along with frictional contact at the brain-skull interface (friction coefficient of 0.2). To model material failure in the occipital bone, element erosion was used. Element failure was predicted using maximum principal stress and maximum shear stress criteria. When the element stresses exceeded one of the threshold values, the element was ‘deleted’. The stress thresholds were based on the skull fracture thresholds of Hajiaghamemar et al. (2018). In the absence of threshold data for the occipital bone, data for the parietal bone was used for all cranial bones. Thresholds of maximum principal stress and maximum shear stress of 36.0 and 28.1 MPa respectively were used. These thresholds represent 95% probability of skull fracture occurring (Hajiaghamemar et al. 2018).

Predictions of fracture propagation using element erosion is highly dependent on the mesh size. Two levels of mesh refinements were used to determine how the fracture pattern differed. The baseline mesh was used as starting point (global element size of 6 mm, with local refinement for all tissues in the form of a sphere of influence that had element sizes ranging from 0.5 to 1 mm within a 25 mm radius of the impact location and 2 mm within a 50 mm radius). The first iteration of mesh refinement increased the sphere of influence radius size to 50 mm for element sizing of 0.5 mm. An additional

sphere of influence with a radius of 70 mm and element sizing of 1 mm (centred at the contact point) was used on the cranial bones and suture. The second iteration used sphere of influence radii of 50 mm and 70 mm respectively. This resulted in a total of 119 674 and 148 558 nodes respectively (compared with 67 640 of the baseline mesh). Readers are referred to Chapter 4 for a detailed description of the baseline mesh.

Results

The baseline model (0.3 m drop height) did not predict skull fracture would occur as the maximum principal stress was 28.0 MPa, which is less than the failure criteria of 36.0 MPa; therefore, a drop height of 0.6 m was used. At this height, skull fracture was predicted to occur. Figure 7.1 presents the acceleration-time plots for the model where tissue failure was not considered, where tissue failure was considered in the occipital bone (using the baseline mesh), and for two levels of mesh refinement in the contact area.

For the baseline mesh, when tissue failure in the occipital bone is considered (red trace in Figure 7.1), there is a definitive spike in the acceleration-time curve at approximately 3.25 ms where the first elements are eroded (fracture initiation). This is followed by the acceleration oscillating between approximately 105 and 135 g before decreasing. The peak acceleration was 136 g, which is comparable with the 0.6 m baseline model with frictional contact (135 g). When material failure is considered,

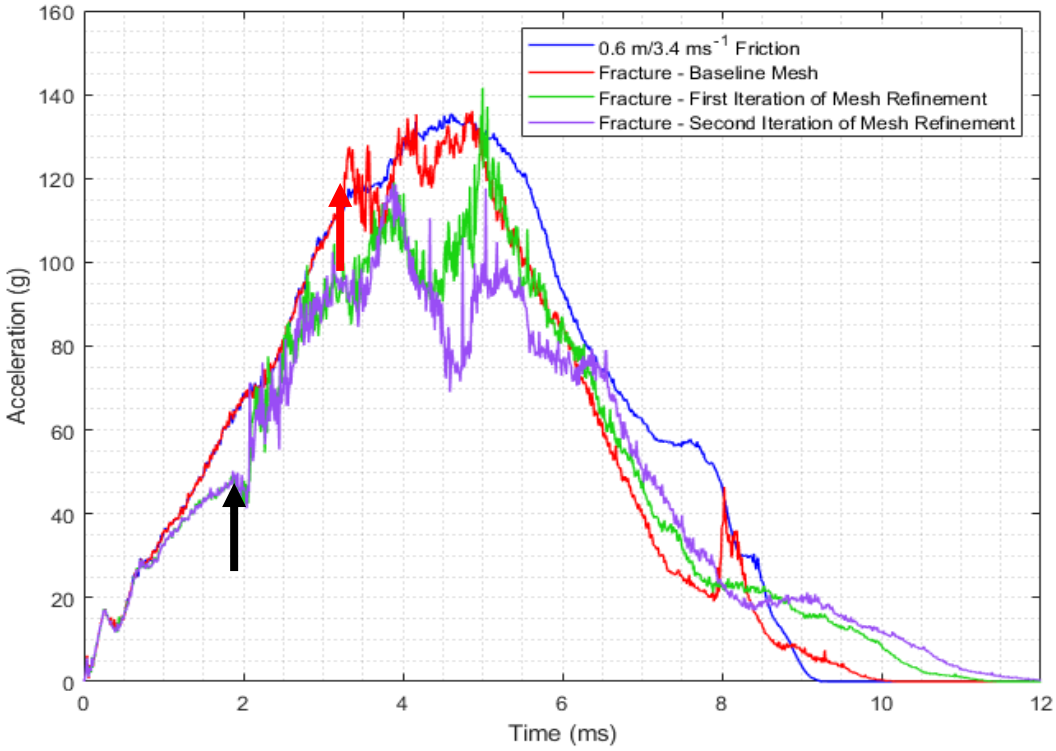

Figure 7.1: Acceleration-time plots for FE models predicting skull fracture in occipital bone. Drop height of 0.6 m and frictional contact between brain and skull. Red and black arrows indicate the point at which fracture first occurs in the baseline and refined meshes respectively.

there is a small increase in the impact duration (10 ms versus 9.2 ms respectively). For the models where additional mesh refinement was used, there is an initial peak in acceleration before it drops off and subsequently increases, reaching a second peak. The impact duration for these models is around 11 ms.

Figures 7.2 and 7.3 show the sequence of fracture from 3.25 ms when fracture was predicted to initiate, through to 6.25 ms. The fracture initiates at the interface of the occipital bone and suture, as can be seen in Figures 7.2 (a) and 7.3 (a). At 4.25 ms, the fracture has propagated perpendicular from the occipital-suture boundary in towards the centre of the depression. While not shown in this sequence, analysis of the model results showed that the area circled in Figure 7.2 (b) had a separate fracture initiation at 3.31 ms and propagated in towards the centre of the depression. This fracture also propagated along the outer ridge of the depression, where bending was occurring. The two fractures then joined up, creating the fracture pattern seen in Figures 7.2 (b) and 7.3 (b). Elements are also eroded along the occipital-suture interface. Figures 7.2 (c) and 7.3 (c) show the fracture pattern at around the time peak acceleration is reached. At this time point, another fracture can be seen to have initiated and propagated in towards the centre of the depression. This is most clearly seen in Figure 7.3 (c).

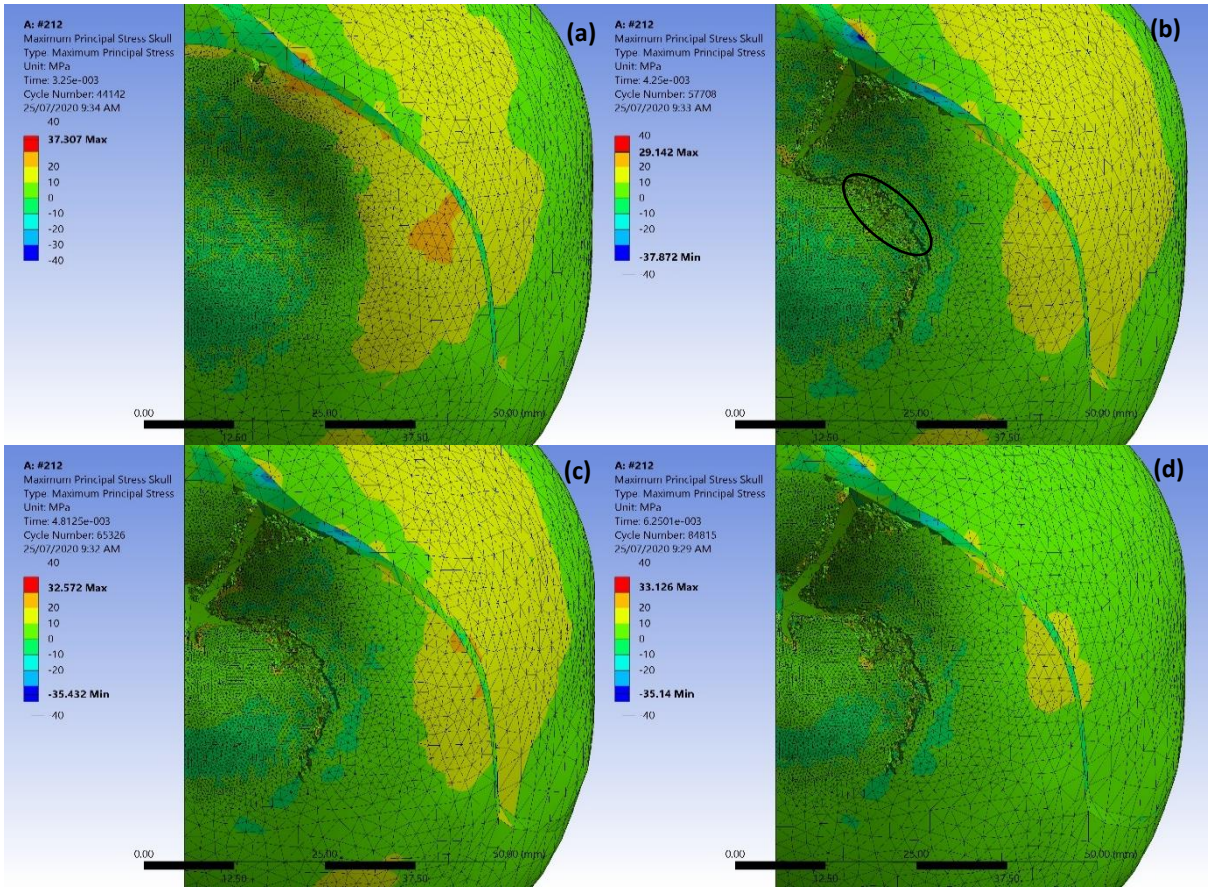

Figure 7.2: Sequence of fracture (bottom view) at 3.25 **(a)**, 4.25 **(b)**, 4.81 **(c)** and 6.25 ms **(d)**. Circled area in **(b)** corresponds to initiation site of second fracture.

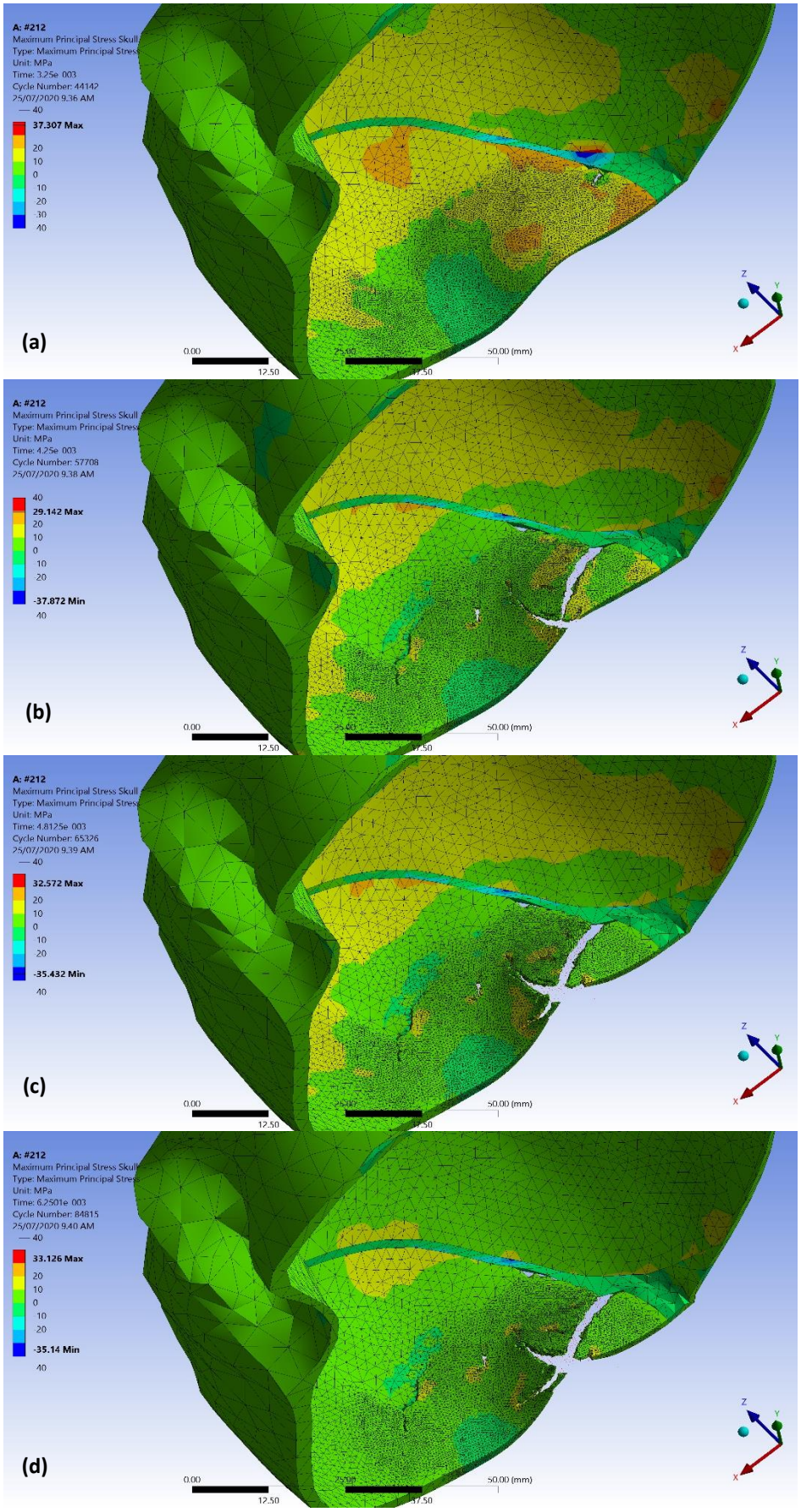

Figure 7.3: Sequence of fracture (view into skull cavity) at 3.25 **(a)**, 4.25 **(b)**, 4.81 **(c)** and 6.25 ms **(d)**.

For the models with the refined mesh, the sudden increase in acceleration occurs much earlier at approximately 2 ms. The acceleration then continues to increase, with many oscillations, until it reaches a first peak at around 4 ms. From there, a decrease in acceleration is observed, with the most refined mesh decreasing much further. This is where the two traces deviate (green and purple traces in Figure 7.1), especially for the secondary peak and the rebound phase of the impact.

Figures 7.4 and 7.5 show the sequence of fracture for the first and second iterations of mesh refinement respectively. In both cases, the fracture initiation occurs in approximately the same place as that for the baseline mesh, although it occurs at a much earlier time in the impact (1.81 ms versus 3.25 ms respectively). One millisecond later, the fracture has propagated in towards the centre of the depression, also similar to the baseline mesh. At 4.0 ms, a second fracture has initiated from the occipital-suture boundary (highlighted by the circles in Figures 7.4 (c) and 7.5 (c)). For the second iteration of mesh refinement, the fracture has propagated slightly further into the occipital bone and several branches have occurred. Elements are also eroded along the occipital-suture boundary, starting from the site of the initial fracture. At 5.0 ms, for both iterations of mesh refinement, the second fracture has propagated into the occipital bone with multiple branches occurring at various locations. The general path of this second fracture is curved. This corresponds to the bending in the occipital bone on the outer edge of the depression, as shown in Figure 7.6 (a) and (b) for the first and second iterations of mesh refinement respectively. That is, the fracture is occurring where the occipital bone bends and conforms to the impact surface. This fracture pattern is not as apparent in the baseline mesh. Between the two iterations of mesh refinement, the branches at the ends of the second fractures are of different lengths. At 5.0 ms, the first fracture has a few small branches at the centre of the depression, but these are not as distinct as in the baseline mesh.

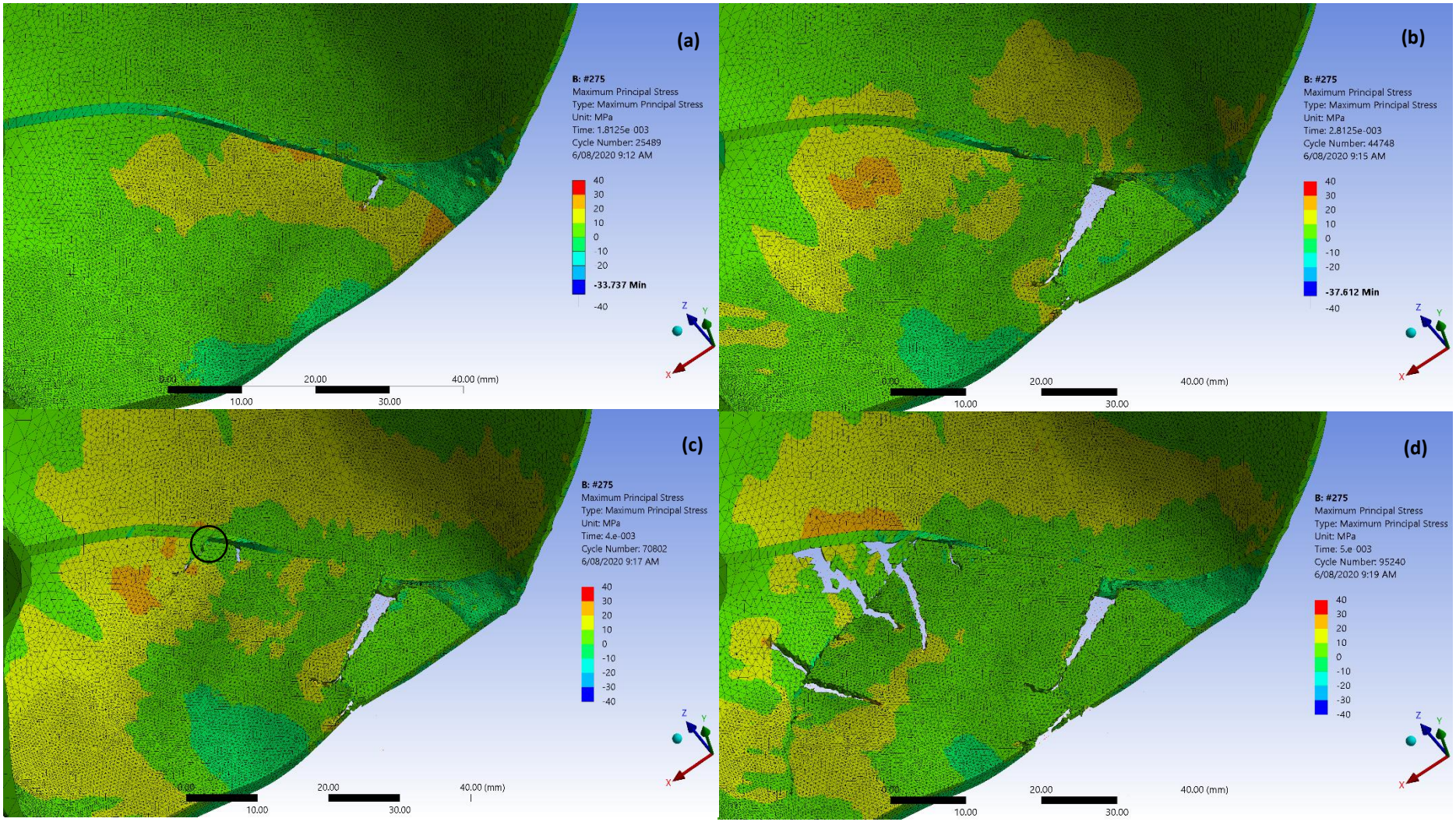

Figure 7.4: Sequence of fracture at 1.8 **(a)**, 2.8 **(b)**, 4.0 **(c)** and 5.0 ms **(d)** for first iteration of mesh refinement. Circled area in **(c)** corresponds to initiation site of second fracture.

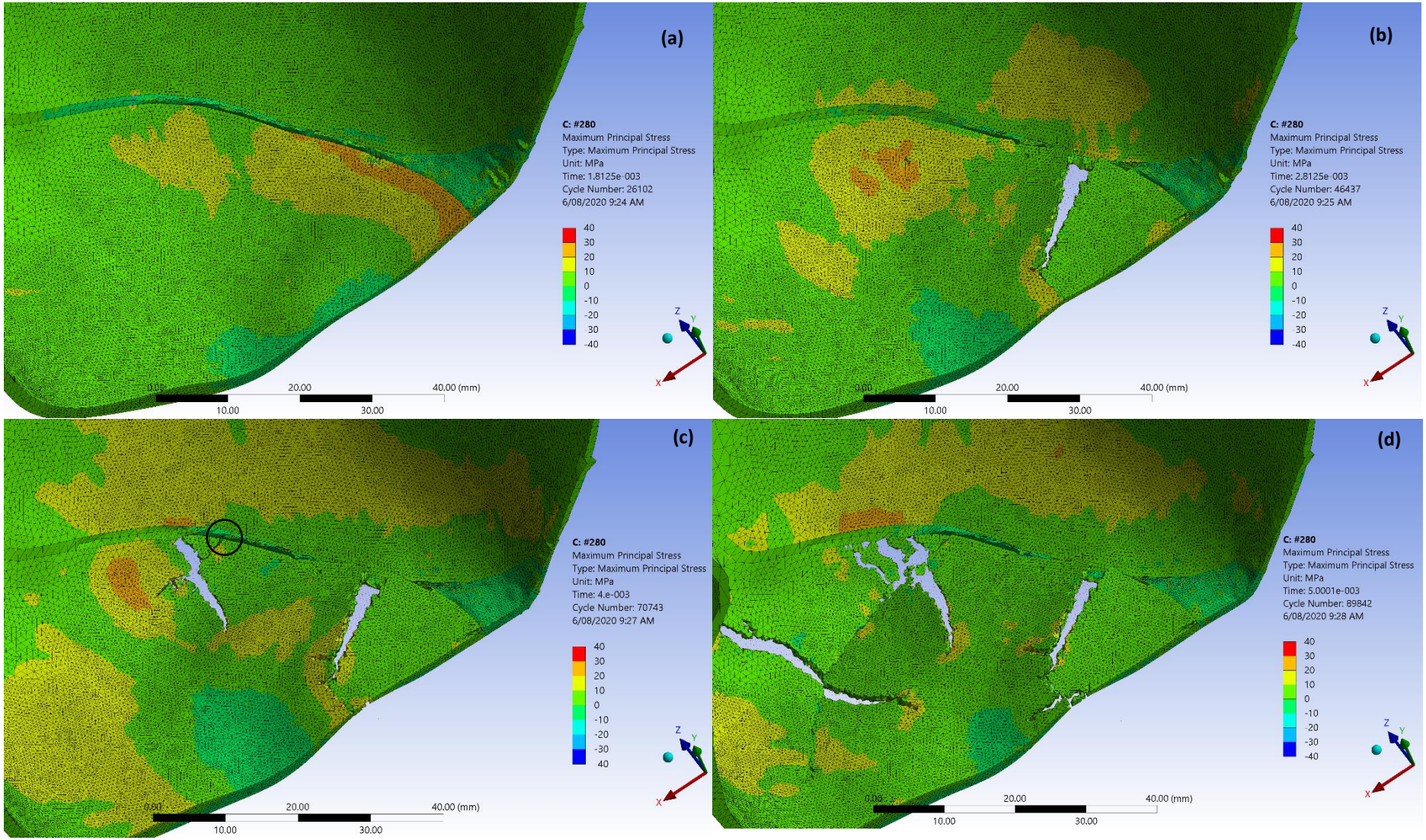

Figure 7.5: Sequence of fracture at 1.8 **(a)**, 2.8 **(b)**, 4.0 **(c)** and 5.0 ms **(d)** for second iteration of mesh refinement. Circled area in **(c)** corresponds to initiation site of second fracture.

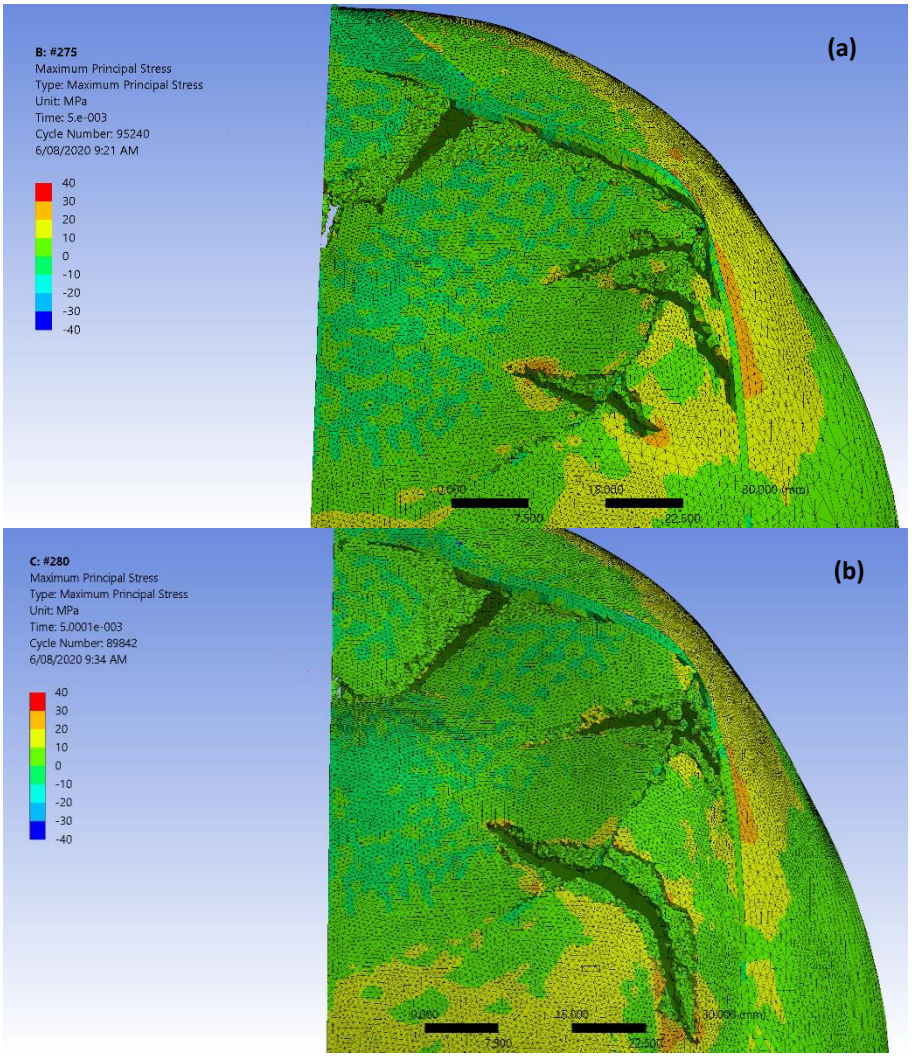

Figure 7.6: Bottom view of occipital bone fracture pattern at 5.0 ms for first **(a)** and second **(b)** iterations of mesh refinement.

Figure 7.7 shows the vector directions of the maximum principal stress in the occipital bone and suture just before fracture initiation. The direction of the stress is circumferential about the point of impact. At the bone-suture interface, the direction is parallel to the interface.

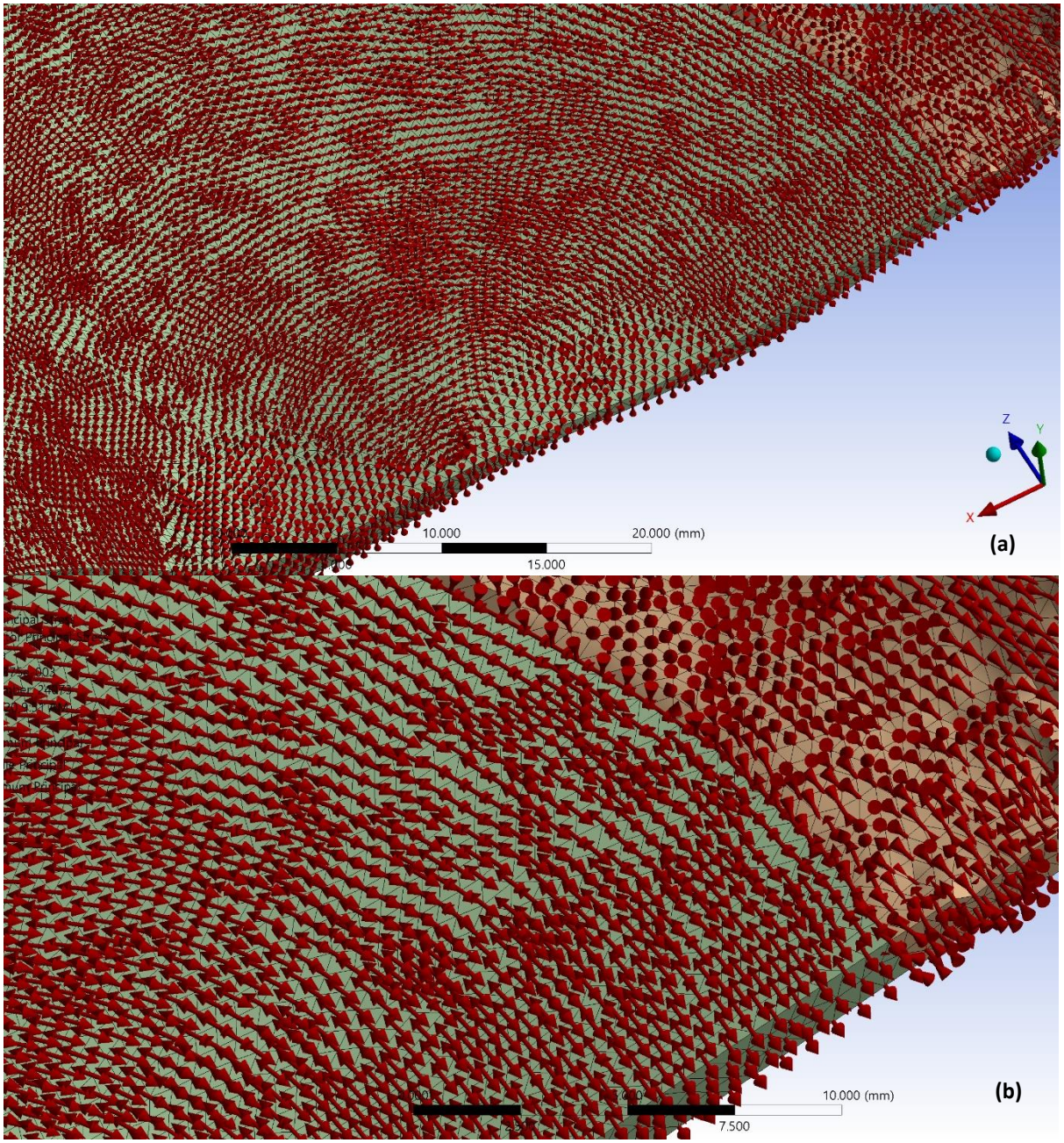

Figure7.7: Vector directions of the maximum principal stress in the occipital bone (green body) and suture (tan body) just before fracture initiation. **(a)** shows overview of deformed region, **(b)** shows a close up of bone-suture interface.

Discussion

The FE model used for the drop height and impact surface simulations in Chapter 6 did not consider tissue failure. Therefore, the results and analysis relating to drop height can only be used to identify trends where skull fracture does not occur. From studies that have investigated the nature of infant and child head injuries from real-world cases, it is well established that, in general, the likelihood of skull fracture occurring increases as the fall height increases (Williams 1991, Johnson et al. 2005, Rangarajan et al. 2017). One of the next steps in infant head FE modelling is incorporating material models with damage variables so that tissue failure, in particular skull fracture, can be modelled.

To date, few infant head FE model studies have considered skull fracture and are reviewed in detail in Chapter 3 (Roth, Raul, and Willinger 2010, Li, Liu, et al. 2015, Hajiaghamemar et al. 2018, Li, Sandler, and Kleiven 2019). Li, Liu, et al. (2015) compared the maximum von Mises stress distributions with the sketched diagrams of Weber (1984, 1985) to check whether the areas of high stress predicted by the FE models matched the location and shape of Weber's experimental drop tests. The stress distributions were described as matching "reasonably well with the skull fracture patterns reported", although, as with all biological model validation, this is subjective. In some cases, the areas of high stresses are in the general area of the reported fracture patterns, but the fracture path varies significantly. A similar method was used by Hajiaghamemar et al. (2018), where they compared the stress and strain distributions to medical images to ensure that the areas with the highest magnitudes were occurring in similar locations as the observed fractures. Both Li, Liu, et al. (2015) and Hajiaghamemar et al. (2018) used their models to develop skull fracture risk curves and determine fracture thresholds for infant cranial bone.

Roth, Raul, and Willinger (2010) used their FE model to reconstruct a real-world accidental fall. They do not specifically state how they considered whether fracture occurred but given that ultimate stress data is provided in the material model for the skull, it is assumed that fracture was considered to occur if the maximum principal stress exceeded the ultimate stress. The location and path of the fracture was compared with the medical images from the patient and showed the fracture was reproduced in a "realistic manner". Li, Sandler, and Kleiven (2019) used their FE model to reconstruct two cases of suspected abuse, comparing the location and path of the predicted fractures with those observed from computed tomography (CT) scans of the victims. Ultimate stress data for infant cranial bone from Coats and Margulies (2006) was used to predict where skull fracture would occur.

A recent study by He et al. (2020) developed the most sophisticated computational framework for modelling skull fracture to date. They used linear elastic fracture mechanics and adaptive remeshing to predict crack propagation. In brief, the FE model of Coats, Margulies, and Ji (2007) was used to

determine where the stress and strain distributions first exceed skull fracture thresholds developed by the same research group (Hajiaghamemar et al. 2018). A crack face is then inserted as a virtual boundary in the geometry and as the crack propagates, the mesh is updated to conform to the virtual boundary. Stress intensity factors are used to determine the crack direction. Readers are referred to the original study for further details (He et al. 2020). Three cadaver experiments from Weber (1984, 1985) and Loyd (2011) were reconstructed and in all cases, they were able to predict similar crack patterns.

The work of He et al. (2020) shows great potential for predicting skull fracture in infant head FE models. They provide no details on the additional computational time required for such modelling, which given the requirement to remesh at every time step and the additional steps for determining the direction of crack propagation, it can be assumed that the computational time increases significantly. Future development and the general increase in computational power over time will no doubt lower the computational cost. In the meantime, existing fracture modelling methods can be considered.

Existing methods for modelling fractures in FE models include the extended finite element method (XFEM) (Song, Areias, and Belytschko 2006), interelement crack method (Xu and Needleman 1994), and element erosion (also known as element deletion). In explicit FE modelling, it is common to use element erosion. Element erosion is where the element stresses are reduced to zero when they meet some failure criterion (Song, Wang, and Belytschko 2008). The reduction in stresses occurs by setting the element stiffness to zero, causing the element to no longer have any load bearing capacity. This effectively deletes the element from the mesh (although deletion does not actually occur). In ANSYS Explicit, the failure criteria can be when the maximum principal stress or strain in an element exceeds a failure threshold (ultimate stress or strain), a geometric strain condition is reached where the element distortion exceeds some ratio of its original size, or when the element time step drops below a specified value. If all the elements connected to a node are eroded, the inertia of the node can be retained. While the mass and momentum of the node is conserved, the ‘material’ is removed and therefore does not represent the reality of a fracture.

Neither Roth, Raul, and Willinger (2010) and Li, Sandler, and Kleiven (2019) specifically state how material failure is included in their models. He et al. (2020) suggest that these two studies use element erosion. The studies of Hajiaghamemar et al. (2018), and Li, Liu, et al. (2015) do not specifically include material failure modelling in their FE models to determine whether skull fracture occurs. Comparing stress and strain magnitudes to ultimate stress and strain magnitudes is a common method in engineering analyses to determine whether material failure occurs. However, this does not account

for the additional energy that is absorbed during material failure and that the areas of fractured material can no longer provide structural load bearing capacity. Therefore, it would be expected that differences in output parameters such as the acceleration-time trace, peak acceleration and impact duration would occur.

When a fracture initiates in a material, it propagates in a direction that mostly depends on the microstructure of the material, the nature of the stresses at the crack tip and the material properties. The mating surfaces of the fracture separate and narrow down to a focal point at the leading edge of the fracture (crack tip). At the crack tip, a very large stress concentration occurs and causes the crack to continue to propagate.

Element erosion upon material failure was used in the present study to investigate the additional challenges of fracture prediction. Skull fracture thresholds for maximum principal stress developed by Hajiaghamemar et al. (2018) were used. The baseline FE model (drop height of 0.3 m) did not predict skull fracture would occur. Therefore, an impact speed equivalent to a drop height of 0.6 m was used. Frictional contact at the brain-skull interface was used as bonded contact would tie the brain nodes to nodes of elements in the skull that were eroded and may unduly affect the predicted fracture pattern.

When material failure was considered, there was little change in the peak head acceleration and a 0.8 ms increase in the impact duration for the baseline mesh. Further mesh refinement caused a fluctuation in the acceleration, with an initial peak followed by a decrease and subsequent increase to a second peak in the acceleration. The impact duration increased by approximately 1 ms compared to the baseline mesh. This is a result of the stiffness of the skull changing as the fractures propagate, leading to a different force response than that of the baseline model. This can affect the results of the FE model, which could lead to different conclusions being drawn regarding the predicted injuries an infant might experience for a given fall scenario.

Skull fracture in the occipital bone was predicted to initiate at the interface of the occipital bone and suture. This is consistent with the findings of Coats and Margulies (2006), Baumer et al. (2010), Li, Sandler, and Kleiven (2017). The bone-suture-bone specimens used in the tensile tests of Coats and Margulies (2006) consistently failed at the bone-suture boundary. Baumer et al. (2010) studied the characteristics of impact-induced fracture in the infant porcine skull. They tested 76 porcine specimens, ranging in age from two to 28 days, using a gravity accelerated mass to impact the right parietal bone. Seventy of 76 specimens showed fractures that initiated at the cranial bone-suture boundary, not at the centre of the impact location (Baumer et al. 2010). For a frontal impact, Li,

Sandler, and Kleiven (2017)'s FE model predicted that the maximum principal strain would be the greatest along the bone-suture boundary, thus skull fracture was likely to initiate there.

In these experimental studies, no explanation was provided for possible reasons for the initiation site being located at the bone-suture interface. However, one explanation could be that the interface is very jagged, causing a stress concentration and hence resulting in the initiation point of a fracture. This is also likely to be the reason for the strain results of Li, Sandler, and Kleiven (2017), assuming that no modification was made to the suture geometry in the modelling process. In the present study, fracture initiation also occurred at the bone-suture interface. The suture geometry in the model was modified as the poor quality of the CT scan resulted in the segmentation of a much wider suture (refer to Chapter 4 for further explanation of this). Therefore, the bone-suture geometry was not jagged as would be expected and hence was not necessarily the cause for fracture initiation at the interface. Another possible reason for initiation at the interface is that there is a sudden change in the stiffness, which would also cause a concentration of stress in this region. The cranial bone stiffness is much greater than that of the suture (approximately 400-500 MPa versus 8 MPa respectively) (Coats and Margulies 2006). This sudden change in stiffness creating a stress concentration is likely to be the cause of the fracture initiation location in the present FE model, and could also be a cause for the experimental findings of Coats and Margulies (2006) and Baumer et al. (2010). In a FE model, the contact forces required to enforce the bonded contact conditions between the two tissues can also induce higher stresses along the boundary. Baumer et al. (2010) does not report fracture propagating along the bone-suture boundary. Therefore, the fracture propagation along the occipital-suture interface predicted in the present study may be a result of the contact force induced stresses.

The general fracture pattern in the baseline mesh consisted of a series of linear fractures that initiated at the outer edges of the depression and propagated in towards the centre of the depression. This is consistent with a depressed fracture. As the skull contacts the impact surface, it starts to bend, forming a ridge that propagates radially from the contact point. Once the depression starts to form, the degree of bending at the outer edges (ridge) of the depression increases, causing the bending stresses to also increase. The greatest tensile stresses occur at the outer surface of the skull. At the centre of the depression, the bending direction is opposite, so the greatest tensile stresses occur on the inner skull surface. The depression forms a dome shape on the inside of the skull, resulting in the circumferential direction of maximum principal stress about the impact point. Fractures propagate in the direction perpendicular to the maximum tensile stresses. Therefore, the circumferential direction of stress would cause the fractures to propagate in towards the centre of the depression. This is observed in the present study and consistent with depressed fractures observed in head impacts (Gurdjian, Webster, and Lissner 1950, Braakman 1972, Oh 1983). In the refined mesh models, the

secondary fractures propagating around the ridge of the depression are caused by the bending stresses in the ridge.

As discussed earlier, when an element meets some failure criterion, the stress in the element is reduced to zero (Song, Wang, and Belytschko 2008). This effectively creates a free boundary on the elements adjacent to the eroded element. Therefore, the fracture does not develop in the direction of the crack width (Murakami and Liu 1995). As the width of the fractured region is also the width of the eroded element, the size of the element dictates the fracture width. If the element size approaches zero, the fracture width also approaches zero, hence the fracture region can be dependent on the size of the mesh. If the mesh is refined, the displacement gradients describing the fracture become greater, providing a more accurate prediction of the fracture path (Hambli 2013). When elements are eroded, the stress is redistributed in the fracture region, causing additional stress in surrounding elements. If the element stress becomes greater than the failure criteria, then element erosion continues, causing the fracture to propagate.

Mesh dependence of the element erosion method was observed in the present study. In the models with greater levels of mesh refinement, the initial fracture site and propagation direction was similar to the baseline mesh. The biggest difference between the refined mesh and baseline mesh models was the prediction of the second fracture. Using the more refined mesh, the second fracture occurred at the outer ridge of the depression, where the occipital bone experienced bending as it conformed to the impact surface. This will be due to the mesh dependence discussed above. Between the two iterations of mesh refinement, the largest difference was the length of the branching at the end of the second fracture. The second iteration predicted a greater length for the branching fractures and is likely due to the smaller elements resulting in greater displacement gradients that can be used to more accurately predict the crack propagation. In the first iteration, this branching occurred at the outer boundary of the mesh refinement where the elements transitioned to the global element size.

Using element erosion to model material failure in the occipital bone has shown that it can be used to predict skull fracture based on where the maximum tensile stresses occur. Skull fracture was predicted to occur in areas of the occipital bone where the maximum tensile stresses are expected for the loading case and head orientation used in the present study. The fracture pattern observed is unique to this study only. Validation of a fracture pattern against a real-world case, where medical imaging can be used to observe the resulting skull fracture, is not carried out in the present study. Further work on such a case would be required in order to conclude more definitively whether element erosion is a suitable method for predicting skull fracture.

One limitation of the present model for fracture prediction is that it uses an isotropic elastic material model for the cranial bones. Infant cranial bone is highly anisotropic, with fibres radiating out from the ossification centres. As fractures follow the path of least resistance, it would be expected that the directional nature of the fibres would highly influence the path the fracture would take. This can be observed in CT scans where linear fractures often have a jagged appearance, and was also found by He et al. (2020) in their more sophisticated modelling of skull fracture. The use of an isotropic elastic material model does not account for the anisotropy in infant cranial bone and therefore would limit the accuracy of the predicted path. Li, Liu, et al. (2015) used an isotropic elastic model for the cranial bones in their FE model, which they used to develop skull fracture risk curves. As noted earlier, the agreement of the path of the fractures predicted by the FE model do vary significantly in some cases. The use of the isotropic elastic model is likely to be a reason for this. Areas of high stress seem to correspond with areas where the curvature of the deformed skull increases as it flattens against the impacting surface. This would be expected as the highest tensile stresses would occur in these areas (due to the bending).

Another limitation is the mesh dependence of the fracture pattern. As shown by the different fracture patterns predicted by the baseline mesh and refined mesh models, as well as existing literature (Murakami and Liu 1995, Song, Wang, and Belytschko 2008), the use of element erosion to predict skull fracture is mesh dependent. Further mesh refinement needs to be considered in order to determine how much the fracture pattern changes for even denser meshes (that is, to check the fracture pattern for mesh convergence). There is likely to be an optimal mesh density that is dependent on the material and the geometric structure. Using a greater mesh density significantly increases the computational cost of solving FE models to predict skull fracture and may make such analyses inefficient in forensic case work. However, fracture modelling increases the complexity of FE models in general, so the computational cost is likely to be greater regardless of the method used.

The use of element erosion to predict the fracture pattern is also limited when compressive forces are present. As elements are eroded, a gap occurs where the eroded element has been removed. In tension, this gap has little effect as the tensile forces naturally create a gap in the material as the crack propagates. However, in compression, the gap allows the material to move into the place vacated by the element. In reality, there is a discontinuity in the material structure, but no gap. Therefore, element erosion is unsuitable for predicting fracture patterns in areas of the skull where compressive forces exist. This limitation needs to be considered when interpreting any fracture pattern results.

The skull fracture pattern is a function of the loading condition (orientation of the head and impact velocity), the geometry and material properties. Combined with FE modelling, it also becomes a

function of the FE formulation and mesh. To accurately model fracture propagation, all these variables need to be modelled in detail. However, the level of detail required is currently unknown. Significant future research will be required to determine the level of detail required for realistic fracture pattern predictions as it is a challenge from both an experimental and modelling standpoint. The load history during an impact event is dependent on the fracture history and vice versa as the stiffness of the skull changes as the fractures propagate. This alters the force response to ongoing motion and contact. While using anisotropy is a first step towards more accurate skull fracture modelling, it only represents the average behaviour of the skull. The fibrous nature of the infant skull that an anisotropic model is trying to capture is the trabeculae (cylindrical struts in the cancellous bone). Trabeculae cause variation in the properties from place to place within the skull and are too small to model explicitly. To truly model a realistic fracture pattern, the skull, as well as the whole head, needs to be modelled in as much detail as possible so as to represent the true behaviour of the head. From a material properties perspective, future models could do this by accounting for the differences in material properties throughout the skull.

Overall, while element erosion has been shown to have the ability to predict tissue failure in areas where it would be expected, the limitations around mesh dependence and the way it reduces the element stiffness to zero to effectively remove the element from the mesh, means that the direction and extent of crack propagation may not be accurate. Ideally, a particular mesh and material properties would be calibrated against a known fracture, and then used to model more specific cases in order to ensure an appropriate mesh is being used. Future work could investigate this, as well as other methods of predicting material fracture in FE models, such as XFEM or interelement crack method. Validation of local parameters (such as stress and strain) must also be improved (as recommended in Chapter 4) as accurate values are required to accurately predict fracture. Until such work has been completed, it appears that skull fracture prediction using element erosion can provide some value but should be used with the above limitations in mind when interpreting results or making comparisons against medical images of real-world cases.

Conclusions

This study investigated the ability to predict skull fracture in the baseline model presented in Chapter 6. The method of material failure modelling was element erosion and used threshold data for maximum principal and maximum shear stress criteria. It was found that skull fracture was predicted to initiate at the occipital bone and suture interface, which is consistent with fracture initiation sites found in existing experimental work in the literature. The fractures then propagated in towards the centre of the depression due to the circumferential direction of the maximum principal stresses about

the contact point. Secondary fractures occurred along the ridge of the depression where there were high bending stresses as the bone conformed to the flat impact surface.

There are a range of methods for fracture prediction in FE models, all with their own strengths and weaknesses. Element erosion is a common method in explicit dynamics analyses and is relatively easy to implement in conjunction with a failure criterion. In this study, element erosion predicted skull fracture to occur in places that it would be reasonably expected. However, one limitation is the dependence on mesh size. A more refined mesh predicted a different fracture pattern than the mesh used in the baseline model. Greater mesh refinement increases the computational cost of FE modelling and may make fracture prediction in forensic case modelling too inefficient. If element erosion is used for such modelling, it is recommended that its limitations be considered when interpreting results. Future work should include further investigating the effect of greater mesh refinement, as well as using other methods of fracture prediction.

Chapter 8 Variations to Baseline Model

Introduction

Simplifying assumptions regarding geometry were used in the baseline models presented in Chapters 4 and 6 to make the computational time more tractable for the large number of simulations required. These assumptions included not modelling a dual layered scalp, the dura or cerebrospinal fluid (CSF). As identified in Brooks et al. (2018) (Chapter 3 of this thesis), in published models, there is large variation in which head tissues are explicitly modelled. Burgos-Flórez and Garzón-Alvarado (2020) do not model the scalp, while Coats, Margulies, and Ji (2007) and Khalid et al. (2019) do not model the CSF. Li, Luo, and Zhang (2013) and Li, Sandler, and Kleiven (2017) model six head tissues (scalp, skull, suture, dura, CSF and brain). Decisions around which tissues to include will be driven by the individual purpose and requirements of each research group.

Another assumption that all infant head finite element (FE) models must consider is whether the foramen magnum (FM) should be sealed or left open. The foramen magnum is an opening in the base of the skull which allows for the passage of the central nervous system through the skull, connecting the spinal cord and brain. In the experimental cadaver head impacts of Prange et al. (2004) and Loyd (2011), the FM was sealed over to stop the intracranial contents from escaping the head. The FE model by Li, Sandler, and Kleiven (2017) closed the FM to replicate the experiments of Loyd (2011), while Coats, Margulies, and Ji (2007) left it open so that the brain was free to move past it during the impact. In the baseline models presented in Chapters 4 and 6 of this thesis, the FM was closed over.

As noted in Chapter 6 of this thesis, the impact angle should be investigated to determine whether it will influence the response of the infant head impact. Li, Sandler, and Kleiven (2017) found that impact angle had a profound influence on the acceleration-time curve characteristics and peak acceleration. In the baseline model of the present thesis, the impact angle was determined by aligning the line of action of the centre of mass with the contact point to avoid any rotational motion of the head. Therefore, the impact angle needs to be investigated to determine how much of an influence it has on the response outputs.

This chapter investigates how changes made to the baseline model affect the response of the FE model. Changing the impact angle is investigated first, followed by the addition of a dual layered scalp, the CSF and the dura individually, before including all three into the same model. Finally, the addition of the foramen magnum is investigated. These changes to the baseline model can provide direction

on how to improve the biofidelity and validity of the baseline model while keeping computations to a minimum.

Methods

The infant head FE model presented on Chapter 4 was used as a baseline for the variations investigated in the present chapter.

Impact Angle

The baseline model was rotated about the axis normal to the symmetry plane, with the centroid of the head geometry being the centre of rotation. When viewing the geometry from the symmetry plane, the positive direction was defined as anticlockwise, as shown in Figure 8.1; zero degrees is defined as the orientation of the baseline model. The position of the head was adjusted in the vertical direction so that it still maintained tangency with the impact surface.

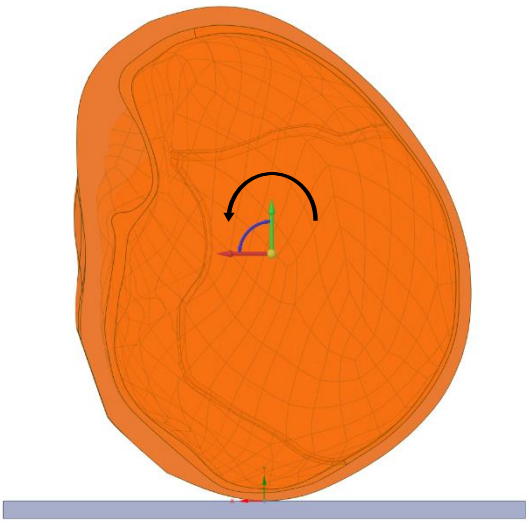

Figure 8.1: Infant head geometry was rotated about the centroid. Arrow represents positive direction (anticlockwise).

Addition of a Dual Layer Scalp

To model a dual layer scalp, similar to that of Li, Sandler, and Kleiven (2017), the baseline scalp geometry was modified using a series of computer aided design (CAD) operations in SOLIDWORKS (Dassault Systèmes SOLIDWORKS Corp, Waltham, Massachusetts, USA). The original scalp geometry was mirrored, and the outer faces of the scalp volume copied to create a surface body of the outer scalp surface. This surface was thickened by 0.5 mm to form a solid body for the outer scalp. A copy of the solid body was made and used to subtract from the original scalp geometry using a Boolean operation; this formed the inner scalp geometry. The inner and outer scalp geometries were split in the sagittal plane to form the symmetry plane. Figure 8.2 shows the head geometry with the dual layer scalp.

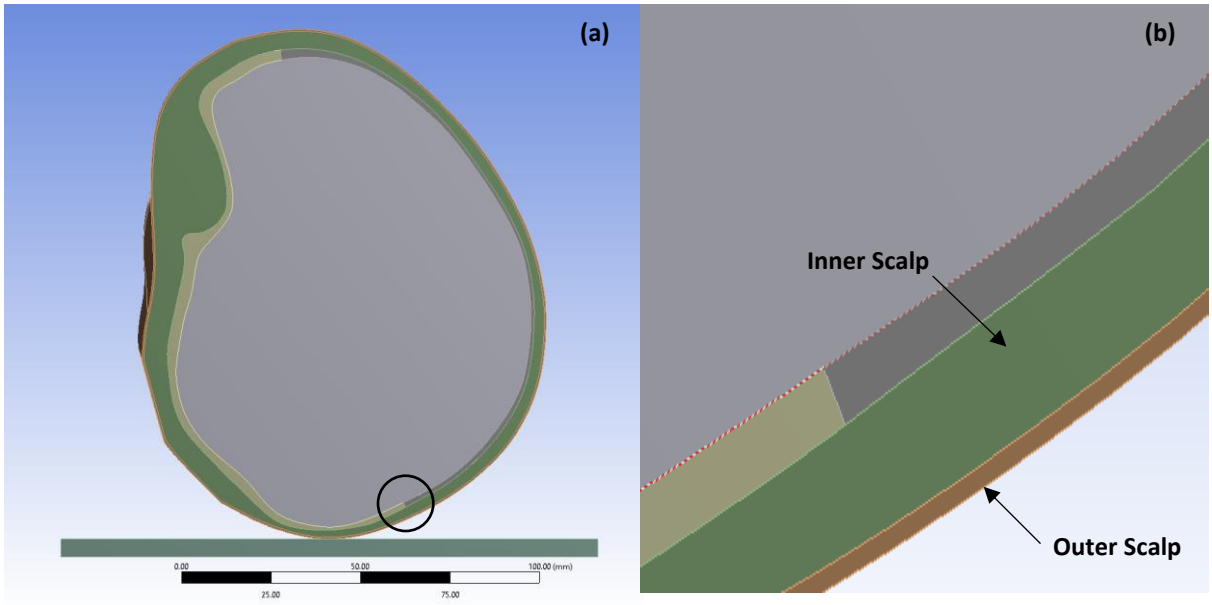

Figure 8.2: FE model geometry for dual layer scalp **(a)**. **(b)** is enlarged view of circled area in **(a)** showing the dual layer scalp.

The same mesh as that for the baseline model was used, with the addition of a sphere of influence (SOI) on the outer scalp (centred at the contact point). A radius of 25 mm and element sizing of 1.0 mm was used for this SOI. The mesh consisted of 80 660 nodes and 359 103 elements. Boundary conditions and contact methods were also the same as that for the baseline model. The material model used for the outer scalp was the same as that used for the scalp in the baseline model, while the inner scalp tissue was modelled using the hyperelastic material model (μ_1=3 990 Pa, α_1=8.8) for the 'inner scalp' from Li, Sandler, and Kleiven (2017).

As a check for the change in geometry compared to the baseline, a model with the inner scalp geometry having an identical material model as that for the outer scalp was also simulated. This will allow for comparisons to be made with the baseline model due to only the change in geometry.

Addition of CSF

To add geometry for the CSF to the baseline model, a similar process was used as that for the dual layer scalp described in the previous section. However, the outer surface of the brain was used instead of the scalp. Figure 8.3 shows the head geometry with the addition of the CSF. The same mesh as that for the baseline model was used, with the addition of a SOI on the CSF. A radius of 25 mm and element sizing of 1.0 mm was used. The mesh consisted of 74 089 nodes and 338 659 elements. Boundary conditions and contact methods were also the same as that for the baseline model. However, friction between the brain and CSF, and CSF and skull were used, with a coefficient of 0.2 as used in the frictional baseline model presented in Chapter 6. The CSF was modelled as isotropic elastic, using a bulk modulus of 2.1 GPa and a Poisson's ratio of 0.49, similar to Li, Sandler, and Kleiven (2017). This model has no viscous property and therefore cannot flow, as would be expected of the CSF.

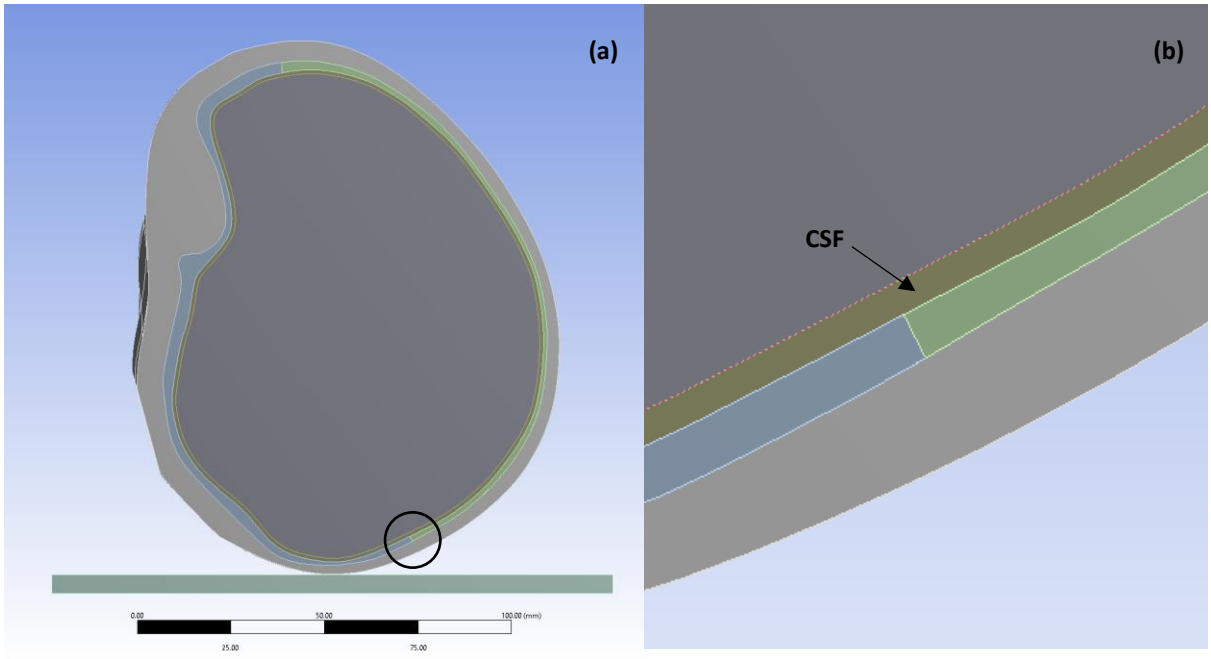

Figure 8.3: FE model geometry for the addition of the CSF **(a)**. **(b)** is enlarged view of circled area in **(a)** showing the CSF.

Addition of Dura

As with the CSF, the geometry for the dura was created using a similar process for the dual layered scalp. The outer surface of the brain was used as the initial surface and thickened 0.5 mm, representing an average infant dura thickness (Bylski et al. 1986). Figure 8.4 shows the head geometry with the addition of the dura.

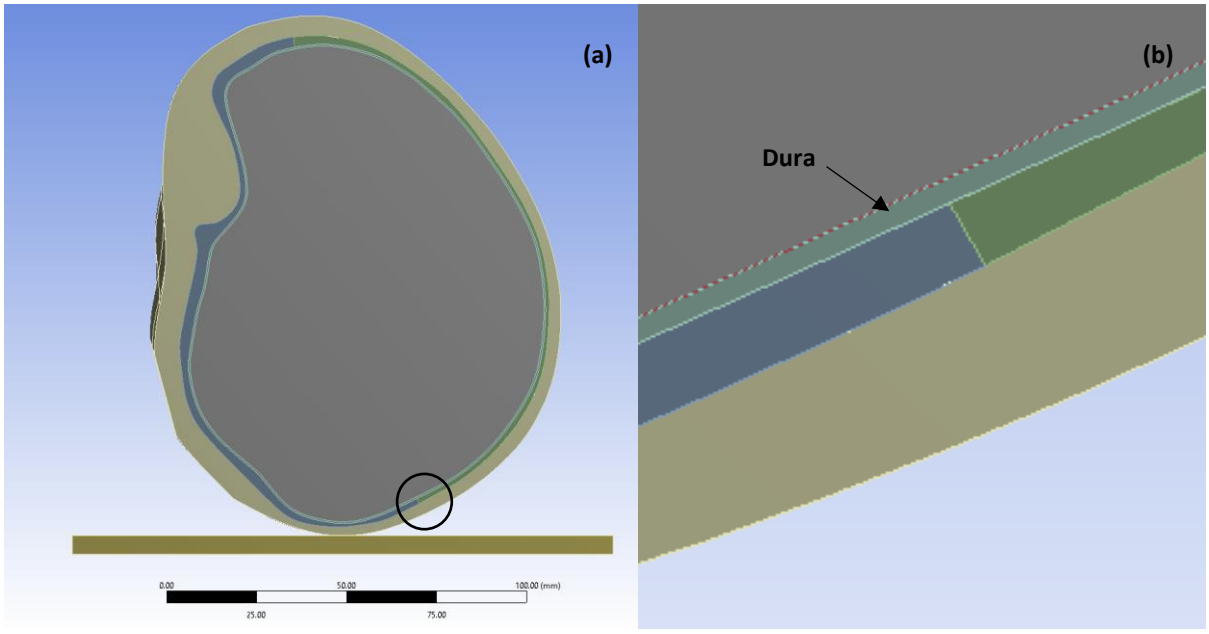

Figure 8.4: FE model geometry for the addition of the dura **(a)**. **(b)** is enlarged view of circled area in **(a)** showing the dura.

The same mesh as used for the addition of the CSF model was used, with the addition of an element size of 2 mm for the whole dura body outside of the refined area. This resulted in 78 896 nodes and

350 159 elements. Boundary conditions and contact methods were the same as that for the baseline model. A second model using frictional contact (coefficient of 0.2) between the dura and brain was also investigated. A two parameter Mooney-Rivlin hyperelastic material model (C_{10}=1.18 MPa and C_{01}=0.295 MPa) was used to represent the behaviour of the dura (Li, Sandler, and Kleiven 2017).

Addition of Dual Layered Scalp, CSF and Dura

After considering the addition of a dual layered scalp, CSF and dura individually, all three were added to the infant head geometry. While the geometry for the scalp remained the same as that used for the dual layered model, the addition of both dura and CSF inside the cranial cavity required new geometry to be built. A similar method used previously (copying a surface and performing thickening functions) was used to create these two tissues. The thickness of the dura was the same as that used previously (0.5 mm), however, the thickness of the CSF was 0.75 mm, not 1 mm as used previously. This was because the curvature in areas around the lower orbits could not be offset by more than 0.75 mm; a direct result of using the thickening CAD operations. Figure 8.6 shows the infant head geometry with all tissues.

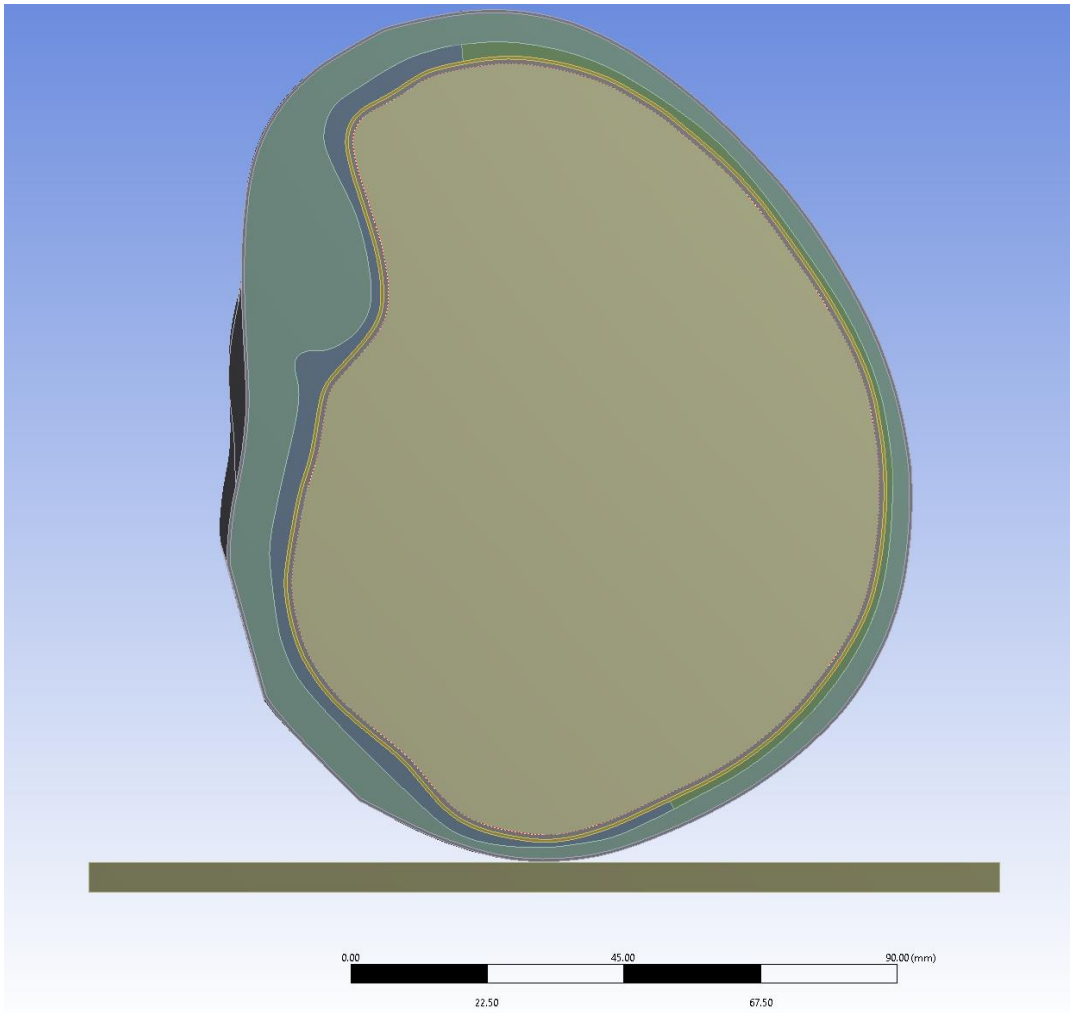

Figure 8.6: Infant head geometry with the addition of the dual layered scalp, CSF and dura.

As with the previous models in this chapter, the same boundary conditions were used as those for the baseline model. The mesh described in the previous sections for the addition of the tissues individually were combined for this FE model. This resulted in 97 461 nodes and 399 644 elements. Both bonded and frictional (coefficient of 0.2) contact at the brain-CSF and CSF-dura interfaces were investigated (all other interfaces remained bonded).

Addition of Foramen Magnum

The foramen magnum was added to the baseline geometry by using an extruded cut through the scalp and skull geometry at the skull base. A circle with a diameter of 25 mm was used as a base sketch for the extruded cut. This diameter was determined from taking measurements on the original computed tomography (CT) scan that baseline geometry was based upon. A series of measurements were made and averaged. The CT scan was also used to ensure the correct position of the FM at the skull base. The FM was added to both the baseline model and the model with the addition of the CSF. An open FM represents an extreme case.

Due to the additional contact between the brain and skull that will be experienced at the foramen magnum as the brain passes through, the mesh had to be refined in this region. A SOI located at the centre of the foramen magnum was used for this refinement. A radius of 45 mm and element sizing of 2 mm were used. The same boundary conditions as the baseline model were used. Frictional contact between the brain and skull was used to allow the brain to move past the foramen magnum boundary. This was the same for the addition of the CSF model. Figure 8.7 (a) and (b) show the geometry and mesh for the baseline geometry with foramen magnum and the addition of the CSF model with the foramen magnum respectively.

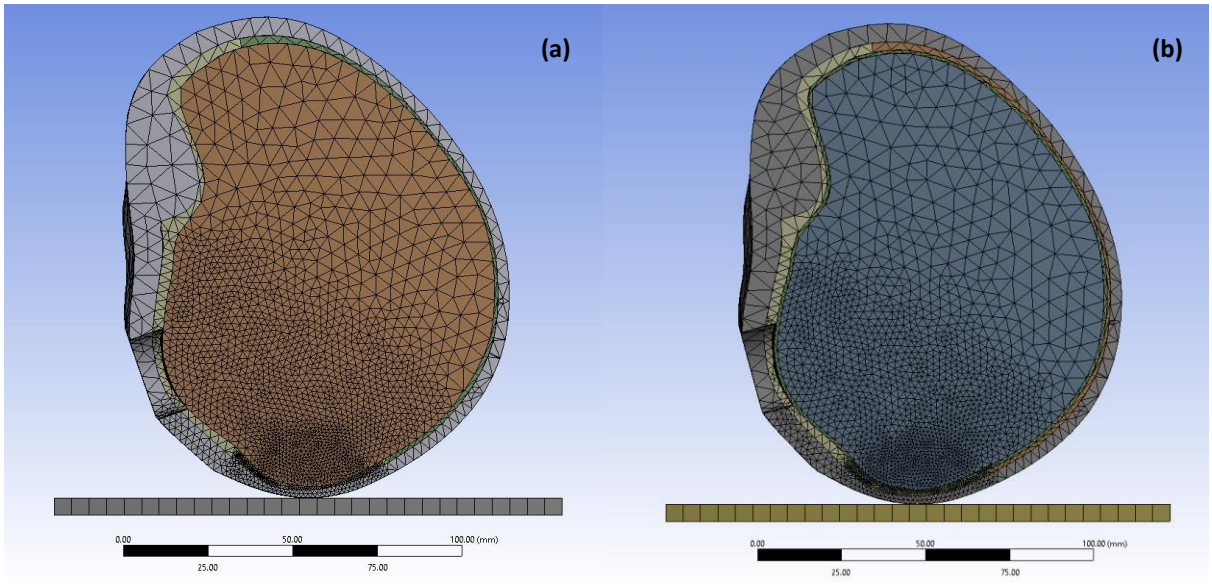

Figure 8.7: Geometry and mesh for baseline model with foramen magnum removed **(a)** and addition of CSF model with foramen magnum removed **(b)**.

Results

Impact Angle

The parametric study for impact angle showed significant differences in peak head acceleration, impact duration and HIC_{max}. Peak acceleration increased up to 32% for relative changes in orientation up to -20°, while the impact duration decreased by up to 5.4% and HIC_{max} increased by up to 38%. For relative angles ranging from 2.5 to 10°, there was relatively much less difference in peak acceleration and HIC_{max} (up to 6.6% and -0.8% respectively). Difference in impact duration for angles of 2.5 and 5° were greater than those for the same magnitude, but opposite direction, while there was a considerable difference for an angle of 10° relative to the baseline (12.7%). Table 8.1 summarises the differences in each of the three parameters for each impact angle, while Figure 8.8 presents the acceleration-time plots for each angle investigated.

Table 8.1: Results from changes to impact angle.

Impact Angle Relative to Baseline (°)	Peak Head Acceleration (g)		Impact Duration (ms)		HIC_{max}	
	Absolute	Percentage Difference	Absolute	Percentage Difference	Absolute	Percentage Difference
-20	123.0	31.9	9.4	-5.4	358	38.1
-15	118.7	29.4	9.5	-4.6	337	34.3
-10	109.4	23.4	9.6	-3.8	312	29.0
-7.5	108.6	22.8	9.5	-4.3	298	25.9
-5	105.2	20.3	9.7	-2.2	272	18.6
-2.5	95.6	12.3	9.8	-1.0	244	9.3
Baseline	**83.8**		**9.9**		**221**	
2.5	79.4	-5.6	9.8	-1.9	219	-0.8
5	78.7	-6.6	9.5	-4.7	221	0.0
10	81.2	-3.2	8.8	-12.7	220	-0.7

Note: anticlockwise is the positive direction, relative to the orientation of the baseline model.

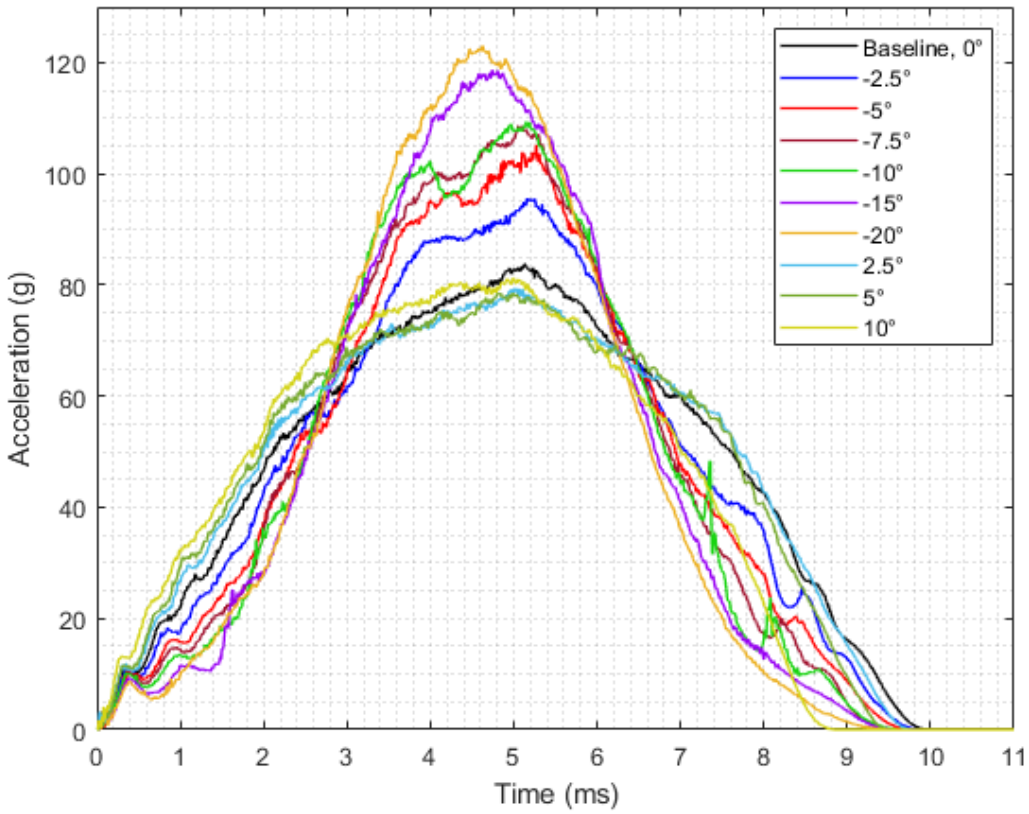

Figure 8.8: Acceleration-time plots for each impact angle.

Dual Layer Scalp

The addition of a dual layer scalp resulted in a peak head acceleration increase of 9.5% compared to the baseline model (91.8 g versus 83.8 g respectively) and a 5.0% increase in the impact duration (10.4 ms versus 9.9 ms). As seen in Figure 8.9, the acceleration-time trace for the dual layer scalp has a lower gradient for approximately the first 2 ms than compared to the baseline model. The gradient then increases relative to the baseline until peak acceleration is reached, where the opposite occurs during the rebound. This indicates the addition of the softer inner scalp tissue provides a greater energy absorption capacity in the early stages of the impact.

A noticeable feature of the dual layer scalp is the amount of element distortion in the inner scalp, as shown in Figure 8.10. This is a result of the much softer inner scalp tissue being sandwiched between two relatively stiffer tissues of the outer scalp and skull. The bonded contact method between the nodes at the inner-outer scalp and inner scalp-skull interfaces causes these nodes to remain in place relative to the respective tissues. This results in the significant skewing (shear strain) of the elements observed in Figure 8.10.

For the case where the inner scalp geometry was modelled using an identical material model as the outer scalp, there was an increase in the global stiffness as the peak acceleration increased relative to

both the original dual layer scalp model and the baseline (101.9 versus 91.8 and 83.8 g respectively), while the impact duration decreased (9.4 versus 10.6 and 9.9 respectively). It is expected that the model with identical material models for the inner and outer scalp is stiffer than that for where different material models are used due to the inner scalp being less stiff than the outer scalp. However, it is not expected that the model with identical material models is stiffer than the baseline as they are essentially the same model, apart from the addition of the extra geometric body and bonded contact interface. This means that bonded contact interface between the inner and outer scalp has significant influence on the response of the model as it is creating additional stiffness when, ideally, it should not.

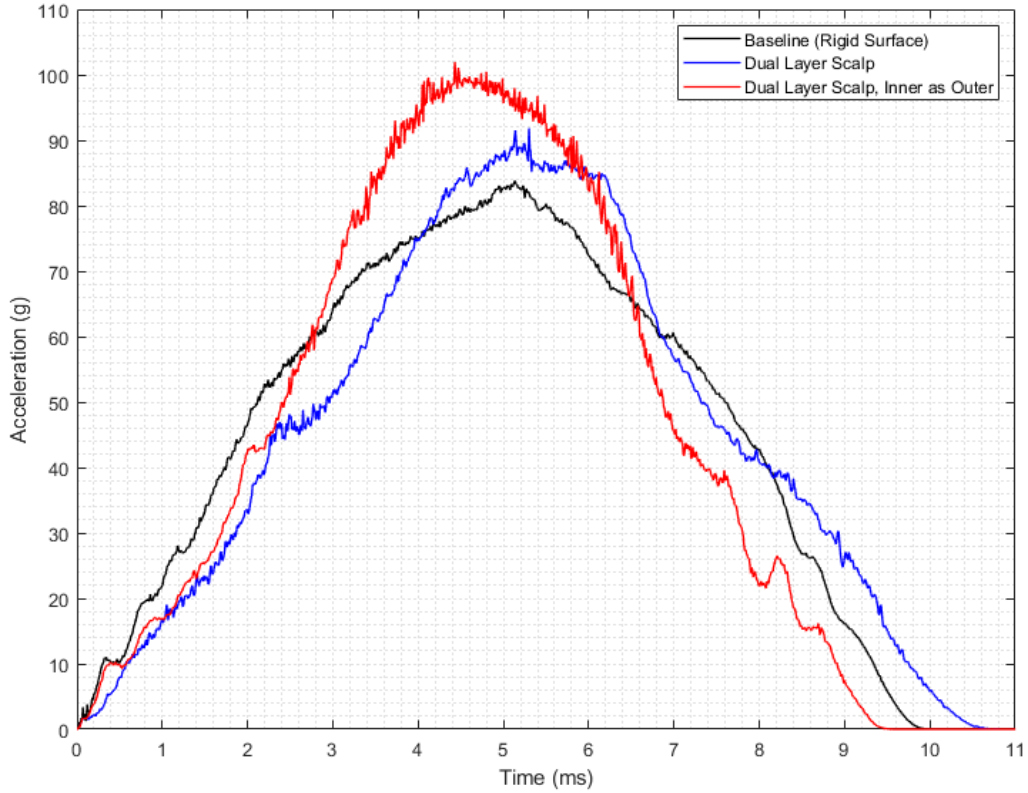

Figure 8.9: Acceleration-time plot for dual layer scalp compared to baseline model.

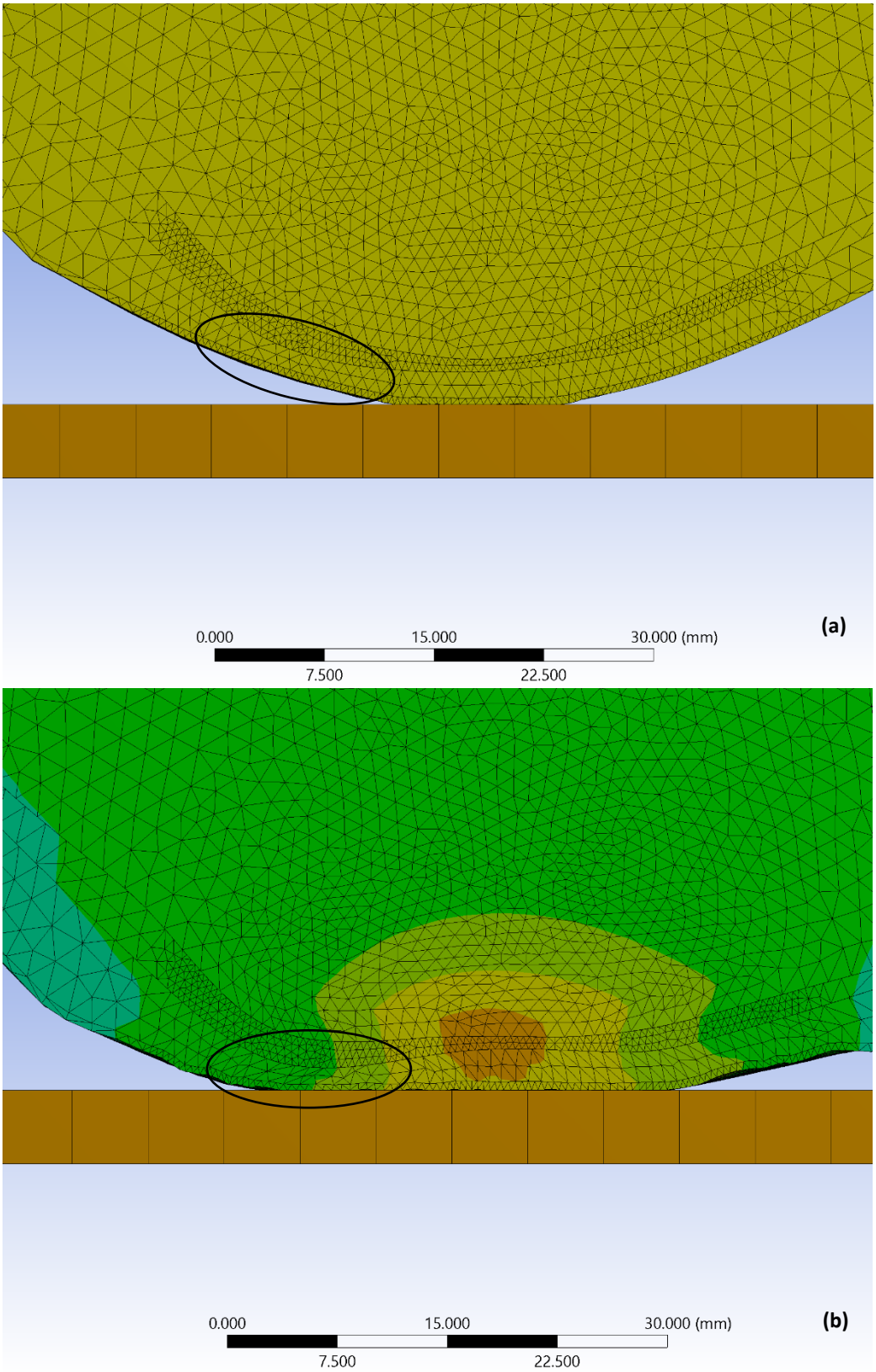

Figure 8.10: Elements of dual layered scalp at initial contact with impact surface **(a)** and at 1.75 ms **(b)** showing significant skewing of inner scalp elements, especially in the region circled.

Addition of CSF

The addition of the CSF resulted in an increase in the global stiffness of the head, as shown in Figure 8.11 where the peak head acceleration and impact duration are greater and shorter respectively than the baseline model. As the CSF model used frictional contact at the brain-CSF and CSF-skull interfaces, comparisons are made with the baseline model where frictional contact at the brain-skull interface is used. The peak acceleration increased 23% (76.0 g to 93.8 g), while the impact duration decreased by 7.7% (10.4 ms to 9.6 ms).

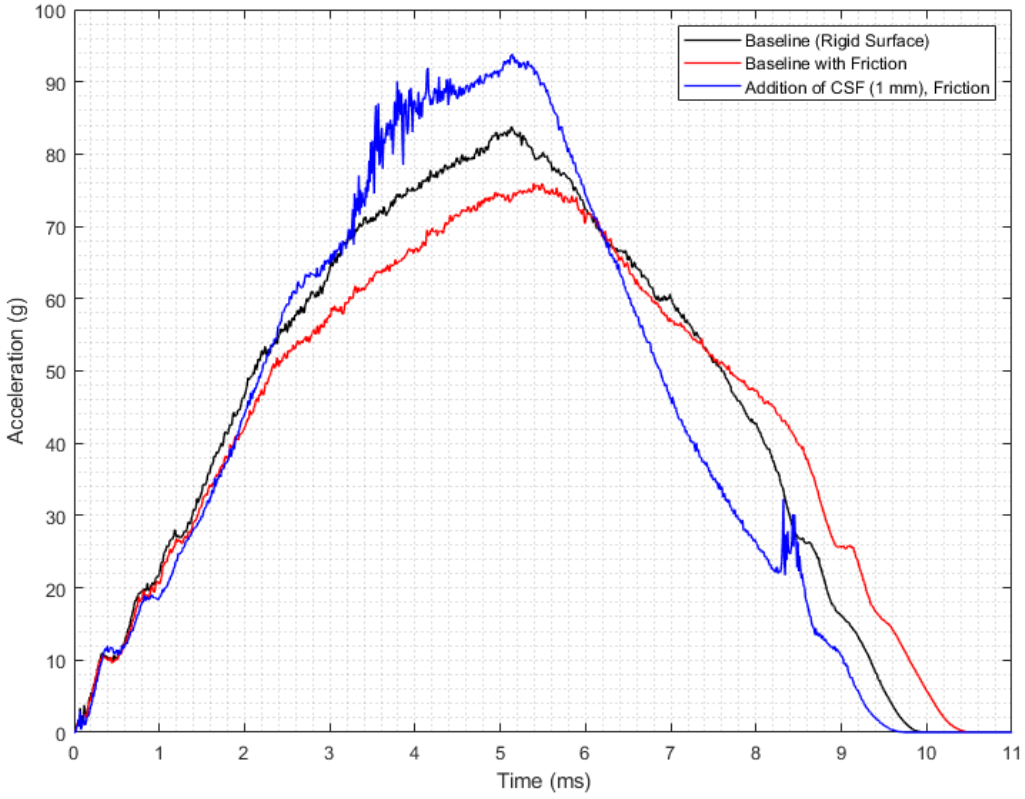

Figure 8.11: Acceleration-time trace for addition of CSF to baseline model.

Addition of Dura

The addition of the dura resulted in a much greater global stiffness than compared to the baseline model, as shown by the acceleration-time traces in Figure 8.12. For bonded contact at the brain-dura interface, the peak acceleration was 18.4% greater and the impact duration was 5.0% shorter (99.2 versus 83.8 g and 9.4 versus 9.9 ms respectively). Using a more refined mesh for the dura so that there were more elements through the thickness of the relatively thin tissue resulted in little difference in peak acceleration and impact duration results, as shown by the traces in Figure 8.12. For frictional contact at the brain-dura interface, the peak acceleration increased by 25% compared to the frictional baseline model, while the impact duration decreased by 5.7% (95.4 versus 79.0 g and 9.8 versus 10.4 ms respectively.

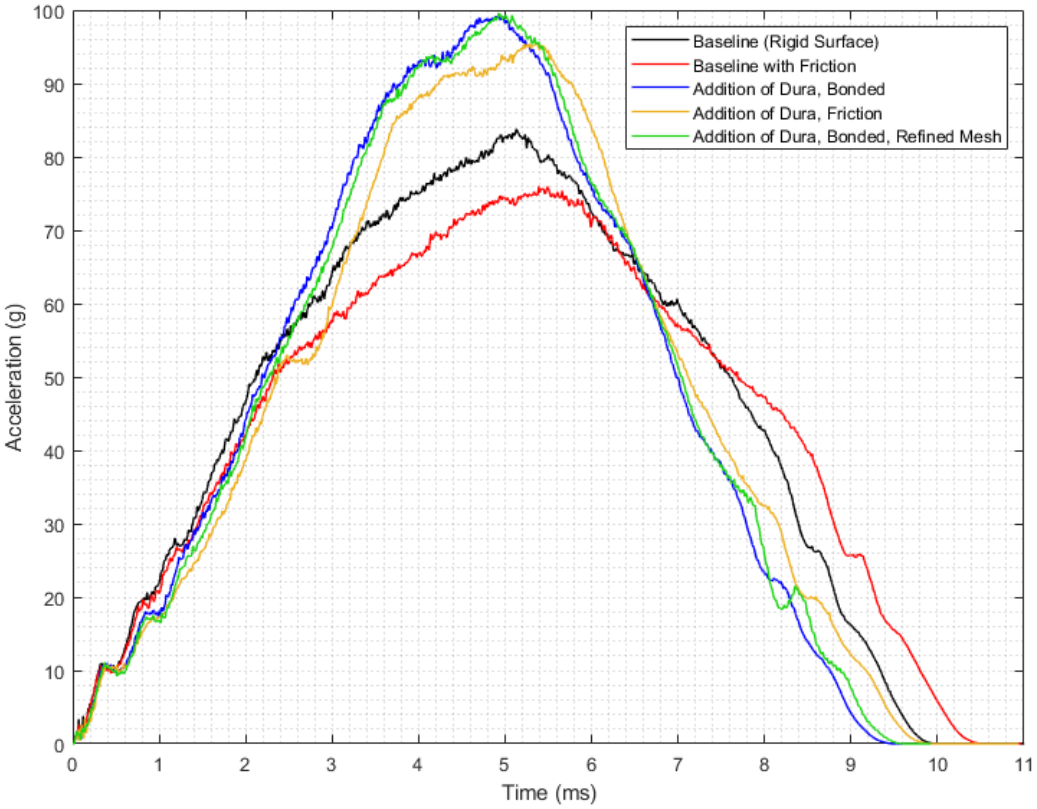

Figure 8.12: Acceleration-time plot for addition of dura to the infant head geometry.

Addition of Dual Layer Scalp, CSF and Dura

The addition of the dual layered scalp, CSF and dura resulted in a model with a greater global stiffness. The acceleration-time traces for both the bonded and frictional (dura-CSF/CSF-brain) interfaces were very noisy, as shown in Figure 8.13 (a). A Gaussian-weighted moving average filter with a window length of 20 was used to smooth the acceleration data. The filtered data overlaid with the unfiltered data is shown in Figure 8.13 (b).

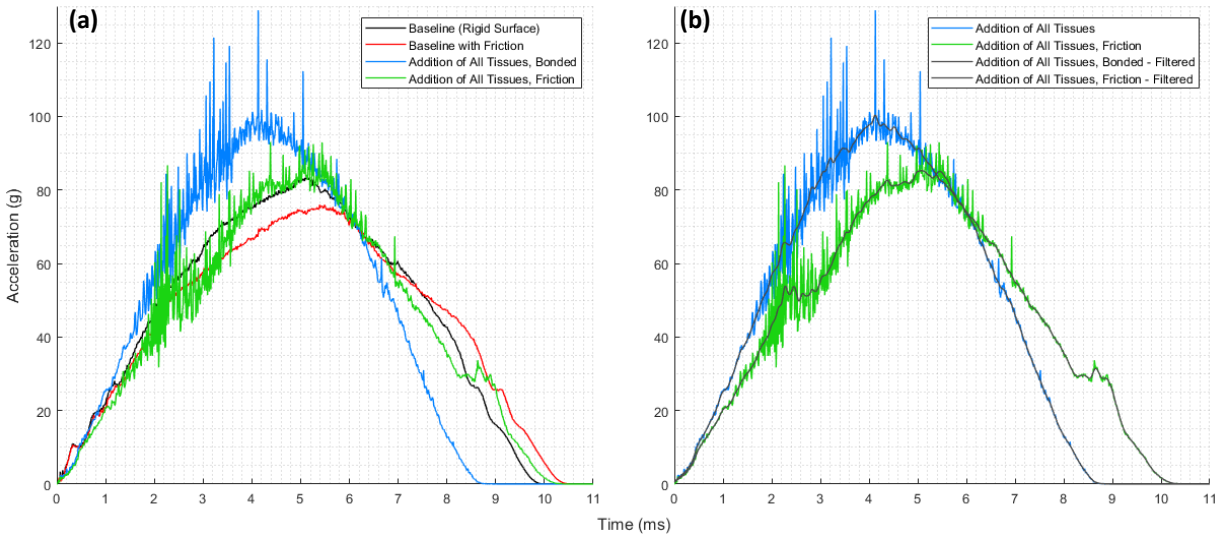

Figure 8.13: (a) Acceleration-time plots for FE model consisting of all head tissues. **(b)** Filtered acceleration data.

For the bonded interface model, the peak acceleration was 19.8% greater than the baseline model (100.4 versus 83.8 g respectively), while the impact duration was 11% shorter (8.8 versus 9.9 ms respectively). For the frictional interface model, the peak acceleration and impact duration was 12.2% greater and 2% shorter respectively compared to the frictional baseline model (85.3 versus 76 g and 10.2 versus 10.4 ms respectively). The acceleration-time traces are shown in Figure 8.14

Compared to the validation studies discussed in Chapter 4 and 6, the frictional interface model is comparable to Loyd (2011)'s five-month-old experimental cadaver (85.3 versus 81.0 g for peak acceleration). Table 8.2 presents a comparison of the original baseline FE model, the frictional interface model with all head tissues and the validation studies. Figure 8.15 presents the acceleration-time traces for these studies.

Table 8.2: Comparison of Peak Head Acceleration and Impact Duration for Occipital Impact

Study	Age	Experiment/FE Model	Drop Height (m)	Peak Head Acceleration (g)	Impact Duration (ms)
Prange et al. (2004)	1 Day	Cadaver Experiment	0.30	55.9	18.8
Prange et al. (2004)	11 Days	Cadaver Experiment	0.30	52.9	20.6
Loyd (2011)	5 Months	Cadaver Experiment	0.15	43.7	14.4
Loyd (2011)	5 Months	Cadaver Experiment	0.30	81.0	12.3
Loyd (2011)	9 Months	Cadaver Experiment	0.30	71.6	14.2
Li, Sandler, and Kleiven (2017)	5 Months	FE Model	0.30	78*	12*
Burgos-Flórez and Garzón-Alvarado (2020)	4 Weeks	FE Model	0.30	79*	8+*
Present Study, Baseline	3 Months	FE Model	0.30	83.8	9.9
Present Study, All Tissues, Frictional Interfaces	3 Months	FE Model	0.30	85.3	10.2

*Data inferred from plots presented in respective studies; no specific data provided

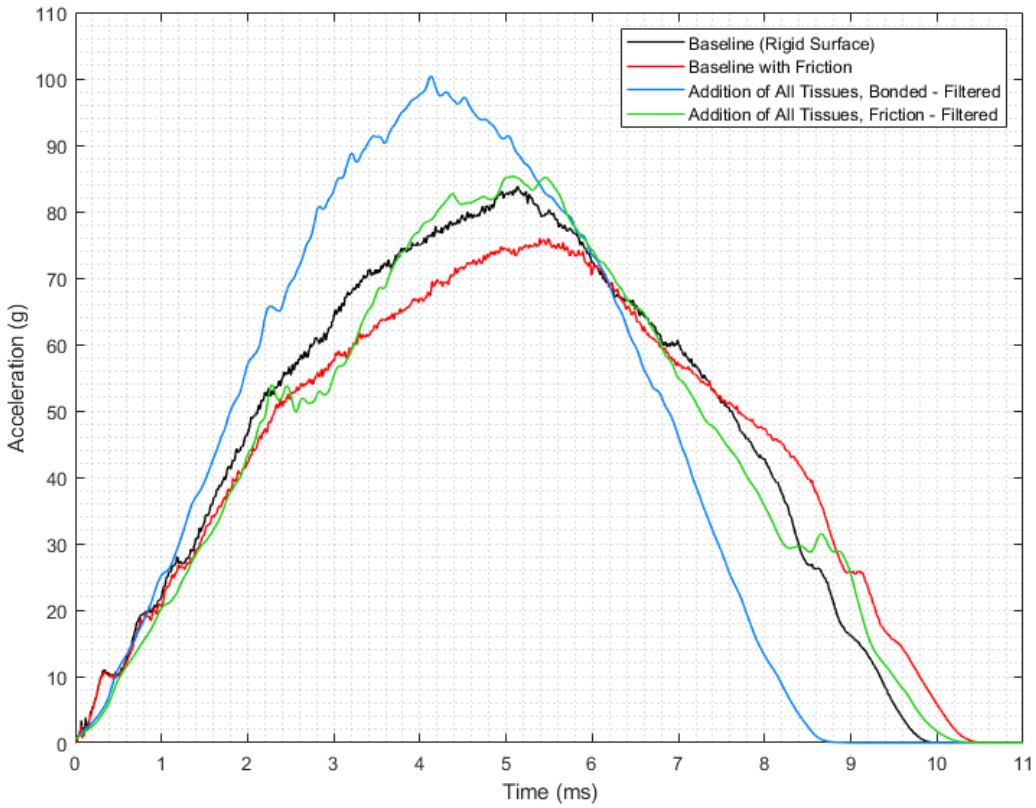

Figure 8.14: Acceleration-time plots for the addition of all tissues compared to the baseline model.

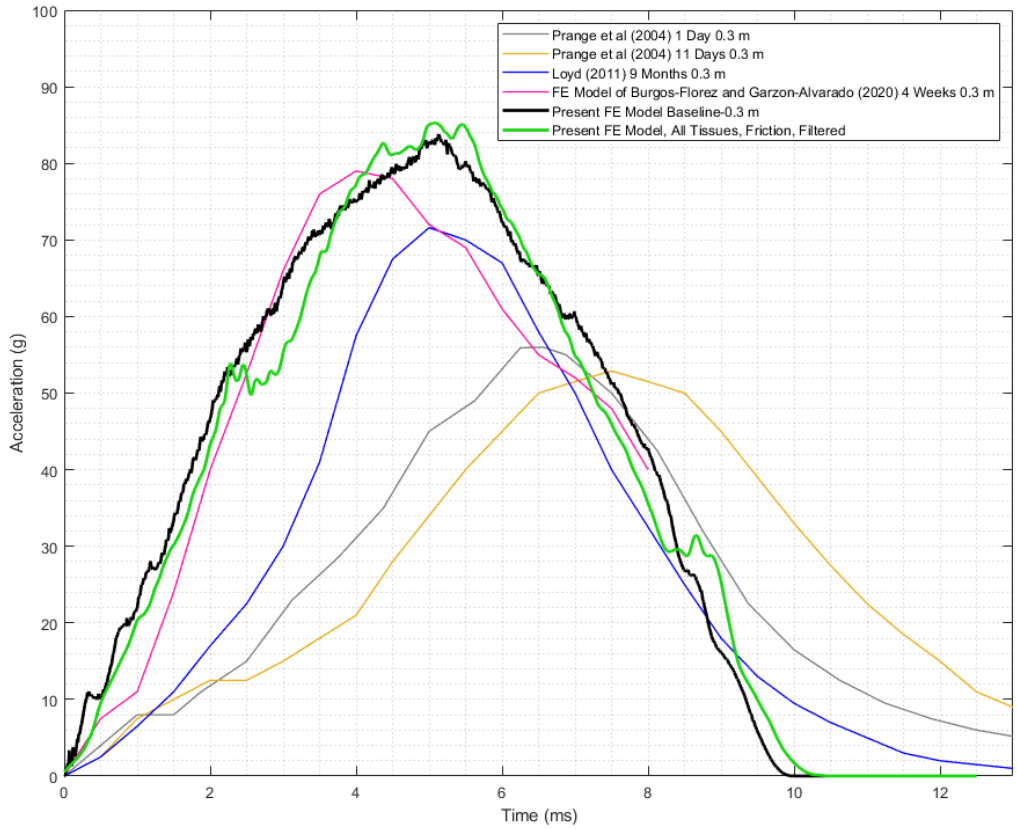

Figure 8.15: Acceleration-time plots for all tissue (frictional) FE model and validation studies.

Addition of Foramen Magnum

The addition of the FM to the baseline model allowed the brain to pass through the opening (Figure 8.16), effectively relieving the pressure in the cranial cavity. This resulted in a 9.2% decrease in peak head acceleration and a 20% increase in the impact duration relative to the baseline model where frictional contact was used at the brain-skull interface (76.0 versus 69.4 g and 10.4 versus 12.5 ms respectively). The global stiffness when the FM is included in the geometry is therefore less than the frictional baseline model. It is noted in Figure 8.16 that some nodes of the brain interfere with elements of the skull (circled areas). This shows that the frictional contact condition was not being adhered to. In this case, the brain was the slave surface while the skull was the master surface. Figure 8.17 presents the acceleration-time plots.

When the CSF is also included in the head geometry, the brain and CSF tissues do not pass through the FM (Figure 8.18). As a result, the peak acceleration and impact duration are similar for the model with the addition of the CSF but no FM (91.2 versus 93.8 g and 9.7 versus 9.6 ms with and without the FM respectively). It is expected that the CSF would pass through the FM due to its fluid-like properties. As it does not, the material model used to model its behaviour is unrealistic.

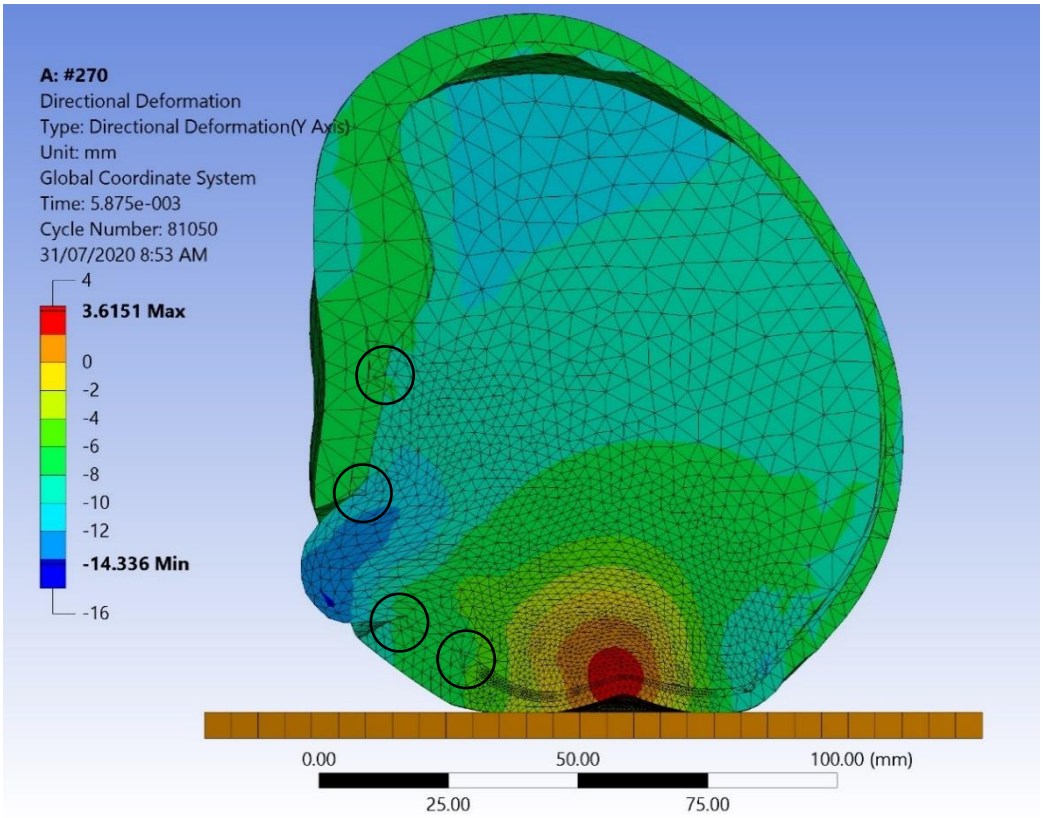

Figure 8.16: Brain passing through foramen magnum. Circled areas highlight interference of nodes not adhering to contact conditions.

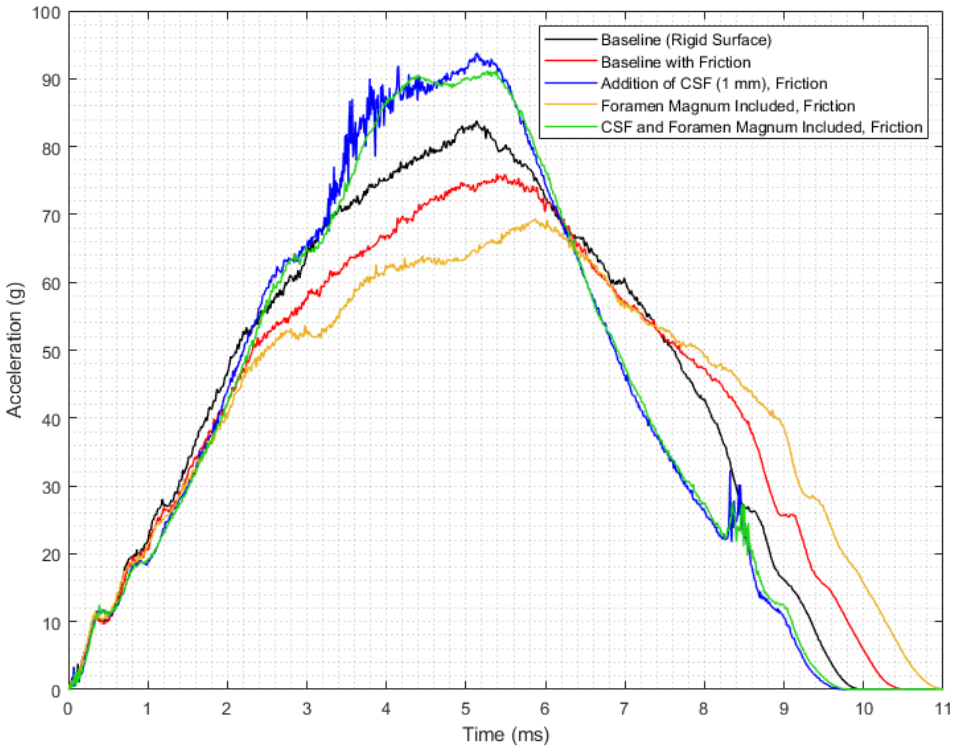

Figure 8.17: Acceleration-time plot for addition of foramen magnum in the infant head geometry.

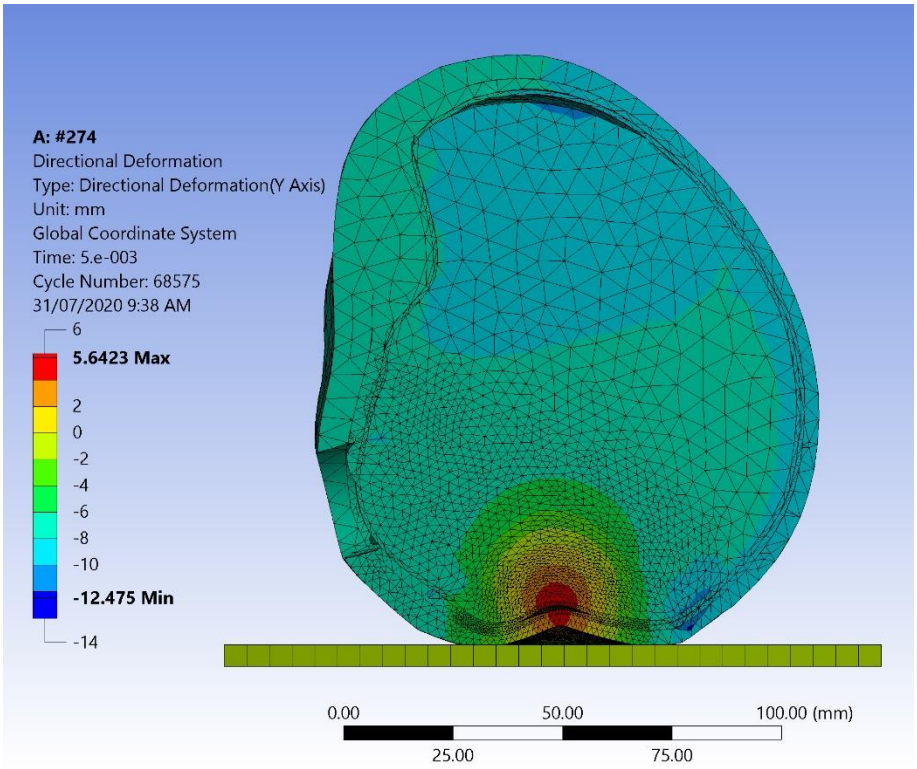

Figure 8.18: Inclusion of CSF with the foramen magnum does not result in the brain/CSF passing through the opening.

Discussion

Impact Angle

Only Li, Sandler, and Kleiven (2017) have used a FE model to investigate the influence of impact angle on the response of the infant head during an impact. The orientation of the head for all their impact locations (frontal, parietal, vertex and occipital) was determined based on the angles provided by Loyd (2011) so that they could ensure that they were correctly validating their FE model against the experimental cadaver data. Loyd (2011) presented data for the impact angle, which was measured as being the angle between the Frankfort plane and the impact surface. The Frankfort plane is a plane determined form the highest point on the opening of each auditory canal and the lower margin of the left orbit. Li, Sandler, and Kleiven (2017) found that some of their acceleration-time traces did not match those presented by Loyd (2011) for the same impact. Therefore, they investigated the influence of the impact angle on an occipital and right parietal impact for their newborn model, and a right parietal impact for their five-month-old model. In their baseline models, they observed a secondary peak in their newborn occipital impact that was not observed in the experimental cadaver impact test of Loyd (2011). The model was rotated 15° (to give a Frankfort angle of 102°) and the resulting acceleration-time trace was similar to the original, but the secondary peak did not occur, thus becoming more consistent with the experimental data. For the right parietal impacts, both the newborn and five-month-old models were rotated so that they had a Frankfort angle of 90°. The impact angle was found to have a profound influence on the curve characteristics and peak acceleration for the parietal impacts, as shown in their Figure 12 (Li, Sandler, and Kleiven 2017).

The findings from Li, Sandler, and Kleiven (2017) show that it is important to consider the impact angle when validating infant head FE models for modelling head impacts. This is also shown in the present study where there were differences in peak accelerations up to 32% for relative angles of up to 20°, as well as distinct differences in the acceleration-time traces.

The baseline model used a Frankfort angle of 65°, which is significantly different to the angle of 108° used by Li, Sandler, and Kleiven (2017) for their five-month-old occipital impact model. The angle used in the baseline model was chosen as it placed the contact point on the line of action of the centre of mass (COM) to minimise the degree of rotation during the impact. Due to the removal of the facial region in the geometry of the baseline model, the COM for an occipital impact shifts towards the vertex of the head, requiring a lower Frankfort angle to maintain the contact point on the COM's line of action.

When the baseline model is rotated in the positive direction, the acceleration-time traces are very similar to the baseline. However, when rotated in the negative direction, there are significant

differences in peak acceleration. When the model is rotated in the positive direction, the contact point of the geometry gets closer to the skull base, which was simplified to close the foramen magnum. Scalp tissue also exists in this region of the model, which is not consistent with reality. The thicker cranial bone in this region would act to stiffen the model, while the thicker scalp would result in the model becoming less stiff as the softer tissue can absorb more energy. These two opposing effects may act to produce the similar acceleration-time traces observed for the rotation in the positive direction. When the head geometry is rotated in the negative direction, the orientation of the head approaches that of a vertex impact. This means that the parietal bone has more of an influence on the global stiffness as more of the stiffer bone is in the deformation region. The parietal bone is 38% stiffer than the occipital bone (elastic moduli for the occipital and parietal bones are 430 and 592 MPa respectively), thus is likely to be the cause of the greater global stiffness.

Li, Sandler, and Kleiven (2017) identified the impact angle for an occipital impact as requiring further investigation to see how the characteristics of the acceleration-time trace varies. The present study confirms that there is significant difference in the peak acceleration and HIC_{max}, and minor differences in impact duration. However, the differences may be due to features unique to the baseline model, (such as the simplified geometry) and may not translate to other models that use a detailed geometry with the inclusion of the facial region. Although, it is expected that the findings for the rotation towards a vertex impact are relevant due to the geometry being anatomically correct in this region and the differences in the stiffness of the occipital and parietal bones.

Addition of a Dual Layered Scalp

The scalp is commonly modelled as a single layer, using an isotropic elastic material model (Brooks et al. 2018). In some studies, the scalp is not modelled (Burgos-Flórez and Garzón-Alvarado 2020). Li, Sandler, and Kleiven (2017) modelled the scalp as two layers: a dense connective tissue layer and an adipose tissue layer. The adipose tissue layer largely consists of fat and is softer than the outer connective tissue layer. As reviewed in Chapter 4, no paediatric data was available, so Li, Sandler, and Kleiven (2017) used adult parameters for the adipose layer and scaled the connective tissue layer to be one tenth of that for adults. Parameter data came from Fahlstedt et al. (2015). Fahlstedt et al. (2015) modelled the scalp as four elements thick, with three elements for the adipose tissue and the outer layer of elements as the connective tissue. Based on an average infant scalp thickness ranging from 2.0 to 3.4 mm (as measured by Li, Sandler, and Kleiven (2017)), this suggests the outer scalp layer is around 0.5 mm thick at a minimum. In this study, the outer scalp was modelled as 0.5 mm thick, resulting in an increase of 100% in computational time due to a smaller minimum characteristic element length that caused a smaller time step compared to the baseline model. Due to the large

number of simulations performed for the studies in Chapters 4 and 6, this increase in computational time was deemed untenable and therefore was a trade-off against model biofidelity.

Li, Sandler, and Kleiven (2017) do not detail how each tissue layer interacts with one another; that is, it is unclear whether there is bonded or sliding contact between tissues, or if shared topology is used (shared topology shares nodes at the interface of different geometric bodies). This has implications for determining how their dual scalp layer model behaves. If the scalp and skull tissues are bonded together, the nodes of the softer inner scalp will not be able to move relative to the skull and outer scalp tissues. This would result in high shear strains in the inner scalp tissue layer, causing the elements to become highly distorted. This was observed in the present FE model where bonded contact between the tissues was used. As a result, the highly distorted elements resulted in solver failures due to the time step becoming too small. When running the same model but with the inner scalp layer set to the same material as the outer scalp, the model solved successfully. Therefore, the softer inner layer and the bonded contact were the direct cause of the solver failure. As Li, Sandler, and Kleiven (2017) do not detail the contacts used between their tissue layers, it cannot be determined whether they experienced similar behaviour. To get the FE model to solve, adjustments to the mesh for the inner scalp were made until a suitable mesh was found. This mesh was used in the final model and was described earlier in the methods section. However, it is clear that the model was dependent on the mesh and hence provides some uncertainty over the validity of the results.

The addition of the dual layer scalp resulted in a peak head acceleration that was 9.5% greater than the baseline model and the impact duration was 5.0% longer. This indicates that the global stiffness is both greater and less than the baseline model, which is a contradiction. It is expected that the softer inner scalp layer will absorb more energy during the initial impact, leading to a lower initial stiffness. This is observed when comparing the acceleration-time traces of the current model and the baseline. A stiffer material requires a greater force to produce the same magnitude of strain as that of a material that is less stiff. Therefore, differences in the gradient of the acceleration-time curve (the force-time curved when acceleration is multiplied by the head mass) indicate relative differences in the global stiffness of the infant head. The initial gradient of the curve for the dual layered scalp model is lower than that of the baseline model. This indicates that the initial contact stiffness of the dual layered scalp model is less than that of the baseline, hence, the softer inner scalp is providing additional energy absorption. However, the softer inner scalp does not explain the increase in peak acceleration.

An increase in the global stiffness of the current model compared to the baseline model could be explained by the addition of the bonded contact interface between the inner and outer scalp bodies. Bonded contact is implemented in the FE method by adding constraint equations to the global system

of equations. These constraint equations force each node on one contacting surface to move with the point on the surface of one of the elements making up the other connecting surface. Hence the nodes on one surface are 'bonded' to the other surface. When the meshes on the two surfaces are different, these constraints connect adjacent elements in ways they would not otherwise be connected in a matching mesh or shared node interface. This effect can be reduced by increasing the mesh density as the layer of affected elements would become thinner.

The artificial stiffening effect of the additional bonded contact interface is also observed when the inner scalp material model was changed to that of the outer scalp (so the inner and outer scalp had identical material models). This change resulted in an increase in the global stiffness compared to using the inner scalp material model, which was expected as the outer scalp is stiffer than the inner. However, the global stiffness was also much greater than the baseline model, which was unexpected due to there being no difference in the material models used. The only difference between the two models was the splitting of the scalp geometry, which created a boundary between the inner and outer scalp and thus the additional bonded contact interface. Therefore, the artificial stiffness resulting from the bonded interface is the likely cause of the increase in global stiffness observed when a dual layer scalp is added to the FE model. Future work is required to better understand the effect this has on the stiffness of the model. This could include running models with a matching mesh on each connecting surface so that the nodes are constrained to nodes (rather than points on an element) and comparing the results with a model using a shared node interface and a mismatched mesh at the interface.

Addition of CSF

As reviewed by Brooks et al. (2018) (Chapter 3 of this thesis), the CSF is commonly included in infant head FE models; only Coats, Margulies, and Ji (2007) and Khalid et al. (2019) did not include it in their models. Coats, Margulies, and Ji (2007) modelled a one-millimetre gap between the brain and skull to represent the subarachnoid space. There is no reference to CSF in their study and therefore it is assumed that it was not modelled, leaving the subarachnoid space as a void. As discussed in Chapters 4 and 6, Khalid et al. (2019) used a sliding contact method for the interface between the brain and skull. The behaviour of the CSF is commonly modelled using an isotropic elastic material model (Brooks et al. 2018). Most studies define the elastic model using an elastic modulus and Poisson's ratio (Brooks et al. 2018), with the data originating from adults (Willinger, Taleb, and Kopp 1995). Li, Sandler, and Kleiven (2017) use a bulk modulus originating from Kleiven (2007), which was also used in the present study.

A common challenge with biomechanical modelling is that there are often fluids involved that have high bulk modulus but no shear stiffness. In FE modelling, this can be approximated using a large Poisson's ratio (approaching 0.5), however, this can lead to highly distorted elements if there is even a small amount of flow. Careful engineering judgement is required to maintain the validity of such models, and in some cases, combined fluid structure interaction (FSI) modelling is required. Fluid structure interaction generally involves using a Eulerian mesh for the fluid like material rather than a Lagrangian mesh typically used in structural modelling. However, FSI typically adds additional complexity to an already complex model. In the case of the human head, the CSF is a fluid that surrounds the brain and spinal cord. Therefore, fluid structure interaction (FSI) is a more suitable FE modelling technique to accurately model the behaviour of the CSF. However, the method of modelling the CSF as a quasi-fluid (has a realistic bulk modulus and low shear modulus) is most used in the current literature (using an isotropic elastic material model).

The addition of the CSF increased the global stiffness relative to the baseline model. Peak acceleration and impact duration were 23% greater and 7.7% shorter than the baseline model respectively. Using a bulk modulus and Poisson's ratio of 2.1 GPa and 0.49 respectively, the equivalent elastic modulus is 126 MPa. This modulus is approximately 30% of the stiffness of the occipital cranial bone. Therefore, the CSF will contribute a reasonable level of stiffness to the global stiffness and hence is likely the reason for the increase in global stiffness observed. In the existing FE models in the literature, an elastic modulus of 0.012 MPa is used (Brooks et al. 2018). This is considerably smaller than the equivalent elastic modulus if a bulk modulus of 2.1 GPa and Poisson's ratio of 0.49 is used. When this modulus is used to define the CSF material model, the FE model crashes due to a significant decrease in the time step. This was because the CSF elements became severely distorted (as would be expected), hence decreasing the minimum element characteristic length. Lagrangian meshes typically cannot handle large mesh deformations.

Using the elastic equations, the elastic modulus, *E,* can be defined using the bulk modulus, *K,* and Poisson's ratio, *v* (Bower 2009):

$$E = 3K(1 - 2v) \tag{8.1}$$

When the Poisson's ratio is changed from 0.49 to 0.499 for example, there is an order of magnitude change in the elastic modulus. For an elastic modulus of 0.012 MPa and Poisson's ratio of 0.49 (as used in existing infant head FE models (Brooks et al. 2018)), the calculated bulk modulus is 0.2 MPa, which is significantly smaller than the 2.1 GPa used by Li, Sandler, and Kleiven (2017). Therefore, there is a significant discrepancy in the material properties of the CSF used in the literature. Further research in this area is required to develop an appropriate method to model the CSF in FE head impact models.

As discussed in Chapter 4, the CSF was not included in the baseline model due to the increased computational time resulting from a much smaller element characteristic length. This was due to the relatively thinner geometry and complex curvature of the geometry in the facial and orbits region requiring smaller elements or relatively larger elements that were more skewed. Including the CSF in the FE model resulted in a 22% increase in computational time over the baseline model.

Addition of Dura

Including the dura in infant head FE models is inconsistent in previous models. Roth, Raul, and Willinger (2010), Li et al. (2013), Li, Sandler, and Kleiven (2017) include the dura, while Coats, Margulies, and Ji (2007), Khalid et al. (2019), Burgos-Flórez and Garzón-Alvarado (2020) do not. Similar to the CSF, the baseline model in Chapter 4 did not include the dura due to the relatively smaller thickness increasing the total computational time. At 0.5 mm thick, the dura was over 50% thinner than the next thinnest tissue in the baseline model. In the refined mesh region, some areas had two elements in the through thickness direction, while other areas had only one. Having one element in the through thickness direction for tetrahedral elements does not capture the bending effects of the dura. Using a much smaller element size would increase the number of elements in the through thickness direction but would also increase the computational time significantly. Fortunately, because it is so thin, the dura behaves mechanically as a membrane, so bending effects are negligible. The addition of the dura to the baseline FE model (using the described mesh) resulted in an increase of 28% in computational time.

The global stiffness of the infant head FE model increased relative to the baseline model when the dura was added to the geometry. Peak head acceleration and impact duration were 18.4% greater and 5.0% shorter than the baseline respectively.

A Mooney-Rivlin hyperelastic model was used to model the behaviour of the dura. The initial shear modulus, G can be calculated using the Mooney-Rivlin parameters C_{10} and C_{01} by (ANSYS Inc. 2019b):

$$G = 2(C_{10} + C_{01}) \tag{8.2}$$

This gave an initial shear modulus of 2.8 MPa. As an approximation of the stiffness of the dura, the equivalent elastic modulus is 8 MPa (using a Poisson's ratio of 0.45 as used in the literature (Brooks et al. 2018)), which is significantly less than that of the occipital bone (430 MPa). Therefore, unlike the CSF, the stiffness of the dura is not the cause of the greater global stiffness.

Compared to the baseline model, only the addition of 0.5 mm thick layer to the geometry was changed. However, such a geometric change also resulted in a slight decrease in the physical size and volume of the brain, an additional bonded contact boundary between the dura and skull, and a

different mesh for the cranial cavity tissues. All these could be a cause for the difference in the global stiffness. As a check, the dura was modelled as brain tissue. This meant that the model was the same as the baseline model except for the additional boundary at the interface of the dura and brain geometry the mesh is forced to be created along (this interface had a bonded contact condition). There was very little change in the peak head acceleration and impact duration (less than 1%). This suggests that the dura has very little effect on the stiffness of the FE model. However, it does not explain the difference in the global stiffness relative to the baseline model. Similar to the dual layered scalp, the use of a bonded contact condition at the dura-skull interface will create artificial stiffness in this region, resulting in the increase in the global stiffness relative to the baseline model.

Addition of Dual Layer Scalp, CSF and Dura

The addition of the dual layer scalp, CSF and dura combines all the additional tissues previously investigated individually and results in a more biofidelic geometry. Using such a geometry brings it in line with the geometry used by Li, Sandler, and Kleiven (2017) in terms of the different head tissues modelled.

For both models consisting of bonded and frictional contact interfaces, the global stiffness is greater than that of the respective baseline models. For the bonded interface model, peak acceleration was 19.8% greater, while the impact duration was 11% shorter. For the frictional interface model, the peak acceleration and duration were 12.2% greater and 2% shorter respectively. Given that the addition of each tissue individually all resulted in an increase in the global stiffness, it is not unexpected that the global stiffness increases relative to the baseline model. It could be expected that the global stiffness increase for this model would be the sum of each individual increase; that is, the peak acceleration should increase by greater than 50%. However, this is not the case. The increase in global stiffness from adding the dual layer scalp and dura individually was due the addition of a bonded contact interface artificially stiffening the model due to the presence of the associated constraints, whereas they would have been free to displace in the volume had the interface not been present (as is the case in the baseline model). In the present model for all three additional tissues, this effect also occurs, but does not sum together to provide a ‘double’ effect. The relative stiffness of the CSF is likely to also play a part in the present model.

Contact modelling of the tissue interfaces can be bonded, sliding or frictional. Another method of modelling different adjacent materials in a geometry is to partition the geometry, effectively creating multiple bodies within the same geometric body. When meshed, shared nodes are forced to be created at the partition boundaries. The shared nodes, in principle, are the same as bonded contact except that no added constraint equations are required to force the surfaces to move as one. This

avoids the artificial stiffening effect that results from the bonding surfaces with miss-matched meshes. This method is known as 'shared topology' in ANSYS Mechanical (ANSYS, Inc., Canonsburg, Pennsylvania, USA). While such a method is suitable for 'simple' geometries, complex geometries (such as the human head) can be challenging to partition. This was found in the preparation for this thesis where an attempt was made to partition a solid head geometry into the various tissue layers. Due to the complex curves involved, the mesh did not adhere to the partition boundaries, hence node sharing did not occur.

As identified in Chapter 3, there is very little explanation or discussion in the existing literature on the contact methods used between each tissue layer. The findings in this chapter of the bonded contact methods used at the tissue interfaces indicates that such a method could be causing an over stiffening of the FE models. This is likely to be another cause for the stiffer response of the baseline model relative to experimental cadaver data. The baseline model in Chapters 4 and 6 use bonded contact at the scalp-skull and skull-suture interfaces. Future work should investigate more the influence of different contact types on the global stiffness of the model. This would provide an understanding of how much of the global stiffness is due to the contact constraints and what is an appropriate method for modelling the interfaces between each tissue. A lack of discussion in the existing literature suggests that over stiffening due to the contact constraints has not been previously considered.

In forensic reconstructions using FE models, it is desirable to compare the predicted injury patterns with those observed from the case being reconstructed. To make accurate injury predictions, a high-fidelity FE model is required. Such a model must include all head tissues that reasonably contribute to the overall stiffness, along with appropriate tissue failure models for each tissue. Achieving this requires a high computational cost, making modelling only feasible on expensive high-performance computers. To make the computational time tractable on standard professional grade computers, trade-offs with the biofidelity of the model are required. The all-tissue frictional interface model in the present study produces a similar response as that of the baseline model (using bonded contact interfaces). It is, therefore, comparable to the five-month-old experimental cadaver impact by Loyd (2011), as well as the five-month-old FE model by Li, Sandler, and Kleiven (2017). However, while it is a higher fidelity model in terms of the number of head tissues included, it has a 70% greater computational time. Given the significant number of simulations performed with the baseline model, the simplifying assumptions used for the baseline model to reduce the computational time were somewhat justified.

Addition of Foramen Magnum

The experimental cadaver head impacts of both Loyd (2011), Prange et al. (2004) sealed off the foramen magnum (FM) to stop the cranial contents from extruding out. Prange et al. (2004) used gauze to block the FM, while Loyd (2011) sealed it using poly-methyl methacrylate. In existing FE models, the FM is typically not mentioned (Roth et al. 2007, Li et al. 2013, Burgos-Flórez and Garzón-Alvarado 2020). In the studies where it is mentioned, the FM is either left open or sealed off. Coats, Margulies, and Ji (2007) left the FM open so that the brain could freely pass through it, while Li, Sandler, and Kleiven (2017) fixed it so that it replicated the experiments of Loyd (2011). Li, Sandler, and Kleiven (2017) noted that in their model of the five-month-old replicating the compression experiments also conducted by Loyd (2011), the CSF was extruded out of the FM. This caused the FE model to crash due to the distortion, as a Lagrange mesh cannot handle large mesh distortions. Loyd (2011) left the FM free for the compression tests, which is also replicated for Li, Sandler, and Kleiven (2017) compression models.

The CSF is relatively incompressible and so would flow out of the cranial cavity and into the spinal cord via the FM. This would have an influence on the response of the infant head during the impact as the flow of the CSF will not impede the motion of the brain as much compared to if the FM was sealed. Therefore, it is important to investigate the effect of the inclusion of the FM. However, for the purposes of FE model validation, the FM should be either sealed or left free depending on how it was left for the experimental tests.

The addition of the FM to the geometry of the baseline model resulted in the peak acceleration decreasing by 9.2% and the impact duration increasing by 20% compared to the baseline model (with frictional contact at the brain-skull interface). Therefore, the global stiffness decreased with the addition of the FM. This is expected as the brain is able to move through the opening of the FM. The FE model showed a relatively large volume of brain passing through the FM. This is unlikely to occur in reality due to the physical constraints created by the spinal cord and other anatomical features, as well as resisting back pressure from the CSF already present in the spinal cord. No mention is made by Coats, Margulies, and Ji (2007) on how much of the brain passed through the FM, so no comparisons to existing literature can be made. As no experimental data currently exists for cadaver infant head impacts with an open FM, the results of this FE model cannot be validated.

When the CSF is included in the head geometry, there is little difference in the peak acceleration and impact duration (less than 3%). The CSF and brain do not pass through the FM. It would be expected that at least the CSF would start to pass through the FM as this is what is expected in reality. Therefore,

this indicates that the material model used to predict the behaviour of the CSF is inappropriate, further confirming the conclusions made in the *Addition of the CSF* section previously discussed.

One limitation with this FE model is the mesh was not refined enough in the region of the FM. Additional refinement to the mesh in this region was made compared to the baseline model. However, it was not enough due to some nodes of the brain penetrating the cranial bone at the edges of the FM and closer to the contact area. This could have influenced the response of the head during the impact as the motion of the brain may have been altered if the contact boundary was adhered to. This could have been improved by using a significantly finer mesh, however, the computational time increased significantly.

The opening for the FM was created by extruding a circle of diameter 25 mm through the scalp and skull. In reality, the geometry of the FM is much more irregular and does not have sharp edges on the inside surface of the skull. As discussed previously, there would also be the presence of the top of the spinal cord and other anatomical features.

Conclusions

This chapter described variations to the baseline model and an investigation of the effects of these changes on the global stiffness of the FE model. The baseline model utilised simplifying assumptions made to reduce the computational time. This resulted in a FE model that was not as biofidelic as some of those in the existing literature.

The impact angle was investigated to determine how it influenced the global stiffness relative to the baseline model as Li, Sandler, and Kleiven (2017) found that it had a profound influence on the acceleration-time curve characteristics and peak acceleration. In this study for an occipital impact, it was found that rotating the head towards the vertex had a significant effect on the global stiffness. This is likely due to the parietal bone playing a greater role in the impact than at the original impact angle. The parietal bone is 37% stiffer than the occipital bone.

In the baseline model, a dual scalp layer (similar to Li, Sandler, and Kleiven (2017)), the CSF and dura were not included. When each tissue was added individually, the global stiffness increased relative to the baseline for each tissue. This was unexpected in all cases as each tissue should have resulted in a decrease in the stiffness. For the dual scalp, the inner scalp is softer than the outer scalp, hence the global stiffness should have decreased. When the inner scalp material was changed to be identical to that of the outer scalp, the global stiffness still increased relative to the baseline. The geometric boundary between the inner and outer scalp geometries required an additional bonded contact interface. This contributed to the observed increase in the global stiffness due to the artificial

stiffening resulting from the associated constraint equations. An increase in stiffness occurred even when the inner and outer scalp had identical material models. Little discussion is present in the existing literature of the contact methods used at the various tissue interfaces. As the bonded contact increases the stiffness at the interfaces, future work needs to investigate more closely suitable tissue interface contact conditions and assess how it influences the response predicted by the FE model.

The increase in the global stiffness as a result of modelling the CSF was due to the equivalent elastic modulus being 30% of that of the occipital bone. Therefore, it had a greater contribution to the overall stiffness of the model, which is unrealistic as the CSF is a fluid. Future work is required to determine a more suitable method of modelling the behaviour of the CSF.

With the addition of all three tissues, the global stiffness increased relative to the respective baseline models for bonded and frictional contact at the dura-CSF and brain-CSF interfaces. The frictional contact interface model was comparable to the baseline model, as well as the five-month-old cadaver experimental data of Loyd (2011) and the FE model of Li, Sandler, and Kleiven (2017). This suggests that the simplifying assumptions used in the baseline model can produce a model that has a similar stiffness as a model of greater biofidelity but has a 70% reduction in computational time.

The addition of the foramen magnum allowed the brain to pass through the opening, reducing the global stiffness of the model relative to the baseline model. However, due to other anatomical features not being modelled (such as the spinal cord), the degree of displacement of the brain tissue is not likely to be representative of reality. When the CSF was also included, there was very little displacement of the CSF and brain through the foramen magnum. Considering that the CSF naturally flows through the foramen magnum, this provides further evidence that modelling the behaviour of the CSF requires attention.

Using FE models of the infant head to accurately reconstruct the injury patterns in forensic cases requires high-fidelity models. However, this comes at a significant computational cost. This cost is exacerbated by the fact that a greater mesh density can resolve many of the issues identified in this study, such as the artificial stiffness caused by the bonded contact interfaces. Standard professional grade desktop computers are inadequate and high-performance computers have significant financial cost. Therefore, trade-offs with the computational cost and model fidelity are required to make forensic reconstructions tractable. However, innovative modelling techniques can be used to maintain a suitable level of accuracy while minimising computations.

Chapter 9 Conclusions and Future Work

The overall goal of this thesis was to contribute towards developing infant head finite element (FE) models. Such models can be used in forensic reconstructions to help determine whether an infant's head injuries were a result of an accident or abusive head trauma. Modelling the human infant head involves many complex challenges, such as unique head geometry, age-dependent tissue properties, lack of infant tissue material property data, rate-dependent tissue properties, complex loading scenarios and a lack of available experimental data to validate such models against. Use in forensic reconstructions requires high-fidelity models, which are computationally expensive.

The overarching question that guided the research presented in this thesis was:

What is required to further develop infant head finite element models to make them sufficiently accurate for use in forensic reconstructions while having an acceptable computational cost?

A review of the current literature found that several areas of the FE modelling process could be improved to further develop such models. However, the greatest limitation was the material property data for infant head tissues due to a lack of human infant head tissues available for material testing. Other findings include:

- For the geometry, a lot of work has already been carried out for obtaining both specific and generalised geometry of the infant head from computed tomography scans. Therefore, future work should be concentrated in other areas of the modelling process.
- A variety of element types have been used to create the meshes in the FE models. To date, no research has been conducted on the suitability of one element type over another, especially for solid elements, where there are trade-offs between using hexahedral and tetrahedral elements.
- Most FE models to date are used principally to model low height falls onto a flat, rigid surface. There is value in investigating the effects of drop height and impact surface stiffness on the response of the FE model, as well as different surface types (such as an edge of a surface) and blunt force impacts from weapons. This would allow for greater understanding of the predicted injury patterns expected from such impacts. Contact conditions at tissue interfaces in the current FE models also lack details and would benefit from further investigation, as would methods for predicting skull fracture.
- Validation of the FE models to date largely consists of comparing acceleration and force-deflection plots to cadaver drop and compression tests, with only a few studies comparing

stress and strain patterns with observed fracture patterns. Comparison of the acceleration and force-deflection plots allows for validation of the models at a global level but does not necessarily mean that the local parameters are accurate. Validation of individual material models for each tissue has not been completed.

These findings were used to develop specific aims for the remainder of this thesis so that it can contribute to the development of infant head FE models. These aims and their respective conclusions are outlined in the following section.

Conclusions

Aim #1

Determine which material model parameters have the most influence on the response of an infant head FE model.

In Chapter 4 of this thesis, a sensitivity analysis was conducted for the material model parameters on a FE model of an infant occipital head impact. The scalp, skull, suture and brain tissues were included in a simplified geometry of a three-month-old infant with symmetry in the sagittal plane. As 300 simulations were required for the sensitivity analysis, compromises with the mesh and the biofidelity of the model had to be made in order to reduce the computational time. It was found that:

- The elastic modulus of the skull had the most influence on the response of the FE model as it is the stiffest head tissue. This was followed by the skull Poisson's ratio.
- The brain hyperelastic constants are important for determining the local response of the brain tissue but do not have strong influence upon the global response.
- The scalp and suture hyperelastic constants have some influence over the global response of the model.

Aim #2

Determine which material model parameters are the most important for future experimental work, based on their influence (Aim #1) and the origin of existing data.

The sensitivity study presented in Chapter 4 also found that:

- Further work is required to build the data set for infant cranial bone material properties as their material properties have the greatest influence on the response of the FE model. Even though data from infant tissues exists, additional data will only improve the accuracy. Data for higher loading rates is also required to investigate rate-dependence. To date, only loading rates up to 2.81 ms^{-1} have been investigated.

- The brain hyperelastic constants are determined using adult data and therefore can be improved by conducting experiments using infant brain tissue. It is acknowledged though that experimental work with brain tissue is more challenging than using other tissues such as cranial bone. Brain injury related outputs should be used with caution until improvements to the material models can be made.
- As with the brain, the scalp hyperelastic constants are determined from adult data and can be improved by conducting experiments using infant scalp tissue.
- Existing data for the suture originates from infant tissue experiments. However, data for the bulk modulus can be improved considering the incompressibility factor of the suture hyperelastic model has strong influence on the suture outputs.
- The next step in human infant head modelling would be to delve into tissue failure and damage modelling to determine which material parameters are most important for accurate failure prediction. This will, of course, be important for relating modelling results to forensic data.

Aim #3

Conduct dynamic materials testing on human child cranial bone to advance the current data (based on the findings of Aim #2).

Based on the findings of Aim #1 and #2 in Chapter 4, experimental impact testing of human infant and child cranial bone was carried out. Due to hardware constraints and the prompt brittle fracture, the anticipated material properties could not be obtained. Rather, Chapter 5 presents preliminary observations of excised infant and child cranial bone under three-point-bend impact tests at speeds equivalent to a fall height of 1.6 m. This work found that:

- The failure mode in impacts of a 2 mm radius impactor at 5.65 ± 0.14 ms^{-1} was brittle fracture (with little or no bending observed) for samples aged two to 18 years. For the two specimens aged three-weeks, bending (resulting in inverted curvature of the specimens) occurred, followed by brittle fracture.
- Impact force peaks at 200 to 6 000 N, increasing with age (or thickness). Impact force is higher for occipital than for parietal or frontal bone.
- The energy absorbed to failure follows the same trend of increase with age or thickness. It was highest for occipital bone. The values of energy absorbed to failure were 0.11 and 0.35 mJ/mm^3 for the two specimens aged three-weeks, agreeing with previously published static tests. Energy absorbed to failure increased with age up to around 9 mJ/mm^3 for 18-year-old occipital bone.

- The increase in stiffness with age and the differences in mechanical properties of the different cranial bones as seen by others is supported by the present data.
- The use of this data in FE modelling will contribute to answering the mechanical as well as the forensic questions in the identification of abusive head trauma.

Aim #4

Investigate the effects of drop height and different impact surfaces on the response of an infant head FE model.

Chapter 6 presents an investigation into the effect of drop height and different domestic flooring surfaces on the response of the FE model using a baseline model presented in Chapter 4. It was found that:

- The peak head acceleration and HIC_{max} increases with drop height, while the impact duration decreases.
- These three output parameters fit a power law function with drop height.
- Softer flooring surfaces did not overly affect the peak acceleration as the compliant nature of the infant head resulted in high deformation, leading to an increase in the contact area and hence an elevated effective impact stiffness.
- The softer top surfaces increased the impact duration as their initial deformation affected the early contact stiffness.
- Concrete and wooden base floorings produced similar results and therefore are likely to result in similar injuries.
- An impact onto a surface edge resulted in a comparable peak head acceleration and increase in impact duration relative to the baseline model. Compared to an impact with a flat surface, a similar depression as that observed in the baseline model occurred, however, the area of the head not in contact with the surface passed down below the surface, causing it to 'wrap' around the edge of the of the surface. Peak head acceleration was comparable to the baseline model, while the impact duration increased by 26%.

Aim #5

Investigate possible methods for predicting skull fracture in infant head FE models.

The FE models used in Chapter 6 to investigate Aim #4 did not account for tissue failure. As the drop height increases, there is an increased likelihood of tissue failure occurring considering the greater energy and forces involved. Therefore, Chapter 7 investigated the use of element erosion to predict skull fracture. It was found that:

- While not necessarily the best method for predicting skull fracture, element erosion can be used to predict skull fracture to some degree.
- Skull fracture was predicted to initiate at the occipital bone and suture interface, which is consistent with fracture initiation sites found in existing experimental work in the literature.
- Fractures propagated in towards the centre of the depression due to the circumferential direction of the maximum principal stresses about the contact point. Secondary fractures occurred along the ridge of the depression where there were high bending stresses as the bone conformed to the flat impact surface.
- The resulting fracture pattern is mesh dependent. This was shown by the difference in the fracture patterns when the baseline mesh was further refined.
- If element erosion is used for such modelling, it is recommended that its limitations be considered when interpreting results.

Aim #6

Investigate how differences in the fidelity of the FE model affect the output metrics and computational cost of an infant head FE model.

Chapter 8 made changes to the baseline model to investigate the effect on the response of the FE model. Simplifying assumptions were used in the baseline model due to computational time constraints. Therefore, the changes investigated how increasing the biofidelity of the geometry affected the response and the computational time. It was found that:

- The impact angle had a significant effect on the global stiffness relative to the baseline model when the head was rotated towards the vertex. This was due to the much stiffer parietal bone (compared to the occipital bone) having a greater effect on the response as the impact angle approached that of which a vertex impact would occur.
- The individual addition of a dual layer scalp, the cerebrospinal fluid (CSF) and dura all resulted in an increase in the global stiffness relative to the baseline model, which was unexpected. For both the dual layer scalp and dura, the increase was due to the addition of a geometric boundary requiring an additional bonded contact interface that introduced an artificial stiffness to these regions. A better method is required for modelling these material interfaces.
- The increase in the global stiffness due to the addition of the CSF was likely to be a result of the equivalent stiffness of the CSF being 30% of that of the occipital bone. Given that the CSF is in reality a fluid, such an influence is unexpected and therefore this method of modelling the CSF has important limitations.

- When all three tissues are added to the model, and frictional contact used at the dura-CSF and brain-CSF interfaces, the global stiffness is comparable to the baseline model, as well as experimental cadaver tests. This indicates that the simplifying assumptions in the baseline model still produce some results comparable to a model that has a greater biofidelity but at the cost of 70% greater computational time.
- The addition of the foramen magnum allowed the brain to pass through the opening, reducing the global stiffness relative to the baseline model. However, due to other anatomical features not being modelled (such as the spinal cord), the degree of displacement of the brain tissue is not likely to be representative of reality. When the CSF was also included, there was very little displacement of the CSF and brain through the foramen magnum. Considering that the CSF naturally flows through the foramen magnum, this provides further evidence that modelling the behaviour of the CSF requires further work.

Future Work

The two biggest limitations of the FE model in this thesis was the FE software and infant head geometry used. Future work to improve these two aspects of the present work will hopefully produce a FE model with greater validity. Only then can significant steps forward be taken to develop the field of infant head FE models. Suggested future work includes:

- The computed tomography scan from which the geometry was obtained for use in the present work could not be used to distinguish between the soft tissues. Therefore, manual generation of these tissues were required, which led to not only extra work, but a less anatomically correct geometry. Improvements to the FE model used in this thesis would require scan data with more detail so that the individual soft tissues can be segmented.
- A more sophisticated explicit FE software should be used. ANSYS Explicit (ANSYS, Inc., Canonsburg, Pennsylvania, USA) had limitations such as a poor hexahedral element meshing algorithm, the inability to use an orthotropic elastic material model in local element coordinates, and inability to use sliding contacts. All these can be used in the likes of LS-DYNA (ANSYS, Inc., Canonsburg, Pennsylvania, USA) and Abaqus/Explicit (Dassault Systèmes Simulia Corp., Providence, Rhode Island, USA). The inability of ANSYS Explicit to use an orthotropic material model in local element coordinates was the greatest limitation to the model in this thesis as an isotropic elastic model had to be used for the cranial bones instead of an orthotropic model. The cranial bones are highly anisotropic in infants; hence an isotropic elastic model is less desirable. ANSYS Explicit was used as it is a part of the ANSYS software

package commonly used in industry and academic research institutes. The limitations of ANSYS Explicit were not discovered until they were required in the FE modelling process.

- Validation of individual material models for each of the tissues can be further improved to increase the accuracy of the local variables such as stress and strain, as well as ensuring they can model the effects of loading rate, age and direction dependence.
- Investigation and development of more advanced material models to better model the behaviour of the biological tissues will allow for more accurate FE models. The material models presently used, both in the current thesis and in the literature, may not represent the full behaviour of the tissues.
- Investigation into the difference in the results of a FE model when only element type is changed would be beneficial for determining whether certain element types can be used to produce a similar accuracy but at less computational expense. This is especially important for solid elements (hexahedral and tetrahedral), where there are trade-offs for each.
- As infant head FE models become more accurate, a sensitivity study like that in Chapter 4 should be conducted on the damage variables in material models so that the important parameters for modelling tissue failure can be identified. This would provide direction for future experimental work.
- It was identified that prompt brittle fracture occurs in infant and child cranial bone at speeds equivalent to a drop height of 1.6 m. More suitable high-speed cameras could be used to capture images of similar impacts to those conducted in Chapter 5 in order to obtain more images before fracture occurs. This would allow digital image correlation to be used to measure the displacement and strain fields, which can be used to reverse engineer FE models to identify the material properties.
- Further work is required to validate the carpet and underlay material models, as well as obtain data for the many different types of both materials. This will allow further FE models to be constructed and used to determine if there is a practical thickness of carpet and underlay that would significantly alter the physics of the impact. This would help investigators determine whether a particular surface mitigated the effects of a fall.
- Element erosion as a method of predicting skull fracture has many limitations. Future work should include further investigating the effect of greater mesh refinement, as well as using other methods of fracture prediction.
- An isotropic elastic material model with a high bulk modulus and relatively low shear modulus was not suitable for modelling the behaviour of the CSF. Therefore, further work is required

to improve the material model, or other FE modelling techniques such as fluid-structure interaction should be investigated.

- Using bonded contact conditions at tissue interfaces introduced an artificial stiffness that increased the global stiffness of the FE model. Further work is required to establish suitable contact methods at tissue interfaces and better understand the influence the artificial stiffness resulting from the bonded contact has on the stiffness of the model. This could include running models with a matching mesh on each connecting surface so that the nodes are constrained to nodes (rather than points on an element) and comparing the results with a model using a shared node interface and a mismatched mesh at the interface.
- Forces transmitted through the neck resulting from the inertia of the rest of the body were not considered in this thesis. There are an infinite number of possibilities in terms of relative body orientation and motion that will influence the impact velocity of the head when it strikes any surface type. Including the inertial effects of the body into the FE model is an important area for future work. A sensitivity study could be carried out to determine how these influence the resulting injury patterns as there will likely be a significant increase in computational time.

Final Words

Infant FE models can be used in forensic or legal cases to reconstruct potential scenarios to predict the nature of the head injuries an infant is likely to receive. Factors that are required to model any scenario include head orientation, impact velocity, age and impact surface properties. Using these inputs, an FE model will provide results that can be interpreted to determine the degree and type of injury. However, there are an infinite number of different scenarios that may lead to these inputs. Therefore, FE models cannot determine whether the events leading up to the impact event may have been accidental or non-accidental. In legal cases, FE models can be used to predict whether injuries could result from a particular scenario offered by either the defence or prosecution. Thus, the FE models can only be offered as additional indirect evidence, which can be weighed with other types of evidence during the legal process.

Using FE models of the infant head to accurately reconstruct the injury patterns in forensic cases requires high-fidelity models. However, this comes at a significant computational cost. Standard professional grade computers are inadequate and high-performance computers have significant financial cost. Therefore, trade-offs with the computational cost and model fidelity are required to make forensic reconstructions tractable. This thesis has investigated what is required to further develop infant head FE models. Some of these requirements have been addressed in this thesis, or preliminary research undertaken to provide guidance for future work. As the field of infant head FE

modelling develops, and computational power becomes more cost effective, the accuracy of such models and the financial cost will improve. This will allow forensic reconstructions of suspected abusive head trauma to be more rigorously investigated, bring justice for those children who have been fatally injured from such trauma or protect survivors from future abuse.

Appendix A

Digital Image Correlation

Strain gauges are often used in experimental solid mechanics to measure surface strains; however, they are limited to measuring local strains only. An array of gauges can be used to measure the strain at multiple points on a surface, but assumptions have to be made about how the strain varies between each gauge. Rather than using strain gauges, a method to measure the full-field displacement and deformation of a surface is digital image correlation. DIC is a non-contact method that uses a series of digital images to measure the full-field displacement and deformation of an object's surface under load.

In general, a contrasting pattern is applied to the surface of interest and this surface is then imaged while undergoing a particular load. A subset of an undeformed image (reference image) is correlated to one or more images of the deformed object (deformed image). Calculation of the displacement field is based on the distance the subset has moved from the reference image to its correlated location in the deformed images. The strain field can then be calculated by differentiation of the displacement field.

Digital image correlation was first developed in the 1980s by researchers at the University of South Carolina (Peters and Ranson 1982a, Peters and Ranson 1982b, Peters et al. 1983, Sutton et al. 1983). It is similar to particle image velocimetry (PIV) that is used in experimental fluid mechanics. PIV tracks particles in a fluid by digital imaging and calculates the particles' velocities from their displacement in each frame of the image series.

As described by Pan, Qian, et al. (2009), the DIC method consists of three main steps. The first step is to prepare the specimen and experimental setup, followed by imaging the specimen before and after loading, before finally, processing the images to determine the displacement and strain fields. These steps are outlined in detail in the following sections.

Specimen Preparation

In order for the DIC algorithm to track the displacement from one image to the next, the specimen must have a random, contrasting speckle pattern applied to the surfaces of interest. Correlation of a subset in the reference image to its subsequent location in the deformed image requires the images to be in grayscale. Therefore, a speckle pattern that consists of a black and white contrast is the most suitable. A common method of creating the speckle pattern is to paint the surface white and then use black spray paint to create the speckles by way of using the spray can nozzle to generate small

droplets. Other methods include using permanent marker to create the speckles or use the surface's natural texture if it has a suitable contrast.

Speckle Pattern Considerations

There are many factors that need to be considered when generating a speckle pattern to be used in DIC. These include the speckle size, aliasing, contrast, speckle edge sharpness and the speckle density (Reu 2014b).

A speckle should be at least three pixels in size, with the same again in spacing between each speckle (Reu 2014a). The physical size of the speckle is dependent on the resolution of the camera being used and the distance of the camera from the surface containing the speckle pattern. Any changes to these require the size of the speckle to be changed to ensure the speckle is three to five pixels in size on the image.

A minimum speckle size of three pixels is required to ensure that aliasing does not occur and hence information is not lost. In Figure A1, speckles of one pixel in size are shown on the left while a speckle of three to four pixels is shown on the right, as they are imaged by the camera onto a pixel array. For the one pixel speckles, the centre of the speckle is difficult to locate, however, the centre of the larger speckle is easy to locate (Reu 2014a). The difficulty in locating the centre of the one-pixel speckles is due to only part of the speckle being captured in a pixel, with the rest of the pixel capturing black. Therefore, the pixel intensity is not going to be that of the original speckle; instead, it will be a combination of the intensities from the speckle and its surroundings. This results in the different shades of grey as seen in the bottom left of Figure A1, where there is no clear resemblance to the speckle imaged by the lens as seen in the top of Figure A1. As the centres of the speckles are unable to be located, there is a loss of information (aliasing). Therefore, the minimum speckle size should be at least three pixels. Aliased speckles can result in a 'twinkle' that can be seen in the images when moving from one frame to the next. This 'twinkle' adds noise to the speckle pattern and so will affect the accuracy of the DIC analysis (Reu 2014a).

An ideal speckle pattern would have equal sized areas of black and white. However, this is often difficult to achieve if using manual techniques, such as spray paint or permanent marker, to create the speckles. Spray paints create overspray as a fine mist is produced and slightly covers the background, affecting the contrast of the pattern. No real effort is required to create a random speckle pattern when manually creating the pattern as imperfections will always occur (Reu 2015). As long as there is no directionality in the pattern, then the pattern will be random enough.

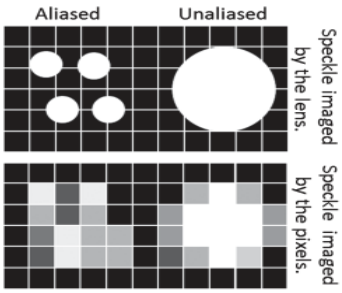

Figure A1: Concept of Aliasing (adapted from Reu (2014a))

Hardware Setup

In order to perform a DIC analysis, a series of images of the deformation is required. This involves selecting a suitable camera and lens, as well as providing suitable lighting.

Generally, any DSLR camera is suitable to capture images of the deformation. A monochrome camera is generally the best option as the deformation images need to be in grayscale. However, a colour camera can be used with the images converted to grayscale later, but the method of filtering to create the colour image can lead to a loss of resolution for DIC purposes (Reu 2012).

Once the camera has been selected, a suitable lens is required. The field of view (FOV) of the camera is the view that the camera images. The surface of interest should fill up as much of the FOV as possible so that more pixels cover the surface. Based on the size of the field of view and any limitations to the stand-off distance (the distance from the camera sensor to the surface of interest), a lens with a suitable focal length can be selected. The focal length of a lens is the distance from the lens to the camera sensor and the longer the focal length, the greater the magnification and the smaller the FOV. Given the stand-off distance, L, and the horizontal distance of the FOV, w, the required focal length, f, can be calculated by:

$$f = \frac{Lh}{w} \tag{A1}$$

Where h is the width of the camera sensor and can be determined from the camera specifications. Based on the calculated focal length, a lens with a focal length closest to that calculated can be used with the camera.

Another hardware requirement is suitable lighting to light the speckle pattern as lighting quality is directly related to measurement quality (Reu 2013). Adequate lighting is required so that the surface of interest has flat and uniform lighting. This eliminates relatively brighter areas appearing on the surface. LED (light emitting diode) lights are most preferred as they can provide a lot of light with significantly less heat than the likes of halogen lights. Used with a good quality driver circuit, LED lights will almost have non-existent flickering. Flickering that results from lights that are powered by alternating current (such as incandescent lights) affects the DIC as the light intensity changes, resulting

in changes to the pixel intensities. This means that the DIC algorithm may indicate a displacement, even though the surface may have been static.

The physical setup requires the camera's image sensor to be parallel to the surface of interest. This is to minimise the out of plane displacement and hence it can be assumed negligible.

Image Correlation

Once the deformation images have been acquired, DIC can be carried out to determine the displacement and strain fields. In general, a region of interest (ROI) is selected on the reference image. The ROI should only contain the speckle pattern. A subset window of (2N+1) x (2N+1) pixels centred at $P(x_0, y_0)$ is selected from the reference image, generally starting in the upper left corner of the ROI. The size of the subset window must be an odd number to ensure that the centre, $P(x, y)$, is centred at a whole pixel and not a fraction of a pixel. N is the number of pixels either side of $P(x, y)$.

The subset's location is found in the deformation images by using a correlation criterion. There are multiple definitions for the correlation criterion in literature, although they can be generally categorised into cross correlation criteria and sum of squared differences criteria (Pan, Qian, et al. 2009). A common cross correlation criterion is the normalised cross correlation coefficient, C_{norm}, and is defined as:

$$C_{norm} = \sum_{i=-N}^{N} \sum_{j=-N}^{N} \left[\frac{F(x_i, y_j) F'(x_i', y_j')}{\left[\left[F(x_i, y_j) \right]^2 \left[F'(x_i', y_j') \right]^2 \right]^{\frac{1}{2}}} \right] \quad \text{(A2)}$$

Where $F(x_i, y_j)$ is the pixel intensity of the subset in the reference image at (i, j), $F'(x_i', y_j')$ is the pixel intensity in the deformed image and (x_i', y_j') is a point in the deformed image. Calculation of the correlation coefficient is carried out for multiple points surrounding an initial point guess. The initial point is generally taken as the location of the subset in the reference image or the previous deformation image. The specific location of the subset in the deformation images is where the correlation coefficient is a maximum. Generally, there is a definitive peak when plotting the coefficient at multiple points. The difference in the location of the centre of the subset in both the reference image and the deformed image gives the in-plane displacement vector.

In the deformed image, the coordinates of a point (x_i', y_j') in the subset may be located between pixels; that is, it may have a sub-pixel location. To determine the intensity of any points that have a sub-pixel location, an interpolation scheme should be used. There are many interpolation schemes that can be used, including bilinear, bicubic, bicubic B-spline and bicubic spline interpolation to name a few (Pan, Qian, et al. 2009, Freddi et al. 2015).

Displacement Calculation

The displacement vector that has been calculated in the correlation process has units of pixels. A scale is required to calculate the vector into a unit of measure. For example, the displacement vector needs to be multiplied by the number of millimetres per pixel to get the displacement in terms of millimetres.

The shape of the subset window in the deformed image may change shape compared to the reference subset. The displacements of points within the subset can be calculated using shape functions. If deformation continuity of a deformed solid object is assumed, then neighbouring points in the reference subset remain neighbours in the deformed subset (Pan, Qian, et al. 2009). Therefore, the coordinates of point $Q(x_i, y_j)$ around $P(x_0, y_0)$ can be mapped to $Q'(x_i', y_j')$ in the deformed subset by the shape functions (Pan, Qian, et al. 2009):

$$x_i' = x_i + \xi(x_i, y_j) \tag{A3a}$$

$$y_i' = y_i + \eta(x_i, y_j) \tag{A3a}$$

Where $i, j = -N: N$. For rigid body translation, the displacements of each point in the subset are equal, therefore, a zero-order shape function can be used. That is:

$$\xi_0(x_i, y_j) = u \qquad \eta_0(x_i, y_j) = v \tag{A4}$$

Where u and v are the x and y directional displacements respectively. However, a zero-order shape function is not able to depict a change in the shape of the subset (Pan, Qian, et al. 2009). To account for this, a first-order shape function can be used that allows for combinations of translation, rotation, shear and normal strains:

$$\xi_0(x_i, y_j) = u + u_x \Delta x + u_y \Delta y \tag{A5a}$$

$$\eta_0(x_i, y_j) = v + v_x \Delta x + v_y \Delta y \tag{A5b}$$

Higher order shape functions can also be used to depict more complex deformations of the subset window.

Strain Field Calculation

The relationship between displacement and strain is mathematically defined as the derivative of the displacements. Numerical differentiation of the displacement field in DIC often leads to an unreliable and inaccurate strain field as the differentiation amplifies any noise in the displacement field (Pan, Qian, et al. 2009). Smoothing the displacement field first can often improve the accuracy of the strain field. One practical method of smoothing the displacement field is to use a pointwise local least-squares fitting technique (Pan, Asundi, et al. 2009).

The use of the local least-squares fitting technique is outlined in Pan, Asundi, et al. (2009), and Pan, Qian, et al. (2009). First, a point in the displacement field is selected. A strain calculation window consisting of (2*n*+1) x (2*n*+1) discrete points is defined around this point (*n* is the number of pixels either side of this point). The distribution of the displacements can be approximated as a linear plane if the strain calculation window is small enough. This gives:

$$u(i,j) = a_0 + a_1 x + a_2 y \tag{A6a}$$

$$v(i,j) = b_0 + b_1 x + b_2 y \tag{A6b}$$

Where *u(i, j)* and *v(i, j)* are the original displacements at the point *(i, j)*, *i, j=-n: n* are the local coordinates in the strain calculation window, and *a* and *b* are the unknown polynomial coefficients (Pan et al. 2007). The above two equations can be written in matrix form and the least-squares method used to solve the unknown coefficients. Carrying out the differentiation to calculate the strains results in:

$$\varepsilon_x = \frac{\partial u}{\partial x} = a_1 \tag{A7a}$$

$$\varepsilon_y = \frac{\partial v}{\partial y} = b_2 \tag{A7b}$$

$$\varepsilon_{xy} = \frac{\partial u}{\partial y} + \frac{\partial v}{\partial x} = a_2 + b_1 \tag{A7c}$$

Therefore, the strains can be determined from the coefficients. This process can be carried out for each point in the displacement field to get the overall strain field.

The size of the strain calculation window should be selected to get a balance between the strain, accuracy and smoothness. Smaller windows cannot filter out any noise in the displacement field whereas a larger window will, however the larger window may lead to an unreasonable linear approximation of the deformation (Pan et al. 2007).

Any noise in the displacement field is amplified in the strain field due to the differentiation of the displacements. Pan et al. (2007) describes this in the following example. If the error of the displacement field is ±0.02 pixels and the subset spacing is five pixels, then the error in the strain is:

Forward difference: $$\Delta\varepsilon = \frac{(|\pm 0.02| + |\pm 0.02|)}{5} = 8000\ \mu\varepsilon \tag{A8a}$$

Central difference: $$\Delta\varepsilon = \frac{(|\pm 0.02| + |\pm 0.02|)}{10} = 4000\ \mu\varepsilon \tag{A8b}$$

Therefore, an error of these magnitudes is likely to hide the underlying strain information (Pan et al. 2007).

Appendix B

Additional figures from Chapter 5 showing maximum impact force and energy absorbed to failure with uncertainties.

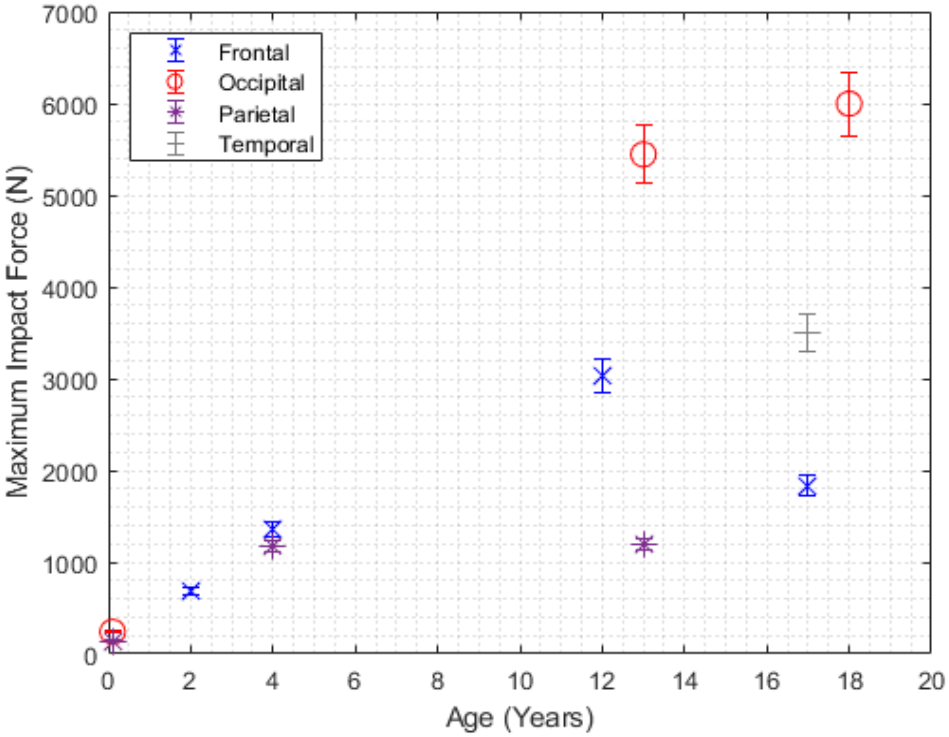

Figure B1: Maximum impact force versus age (with uncertainties).

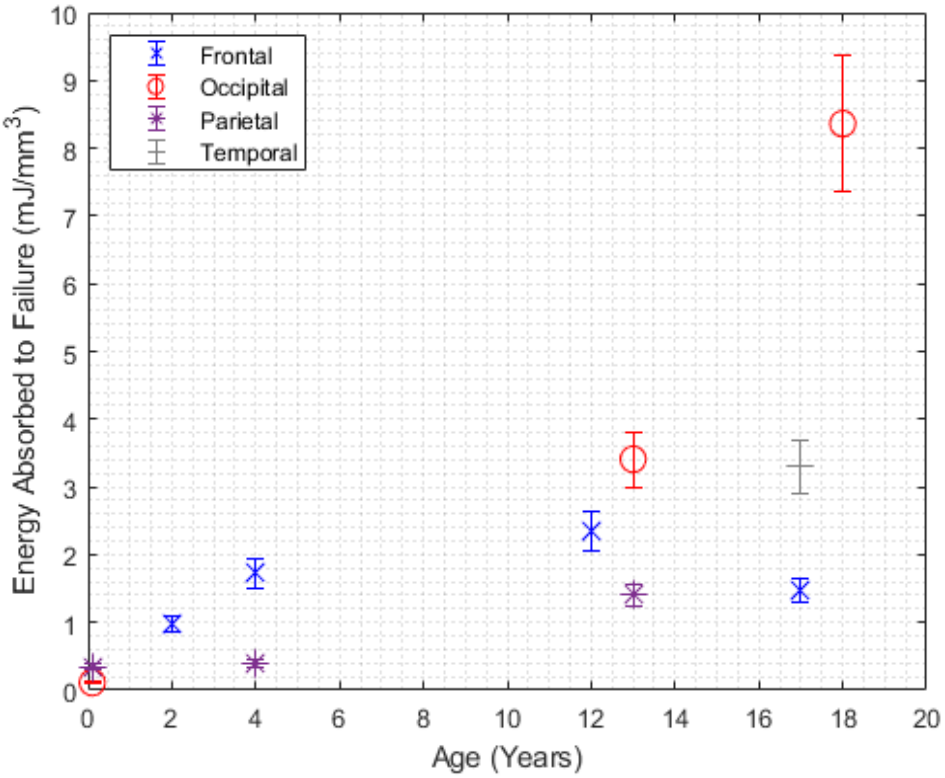

Figure B2: Energy absorbed to failure versus age (with uncertainties).

Appendix C

Additional figures from Chapter 6 showing acceleration-time plots for the impact surfaces at each drop height.

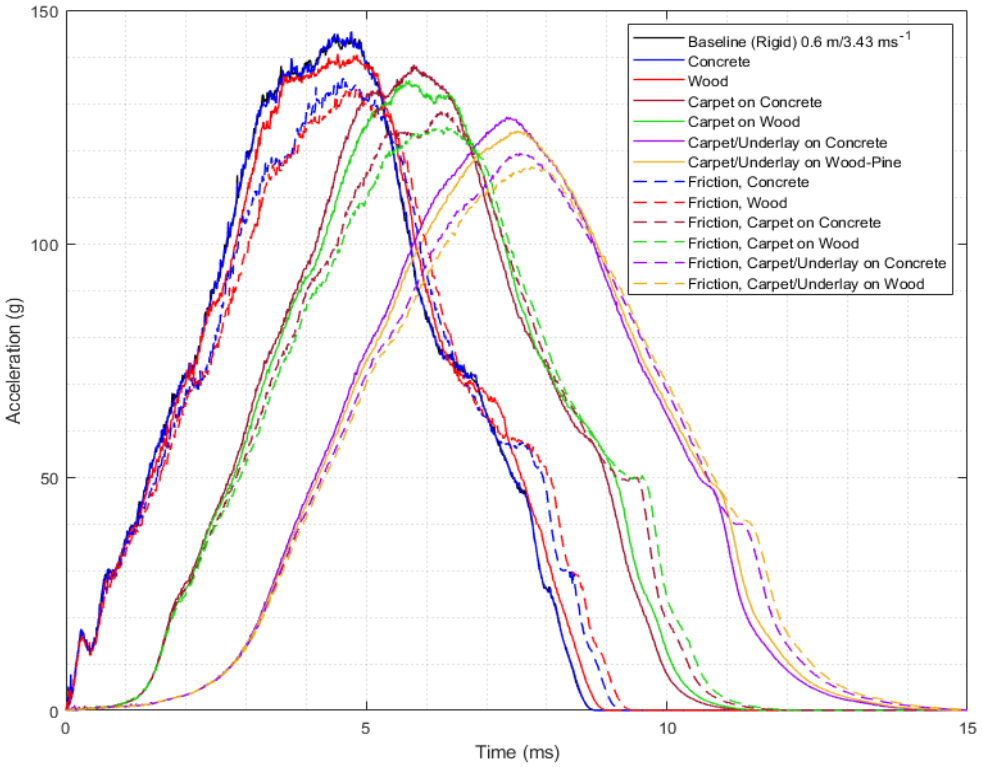

Figure C1: Acceleration-time plot for each impact surface for a drop height of 0.6 m. Solid lines represent bonded contact at the brain-skull interface, while broken lines represent frictional contact. Note: the 'concrete' trace overlays that of the baseline, making the baseline somewhat indistinguishable.

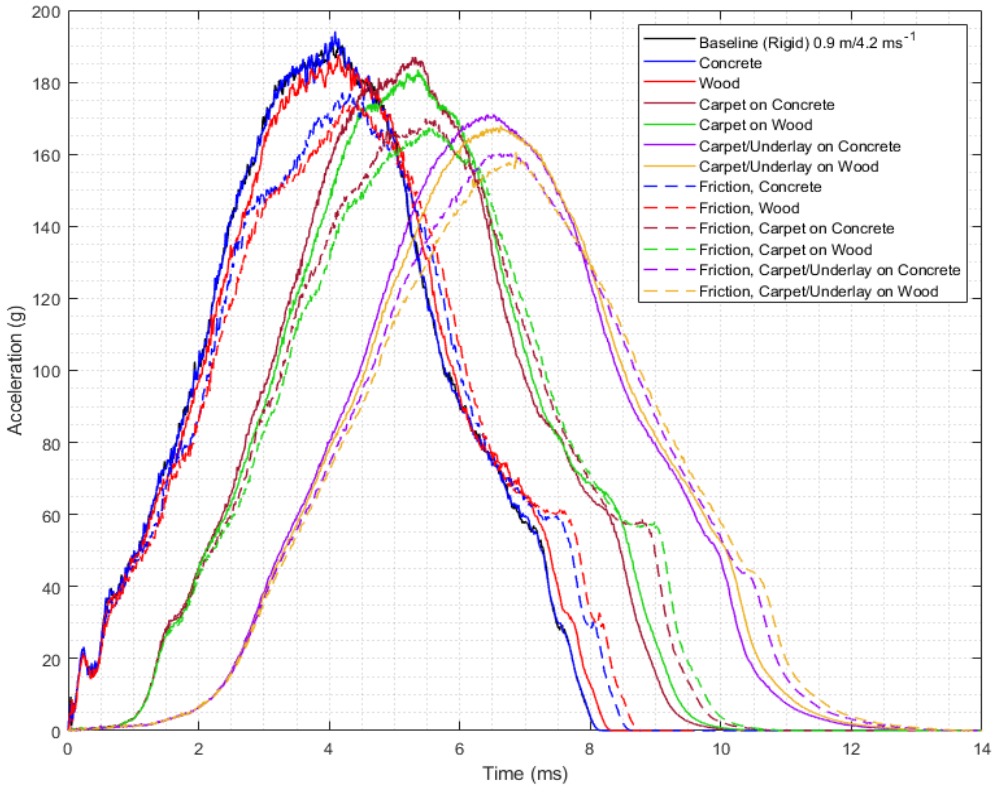

Figure C2: Acceleration-time plot for each impact surface for a drop height of 0.9 m. Solid lines represent bonded contact at the brain-skull interface, while broken lines represent frictional contact. Note: the 'concrete' trace overlays that of the baseline, making the baseline somewhat indistinguishable.

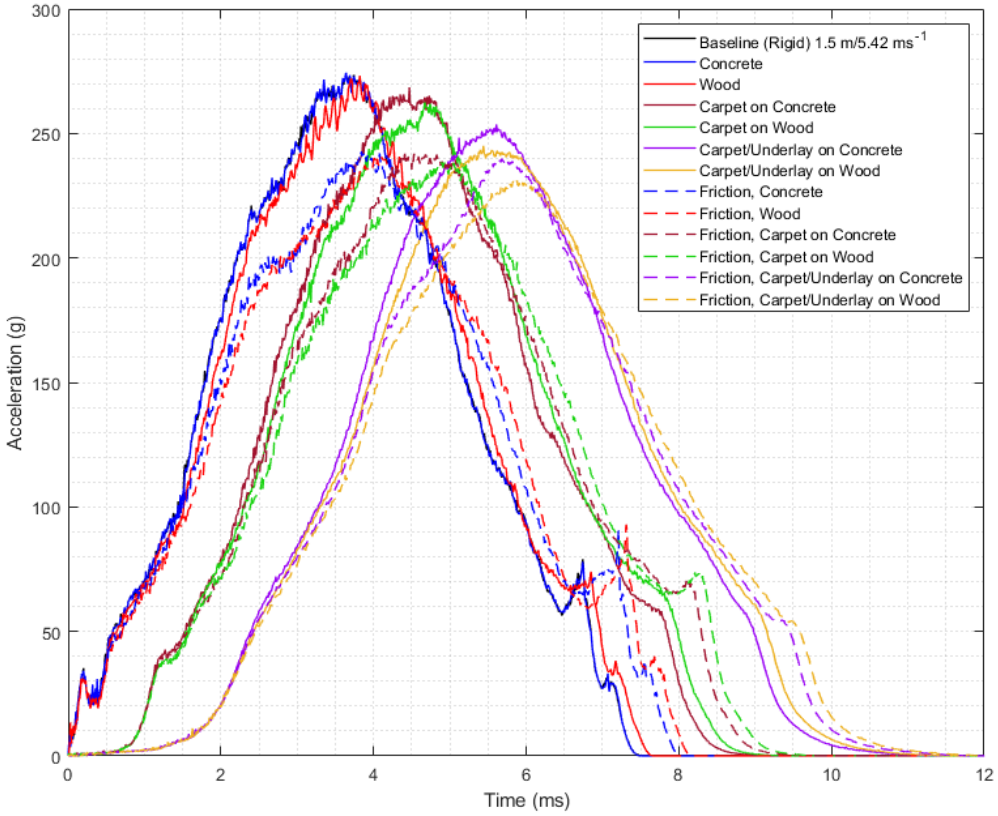

Figure C3: Acceleration-time plot for each impact surface for a drop height of 1.2 m. Solid lines represent bonded contact at the brain-skull interface, while broken lines represent frictional contact. Note: the 'concrete' trace overlays that of the baseline, making the baseline somewhat indistinguishable.

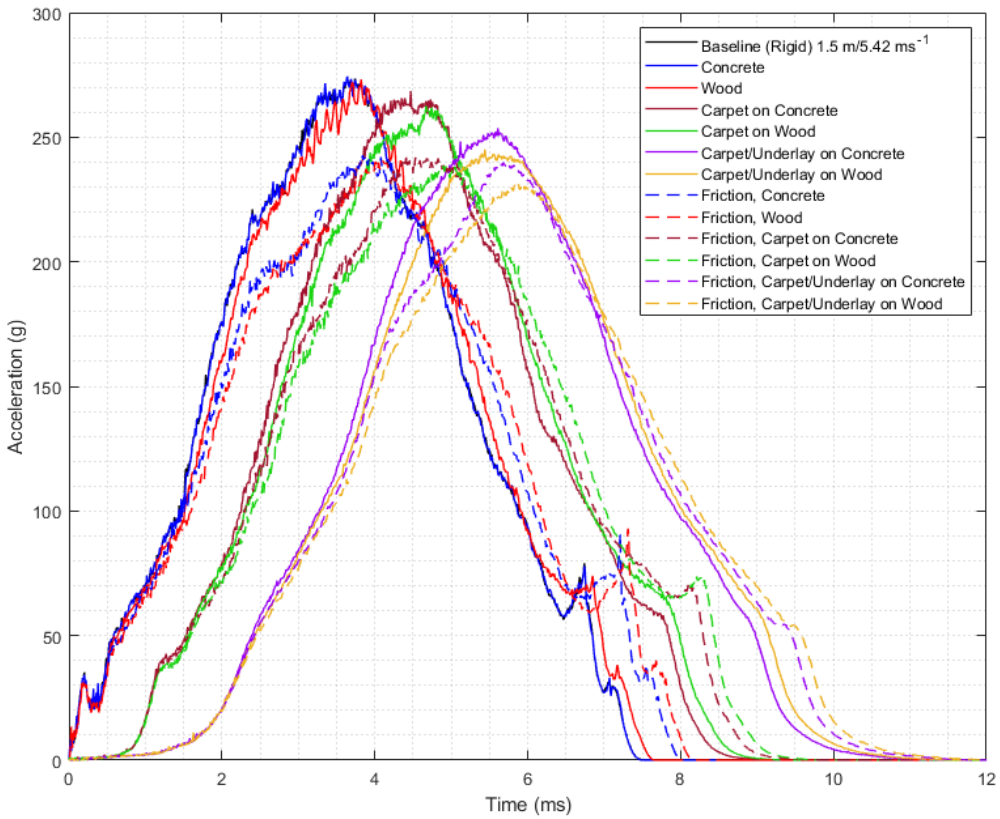

Figure C4: Acceleration-time plot for each impact surface for a drop height of 1.5 m. Solid lines represent bonded contact at the brain-skull interface, while broken lines represent frictional contact. Note: the 'concrete' trace overlays that of the baseline, making the baseline somewhat indistinguishable.

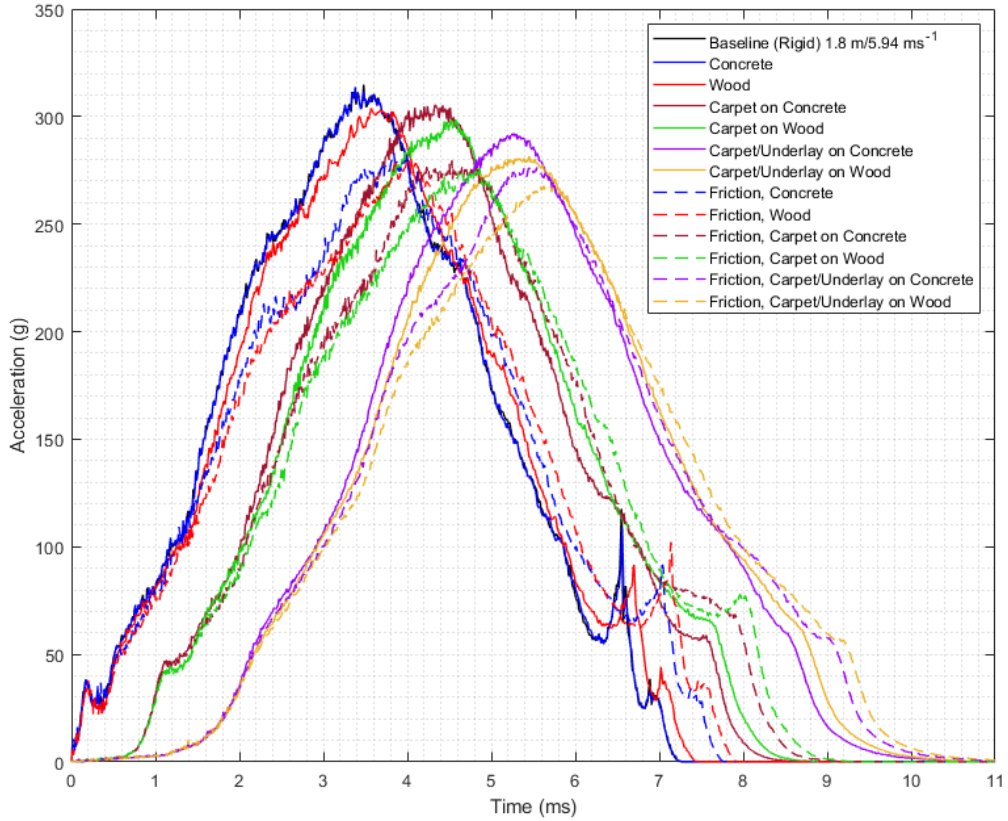

Figure C5: Acceleration-time plot for each impact surface for a drop height of 1.8 m. Solid lines represent bonded contact at the brain-skull interface, while broken lines represent frictional contact. Note: the 'concrete' trace overlays that of the baseline, making the baseline somewhat indistinguishable.

References

Aare, Magnus, and Svein Kleiven. 2007. "Evaluation of head response to ballistic helmet impacts using the finite element method." *International Journal of Impact Engineering* 34 (3):596-608.

Anjomrouz, Marzieh. 2017. "Investigation of MARS spectral CT: X-ray source and detector characterization." University of Otago.

ANSYS Inc. 2019a. ANSYS® Academic Research Mechanical, Release 2019 R3, Help System, DesignXplorer User's Guide.

ANSYS Inc. 2019b. ANSYS® Academic Research Mechanical, Release 2019 R3, Help System, Explicit Dynamics Analysis Guide.

Arbogast, Kristy B, and Susan S Margulies. 1997. Regional differences in mechanical properties of the porcine central nervous system. SAE Technical Paper.

Bain, Allison C, and David F Meaney. 2000. "Tissue-level thresholds for axonal damage in an experimental model of central nervous system white matter injury." *Journal of biomechanical engineering* 122 (6):615-622.

Bandak, FA, AX Zhang, RE Tannous, F DiMasi, P Masiello, and R Eppinger. 2001. Simon: a simulated injury monitor; application to head injury assessment. SAE Technical Paper.

Bateman, Christopher James. 2015. "Methods for material discrimination in MARS multi-energy CT." University of Otago.

Bathe, Klaus-Jürgen. 2006. *Finite element procedures*: Klaus-Jurgen Bathe.

Baumer, Timothy G, Nicholas V Passalacqua, Brian J Powell, William N Newberry, Todd W Fenton, and Roger C Haut. 2010. "Age-dependent fracture characteristics of rigid and compliant surface impacts on the infant skull—a porcine model." *Journal of forensic sciences* 55 (4):993-997.

Belingardi, Giovanni, Giorgio Chiandussi, and Ivan Gaviglio. 2005. "Development and validation of a new finite element model of human head." Proc. 19th International Technical Conference of the Enhanced Safety of Vehicle (ESV), Washington, DC.

Belytschko, Ted, Wing Kam Liu, Brian Moran, and Khalil Elkhodary. 2013. *Nonlinear finite elements for continua and structures*: John wiley & sons.

Bondy, Matthew, William Altenhof, Xilin Chen, Anne Snowdon, and Brenda Vrkljan. 2014. "Development of a finite element/multi-body model of a newborn infant for restraint analysis and design." *Computer methods in biomechanics and biomedical engineering* 17 (2):149-162.

Bower, Allan F. 2009. *Applied mechanics of solids*: CRC press.

Braakman, R. 1972. "Depressed skull fracture: data, treatment, and follow-up in 225 consecutive cases." *Journal of Neurology, Neurosurgery & Psychiatry* 35 (3):395-402.

Brewick, Patrick, Robert Saunders, and Amit Bagchi. 2017. Biomechanical modeling of the human head. NAVAL RESEARCH LAB WASHINGTON DC WASHINGTON United States.

Brooks, Tom, Jung Eun Choi, Mark Garnich, Niels Hammer, John Neil Waddell, Warwick Duncan, and Mark Jermy. 2018. "Finite element models and material data for analysis of infant head impacts." *Heliyon* 4 (12):e01010.

Brooks, Tom, Mark Garnich, and Mark Jermy. 2020. "Sensitivity of Material Model Parameters on Finite Element Models of Infant Head Impacts." Under Review.

Brooks, Tom, Johann Zwirner, Niels Hammer, Benjamin Ondruschka, and Mark Jermy. 2020. "Preliminary observations of the sequence of damage in excised human juvenile cranial bone at speeds equivalent to falls from 1.6 m." *International Journal of Legal Medicine*:1-12.

Brown, Robert W., Yu-Chung N. Cheng, E. Mark Haacke, Michael R. Thompson, Ramesh Venkatesan, and InterScience Wiley. 2014. *Magnetic resonance imaging: physical principles and sequence design*. Second;2;2nd; ed. Hoboken, New Jersey: John Wiley & Sons, Inc.

Burdi, Alphonse R, Donald F Huelke, Richard G Snyder, and GH Lowrey. 1969. "Infants and children in the adult world of automobile safety design: pediatric and anatomical considerations for design of child restraints." *Journal of Biomechanics* 2 (3):267-280.

Burgos-Flórez, FJ, and Diego Alexander Garzón-Alvarado. 2020. "Stress and strain propagation on infant skull from impact loads during falls: a finite element analysis." *International Biomechanics* 7 (1):19-34.

Butchart, A., T. Kahane, A. Phinney Harvey, M. Mian, and T. Furniss. 2006. Preventing Child Maltreatment: A Guide to Taking Action and Generating Evidence. Geneva: WHO and International Society for the Prevention of Child Abuse and Neglect.

Bylski, Donita I, Timothy J Kriewall, Nuri Akkas, and John W Melvin. 1986. "Mechanical behavior of fetal dura mater under large deformation biaxial tension." *Journal of biomechanics* 19 (1):19-26.

Carroll, L.D., J.D. Cassidy, L. Holm, J. Kraus, and V.G. Coronado. 2004. "Methodological issues and research recommendations for mild traumatic brain injury: the WHO Collaborating Centre Task Force on Mild Traumatic Brain Injury." *J Rehabil Med* 43:113-25.

Castellani, Rudy J, and Carl J Schmidt. 2018. "Brain injury biomechanics and abusive head trauma." *Journal of Forensic Science and Medicine* 4 (2):91.

Chadwick, D. L., S. Chin, C. Salerno, J. Landsverk, and L. Kitchen. 1991. "DEATHS FROM FALLS IN CHILDREN - HOW FAR IS FATAL." *JOURNAL OF TRAUMA-INJURY INFECTION AND CRITICAL CARE* 31 (10):1353-1355.

Chalmers, David J, Stephen W Marshall, John D Langley, M Jean Evans, Cheryl R Brunton, Anne-Maree Kelly, and Alison F Pickering. 1996. "Height and surfacing as risk factors for injury in falls from playground equipment: a case-control study." *Injury Prevention* 2 (2):98-104.

Cierniak, Robert. 2011. *X-ray computed tomography in biomedical engineering*. London: Springer.

Coats, B., S. S. Margulies, and S. Ji. 2007. "Parametric study of head impact in the infant." *Stapp Car Crash J* 51:1-15.

Coats, Brittany, and Susan S. Margulies. 2006. "Material properties of human infant skull and suture at high rates." *Journal of Neurotrauma* 23 (8):1222-1232. doi: 10.1089/neu.2006.23.1222.

Coats, Brittany, and Susan S. Margulies. 2008. "Potential for head injuries in infants from low-height falls: Laboratory investigation." *Journal of Neurosurgery: Pediatrics* 2 (5):321-330. doi: 10.3171/PED.2008.2.11.321.

Cory, CZ, and Michael D Jones. 2006. "Development of a simulation system for performing in situ surface tests to assess the potential severity of head impacts from alleged childhood short falls." *Forensic science international* 163 (1-2):102-114.

Courant, Richard, Kurt Friedrichs, and Hans Lewy. 1928. "Über die partiellen Differenzengleichungen der mathematischen Physik." *Mathematische annalen* 100 (1):32-74.

Crichton, Michael L, Bogdan C Donose, Xianfeng Chen, Anthony P Raphael, Han Huang, and Mark AF Kendall. 2011. "The viscoelastic, hyperelastic and scale dependent behaviour of freshly excised individual skin layers." *Biomaterials* 32 (20):4670-4681.

Currey, John D. 2013. *Bones*: Princeton University Press.

Dagro, Amy M, Philip J McKee, Reuben H Kraft, Timothy G Zhang, and Sikhanda S Satapathy. 2013. A preliminary investigation of traumatically induced axonal injury in a three-dimensional (3-D) finite element model (FEM) of the human head during blast-loading. ARMY RESEARCH LAB ABERDEEN PROVING GROUND MD WEAPONS AND MATERIALS RESEARCH DIRECTORATE.

Daniel, Baumgartner, and Willinger Rémy. 2005. "Finite element modelling of human head injuries caused by ballistic projectiles." *Revue Européenne des Eléments* 14 (4-5):559-576.

Davis, Matthew T., Andre M. Loyd, Han-yu Henry Shen, Maura H. Mulroy, Roger W. Nightingale, Barry S. Myers, and Cameron Dale Bass. 2012. "The mechanical and morphological properties of 6 year-old cranial bone." *Journal of Biomechanics* 45 (15):2493-2498. doi: 10.1016/j.jbiomech.2012.07.001.

Delye, Hans, Tim Clijmans, Maurice Yves Mommaerts, Jos Vnder Sloten, and Jan Goffin. 2015. "Creating a normative database of age-specific 3D geometrical data, bone density, and bone thickness of the developing skull: a pilot study." *Journal of Neurosurgery: Pediatrics* 16 (6):687-702.

Dickerson, JWT, and J Dobbing. 1967. "Prenatal and postnatal growth and development of the central nervous system of the pig." *Proceedings of the Royal Society of London. Series B. Biological Sciences* 166 (1005):384-395.

Dobbing, John. 1981. "The later development of the brain and its vulnerability." *Scientific foundations of pediatrics*:744-759.

Doorly, Mary C, and Michael D Gilchrist. 2006. "The use of accident reconstruction for the analysis of traumatic brain injury due to head impacts arising from falls." *Computer methods in biomechanics and biomedical engineering* 9 (6):371-377.

Duhaime, A. C., T. A. Gennarelli, L. E. Thibault, D. A. Bruce, S. S. Margulies, and R. Wiser. 1987. "The shaken baby syndrome. A clinical, pathological, and biomechanical study." *Journal of Neurosurgery* 66 (3):409-415.

Dupuis, Olivier, Ruimark Silveira, Corinne Dupont, Carmine Mottolese, Pierre Kahn, Andre Dittmar, and René-Charles Rudigoz. 2005. "Comparison of “instrument-associated” and “spontaneous” obstetric depressed skull fractures in a cohort of 68 neonates." *American journal of obstetrics and gynecology* 192 (1):165-170.

Ersahin, Y, S Mutluer, H Mirzai, and I Palali. 1996. "Pediatric depressed skull fractures: analysis of 530 cases." *Child's nervous system* 12 (6):323-331.

Fahlstedt, Madelen, Bart Depreitere, Peter Halldin, Jos Vander Sloten, and Svein Kleiven. 2015. "Correlation between injury pattern and finite element analysis in biomechanical reconstructions of traumatic brain injuries." *Journal of biomechanics* 48 (7):1331-1335.

Ferry, John D. 1980. *Viscoelastic properties of polymers*: John Wiley & Sons.

Franceschini, Giulia, Davide Bigoni, Peter Regitnig, and Gerhard A Holzapfel. 2006. "Brain tissue deforms similarly to filled elastomers and follows consolidation theory." *Journal of the Mechanics and Physics of Solids* 54 (12):2592-2620.

Freddi, Alessandro, Giorgio Olmi, Luca Cristofolini, and SpringerLink. 2015. *Experimental Stress Analysis for Materials and Structures: Stress Analysis Models for Developing Design Methodologies*. Vol. 4. Cham: Springer International Publishing.

Gadd, C. 1964. "Criteria for Injury Potential." Impact Acceleration Stress Symposium, Washington.

Ganpule, S, A Alai, E Plougonven, and N Chandra. 2013. "Mechanics of blast loading on the head models in the study of traumatic brain injury using experimental and computational approaches." *Biomechanics and modeling in mechanobiology* 12 (3):511-531.

Gerber, Paula, and Kathryn Coffman. 2007. "Nonaccidental head trauma in infants." *Child's nervous system* 23 (5):499-507.

Gilchrist, MD, and Diarmuid O'Donoghue. 2000. "Simulation of the development of frontal head impact injury." *Computational Mechanics* 26 (3):229-235.

Gurdjian, ES, John E Webster, and HR Lissner. 1950. "The mechanism of skull fracture." *Radiology* 54 (3):313-339.

Hajiaghamemar, Marzieh, Ingrid S Lan, Cindy W Christian, Brittany Coats, and Susan S Margulies. 2018. "Infant skull fracture risk for low height falls." *International journal of legal medicine*:1-16.

Hambli, Ridha. 2013. "A quasi-brittle continuum damage finite element model of the human proximal femur based on element deletion." *Medical & biological engineering & computing* 51 (1-2):219-231.

Hammer, Niels, Christian Voigt, Michael Werner, Falk Hoffmann, Klaus Bente, Holger Kunze, Roger Scholz, and Hanno Steinke. 2014. "Ethanol and formaldehyde fixation irreversibly alter bones' organic matrix." *Journal of the mechanical behavior of biomedical materials* 29:252-258.

Hardy, Claude H, and Pedro V Marcal. 1973. "Elastic analysis of a skull." *Journal of Applied Mechanics* 40 (4):838-842.

He, Junyan, Jiawei Yan, Susan Margulies, Brittany Coats, and Ashley D Spear. 2020. "An adaptive-remeshing framework to predict impact-induced skull fracture in infants." *Biomechanics and Modeling in Mechanobiology*:1-11.

Hobbs, C. J. 1984. "Skull fracture and the diagnosis of abuse." *Archives of Disease in Childhood* 59 (3):246-252. doi: 10.1136/adc.59.3.246.

Holbourn, AHS. 1943. "Mechanics of head injuries." *The Lancet* 242 (6267):438-441.

Horgan, TJ, and MD Gilchrist. 2004. "Influence of FE model variability in predicting brain motion and intracranial pressure changes in head impact simulations." *International Journal of Crashworthiness* 9 (4):401-418.

Horgan, TJ, and Michael D Gilchrist. 2003. "The creation of three-dimensional finite element models for simulating head impact biomechanics." *International Journal of Crashworthiness* 8 (4):353-366.

Hubbard, Robert P. 1971. "Flexure of layered cranial bone." *Journal of Biomechanics* 4 (4):251-263.

Hubbard, Robert P, John W Melvin, and Iqbal T Barodawala. 1971. "Flexure of cranial sutures." *Journal of biomechanics* 4 (6):491-496.

Institute, University of Michigan. Highway Safety Research, and Richard G Snyder. 1977. *Anthropometry of infants, children, and youths to age 18 for product safety design*: US Government Printing Office.

Jaslow, C. R. 1990. "Mechanical properties of cranial sutures." *Journal of Biomechanics* 23 (4):313-321. doi: 10.1016/0021-9290(90)90059-C.

Jenson, Daniel, and Vinu U Unnikrishnan. 2015. "Energy dissipation of nanocomposite based helmets for blast-induced traumatic brain injury mitigation." *Composite structures* 121:211-216.

Jiang, Binhui, Feng Zhu, Libo Cao, Barbara R. Presley, Ming Shen, and King H. Yang. 2017. "Computational Study of Fracture Characteristics in Infant Skulls Using a Simplified Finite Element Model." *Journal of Forensic Sciences* 62 (1):39-49. doi: 10.1111/1556-4029.13241.

Johnson, K., T. Fischer, S. Chapman, and B. Wilson. 2005. "Accidental head injuries in children under 5 years of age." *Clinical Radiology* 60 (4):464-468. doi: 10.1016/j.crad.2004.09.013.

Johnson, L, and Roland Auer. 2018. "Commentary on: Jiang B, Zhu F, Cao L, Presley BR, Shen MS, Yang KH. Computational study of fracture characteristics in infant skulls using a simplified finite element model. J Forensic Sci 2017; 62 (1): 39–49." *Journal of forensic sciences* 63 (1):345-348.

Jones, Michael, D Darwall, G Khalid, R Prabhu, A Kemp, Owen J Arthurs, and P Theobald. 2017. "Development and validation of a physical model to investigate the biomechanics of infant head impact." *Forensic science international* 276:111-119.

Kang, Ho-Sung, Rémy Willinger, Baye M Diaw, and Bryan Chinn. 1997. Validation of a 3D anatomic human head model and replication of head impact in motorcycle accident by finite element modeling. SAE Technical Paper.

Katzenberger, Michael J, Devon L Albert, Amanda M Agnew, and Andrew R Kemper. 2020. "Effects of sex, age, and two loading rates on the tensile material properties of human rib cortical bone." *Journal of the mechanical behavior of biomedical materials* 102:103410.

Kelly, P., S. John, A. L. Vincent, and P. Reed. 2015. "Abusive head trauma and accidental head injury: a 20-year comparative study of referrals to a hospital child protection team." *ARCHIVES OF DISEASE IN CHILDHOOD* 100 (12):1123-1130. doi: 10.1136/archdischild-2014-306960.

Khalid, Ghaidaa A, Raj K Prabhu, Owen Arthurs, and Michael D Jones. 2019. "A coupled physical-computational methodology for the investigation of short fall related infant head impact injury." *Forensic science international* 300:170-186.

Kieser, Jules. 2012. "Biomechanics of Bone and Bony Trauma." In *Forensic biomechanics*, edited by Jules Kieser, Michael Taylor and Debra D. Carr. Chichester, West Sussex, UK: Wiley-Blackwell.

King, Albert I, King H Yang, Liying Zhang, Warren Hardy, and David C Viano. 2003. "Is head injury caused by linear or angular acceleration." IRCOBI conference.

Kleiven, Svein. 2006. "Evaluation of head injury criteria using a finite element model validated against experiments on localized brain motion, intracerebral acceleration, and intracranial pressure." *International Journal of Crashworthiness* 11 (1):65-79.

Kleiven, Svein. 2007. "Predictors for traumatic brain injuries evaluated through accident reconstructions." *Stapp car crash journal* 51:81-114.

Kleiven, Svein, and Warren N Hardy. 2002. "Correlation of an FE model of the human head with local brain motion: Consequences for injury prediction." *Stapp Car Crash Journal* 46:123-144.

Klinich, Kathleen DeSantis, Gregory M Hulbert, and Lawrence W Schneider. 2002. Estimating infant head injury criteria and impact response using crash reconstruction and finite element modeling. SAE Technical Paper.

Kriewall, Timothy J. 1982. "Structural, mechanical, and material properties of fetal cranial bone." *American journal of obstetrics and gynecology* 143 (6):707-714.

Krouskop, Thomas A, Thomas M Wheeler, Faouzi Kallel, Brian S Garra, and Timothy Hall. 1998. "Elastic moduli of breast and prostate tissues under compression." *Ultrasonic imaging* 20 (4):260-274.

Kulkarni, SG, X-L Gao, SE Horner, JQ Zheng, and NV David. 2013. "Ballistic helmets–their design, materials, and performance against traumatic brain injury." *Composite Structures* 101:313-331.

Laforest, Sophie, Yvonne Robitaille, Dominique Lesage, and Danièle Dorval. 2001. "Surface characteristics, equipment height, and the occurrence and severity of playground injuries." *Injury Prevention* 7 (1):35-40.

Leask, Anna. 2016. "61 Little Names on New Zealand's Roll of Dishonour." *NZ Herald*, 21 March 2016.

Lee, Hwa-Pyung, and SW Gong. 2010. "Finite element analysis for the evaluation of protective functions of helmets against ballistic impact." *Computer methods in biomechanics and biomedical engineering* 13 (5):537-550.

Lewis, Lawrence M, Rosanne Naunheim, John Standeven, and Keith S Naunheim. 1993. "Quantitation of impact attenuation of different playground surfaces under various environmental conditions using a tri-axial accelerometer." *The Journal of trauma* 35 (6):932-935.

Li, Xiaogai, Håkan Sandler, and Svein Kleiven. 2017. "The importance of nonlinear tissue modelling in finite element simulations of infant head impacts." *Biomechanics and Modeling in Mechanobiology* 16:823-840. doi: 10.1007/s10237-016-0855-5.

Li, Xiaogai, Håkan Sandler, and Svein Kleiven. 2019. "Infant skull fractures: Accident or abuse?: Evidences from biomechanical analysis using finite element head models." *Forensic science international* 294:173-182.

Li, Z. G., X. Luo, and J. H. Zhang. 2013. "Development/global validation of a 6-month-old pediatric head finite element model and application in investigation of drop-induced infant head injury." *COMPUTER METHODS AND PROGRAMS IN BIOMEDICINE* 112 (3):309-319. doi: 10.1016/j.cmpb.2013.05.008.

Li, Z., W. Liu, J. Zhang, and J. Hu. 2015. "Prediction of skull fracture risk for children 0-9 months old through validated parametric finite element model and cadaver test reconstruction." *Int J Legal Med* 129 (5):1055-66. doi: 10.1007/s00414-015-1190-6.

Li, Zhigang, Xiaoqiang Han, Hao Ge, and Chunsheng Ma. 2016. "A semi-automatic method of generating subject-specific pediatric head finite element models for impact dynamic responses to head injury." *Journal of the Mechanical Behavior of Biomedical Materials* 60:557-567. doi: 10.1016/j.jmbbm.2016.03.021.

Li, Zhigang, Jingwen Hu, Matthew P. Reed, Jonathan D. Rupp, Carrie N. Hoff, Jinhuan Zhang, and Bo Cheng. 2013. "Erratum to: Development, Validation, and Application of a Parametric Pediatric Head Finite Element Model for Impact Simulations." *Annals of Biomedical Engineering* 41 (1):215-220. doi: 10.1007/s10439-012-0682-5.

Li, Zhigang, Byoung-Keon Park, Weiguo Liu, Jinhuan Zhang, Matthew P Reed, Jonathan D Rupp, Carrie N Hoff, and Jingwen Hu. 2015. "A statistical skull geometry model for children 0-3 years old." *PloS one* 10 (5).

Li, Zhigang, Jinhuan Zhang, and Jingwen Hu. 2013. "Surface material effects on fall-induced paediatric head injuries: a combined approach of testing, modelling and optimisation." *International journal of crashworthiness* 18 (4):371-384.

Look Floors. 2018. "Look Floors Underlay Range." accessed 17 June 2020. https://www.lookfloors.co.nz/cdn/images/productdocument/LF-Underlay-brochure-range-Oct18-v3.pdf.

Loyd, Andre Matthew. 2011. "Studies of the human head from neonate to adult: an inertial, geometrical and structural analysis with comparisons to the ATD head." Citeseer.

Loyd, Andre Matthew, Roger W Nightingale, Jason F Luck, Yin Song, Lucy Fronheiser, Hattie Cutcliffe, Barry S Myers, and Cameron R Dale Bass. 2015. "The compressive stiffness of human pediatric heads." *Journal of biomechanics* 48 (14):3766-3775.

Mac Donald, Bryan J. 2011. *Practical stress analysis with finite elements*. 2nd ed. Dublin: Glasnevin Publishing.

Margulies, S. S., and K. L. Thibault. 2000. "Infant skull and suture properties: Measurements and implications for mechanisms of pediatric brain injury." *Journal of Biomechanical Engineering* 122 (4):364-371. doi: 10.1115/1.1287160.

Matanaghi, Aysouda, Aamir Raja, Celeste Leary, Maya Rajeswari Amma, Raj Panta, Marzieh Anjomrouz, Mahdieh Moghiseh, Anthony Butler, Benjamin Bamford, and Mars Collaboration. 2019. "Semi-automatic quantitative assessment of site-specific bone health using spectral photon counting CT." *Journal of Nuclear Medicine* 60 (supplement 1):1297-1297.

McElhaney, James H, John L Fogle, John W Melvin, Russell R Haynes, Verne L Roberts, and Nabih M Alem. 1970. "Mechanical properties of cranial bone." *Journal of biomechanics* 3 (5):495IN5497-496511.

McElhaney, James H, Verne L Roberts, and Joseph F Hilyard. 1976. *Handbook of human tolerance*: Japan Automobile Research Institute, Incorporated (JARI).

McKay, Michael D, Richard J Beckman, and William J Conover. 1979. "Comparison of three methods for selecting values of input variables in the analysis of output from a computer code." *Technometrics* 21 (2):239-245.

McKenzie and Willis. 2020. "Choosing the Right Carpet Underlay." accessed 17 June 2020. https://www.mckenzieandwillis.co.nz/choosing-the-right-carpet-underlay-6-must-ask-questions/#:~:text=What%20is%20the%20thickness%20and,the%20carpet%20underlay%20will%20feel.

McPherson, Gregg K, and Timothy J Kriewall. 1980. "The elastic modulus of fetal cranial bone: a first step towards an understanding of the biomechanics of fetal head molding." *Journal of biomechanics* 13 (1):9-16.

Meyers, Marc André, Po-Yu Chen, Albert Yu-Min Lin, and Yasuaki Seki. 2008. "Biological materials: Structure and mechanical properties." *Progress in Materials Science* 53 (1):1-206. doi: 10.1016/j.pmatsci.2007.05.002.

Miller, Reid T, Susan S Margulies, Matt Leoni, Masahiro Nonaka, Xiaohan Chen, Douglas H Smith, and David F Meaney. 1998. "Finite element modeling approaches for predicting injury in an experimental model of severe diffuse axonal injury." *SAE transactions*:2798-2810.

Minns, R. A., and J. Keith Brown. 2005. *Shaking and other non-accidental head injuries in children*. Vol. no. 162. London: Mac Keith.

Mooney, Melvin. 1940. "A theory of large elastic deformation." *Journal of applied physics* 11 (9):582-592.

Morrison, B, HL Cater, CC Wang, FC Thomas, CT Hung, GA Ateshian, and LE Sundstrom. 2003. "A tissue level tolerance criterion for living brain developed with an in vitro model of traumatic mechanical loading." *Stapp car crash journal* 47 (47):93-105.

Mota, A, WS Klug, M Ortiz, and A Pandolfi. 2003. "Finite-element simulation of firearm injury to the human cranium." *Computational Mechanics* 31 (1-2):115-121.

Mouzon, Benoit C, Corbin Bachmeier, Joseph O Ojo, Christopher M Acker, Scott Ferguson, Daniel Paris, Ghania Ait-Ghezala, Gogce Crynen, Peter Davies, and Michael Mullan. 2018. "Lifelong

behavioral and neuropathological consequences of repetitive mild traumatic brain injury." *Annals of clinical and translational neurology* 5 (1):64-80.

Murakami, S, and Y Liu. 1995. "Mesh-dependence in local approach to creep fracture." *International Journal of Damage Mechanics* 4 (3):230-250.

Ogden, Ray W. 1984. Non-linear elastic deformations. Elsevier.

Oh, S. 1983. "Clinical and experimental morphological study of depressed skull fracture." *Acta neurochirurgica* 68 (1-2):111-121.

Olver, John H, Jennie L Ponsford, and Carolyn A Curran. 1996. "Outcome following traumatic brain injury: a comparison between 2 and 5 years after injury." *Brain injury* 10 (11):841-848.

Ommaya, AK, W Goldsmith, and L Thibault. 2002. "Biomechanics and neuropathology of adult and paediatric head injury." *British journal of neurosurgery* 16 (3):220-242.

Pan, Bing, Anand Asundi, Huimin Xie, and Jianxin Gao. 2009. "Digital image correlation using iterative least squares and pointwise least squares for displacement field and strain field measurements." *Optics and Lasers in Engineering* 47 (7-8):865-874.

Pan, Bing, Kemao Qian, Huimin Xie, and Anand Asundi. 2009. "Two-dimensional digital image correlation for in-plane displacement and strain measurement: a review." *Measurement science and technology* 20 (6):062001.

Pan, Bing, Huimin Xie, Zhiqing Guo, and Tao Hua. 2007. "Full-field strain measurement using a two-dimensional Savitzky-Golay digital differentiator in digital image correlation." *Optical Engineering* 46 (3):033601.

Panzer, Matthew B, Barry S Myers, Bruce P Capehart, and Cameron R Bass. 2012. "Development of a finite element model for blast brain injury and the effects of CSF cavitation." *Annals of biomedical engineering* 40 (7):1530-1544.

Peters, W. H., and W. F. Ranson. 1982a. "DIGITAL IMAGING TECHNIQUES IN EXPERIMENTAL STRESS ANALYSIS." *Optical Engineering* 21 (3):427-431. doi: 10.1117/12.7972925.

Peters, WH, and WF Ranson. 1982b. "Digital imaging techniques in experimental stress analysis." *Optical engineering* 21 (3):213427.

Peters, WH, WF Ranson, MA Sutton, TC Chu, and J Anderson. 1983. "Application of digital correlation methods to rigid body mechanics." *Optical Engineering* 22 (6):226738.

Pintar, Frank A, Mat MGM Philippens, JiangYue Zhang, and Narayan Yoganandan. 2013. "Methodology to determine skull bone and brain responses from ballistic helmet-to-head contact loading using experiments and finite element analysis." *Medical engineering & physics* 35 (11):1682-1687.

Plunkett, John. 2001. "Fatal pediatric head injuries caused by short-distance falls." *The American journal of forensic medicine and pathology* 22 (1):1-12.

Ponce, E., and D. Ponce. 2011. "Modeling Neck and Brain Injuries in Infants." 90-96.

Prange, Michael T., Brittany Coats, Ann-Christine Duhaime, and Susan S. Margulies. 2003. "Anthropomorphic simulations of falls, shakes, and inflicted impacts in infants." *Journal of Neurosurgery* 99 (1):143-150.

Prange, Michael T., Jason F. Luck, Alan Dibb, Chris A. Van Ee, Roger W. Nightingale, and Barry S. Myers. 2004. "Mechanical properties and anthropometry of the human infant head." *Stapp car crash journal* 48:279.

Prange, Michael T., and Susan S. Margulies. 2002. "Regional, directional, and age-dependent properties of the brain undergoing large deformation." *Journal of Biomechanical Engineering* 124 (2):244-252. doi: 10.1115/1.1449907.

Rangarajan, Nagarajan, Tariq Shams, Carole Jenny, and Tsuguhiro Fukuda. 2017. "Probability of pediatric skull fracture at various contact velocities." Enhanced Safety Vehicle Conference Proceedings, Detroit.

Raul, Jean-Sébastien, Daniel Baumgartner, Rémy Willinger, and Bertrand Ludes. 2006. "Finite element modelling of human head injuries caused by a fall." *International Journal of Legal Medicine* 120 (4):212-218.

Raul, Jean-Sébastien, Caroline Deck, Franck Meyer, Annie Geraut, Rémy Willinger, and Bertrand Ludes. 2007. "A finite element model investigation of gunshot injury." *International journal of legal medicine* 121 (2):143-146.

Raul, Jean-Sébastien, Caroline Deck, Rémy Willinger, and Bertrand Ludes. 2008. "Finite-element models of the human head and their applications in forensic practice." *International journal of legal medicine* 122 (5):359-366.

Reddy, Junuthula Narasimha. 1993. *An introduction to the finite element method*. Vol. 2: McGraw-Hill New York.

Reece, Robert M., and Robert Sege. 2000. "Childhood head injuries: Accidental or inflicted?" *Archives of Pediatrics and Adolescent Medicine* 154 (1):11-15.

Reu, Phillip. 2012. "Stereo-rig Design: Camera Selection—Part 2." *Experimental Techniques* 36 (6):3-4.

Reu, Phillip. 2013. "Stereo-rig Design: Lighting—Part 5." *Experimental Techniques* 37 (3):1-2.

Reu, Phillip. 2014a. "All about speckles: aliasing." *Experimental Techniques* 38 (5):1-3.

Reu, Phillip. 2014b. "Speckles and their relationship to the digital camera." *Experimental Techniques* 38 (4):1-2.

Reu, Phillip. 2015. "All about speckles: speckle density." *Experimental Techniques* 39 (3):1-2.

Ridgway, Emily B., and Howard L. Weiner. 2004. "Skull deformities." *Pediatric Clinics of North America* 51 (2):359-387. doi: 10.1016/j.pcl.2003.12.001.

Rimel, R. W., B. Giordani, J. T. Barth, and J. A. Jane. 1982. "Moderate head injury: Completing the clinical spectrum of brain trauma." *Neurosurgery* 11 (3):344-351.

Rivlin, RS. 1948. "Large elastic deformations of isotropic materials IV. Further developments of the general theory." *Phil. Trans. R. Soc. Lond. A* 241 (835):379-397.

Roach, Jonathan P., Shannon N. Acker, Denis D. Bensard, Andrew P. Sirotnak, Frederick M. Karrer, and David A. Partrick. 2014. "Head injury pattern in children can help differentiate accidental from non-accidental trauma." *Pediatric Surgery International* 30 (11):1103-1106. doi: 10.1007/s00383-014-3598-3.

Roth, Sébastien, Jean-Sébastien Raul, Bertrand Ludes, and Rémy Willinger. 2007. "Finite element analysis of impact and shaking inflicted to a child." *International Journal of Legal Medicine* 121 (3):223-228. doi: 10.1007/s00414-006-0129-3.

Roth, Sebastien, Jean-Sebastien Raul, and Remy Willinger. 2010. "Finite element modelling of paediatric head impact: Global validation against experimental data." *Computer Methods and Programs in Biomedicine* 99 (1):25-33. doi: 10.1016/j.cmpb.2009.10.004.

Roth, Sébastien, Jean-Sébastien Raul, and Rémy Willinger. 2008. "Biofidelic child head FE model to simulate real world trauma." *Computer Methods and Programs in Biomedicine* 90 (3):262-274. doi: 10.1016/j.cmpb.2008.01.007.

Ruan, Jesse S, Tawfik B Khalil, and Albert I King. 1993. Finite element modeling of direct head impact. SAE Technical Paper.

Salimi Jazi, Mehdi, Asghar Rezaei, Ghodrat Karami, Fardad Azarmi, and Mariusz Ziejewski. 2014. "A computational study of influence of helmet padding materials on the human brain under ballistic impacts." *Computer methods in biomechanics and biomedical engineering* 17 (12):1368-1382.

Schindelin, Johannes, Ignacio Arganda-Carreras, Erwin Frise, Verena Kaynig, Mark Longair, Tobias Pietzsch, Stephan Preibisch, Curtis Rueden, Stephan Saalfeld, and Benjamin Schmid. 2012. "Fiji: an open-source platform for biological-image analysis." *Nature methods* 9 (7):676.

Schmitt, Kai-Uwe. 2014. *Trauma biomechanics: an introduction to injury biomechanics*. 4th;4;4th 2014; ed. Heidelberg: Springer.

Schneider, Caroline A, Wayne S Rasband, and Kevin W Eliceiri. 2012. "NIH Image to ImageJ: 25 years of image analysis." *Nature methods* 9 (7):671-675.

Shields, Brenda J, and Gary A Smith. 2009. "The potential for brain injury on selected surfaces used by cheerleaders." *Journal of athletic training* 44 (6):595-602.

Shugar, TA. 1975. Transient structural response of the linear skull-brain system. SAE Technical Paper.

Song, Jeong-Hoon, Hongwu Wang, and Ted Belytschko. 2008. "A comparative study on finite element methods for dynamic fracture." *Computational Mechanics* 42 (2):239-250.

Song, Jeong-Hoon, Pedro MA Areias, and Ted Belytschko. 2006. "A method for dynamic crack and shear band propagation with phantom nodes." *International Journal for Numerical Methods in Engineering* 67 (6):868-893.

Spearman, C. 1904. "The Proof and Measurement of Association between Two Things." *The American Journal of Psychology* 15 (1):72-101. doi: 10.2307/1412159.

Spies, E. L., and J. Klevens. 2016. "Fatal Abusive Head Trauma Among Children Aged < 5 Years - United States, 1999-2014." *MMWR-MORBIDITY AND MORTALITY WEEKLY REPORT* 65 (20):505-509. doi: 10.15585/mmwr.mm6520a1.

Strachan, Donald S. 1970. "The anatomy and physiology of the head and neck." *SAE Technical Papers* 12-22. doi: 10.4271/700195.

Sutton, M. A., W. J. Wolters, W. H. Peters, W. F. Ranson, and S. R. McNeill. 1983. "Determination of displacements using an improved digital correlation method." *Image and Vision Computing* 1 (3):133-139. doi: 10.1016/0262-8856(83)90064-1.

Takhounts, Erik G, Rolf H Eppinger, J Quinn Campbell, and Rabih E Tannous. 2003. "On the development of the SIMon finite element head model." *Stapp car crash journal* 47:107.

Takhounts, Erik G, Stephen A Ridella, Vikas Hasija, Rabih E Tannous, J Quinn Campbell, Dan Malone, Kerry Danelson, Joel Stitzel, Steve Rowson, and Stefan Duma. 2008. "Investigation of traumatic brain injuries using the next generation of simulated injury monitor (SIMon) finite element head model." *Stapp car crash journal* 52:1.

Tan, Long Bin, Kwong Ming Tse, Heow Pueh Lee, Vincent Beng Chye Tan, and Siak Piang Lim. 2012. "Performance of an advanced combat helmet with different interior cushioning systems in ballistic impact: Experiments and finite element simulations." *International Journal of Impact Engineering* 50:99-112.

Teasdale, G., and B. Jennett. 1974. "Assessment of coma and impaired consciousness. A practical scale." *Lancet (London, England)* 2 (7872):81.

Teasdale, G., A. Maas, F. Lecky, G. Manley, N. Stocchetti, and G. Murray. 2014. "The Glasgow Coma Scale at 40 years: standing the test of time." *LANCET NEUROLOGY* 13 (8):844-854. doi: 10.1016/S1474-4422(14)70120-6.

Thibault, Kirk L., and Susan S. Margulies. 1998. "Age-dependent material properties of the porcine cerebrum: effect on pediatric inertial head injury criteria." *Journal of Biomechanics* 31 (12):1119-1126. doi: 10.1016/S0021-9290(98)00122-5.

Transportation;, U.S. Department of. 2016. National Highway Traffic Safety Administration Laboratory Test Procedure for FMVSS No 201U.

Trotta, Antonia, Dimitris Zouzias, Guido De Bruyne, and Aisling Ní Annaidh. 2018. "The importance of the scalp in head impact kinematics." *Annals of biomedical engineering* 46 (6):831-840.

Tse, Kwong Ming, Siak Piang Lim, Vincent Beng Chye Tan, and Heow Pueh Lee. 2014. "A review of head injury and finite element head models." *Am J Eng Technol Soc* 1 (5):28-52.

Tse, Kwong Ming, Long Bin Tan, Shu Jin Lee, Siak Piang Lim, and Heow Pueh Lee. 2014. "Development and validation of two subject-specific finite element models of human head against three cadaveric experiments." *International journal for numerical methods in biomedical engineering* 30 (3):397-415.

Tushak, Sophia, Jalaj Maheshwari, and Aditya Belwadi. 2019. "Responses of the scaled infant human body model in simulated frontal motor vehicle crashes." 2019 ESV Conference.

Versace, John. 1971. A review of the severity index. SAE Technical Paper.

Wang, J. W., D. H. Zou, Z. D. Li, P. Huang, D. R. Li, Y. Shao, H. J. Wang, and Y. J. Chen. 2014a. "Mechanical Properties of Cranial Bones and Sutures in 1-2-Year-Old Infants." *MEDICAL SCIENCE MONITOR* 20:1808-1813. doi: 10.12659/MSM.892278.

Wang, Jiawen, Donghua Zou, Zhengdong Li, Ping Huang, Dongri Li, Yu Shao, Huijun Wang, and Yijiu Chen. 2014b. "Mechanical properties of cranial bones and sutures in 1–2-year-old infants." *Medical science monitor: international medical journal of experimental and clinical research* 20:1808.

Waschke, Jens, and Friedrich Paulsen. 2013. *Sobotta Atlas of Human Anatomy*. Vol. 3: Elsevier.

Weber, W. 1984. "Experimental studies of skull fractures in infants." *Zeitschrift fur Rechtsmedizin. Journal of legal medicine* 92 (2):87-94.

Weber, W. 1985. "Biomechanical fragility of the infant skull." *Zeitschrift fur Rechtsmedizin. Journal of legal medicine* 94 (2):93-101.

Weil, Zachary M, and Kate Karelina. 2019. "Lifelong consequences of brain injuries during development: from risk to resilience." *Frontiers in neuroendocrinology* 55:100793.

Whitfield, Peter C. 2009. *Head injury: a multidisciplinary approach*. Cambridge: Cambridge University Press.

Wilkins, Barry. 1997. "Head injury—abuse or accident?" *Archives of disease in childhood* 76 (5):393-397.

Williams, E. 2008. "The Biomechanics of Blunt Force Trauma." Masters Thesis in Forensic Science, University of Auckland.

Williams, RA. 1991. "Injuries in infants and small children resulting from witnessed and corroborated free falls." *Journal of Trauma and Acute Care Surgery* 31 (10):1350-1352.

Willinger, R., L. Taleb, and C. M. Kopp. 1995. "Modal and temporal analysis of head mathematical models." *Journal of Neurotrauma* 12 (4):743-754.

Wu, Shen R, and Lei Gu. 2012. *Introduction to the explicit finite element method for nonlinear transient dynamics*: John Wiley & Sons.

Xu, X-P, and Alan Needleman. 1994. "Numerical simulations of fast crack growth in brittle solids." *Journal of the Mechanics and Physics of Solids* 42 (9):1397-1434.

Young, Richard W. 1959. "Age changes in the thickness of the scalp in white males." *Human biology* 31 (1):74-79.

Yue, Xianfang, Li Wang, Shufeng Sun, and Lige Tong. 2008. "Viscoelastic finite-element analysis of human skull-dura mater system as intracranial pressure changing." *African Journal of Biotechnology* 7 (6).

Yushkevich, Paul A, Joseph Piven, Heather Cody Hazlett, Rachel Gimpel Smith, Sean Ho, James C Gee, and Guido Gerig. 2006. "User-guided 3D active contour segmentation of anatomical structures: significantly improved efficiency and reliability." *Neuroimage* 31 (3):1116-1128.

Zhang, Jian, Narayan Yoganandan, Frank A Pintar, Thomas A Gennarelli, and Barry S Shender. 2009. "A finite element study of blast traumatic brain injury." *Biomed Sci Instrum* 45:119-124.

Zhang, Liying, Rahul Makwana, and Sumit Sharma. 2013. "Brain response to primary blast wave using validated finite element models of human head and advanced combat helmet." *Frontiers in neurology* 4.

Zhang, Liying, King H Yang, Ramesh Dwarampudi, Kiyoshi Omori, Tieliang Li, Kun Chang, Warren N Hardy, Tom B Khalil, and Albert I King. 2001. "Recent advances in brain injury research: a new human head model development and validation." *Stapp Car Crash J* 45 (11):369-394.

Zhou, Chun, Tawfik B Khalil, and Albert I King. 1995. A new model comparing impact responses of the homogeneous and inhomogeneous human brain. SAE Technical Paper.

Zhou, Chun, Twafik B Khalil, Albert I King, and Ljubisa J Dragovic. 1997. "Head injury assessment of a real world crash by finite element modeling." *NASA* (19980003886).

Zwirner, Johann; Safavi, Sarah; Scholze, Mario; Chun Li, Kai; Waddell, John Neil; Busse, Bjorn; Ondruschka, Benjamin; Hammer, Niels;. 2021. "Topographical Mapping of the Mecahnical Characteristics of the Human Neurocranium Considering the Role of Individual Layers." *Scientific Reports*.